Relationships Between Mechanism of Formation, Microstructure and Properties of Porous Reaction Bonded Silicon Nitride Ceramics

Raheleh Nikonam Mofrad

A Thesis

In the Department

of

Mechanical, Industrial and Aerospace Engineering

Presented in Partial Fulfillment of the Requirements
For the Degree of
Doctor of Philosophy (Mechanical Engineering) at
Concordia University
Montreal, Quebec, Canada

November 2019

@ Raheleh Nikonam Mofrad, 2019

CONCORDIA UNIVERSITY

SCHOOL OF GRADUATE STUDIES

This is to certify that the thesis prepared

By: Raheleh Nikonam Mofrad

Entitled: Relationships Between Mechanism of Formation, Microstructure and Properties of Porous Reaction Bonded Silicon Nitride Ceramics

and submitted in partial fulfillment of the requirements for the degree of

Doctor Of Philosophy (Mechanical Engineering)

complies with the regulations of the University and meets the accepted standards with respect to originality and quality.

Signed by the final examining committee:

_____ Chair
Dr. Catherine Mulligan

_____ External Examiner
Dr. Mathieu Brochu

_____ External to Program
Dr. Michelle Nokken

_____ Examiner
Dr. Christian Moreau

_____ Examiner
Dr. Mehdi Hojjati

_____ Thesis Co-Supervisor
Dr. Robin Drew

_____ Thesis Co-Supervisor
Dr. Martin Pugh

Approved by _____
Dr. Ivan Contreras, Graduate Program Director

January 21, 2020 _____
Dr. Amir Asif, Dean
Gina Cody School of Engineering & Computer Science

Abstract

Relationships Between Mechanism of Formation, Microstructure and Properties of Porous Reaction Bonded Silicon Nitride Ceramics

Raheleh Nikonam Mofrad, Ph.D.

Concordia University, 2019

Silicon nitride (Si_3N_4) is one of the most promising candidates for application in gas turbine and piston engines, catalyst supports, diesel particulate filters and interpenetrating composites mainly because it possesses good thermal and chemical stability, high hardness, and excellent corrosion and wear resistance under harsh conditions. Porous Si_3N_4 ceramics with high porosity have previously been developed by a combination of reaction bonding of Si powder, sacrificial templates and gel-casting. To modify the microstructural and mechanical properties, this technique maybe followed by a post heat-treatment in which samples that contain various oxide aids are heated at elevated temperatures and embedded in a Si_3N_4-based powder bed. Despite many studies on the fabrication and characterization of porous Si_3N_4, there is still a lack of understanding of a) the role of additives on the nitriding mechanism and formation of a specific Si_3N_4 grain morphology, b) the relationship between microstructure and properties of porous ceramics and c) the influence of the powder bed composition on the microstructure of heat-treated Si_3N_4 ceramics.

The main objective of this study was to investigate the microstructure of porous reaction bonded Si_3N_4 and its properties in the presence of MgO, CaO and Al_2O_3. Samples with high porosity were prepared by a process that utilizes a sacrificial template technique, along with gel-casting and nitriding. Mechanisms and thermodynamics of reactions, microstructure of phases present, morphologies of grains and pores, pore size distribution, pore interconnectivity and accessibility, porosity and density, linear shrinkage and weight loss, as well as mechanical strength of the fabricated foams are discussed. For this purpose, microstructural transformations of foams both

during in situ nitridation at T≤ 1425°C and post heat-treatment at T≤ 1700°C have been considered. Throughout the text, 'RBSN' refers to reaction bonded Si_3N_4 samples with no additive, while in the presence of the above-mentioned oxides, samples have been labelled as MgO-RBSN, CaO-RBSN and Al_2O_3-RBSN, respectively.

The results revealed that in an atmosphere of ultra-pure nitrogen and during the in situ nitridation of Si, whiskers grew in globular agglomerates into the large pores and decreased the pore interconnectivity and size. However, upon adding MgO, the grain morphology was altered and eventually at 12 wt.% MgO, whisker formation was completely eliminated, and the microstructure was modified to a combination of Si_3N_4 α-matte grains and β-rods. Based on the results of XRD analyses along with thermodynamic studies, some intermediate phases formed as a result of reactions between volatile MgO and silica, which is naturally present on the surface of Si particles. This possibly decreased the content of SiO (g), as the predominant reactant of α-whisker formation, and altered the ratio of α/β-Si_3N_4 phases. Subsequently, in this microstructure, the formation of fully interconnected pore channels with large pores (< 40 μm) and clean cavities was confirmed by 3D and 2D visualization images.

Subsequently, the microstructural transition of Si_3N_4 grains heat-treated in the presence and absence of MgO in the Si_3N_4-based powder bed (i.e., labelled as SN-MgO and SN powder beds, respectively) was investigated. This illustrated that the grain morphology and microstructures of samples were strongly affected by the presence of volatile MgO in the powder bed. During liquid phase sintering at 1700°C, α-matte dissolved, grains precipitated as coarse β-rods and a Mg-Si-O-N glassy phase was developed. Similarly, α-whiskers gradually disappeared and recrystallized as 100% fine β-grains. During heat-treatment, weight losses and α/β phase ratio were substantially decreased while linear shrinkage and grain coarsening were increased. Unlike α-matte grains, α-whiskers extensively densified upon heat-treatment. This led to a high densification and a sharp decrease in porosity level. Consequently, a macro/microstructure with less interconnectivity, clean spherical cavities and large pore size resulted. The observed microstructural changes occurred due to the high volatility of magnesia, by vapor phase transport of species from the MgO-SN powder bed to the porous structure, and through a subsequent solution-precipitation mechanism. No significant morphology change, shrinkage, densification or phase transformation were observed in the samples heat-treated in SN powder bed.

Subsequently, morphology and microstructures of samples were correlated to the structure of pores, pore size distribution, level of porosity and density. Pores were classified based on their shape (spherical or irregular), size, interconnectivity (open or isolated) and their fabrication mechanism. Pores with large and whisker-free spherical cavities and unimodal pore size distributions were developed in samples composed of either α-matte grains or β-rods. In contrast, complex, fine and irregular pores were fabricated in the presence of elongated Si_3N_4 whiskers; therefore, a bimodal pore size distribution resulted. This study showed that the obtained foams had tailorable properties allowing mean pore sizes ($\overline{d}$) ranging from 1.3 to 13.8 μm and 30 to 76 vol.% porosity.

In addition, the interaction of CaO, MgO and Al_2O_3 with silicon and nitrogen were examined comparatively. In the presence of CaO and through a reaction between Si (g) and molecular nitrogen, the dominant microstructure was α-matte grains (α/β-Si_3N_4 ratio≈ 3.9) with interconnected, spherical and open cavities. Formation of intermediate phases due to the reactions with surface silica could have possibly affected the content of SiO vapor and thus hindered the formation of whiskers. By substituting CaO (15 mol%≈ 6 wt.%) with the same mol.% of MgO (15 mol%≈ 4.3 wt.%), the content of intermediate phases in the microstructure was reduced, a low number of α-whiskers formed, and the α/β-Si_3N_4 ratio was decreased by almost 55%. Yet, the highest quantity of whiskers and the lowest α/β-Si_3N_4 ratio were developed in the presence of Al_2O_3 (15 mol%≈ 11 wt.%). High thermal and chemical stability of Al_2O_3 possibly decreased the content of oxygen generated and hindered the formation of intermediate phases. This in turn could increase the likelihood of SiO (g), a reactant required for α-whiskers formation, and atomic nitrogen, a reactant needed for β-phase formation, being present in the atmosphere.

Both compressive strength and flexural strength were increased in the presence of interlocked whiskers with fine inter-particle pores or in structures with low porosity levels, whereas a combination of high porosity and large pores limited the strength of the resultant foams. In addition to the microstructure of pores, interconnectivity and accessibility of pore channels, the amount of shrinkage and densification, weight loss and density were strongly dependent on the presence of different oxide additives. Hence by designing the composition of the starting powder mixture and the surrounding powder bed, tailored microstructures with different mechanical strengths can be easily obtained. This research should be of interest to scientists and engineers concerned with the

processing and use of porous ceramics and, in particular, this information and findings can be used in the microstructural design of Si_3N_4 and related materials.

Dedicated to my loving parents,

For their endless encouragement and eternal love,

And to my beloved husband, Farid,

For his never-ending love, supports and patience.

Acknowledgement

First and foremost, I would like to express my sincere gratitude to my supervisors, Prof. Robin A.L. Drew and Prof. Martin D. Pugh, for the continuous support and guidance during my Ph.D. study. Your positive outlook and confidence inspired me in research and gave me encouragement to explore new ideas. I have truly enjoyed working with you over these years and it was a great honour to finish this work under your supervisions.

I would like to acknowledge the financial support provided by Natural Sciences and Engineering Research Council of Canada (NSERC) through the Discovery Grants program for this research.

Besides, I would like to thank my thesis committee: Prof. Christian Moreau, Prof. Mehdi Hojjati and Prof. Michelle Nokken for their insightful comments and precious time. I am grateful to Prof. Suong Van Hoa, Prof. Christian Moreau and Prof. Ali Dolatabadi for the authorizations to use their laboratory facilities.

I would like to thank Dr. Elmira Moosavi-Khoonsari for her assistance with the thermodynamic calculations. I am also appreciative of Dr. Fariba Tarasi for performing MIP analysis. My gratitude is also extended to Mazen Samara, Henry Szczawinski and Robert Oliver for their excellent technical supports and use of their facilities. I am also appreciative of Leslie Hosein, Sophie Mérineau, Maureen Thuringer, and Arlene Zimmerman for providing great assistance during my Ph.D. study.

I thank my friends, Negar Salimzadeh, Dulani Kodippili, and Ramona Vintila, and my former colleagues.

Special thanks to my loving mom and dad, and to my dear Farid, who believed in me throughout this journey. Words cannot express how grateful I am to you for all the sacrifices that you have made on my behalf. This accomplishment would not have been possible without you and your moral support.

Raheleh Nikonam M.

Contributions of Authors

This thesis contains chapters presenting results that have already been published or have been submitted and are in the form of an unaltered original journal manuscripts. All the articles included in this thesis were co-authored and reviewed prior to submission for publication by Prof. Robin A.L. Drew and Prof. Martin D. Pugh.

CHAPTER 3: Raheleh Nikonam M., Martin D. Pugh and Robin A.L. Drew, Formation mechanism of porous reaction-bonded silicon nitride with interconnected pores in the presence of MgO, Journal of the European Ceramic Society 39 (4), 2019, 915-927, https://doi.org/10.1016/j.jeurceramsoc.2018.10.032

CHAPTER 4: Raheleh Nikonam M., Martin D. Pugh and Robin A.L. Drew, Microstructural evolution mechanism of porous reaction bonded silicon nitride ceramics heat-treated in two powder beds, Ceramics International 45 (17), Part A, 2019, 21986-21997, https://doi.org/10.1016/j.ceramint.2019.07.213

CHAPTER 5: Raheleh Nikonam M., Martin D. Pugh and Robin A.L. Drew, Pore structure, porosity and compressive strength of highly porous reaction bonded silicon nitride ceramics with various grain morphologies, Journal of Materials Science, 55 (2), 2020, 509-523, https://doi.org/10.1007/s10853-019-04078-3

CHAPTER 6: Raheleh Nikonam M., Martin D. Pugh and Robin A.L. Drew, A comparative study on nitridation mechanism and microstructural development of porous reaction bonded silicon nitride in the presence of CaO, MgO and Al_2O_3, Journal of Asian Ceramic Societies, submitted and under review, Sept. 2019.

Table of Contents

List of Figures

List of Tables

Abbreviations and Definitions

AM	Acrylamide
APS	Ammonium Persulfate
DPF	Diesel Particulate Filters
EDX	Energy Dispersive X-ray Spectroscopy
GPSN	Gas Pressure Sintering of Silicon Nitride
HEMA	2-Hydroxyethyl Methacrylate
HIPSN	Hot Isostatic Pressing of Silicon Nitride
HPSN	Hot pressing of Silicon Nitride
ICP-MS	Inductively Coupled Plasma Mass Spectrometry
LPS	Liquid Phase Sintering (process)
MAA	Methacrylic Acid
MAM	Methacrylamide
MBAM	N,N'-methylenebisacrylamide
MIP	Mercury Intrusion Porosimetry
MMA	Methyl Methacrylate
PAM	Polyacrylamide
PM	Diesel Particulate Matter
PMMA	Poly(methyl methacrylate)
PS	Polystyrene
PVA	Polyvinyl Alcohol
RBSN	Reaction Bonded Silicon Nitride
SEM	Scanning Electron Microscopy
SN	Silicon Nitride
SSN	Pressureless Sintering of Silicon Nitride
TEMED	N,N,N',N' tetramethylethylenediamine
TGA	Thermo-gravimetric Analyzer
VLS	Vapor Liquid Solid (mechanism)
XRD	X-ray Diffraction

Chapter 1. Introduction

1.1. General Background

Pores can be found in most solids. In nature, cellular materials appear in the form of wood, sponge and coral; however, industrially produced porous materials have also been fabricated and used on a large scale for many years [1]. Low density, low thermal conductivity, high thermal shock resistance, and controlled heat transfer are the exceptional characteristics of porous ceramics [2]. High permeability and large surface areas in these materials offer a great deal of advantages in various industrial applications including bioreactors, gas or chemical sensors, liquid waste pre-treatment, separation membranes, catalyst supports, as well as insulators and filters [3, 4]. In load-bearing composites, mechanical strength is increased as porosity and pore size decreased [5, 6], yet such a structure is undesirable in a filtration membrane as it produces a large pressure drop across the thickness and therefore open-cell structures, with high porosity and high interconnectivity are preferred to allow free flow of liquid or gas [7]. In other words, to maximize the performance of porous materials, porosity level and pore characteristics such as size, connectivity of channels and internal geometry of pores must be controlled and tailored [8].

With excellent thermal shock resistance and superior thermo-chemical stability at high temperatures, silicon nitride (Si_3N_4) is a promising refractory ceramic that has replaced other materials in fast-heating and cooling processes. Since the 1960's, this material has been researched intensively and the volume of articles published in the last few decades on the production and characterization of silicon nitride-based ceramics is enormous [9, 10]. Si_3N_4 exists either in dense forms with superior mechanical performance or in porous forms with superior performance when in contact with liquids and gases. The latter has a wide range of uses in the production of environmental filters such as diesel particulate filters (DPF) to reduce diesel particulate matter (PM) [11], and can be fabricated either via partial sintering of Si_3N_4 with low sintering additives [12], or through reaction bonding of Si powder (RBSN) [13, 14]. Compared with sintering, in situ nitridation of silicon has the advantages of lower price of raw materials, easy control of dimensions and lower processing temperature [11, 15]. Among several attempts which have concentrated on the development of porous reaction bonded Si_3N_4 [7, 11, 16-18], a homogenous structure with high level of porosity has been produced simply by a combination of sacrificial template technique, gel-

casting and reaction bonding processes. The ability to tailor porosity content, a short nitriding time and high degree of nitridation are the main advantageous of this combination [19]. Nevertheless, the characteristics of the resultant grains are heavily susceptible to the fabrication parameters and this is because there are several distinct routes and mechanisms for the growth of Si_3N_4. With significant influence on the microstructure and mechanical properties, grains exist in various morphologies, namely α-matte, elongated α- or β-whiskers and β-rods [20, 21]. Among the important discoveries were the detailed models explaining the formation mechanisms of α and β-Si_3N_4 polymorphs via different routes. Parameters such as heating rate and types of reactants [20-22], nitriding atmosphere and temperature [21, 23], α- or β-seeding [24], and the presence of impurities such as iron [21, 25] greatly influence the morphology and chemistry of grains and have been discussed in the literature.

The impact of oxide additives mixed with starting Si powder on the post sintering densification, consolidation of the structure and β-grain development has been also investigated previously [7, 11, 16-18]. It has been reported widely that through formation of low-temperature eutectic liquid phase, mainly at $T \geq 1500°C$, oxides play a vital role in microstructural development of heat-treated silicon nitride bodies. For instance, MgO in combination with other oxides such as CaO, Al_2O_3 or Y_2O_3 proved to be one of the most interesting elements for Si_3N_4 densification. Depending on the composition of the ceramic, a diverse range of microstructures and consequently different mechanical strengths could be obtained [11]. However, due to the complexity of the nitriding reactions, particularly in the presence of additives, full details of all the involved reactions and microstructural properties are lacking. The current research is based on the fabrication of porous RBSN structures in the presence of MgO, CaO and Al_2O_3 for high temperature applications. To understand the formation of RBSN ceramics with high porosity, further investigation of the role of these additives on the microstructural development and properties is required.

1.2. Problem Statement

High porosity Si_3N_4 samples have been obtained previously by this research group using a sacrificial template technique, along with gel-casting and nitriding processes. Although this technique was effective in tailoring the porosity content, the resultant microstructures suffered

from the formation of mostly Si_3N_4 whiskers agglomerated within the pore cavities [19]. Consequently, it was found difficult to control and obtain a suitable RBSN microstructure. Up to now, the reason why nitridation of highly porous silicon leads to the predominantly whisker formation has not been clarified.

The development of elongated grains is favourable in improving filtration efficiency of environmental filters [18, 26] and in reinforcing ceramic matrix composites via crack deflection and whisker pull out mechanisms [27, 28]. However, the growth of these grains in cavities may have detrimental effects on interconnectivity, morphology of pores and pore size distribution. To facilitate the production of an open-cell structure with high interconnectivity and to improve the permeability of channels, it is crucial to preserve the granular shape of the Si_3N_4 grains. To date, no in-depth studies have been done yet on the design and modification of the RBSN grains.

It is well-established in many prior studies that oxide sintering aids do not behave as inert materials during the nitridation reaction, and their role is not restricted to liquid phase formation and densification. The type and amount of these additives would change the chemical composition, microstructure and hence mechanical properties of the heat-treated materials [29-32]. Previous studies have mainly focused on dense Si_3N_4 structures and have been concerned mostly with the performances of complex oxide systems [29-32]. However, it is of interest to understand how a simple oxide additive system would alter the morphology of grains, the structure of the pores and the mechanical strength of foams both before and after heat-treatment. A few studies have explored the correlation between the morphology of Si_3N_4 grains and the presence of MgO [33, 34], yet the mechanism behind why MgO was effective in changing the morphology of grains has not been explained. A detailed study on the effect of MgO, CaO and Al_2O_3 on the nitriding mechanism and RBSN grain morphology before high temperature heat-treatment does not exist and thus required further investigation.

During high temperature heat-treatment and above 1500°C, silicon nitride starts to decompose to silicon and nitrogen gas. To stop this common phenomenon and to improve the sintering behaviour of Si_3N_4 by reducing weight loss, samples are embedded in powder bed mixture of Si_3N_4 containing the oxide additives. The vapor pressure of the decomposing additives can be increased within the powder bed and the diffusion and flow rate of gas species can be reduced: this

suppresses the evaporation and decomposition of the ceramic parts during sintering. The efficiency of this protection is related to the size of pores and thickness of the powder bed [35]. However, the important role of the powder bed composition, especially in the presence of volatile oxides such as MgO, on the microstructure of RBSN grains has been neglected and never discussed. Hence, for the optimization of the properties of RBSN ceramics, the chemical stability and volatilization of oxides added to the powder bed should be considered.

Furthermore, it is desirable to have an understanding of how pore size distribution of a complex pore morphology and channel interconnectivity are related to the morphology of Si_3N_4 grains. Many microstructural features including grain morphology, grain aspect ratio, composition of the nitrided body and level of porosity and density influence the ceramic strength and must be considered. In order to correlate the composition and microstructures of the porous RBSN ceramic to its strength, an extensive investigation on the pore morphology, pore size distribution, pore classification, interconnectivity and accessibility of pores is needed.

1.3. Research Objectives

This research aims to contribute in developing the microstructural and mechanical properties of porous reaction bonded silicon nitride ceramics for high temperature applications. For this purpose, porous reaction bonded silicon nitride samples with varying porosity, pore size, and pore morphology are prepared by adding pore-forming agents (Poly(methyl methacrylate), PMMA) to silicon powders through the sacrificial template technique and gel casting. A subsequent reaction bonding process and a post heat-treatment are performed in the presence and absence of MgO, CaO and Al_2O_3 to produce porous structures with tailored properties. Therefore, crystal structures, chemistry and morphology of grains, and pore characteristics and mechanical strength of samples must be critically reviewed and discussed. Five main objectives are being pursued in this research and are summarized as follows:

1. To fabricate porous reaction bonded Si_3N_4 structures with the desired microstructural and mechanical properties. Therefore, having a more precise control over the nitriding reactions and microstructures in terms of phase composition, grain morphology, pore size distribution, pore shape, permeability and mechanical properties is required. The main aim of the study is to develop a physical model to explain the formation

mechanisms of porous RBSN ceramics both in the presence and absence of additives, i.e., MgO, CaO and Al_2O_3.

2. To assess the effectiveness of the above-mentioned additives as morphology modifiers. Hence to understand the microstructural development during the heating process and to investigate the role of these additives on the morphology of grain development during heating, a detailed microstructural study during various stages of reaction is required. To detect various microstructures formed in the presence of additives, heating temperature should be gradually increased to 1700°C and microstructural evolution, phase formation and transformation during nitriding and post-heat-treatment will be studied. Then the influence of oxide additives on the linear shrinkage, weight loss, porosity, density and strength of porous RBSN will be investigated and compared.
3. To classify pores based on their structure, morphology and size and then to correlate pore characteristics to the structure of grains. For this reason, pore morphology, pore size distribution, pore formation mechanism and interconnectivity of channels will be investigated.
4. To study the effects of powder bed composition (based on the presence of MgO) on the liquid-phase sintering of Si_3N_4 as well as microstructural development and grain morphology modifications. Here, an understanding of how porosity, density, linear shrinkage and weight loss are related to the composition of the Si_3N_4 powder beds is necessary.
5. To explore a correlation between microstructure of materials and strength of porous samples. To understand the influence of grain morphology, porosity content, pore volume as well as shape and size distribution of pores, the strength of the prepared samples will be investigated before and after heat-treatment.

1.4. Thesis Layout

This thesis is composed of seven chapters and the structure of the thesis is as follows:

CHAPTER 1 provides a brief introduction to the field of porous silicon nitride ceramics. The research gaps and areas that constitute the basis of this research are identified and the objectives of this study are provided.

CHAPTER 2 is dedicated to the review of the literature on a wide spectrum of subjects pertinent to the research, including a comprehensive literature review of the structures, fabrication and characterization of silicon nitride related materials.

CHAPTER 3 presents the microstructural development of samples in the presence and absence of various amount of MgO. This study investigates the dominant nitriding mechanisms in the porous RBSN structure and the resulting microstructures in terms of phase formation and their morphologies. Thermodynamics of reactions and interconnectivity of channels are the other important aspect of this investigation. The relationship between the microstructure and the obtained compressive strength, porosity and density after heat-treatment are discussed.

CHAPTER 4 discusses the role of heat-treatment on the morphology of RBSN grains and the microstructure of the ceramics. Different parameters such as the chemical composition of the starting materials, chemical composition of the powder beds, heating temperature and duration have been considered in this study.

CHAPTER 5 is focused on the classification of pores and the correlation between grain morphology and structure of pores. This chapter discusses how various grain morphologies can influence the shape of pores, the foam strength and pore size distributions.

CHAPTER 6 presents a comparative study on the microstructural development and properties of porous samples in the presence of CaO, MgO and Al_2O_3. This chapter investigates the influence of oxide additives on nitridation mechanism, grain morphology, foam strength, porosity and density of samples.

CHAPTER 7 presents the conclusions and contributions of this research and provides a list of recommendations for future work.

Chapter 2. Literature Review

2.1. Silicon Nitride Ceramics

Silicon nitride is chemically Si_3N_4 with 3:4 stoichiometry [36]. The SiN_4 tetrahedron, which is composed of a silicon atom at the centre and four nitrogen atoms in trigonal or corners, is the basic unit of Si_3N_4 [37]. As illustrated in **Fig. 2.1**, three SiN_4 unit cells are then linked in such a manner that each N has three Si atoms as neighbours or is shared between three other tetrahedrons [36, 37].

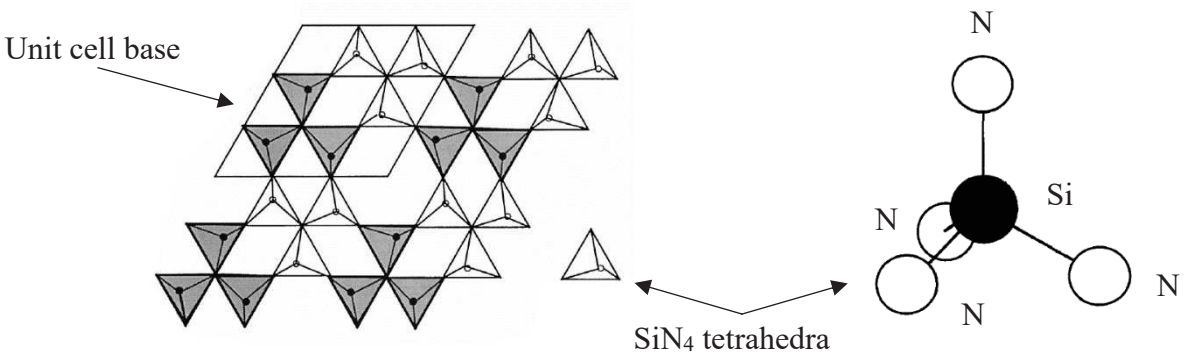

Fig. 2.1. Si_3N_4 crystal structure [36]

Detailed X-ray diffractometry (XRD) analysis in the mid-1950s proved that under normal nitrogen pressure, silicon nitride exists in two crystallographic forms of α and β-Si_3N_4, both with hexagonal crystal structure [22, 36]. At extremely high pressures and high temperature, γ-Si_3N_4, which is a rare polymorph, may also be formed, however, it has found no practical application [9, 37].

Both polymorphs of α and β have structures based on phenacite (Be_2SiO_4) where beryllium atoms are substituted by the silicon atoms and oxygen atoms are replaced by nitrogen atoms [9]. The difference between the two crystallographic modifications designated as the α and β, is then explained by various arrangements of atomic layers which are composed of puckered eight-membered rings of Si and N, as shown in **Fig. 2.2-a** and **b** [36].

β-Si_3N_4 belongs to the space group of $P6_3/m$ with the unit cell consisting of Si_6N_8, as shown in **Fig. 2.2-a**, with two layers, A and B, stacked in the sequence of ABAB… The β-structure is formed with long continuous channels along the c-axis and has a density of 3.203 g cm^{-3} [9, 10, 37].

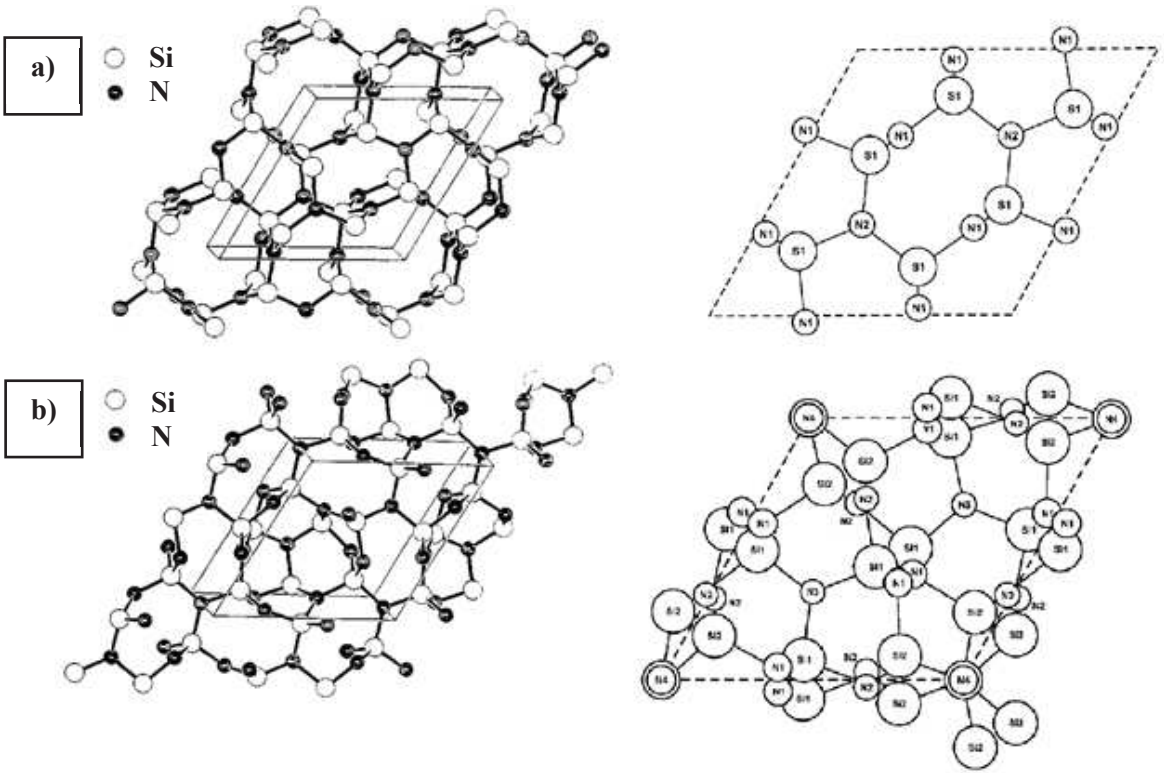

Fig. 2.2. Schematics of the crystal structures (left) and unit cells (right) of a) β-Si_3N_4 and b) α-Si_3N_4, view approximately along c axis [36, 38]

In contrast, as **Fig. 2.2-b** illustrates, the structure of α-Si_3N_4 unit cell is $Si_{12}N_{16}$ and is assigned to the space group of P31c. Stacking the basal planes of four layers in the ABCDABCD … sequence creates the α-phase. In relation to β-Si_3N_4, A and B, C and D have the same atomic arrangement but each is rotated by 180◦ along the c-axis. Therefore, α-structure is composed of alternate sheets of β-Si_3N_4 containing a mirror image of β-Si_3N_4 [9, 10, 36]. Due to the distortion and displacement caused in the position of atoms from the idealized locations, α-Si_3N_4, which is schematically modelled with ball and pin in **Fig. 2.3,** is therefore considered as the more strained structure than the β-Si_3N_4 [36] and is thermodynamically less stable.

By the linking of six eight-member Si-N rings in the β-structure, large voids are created and aligned in each basal sheet and provide a continuous c-axis channel with a diameter of 3Å [36]. Whereas, due to the arrangement of atoms in α-Si_3N_4 structure, the dimension of the unit cell in the c-axis is almost twice that of the β-phase and the continuous channels are interrupted by forming a series of large interstices [36]. This produces a structure with lower density (3.149 g. cm^{-3}) and channels

with smaller diameter (1.4Å) for α-Si_3N_4 compared to those of β-phase [9, 37]. The higher diffusion coefficients of nitrogen in polycrystalline β-structure (D_N^{β}= 5.8×10^{2} exp ($-\frac{777}{RT}$) m^2 sec^{-1}) compared to that of α-Si_3N_4 (D_N^{α}= 1.2×10^{-16} exp ($-\frac{233}{RT}$) m^2 sec^{-1}) is also due to the structural properties of the β-phase and the presence of large channels parallel to the c-axis [37].

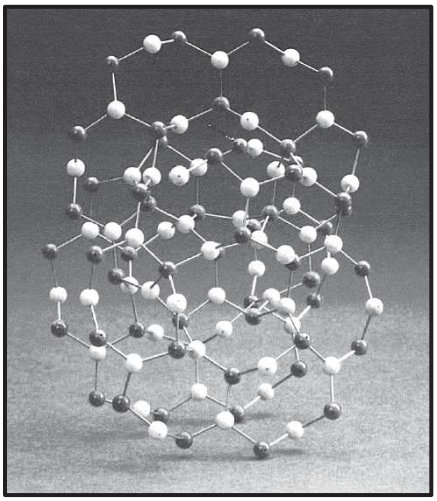

Fig. 2.3. Ball and pin model of α-Si_3N_4 showing rings composed of Si-N bonds, grey is N and white is Si [36]

2.2. Preparation Routes for Si_3N_4 Ceramics

Sintered and reaction bonded ceramics are the two major forms of silicon nitride components which have their own specific production routes, compositions, mechanical properties and microstructures [36].

The former ceramic has a dense structure and has superior quality at both high and room temperature [38]. High strength and creep resistance, high toughness and hardness, high thermal and chemical stability, excellent oxidation and corrosion resistance, good wear resistance, and good thermal shock resistance are some of the outstanding properties of this refractory ceramic [39, 40]. In particular, the good combination of high mechanical strength at temperatures up to 1300°C and excellent thermo-mechanical properties makes sintered Si_3N_4 based ceramics suitable for applications in several engineering and structural applications including bearings, cutting tools, wear parts, valves and heat engine components, as shown in **Fig. 2.4** [38, 41].

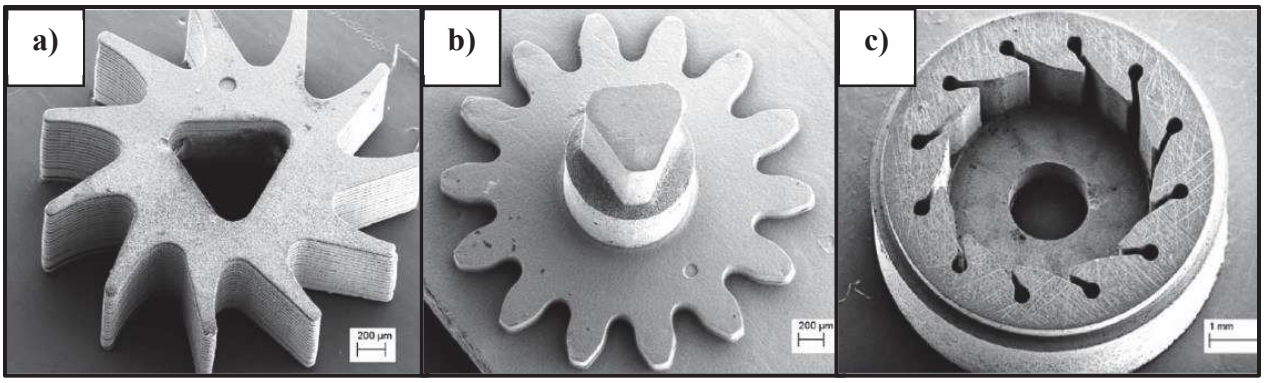

Fig. 2.4. Sintered silicon nitride parts applied in a micro-turbine: a) rotor, b) trigonal axis with sun-wheel, and c) nozzle plate [42]

In the production of its dense form via sintering routes, silicon nitride powder is the starting material. However, the presence of silicon nitride mineral in nature is very rare; therefore, it must be prepared synthetically [37]. To produce Si_3N_4 in the form of powder, there are several routes based on: direct nitridation of silicon powder (**Eq. 2.1**), carbothermal reduction of silica in the presence of nitrogen (**Eq. 2.2**), diimide synthesis (**Eq. 2.3** to **2.5**) and vapor phase synthesis (**Eq. 2.6**) [37, 38]. However, only direct nitridation and the diimide processes are commercially available and both methods have the capability to produce 100% crystalline phase with oxygen contents of < 2 wt.% [37].

$3Si + 2N_2 \rightarrow Si_3N_4$ at T≈ 1100-1400°C **Eq. 2.1**

$3SiO_2 + 6C + 2N_2 \rightarrow Si_3N_4 + 6CO\uparrow$ at T≈ 1450-1600°C **Eq. 2.2**

$SiCl_4 + 6NH_3 \rightarrow Si(NH)_2 + 4NH_4Cl\uparrow$ at T≈ 25°C **Eq. 2.3**

$3Si(NH)_2 \rightarrow Si_3N_4$ (amorphous) $+ 2NH_3\uparrow$ at T≈ 900-1200°C **Eq. 2.4**

Si_3N_4 (amorphous) $\rightarrow$ α-Si_3N_4 at T≈ 1300-1500°C **Eq. 2.5**

$3SiCl_4 + 4NH_3 \rightarrow Si_3N_4 + 12HCl\uparrow$ at T≈ 25-1400°C **Eq. 2.6**

Starting from pre-reacted silicon nitride powder, there are four basic methods for the fabrication of dense silicon nitride materials: Atmospheric pressure sintering (SSN), Gas pressure sintering (GPSN), Hot pressing (HPSN) and Hot isostatic pressing (HIPSN) [43].

Classical sintering of Si_3N_4 is the least expensive method [41] and gas pressure sintering under a high nitrogen pressure is the most commonly used method in the production of dense components

with high flexural strength [37]. HIP densification of reaction bonded Si_3N_4 or of sintered Si_3N_4 is suitable for the fabrication of high strength Si_3N_4 ceramics [37]. Nevertheless, as a consequence of the low lattice mobility of Si and N and the high-temperature volatility of silicon nitride, densification of silicon nitride powder compacts under normal ceramic processing conditions is not applicable [36]. As an illustration, a commercial Si_3N_4 powder compact hot-pressed at 1650°C for 4 hr obtained only 68% of the theoretical density [34].

In Si_3N_4 ceramics, similar to SiC and BN, atomic bonding between Si and N atoms is ≈ 70% covalent [21] and therefore, strong bonding leads to very slow solid-state diffusion in the volume or at the grain boundaries (e.g., at 1400°C $D_{Si} \approx 0.5 \times 10^{-19}$ m^2 s^{-1} and $D_N \approx 6.8 \times 10^{-10}$ m^2 s^{-1}) [37]. Therefore, to accelerate the atomic motion and densification of the powder, the sintering temperature must be raised as high as 1850°C or greater, at which point silicon nitride decomposition begins [10]. To enhance the diffusion rate and sintering kinetics, oxides or non-oxides additives such as MgO, Al_2O_3, ZrO_2 and Y_2O_3 have to be added [44]. Additives reduce the sintering temperature through formation of a eutectic liquid phase, and subsequently liquid phase sintering (LPS) increases the densification rate [37]. However, 15-20% linear shrinkage and large dimensional change are typically observed. Therefore, the high cost of synthetic Si_3N_4 powder and expensive post sintering machining steps are some of the limitations associated with fabrication by sintering [11, 41, 44].

Beside the dense form, which is beyond the scope of the present investigation, Si_3N_4 may be developed in a porous structure as a class of lightweight engineering ceramics with good thermal and chemical stability [38]. In the fabrication of porous ceramics with porosity of > 50%, sintering-based processes are ineffective as full $\alpha \rightarrow \beta$ phase transformation and densification eliminate pores during the LPS mechanism [45]. Reaction bonding of metallic silicon powder (RBSN) is the most commonly used alternative process to sintering which is both simple and low-cost [46] and can be used in the production of porous samples with complex shapes and different crystallinities, microstructures and impurities [37]. This technique is an easy and economical process that overcomes the inconveniences related to the sintering of silicon nitride powder since it employs direct nitridation of inexpensive Si powder instead of sintering of Si_3N_4 powder [21, 47]. Additionally, lower nitriding temperatures reduce the overall cost of the process and leads to the production of components with low shrinkage [19].

In spite of the fact that in the reaction bonding process, the conversion of silicon to silicon nitride is accompanied by a 22 vol.% increase and a weight gain (theoretically 66%), surprisingly no significant dimensional change is observed [22, 34]. The negligible dimensional change (≈ 0.1%) that occurs during nitridation is the most important feature of this process [21]. This means that for its efficient formation there must be sufficient pore space and interconnectivity available, therefore the development of silicon nitride grains is coupled with the presence of some pores to allow transportation of the material either in the molten state or as vapor [22]. Consequently, conventional RBSN components have ≈ 20 vol.% residual porosity, are brittle, have low density (≈ 70-88% theoretical) and exhibit lower mechanical strength (≈ 200-250 MPa) compared to sintered Si_3N_4 components (≥ 700 MPa) [21, 37].

Slow fabrication procedures, unreacted silicon and residual porosity are some of the limitations of reaction bonding for the fabrication of dense and large Si_3N_4 parts [19]. Although this limits the use of reaction bonded Si_3N_4 for engine applications [10], due to the high thermal shock resistance, corrosion resistance and good biocompatibility, RBSN is considered as a promising candidate for many applications such as in gas turbine engines [48], diesel particulate filters (DPF) [49], and structural orthopedic implants [40, 50], **Fig. 2.5**.

Fig. 2.5. Porous silicon nitride parts used as: a) DPF substrate and b) arthroplasty and spinal reconstruction implants [49, 50]

2.3. Nitriding Reactions of Si Powder

Interest in the reaction bonding process was initiated in the early 1960s at the Admiralty Materials Laboratory in England and since 1976 considerable attentions have been made on the details of nitridation reactions and microstructures of silicon nitride [20-22, 41]. Reaction bonded silicon

nitride is formed by heating a silicon powder compact which is prepared either directly into the component shape by slip casting, extrusion, injection-moulding, die-pressing, gel-casting and flame-spraying, or into the form of a billet by isostatic pressing up to 200 MPa [21, 41]. The prepared compact is then heated in an N_2-containing atmosphere (e.g., N_2, N_2-H_2 or NH_3) at temperatures in the range of 1250°C to 1450°C [21]. The reaction then proceeds through two steps of: 1) movement of nitrogen into the pore channels and to the reaction site and, 2) chemical reactions between Si and N_2 [21]. In this mechanism, either transport of the silicon or nitrogen or both to the reaction site or the pore formation mechanism is the rate-limiting process and further facilitated by cracks and dislocations during nitridation [21, 22, 51].

The reaction between silicon and nitrogen has been studied extensively and several theories have been used to describe the formation of silicon nitride grains [21, 22]. At elevated temperatures, formation of RBSN can be achieved through a reaction between solid, liquid or gaseous silicon with pure nitrogen gas, and is shown in the following reactions, **Eq. 2.7** to **Eq. 2.9** [9]:

$3Si\,(g) + 2N_2\,(g) \rightarrow Si_3N_4\,(s)$	$\Delta G^o = -2080 + 0.757T$ kJ. mol^{-1} [21]	**Eq. 2.7**
$3Si\,(l) + 2N_2\,(g) \rightarrow Si_3N_4\,(s)$	$\Delta G^o = -874 + 0.405T$ kJ. mol^{-1} [21]	**Eq. 2.8**
$3Si\,(s) + 2N_2\,(g) \rightarrow Si_3N_4\,(s)$	$\Delta G^o = -723 + 0.315T$ kJ. mol^{-1} [21]	**Eq. 2.9**

Under nitriding conditions and at high temperatures, both α- and β-Si_3N_4 generally are formed but it is observed that β-Si_3N_4 preferentially develops at higher temperatures. Formation of β-Si_3N_4 has slightly lower Gibbs free energy than that of α-Si_3N_4 but due to the presence of large error bars in experimental data, no significant Gibbs free energy difference between the two phases has been distinguished in the literature [22]. Therefore, based on the experimental observations and kinetics of the reactions, the formation of either α- or β-phase is more connected to the growth and reaction mechanisms [22].

The crystallographic structure and morphology of the resultant silicon nitride grains are different based on the dominant reactions [41]. However, as several mechanisms might operate simultaneously, most RBSN microstructures are composed of several microconstituents [10]. Nitriding temperature, heating rate, impurity of the starting powders, the presence of oxide additives, flow rate of nitrogen gas, particle size of silicon powder and heating time are among the

many variables which are involved and encourage the formation of a particular microconstituent [20, 21].

Jennings et al. has suggested that the presence of atomic and molecular nitrogen are important parameters in determining whether α or β would form [9]. A simple theory discusses that if nitrogen gas dissociates and then reacts with silicon, β-silicon nitride would form and if silicon moves to combine with nitrogen molecules, α-Si_3N_4 would form [22]. While atmospheric dissociation of nitrogen is observed only at high temperatures and in the presence of some atoms such as He, Kr or Ar, surface dissociation happens in the presence of hot metallic surfaces by adsorption of N_2 gas on the surface of silicon [22]. Therefore, molecular nitrogen gas, which is very unreactive, may dissociate at 25°C based on the energy and heat of reaction demonstrated in **Eq. 2.10** [22]:

$N_2 \rightarrow 2N$ $\Delta H = 946.76$ kJ. mol^{-1} $\Delta G = 912.46$ kJ. mol^{-1} [22] **Eq. 2.10**

2.3.1. Mechanism of α-Si_3N_4 Formation

Fine, pure silicon powder, a heating temperature of < 1450°C and no gas flow favour the formation of α-matte, and temperature and time of nitridation determine the density of α-grains [20]. Moulson and Jennings have stated that the strained structure of α-Si_3N_4 phase results from a gas phase reaction between silicon vapor and nitrogen gas. Much evidence has supported the idea that the growth and formation of α-Si_3N_4 occurs in the early stages and at lower temperatures compared to β-Si_3N_4 and below the melting point of silicon [21, 22].

For the formation of α-matte, nitrogen is adsorbed chemically on the surface of silicon particles at the initial stages of the reaction [23]. By evaporation of Si from the surface or from the liquid phase and through reacting with molecular nitrogen (**Eq. 2.11** [22]), α-Si_3N_4 forms with the morphology of small granular shaped grains, called α-matte [9, 41].

$3Si\ (g) + 2N_2\ (molecular, g) \rightarrow \alpha\text{-}Si_3N_4\ (s)$, matte grains [22] **Eq. 2.11**

In the absence of a protective silica layer, the initial stage of the reaction is nucleation of small silicon nitride crystals over the surface of silicon particles which later continues by growth of grains on available surfaces. The kinetics of these stages is linear with time [22, 52]. Oswald

ripening controls the growth of granular α-matte grains where the larger grains grow at the cost of smaller ones [9]. The reaction continues by evaporation-condensation or diffusion of Si atoms to the nucleation sites. Gradually, the silicon nitride layer formed covers the surface of the silicon particles and leaves some pores behind through vacancy condensation or via silicon volatilization, as shown in **Fig. 2.6** [22, 41]**.** After the formation of thin nitride layers on the solid silicon surface, more reaction between silicon and nitrogen proceeds at a decreasing rate by formation of silicon nitride in the pores and partially filling the gaps between the silicon particles. Further nitridation of silicon depends on the diffusion of nitrogen atoms through the densely formed Si_3N_4 layer, which controls the reaction rate [22, 36, 41, 52].

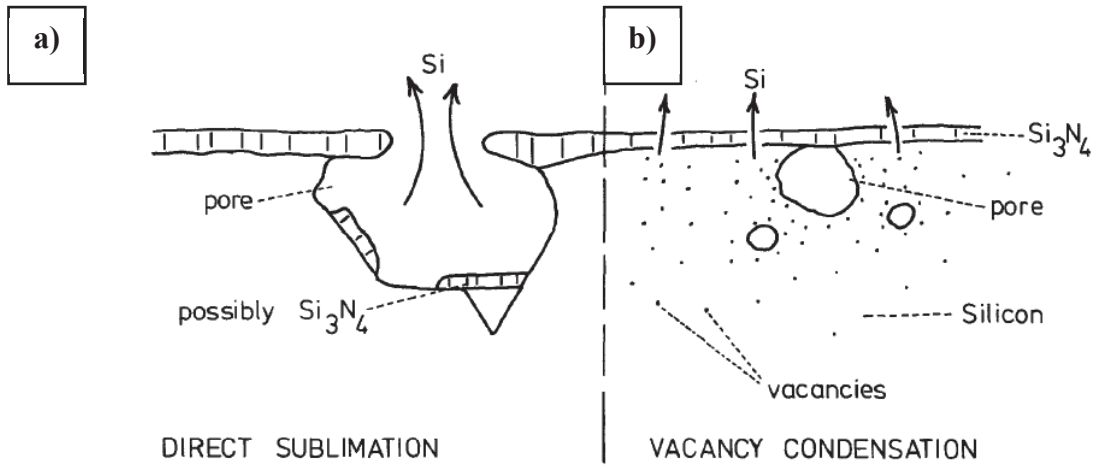

Fig. 2.6. Pore formation mechanisms: a) direct sublimation and b) vacancy condensation [22]

In contrast with the formation of α-matte grains, a possible mechanism of fine needle-like crystals with high aspect ratio (> 25), called α-whiskers, is based on the vapor-liquid-solid (VLS) reaction [41]. Silicon oxide which forms around the Si particles through oxidation by a wet-processing technique or during heating may slow down or even stop the nitridation reactions. However, Si can reduce SiO_2 and enhances the amount of SiO vapor in the nitriding atmosphere, which can contribute later to whisker formation via **Eq. 2.12** [53].

$$3SiO\,(g) + 2N_2\,(g) \rightarrow \alpha\text{-}Si_3N_4\,(s) + 3/2\ O_2\,(g)\ [44] \qquad \textbf{Eq. 2.12}$$

In the presence of impurities, a liquid phase which can make up the main core of the grains, is formed. As schematically shown in **Fig. 2.7**, by transportation of nitrogen on the surface of these

nuclei, it reacts with silicon monoxide at the solid-liquid interface to form α-whiskers [41]. Therefore, a heating temperature of < 1400°C and less pure silicon powders encourage the formation of this microconstituent [20].

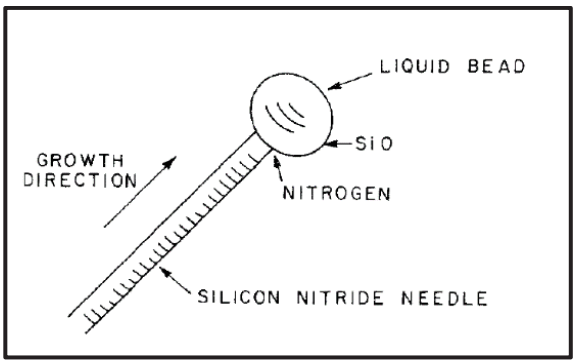

Fig. 2.7. Schematic illustration of growth of α-whiskers by VLS mechanism [20]

2.3.2. Mechanism of β-Si_3N_4 Formation

Above the melting point of silicon, at an increased rate of heating and in the presence of flowing nitrogen, direct nitridation of silicon leads to the formation of β-Si_3N_4 grains with higher density compared to α-Si_3N_4 [20, 36, 53]. Whereas the formation of β-Si_3N_4 in the morphology of coarse rods has been widely accepted, there are some reports suggested that β-Si_3N_4 also exists in the form of whiskers, though with shorter length, larger diameters and lower aspect ratio compared to those of α-whiskers [21, 23]. These grains are comparatively straighter, have higher degree of interlocking and have more uniform size and shape [25]. Through the gaseous phase reaction between silicon vapor and atomic nitrogen, **Eq. 2.13**, β-Si_3N_4 whiskers develop in the pore area [23].

$$3Si\ (g) + 4N\ (atomic,\ g) \rightarrow \beta\text{-}Si_3N_4\ (s),\ \beta\text{-whiskers} \qquad \textbf{Eq. 2.13}$$

Therefore, as shown in **Fig. 2.8-a**, under N_2 atmosphere and in the absence of H_2, formation of β-Si_3N_4 whiskers is very likely while in the presence of H_2, the concentration of atomic nitrogen is lower in the surrounding atmosphere and therefore formation of α-Si_3N_4 whiskers is encouraged, **Fig. 2.8-b** [25].

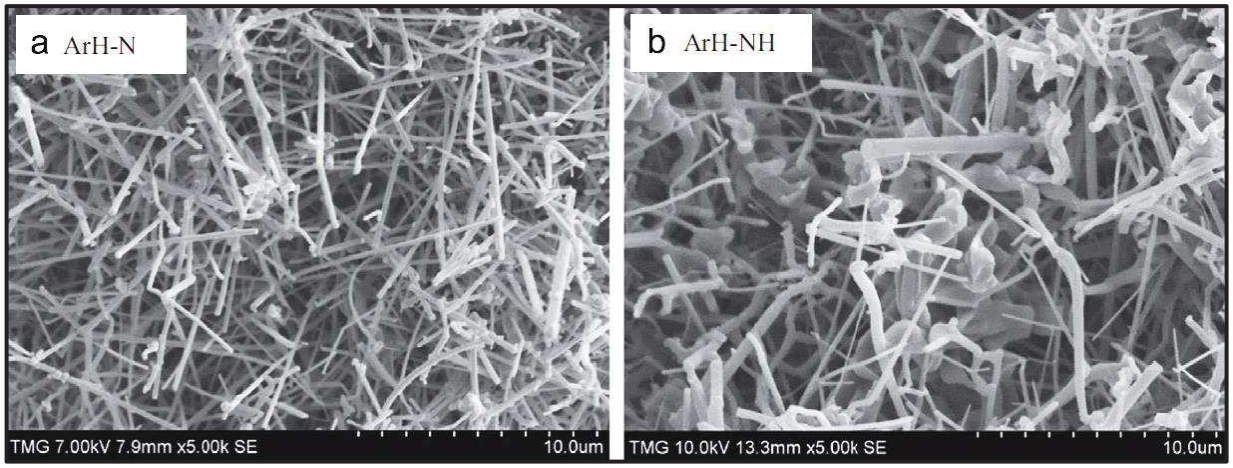

Fig. 2.8. Formation of α- and β-Si_3N_4 whiskers in RBSN foams. Samples are pre-sintered under Ar-H_2 atmosphere and then are heated under a) N_2 and b) N_2-H_2 gas [25]

In contrast to the growth of β-whiskers in pore spaces, when atomic nitrogen reacts with molten or solid silicon (**Eq. 2.14** and **2.15**) via a diffusion controlled mechanism, the growth of β-Si_3N_4 as large and facetted hexagonal grains occurs mostly in the interior of the body [41].

$$3Si\ (l) + 4N\ (atomic, g) \rightarrow \beta\text{-}Si_3N_4\ (s),\ \beta\text{-hexagonal grains} \qquad \textbf{Eq. 2.14}$$

$$3Si\ (s) + 4N\ (atomic, g) \rightarrow \beta\text{-}Si_3N_4\ (s),\ \beta\text{-hexagonal grains} \qquad \textbf{Eq. 2.15}$$

The highly exothermic nitriding reactions enhance the temperature and increase the possibility of molten phase formation [23]. Nitrogen easily dissolves in liquid silicon or other impurity liquids, such as $FeSi_2$, and dissociates into the atomic state [9]. Whereupon, the liquid phase favours the formation of β-structure, which results from the dissolution of nitrogen [9]. Enhancement of β-Si_3N_4 phase formation in the presence of impurities such as iron, which forms low melting point eutectic phases, confirms the important contribution of molten silicon in this mechanism [41].

Jennings and Richman have proposed that after the formation of a thin surface layer of β-Si_3N_4 on silicon particles, reaction only continues by diffusion of nitrogen through the layer and down the hexagonal tunnels of the β-Si_3N_4 crystals to reach the untreated silicon [20]. As shown in **Fig. 2.9**, due to the ease of nitrogen diffusion in these channels, the preferred growth direction of β-Si_3N_4 is along the <001> or the z-direction, hence β-grains grow with high aspect ratio [9, 22].

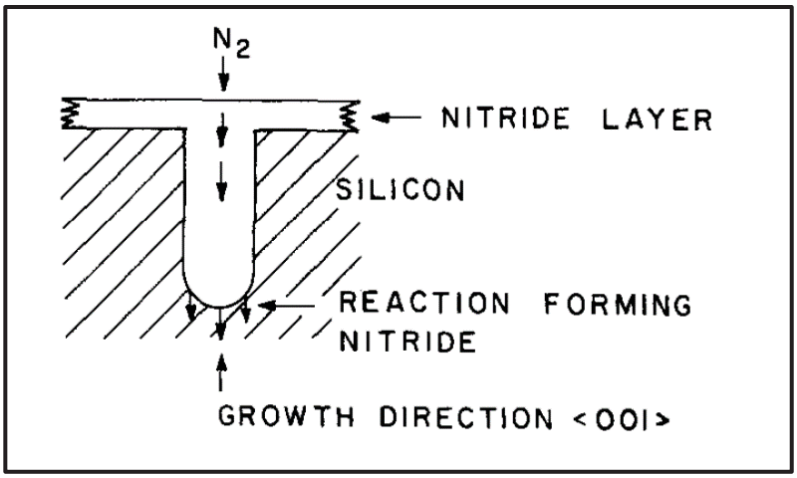

Fig. 2.9. Schematic figure showing the growth of β-spike into silicon through the preferred growth direction [20]

Consequently, the presence of impurities in the composition, high temperatures above the melting point of silicon, atomic nitrogen and increased partial pressure of nitrogen favour β-Si_3N_4 formation [9, 37].

2.4. Factors Influencing the Microstructure of RBSN

It is generally accepted that reproducibility of product quality is extremely difficult in reaction bonding and comparison of experimental data of materials produced in different laboratories is unreliable. The main reason for this is the kinetic competition between α- and β-Si_3N_4 formation, which is controlled by a variety of factors such as starting materials' chemical composition, heating time, temperature and gas composition [22, 36, 44]. As a result, a diverse range of microstructures, mechanical properties, nitridation rate, and proportion of phases are obtained. To clarify the importance of fabrication conditions, the correlation between microstructural properties and processing variables must be described.

2.4.1. Composition of the Nitriding Atmosphere

Depending on the composition of the nitrogen gas, a diverse range of silicon nitride microstructures can develop, since the reaction between silicon and nitrogen is extremely sensitive to the presence of either native or added impurities [21, 36, 44]. Through addition of different amounts of various gases such as helium and argon, the concentration of the nitrogen gas, thermal

conductivity of the gas mixture and the rate of the reaction can be altered and therefore a more homogeneous microstructure is achieved [43, 44]. In addition to these additives, impurities like O_2, H_2 and H_2O contained in the nitrogen gas alter the reaction rate, the product morphology and the ratio of α/β-Si_3N_4 [21, 36, 44]. The existence of oxygen as the major impurity in the gas mixture is almost unavoidable and this is often attributed to the presence of surface SiO_2 and water vapor adsorbed on the furnace lining [36].

In the literature, various mechanisms have been proposed to interlink the presence of oxygen with the α- and β-Si_3N_4 developed in RBSN ceramics. Addition of a small amount of O_2 to the nitrogen atmosphere increases the content of α-Si_3N_4 either by carrying silicon vapor to the site of reaction, by oxidation of Si and formation of SiO vapor, or by release of NO gas [20]. As illustrated in **Eq. 2.16** and **Eq. 2.17**, oxygen can remove active nitrogen and increase the content of molecular nitrogen [54]. As already mentioned, atomic nitrogen encourages the formation of β-phase and decreases the ratio of α/β-Si_3N_4 in the microstructure, while molecular nitrogen increases the content of α-Si_3N_4 phase [54].

$$N + O_2 \rightarrow NO + O \text{ [54]} \qquad \textbf{Eq. 2.16}$$

$$N + NO \rightarrow N_2 + O \text{ [54]} \qquad \textbf{Eq. 2.17}$$

On the other hand, oxygen may increase the content of silicon monoxide gas by active oxidation of silicon which enhances the formation of α-Si_3N_4 whiskers [53]. This happens by formation of SiO (g) escaping from the surface, such that the silicon surface remains oxide-free. In theory, under a high purity nitrogen atmosphere of $\leq 10^{-6}$ atm O_2 and H_2O, nitridation of SiO gas is thermodynamically feasible [44] whereas, in the presence of excess oxygen, nitridation rates become less favourable and therefore both silicon and silicon nitride are oxidized to Si_2N_2O and SiO_2, according to the **Fig. 2.10** [55] and **Eq. 2.18** to **Eq. 2.22** [36, 53].

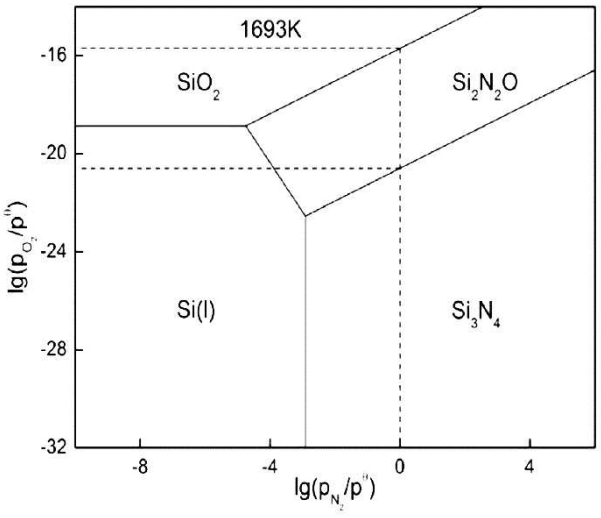

Fig. 2.10. Phase stability diagram in Si-N-O system at 1693K (≈ 1420°C) [55]

$Si\,(s) + O_2\,(g) \rightarrow SiO_2\,(s)$	$\Delta G_1^\circ = -904760 + 173.38T$, 298K<T<1685K [53]	**Eq. 2.18**
$Si\,(l) + O_2\,(g) \rightarrow SiO_2\,(s)$	$\Delta G_2^\circ = -946350 + 197.64T$, 1685K<T<2000K [53]	**Eq. 2.19**
$2Si\,(s) + N_2\,(g) + ½\,O_2\,(g) \rightarrow Si_2N_2O\,(s)$	$\Delta G_3^\circ = -850571 + 230.57T$ 298K<T<1685K [53]	**Eq. 2.20**
$2Si\,(l) + N_2\,(g) + ½\,O_2\,(g) \rightarrow Si_2N_2O\,(s)$	$\Delta G_4^\circ = -951651 + 290.57T$ 1685K<T<2000K [53]	**Eq. 2.21**
$2Si_3N_4\,(s) + 3/2O_2\,(g) \rightarrow Si_2N_2O\,(s) + N_2\,(g)$	$\Delta G_5^\circ = -1106047 + 61.69T$ [53]	**Eq. 2.22**

Fig. 2.11 illustrates the thermodynamic stability between SiO_2-SiO with temperature and partial pressure of gaseous species [55]. While the thickness of native silica layer on the particle of commercial silicon is about 3 nm, by increasing the content of oxygen at a constant temperature, the protective silica layer is stable and passive oxidation occurs by diffusion of the oxidizing species through the silica layer, as shown in **Eq. 2.21** and **Eq. 2.22**. For instance, at an oxygen partial pressures greater than 10^{-8} bar (≈ 10^{-8} atm) at 1370°C (1643K), stability of silicon oxide is increased, and this may lead to the formation of an oxide layer with thickness up to 1 μm [21, 52, 53].

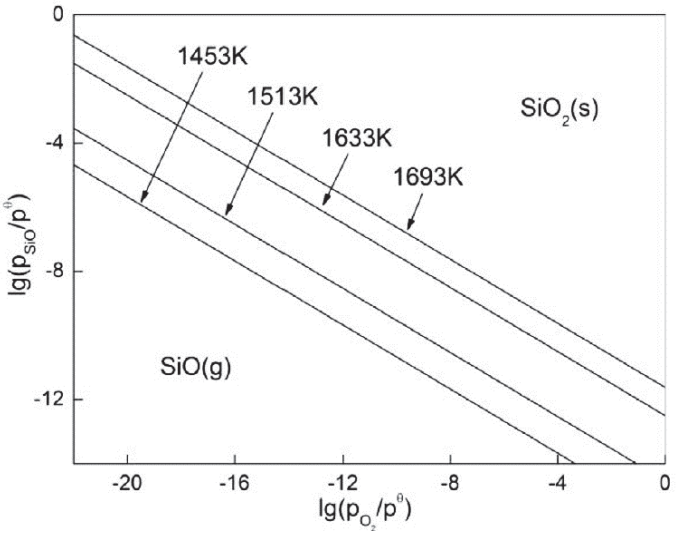

Fig. 2.11. Variation of p(SiO)/p◦ and p(O_2)/p◦ in Si-O system at different temperatures [55]

Accordingly, by a) changing the ratio of gaseous species [25], b) retarding the nitriding reaction [43] or c) reducing the melting temperature, the content of oxygen and surface silica can play significant roles in controlling the dominant nitriding mechanism.

In a similar way to O_2, the presence of H_2 reduces the chance of β-Si_3N_4 formation by eliminating the atomic nitrogen species from the surrounding atmosphere via **Eq. 2.23** and **2.24** [22].

$O + H_2 \rightarrow OH + H$ [22] **Eq. 2.23**

$N + OH \rightarrow NO + H$ [22] **Eq. 2.24**

The main role of hydrogen here is the increase of the reaction kinetics by oxygen removal and reduction of surface silica via **Eq. 2.25** [44] and **Eq. 2.26** [22], respectively.

$2H_2\,(g) + O_2\,(g) \rightarrow 2H_2O\,(g)$ [44] **Eq. 2.25**

$SiO_2\,(s) + H_2\,(g) \rightarrow SiO\,(g) + H_2O\,(g)$ [22] **Eq. 2.26**

Consequently, heating in a N_2-H_2 gas mixture leads to the release of SiO and encourages the formation of α-Si_3N_4 [22]. To determine the thickness of the silica layer and by measuring the resultant weight loss, deoxidation treatments of silicon particles also can be performed in H_2-containing atmosphere at temperatures of around 1350℃ [56].

2.4.2. Composition of the Starting Powders

In conjunction with silica, impurities such as Ca, Al and Fe are also present in commercial silicon powder and highly affect the grain growth and densification of Si_3N_4 [57]. Calcium decreases the high temperature strength of Si_3N_4 samples, aluminum lowers the melting temperature, and 1 wt.% cation impurities such as Mn, Co and Ni accelerate the nitridation reaction [21, 52, 57].

Commercial silicon often has ≈ 0.9 wt.% iron [25], the most important impurity, which alters the nitriding reaction and the resultant microstructural and mechanical properties. Boyer et al. have shown that nitridation rate is highly sensitive to the iron impurity and at contamination levels of < 1000 ppm and $pO_2 < 4$ Torr ($\approx 5 \times 10^{-3}$ atm), the extent of nitridation can be significantly enhanced. At 55 ppm iron contamination, the nitriding reaction increases three-fold compared to when no iron is present [52].

In the presence of this element and at low oxygen partial pressures (e.g., < 4 Torr ≈ 5×10^{-3} atm at 1370°C) the formation and generation of silicon monoxide gas at the Si/SiO_2 interface is promoted by devitrification, disruption and complete removal of the protective silica layer [21, 52]. In this process, silica devitrification reduces the adhesion of the film to the underlying surface and increases the formation of SiO gas at the interface. According to the either of the following reactions in **Eq. 2.27** and **Eq. 2.28,** SiO gas then diffuses away from fissures until the silica layer is completely removed [52].

$$SiO_2\,(s) \rightarrow SiO\,(g) + \tfrac{1}{2}\,O_2\,(g)\ [52] \qquad \textbf{Eq. 2.27}$$

$$Si\,(s) + SiO_2\,(s) \rightarrow 2SiO\,(g)\ [52] \qquad \textbf{Eq. 2.28}$$

Hence by affecting the content of vapour species, Fe may also alter the microstructure and morphology of grains at the initial stages of the reaction [52]. As illustrated in **Fig. 2.12**, formation of whiskers by wet processing of silicon suspension has been observed in the presence of a) 1 wt.% and b) 4 wt.% $FeSi_2$ [25].

Similar to iron contamination, devitrification and disruption of the silica layer have been observed in the presence of Ni at 1370°C. In contrast, Ta and Al have no effect on silica glass devitrification and nitridation kinetics, consequently leaving this layer vitreous and unaffected [52].

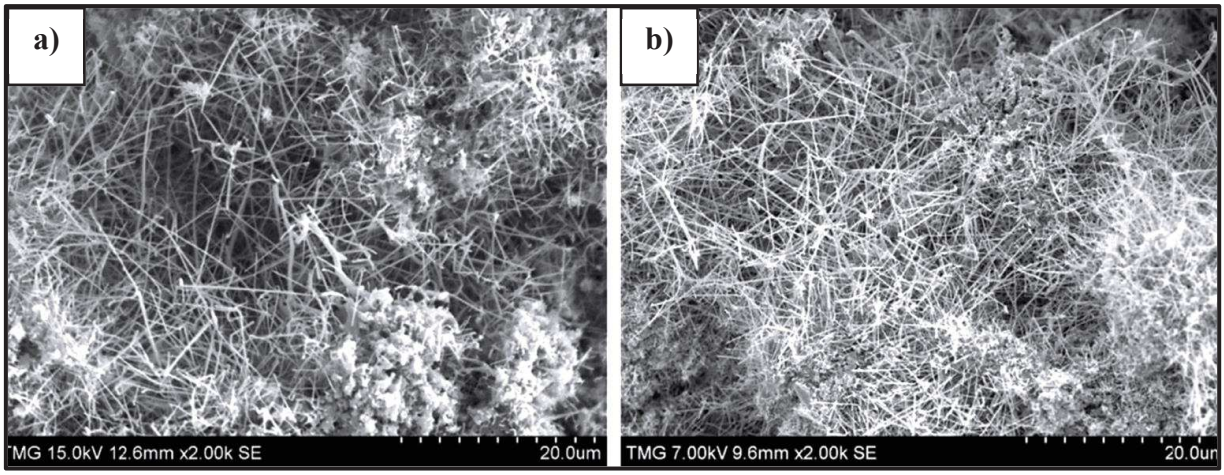

Fig. 2.12. Microstructure of porous RBSN containing a) 1 wt.% $FeSi_2$ and b) 4 wt.% $FeSi_2$ [25]

It has also been suggested that iron might affect the content of α- and β-Si_3N_4 by lowering the melting point and promoting formation of Fe-Si intermetallics [36]. Silicides of iron, i.e., Fe_3Si, $FeSi_2$ and FeSi, have lower melting temperatures than that of Si by as much as 200°C. The minimum solidus temperature in the Fe-Si systems is approximately 1200°C and in regions of locally accumulated impurities it can be as low as 1000°C [52, 53]. Iron may favour the formation of α-Si_3N_4 above the Fe-Si liquid by vaporization of Si (g) from $FeSi_x$ liquid phase [52]. It has been observed elsewhere that the amount of α-Si_3N_4 converted to β-Si_3N_4 was proportional to the concentration of the liquid and iron impurities [52]. Accordingly, formation of β-Si_3N_4, shown in **Fig. 2.13**, was enhanced either by α → β phase transformation or by the formation of liquid, dissolution and diffusion of N gas [52].

In contrast to the above-mentioned additives, α- or β-Si_3N_4 seeds may be introduced to the starting silicon powder as inert phases. Although in this case the seeds are chemically inert and do not react with silicon or nitrogen gas, they may still affect the microstructure of the developed grains, the ratio of α- to β-Si_3N_4 and the mechanical strength. For instance, addition of β-Si_3N_4 seeds into the structure of RBSN promotes the preferential nucleation and growth of β-Si_3N_4 and improves the mechanical strength by controlling the exothermic nitriding reactions and decreases the likelihood of silicon melting [24]. Furthermore, Si_3N_4 seeding may lead to the formation of a bimodal microstructure where coarse elongated β-Si_3N_4 grains with high aspect ratio can develop along

with fine grains. In this case, the microstructure is reinforced by crack bridging and crack deflection mechanisms [24].

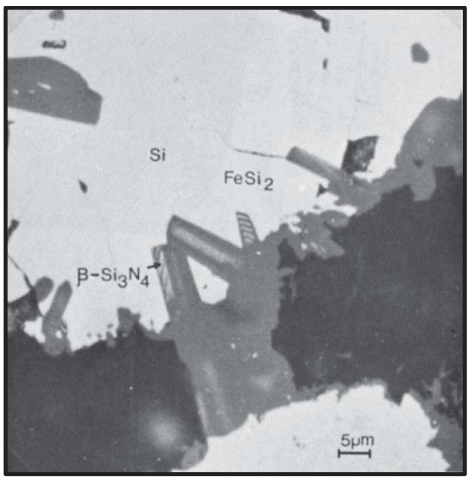

Fig. 2.13. Growth of β-Si_3N_4 crystals within the $FeSi_2$ liquid phase [52]

2.4.3. Nitriding Temperature and Heating Profile

The reaction between silicon and nitrogen is generally slow when there is fusion of silicon particles caused by the heat generated from the exothermic reaction (e.g., 725 kJ. mol^{-1} at 1400°C) [53]. Slow diffusion of nitrogen and silicon in the Si_3N_4 crystal lattice might decrease the nitridation rate and local melting of silicon at 1410°C hinders the complete nitridation. Furthermore, at temperatures much below 1400°C, the reaction rate becomes very slow and eventually completion of the reaction becomes very difficult [36]. To increase the rate of nitridation, prolonging the nitriding time, increasing the nitrogen pressure and adding metals or oxide additives can be effective. However, this may lower the mechanical performances of the ceramics by defect formation [53]. It has been observed that the bending strength has been improved when porous RBSN samples were nitrided under N_2 gas and at 1390°C (below the melting point of silicon) rather than 1425°C [25]. Partial melting of silicon and microstructural defects formed at 1425°C was shown to degrade the mechanical properties [25].

In addition to the temperature, the heating rate also affects the microstructural homogeneity and alters the α/β-Si_3N_4 ratio of thick samples. Jennings and Richman [20] proposed that high temperatures (> 1450°C) and rapid heating rates promote the formation of liquid phase, coarsen the microstructure, increase the content of reacted materials and favour the development of β-Si_3N_4

phase. At high heating rates, the heat generated due to the exothermic nature of the nitriding reaction increases considerably and is localized mainly in the body interior and produces temperature gradients through the thickness of the body [22, 36].

2.4.4. Nitrogen Gas Flow Rate and Pressure

It is widely acknowledged that the furnace environment can significantly change the nitridation conditions and nitriding rate. For instance, under high gas pressure, nucleation rates are increased, and silicon nitride grains form rapidly, and their texture becomes finer [22].

Flowing nitrogen removes vapor species, increases the rate of vaporization and encourages the formation of pores and coarse products [22]. Additionally, impurities are moved over the surface of silicon and therefore flowing nitrogen changes the microstructure of the products by introducing or removing species from the reaction sites. Transporting impurities which discourage active nitrogen from the reaction site would, for instance, hinder the formation of β-phase in the early stages of the reaction and therefore surface reaction and α-phase formation predominates [22].

2.4.5. Porosity Level

By providing free space for grain growth or by increasing the vaporization rate and enhancing the content of vapor species, the level of porosity in the silicon microstructure may affect the nitriding mechanism and the nitridation rate. Microstructure and morphology of Si_3N_4 grains are therefore highly affected in porous structures, compared to “normal” or “conventional” ceramics with low levels of porosity [23]. In highly porous RBSN structures, pore formation through silicon vaporization is dominant compared to vacancy condensation. While full nitridation may take several hours to several days in dense RBSN, nitriding time, even in large foams, is quite short and the possibility of the presence of residual silicon is much lower in porous RBSN because the interconnected channels provide sufficient nitrogen flow to the interior of the sample [23].

2.4.6. Silicon Particle Size

The choice of silicon particle size has an important influence on the nitridation rate, composition, microstructure and properties of the final products [58]. For instance, a high degree of nitridation in samples with larger Si particles has been observed due to differences in pore size, content of

porosity and thickness of the protective silica layer [58]. As shown in **Fig. 2.14**, when increasing the silicon particle size from 3 to 12 μm, the size and the volume of pores increased in the microstructure [54].

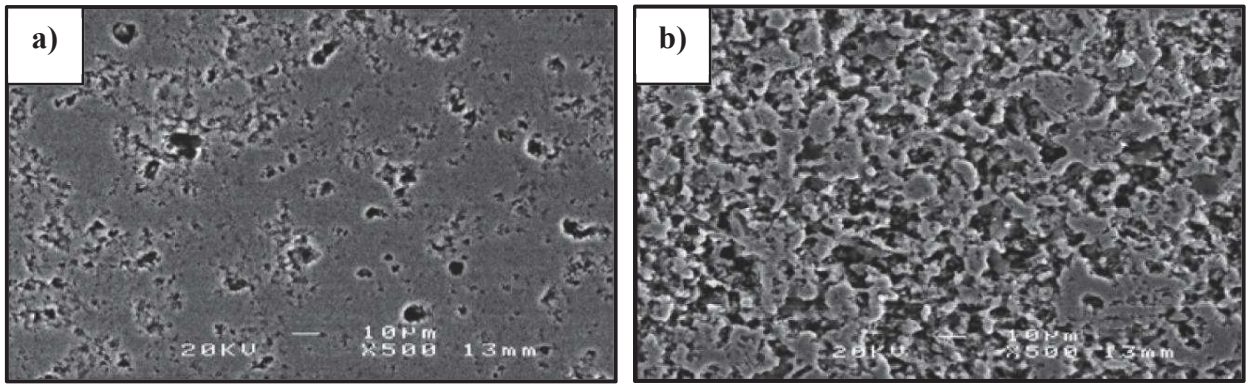

Fig. 2.14. Microstructure of RBSN ceramics using: a) 3 μm silicon powder and b) 12 μm silicon powder [54]

Accordingly, physical and mechanical properties of RBSN ceramics such as bulk density, hardness, Young's modulus and flexural strength are controlled by the size of the starting Si powder particles [54]. Sillapasa et al. have suggested that the ceramic bulk density, hardness, Young's modulus and strength are increased when the silicon powder particle size decreases. The effect of the smaller Si raw particle size on the increasing density and enhanced strength is attributed to the higher surface area, shorter diffusion path and the enhanced sintering driving force [54]. In contrast, Lee has reported higher flexural strength in samples with larger silicon particles [58]. As schematically illustrated in **Fig. 2.15**, when larger Si particles have been employed, a bimodal microstructure with abnormally coarse rod-like β-Si_3N_4 grains was developed due to heterogenous liquid distribution [58]. This enhances the mechanical performance of the sample by crack bridging and crack deflection mechanism [58].

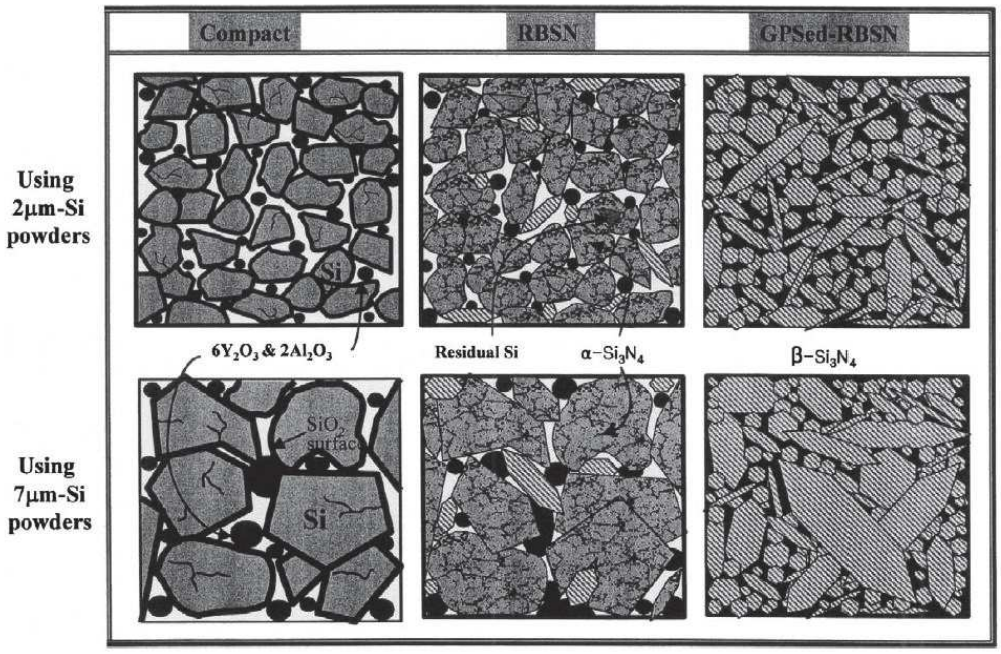

Fig. 2.15. Schematic illustration of microstructural development of samples with various silicon particle sizes [58]

Moreover, the content of α- and β-Si_3N_4 developed during the reaction process highly depends on the particle size of the starting silicon particles. α-Si_3N_4 forms at the surface where the reaction starts, and smaller silicon particles provide higher free surface area. This leads to an increase in the content of α-Si_3N_4 phase and enhances the α/β-Si_3N_4 phase ratio [54]. In contrast, in large particles, the content of silica covering the particle surface would be lower and the distribution of oxide additives within the matrix particles would be less homogeneous. Consequently, inhomogeneous distribution of additives within the silicon particle and local liquid phase formation enhance inhomogeneous β-Si_3N_4 phase formation [58].

2.4.7. Pre-sintering Process

Pre-sintering in an inert atmosphere such as argon is a process prior to the nitridation which typically occurs at ≈ 1200°C with the purpose of enhancing the mechanical strength of the green body for handling, or machining to the required shape [59]. This process may affect the nitriding condition and microstructure of grains developed during the nitriding process. Surface diffusion, lattice diffusion (from surface, grain boundary or dislocations), vapor transport and boundary diffusion are some of the transport paths in solid-state sintering mechanism [59]. During pre-

sintering of pure silicon grains, surface diffusion (as the dominant mass-transport path) along with vaporization/condensation are simultaneously operating which lead to neck growth and densification of the powder compact [59]. This decreases the nitridation rate by reducing the available silicon surface and silicon vaporization, and by hindering the diffusion of nitrogen gas to the interior part of the body [44]. It has been also reported that Ar-H_2 pre-sintering prior to nitridation has removed the silica layer and thus increased the strength of RBSN foams [23, 25].

2.5. Post Heat-treatment Process

To enhance the densification and strength of ceramics, post heat-treatment of RBSN containing sintering aids has been widely performed at T ≤ 1750℃ [41, 47, 51]. Via a reaction between additives (e.g., Y_2O_3-Al_2O_3 or Y_2O_3-MgO) and surface silica present naturally on silicon particles, a liquid phase forms and relatively fast mass transportation occurs through a liquid diffusion path. This accelerates the densification via particle rearrangement and a solution-precipitation mechanism and can lead to a full nitridation of any residual silicon remaining in the RBSN [51, 56]. In the production of silicon nitride components via pressureless sintering, gas-pressure sintering, hot-pressing and hot-isostatic pressing, and during the post heat-treatment of Si_3N_4, liquid phase sintering (LPS) occurs [37].

2.5.1. Liquid-phase Sintering Mechanism

Liquid phase sintering is a process which has been applied especially for the production of ceramic solids with high mechanical performance for a wide range of engineering applications such as automobile engine connecting rods and high-speed metal cutting inserts [60]. As illustrated in **Fig. 2.16**, it is widely accepted that LPS occurs in three stages of 1) particle rearrangement, 2) solution-reprecipitation and 3) solid-state or skeleton sintering with some degree of overlapping [37].

In the first stage of the LPS process, liquid forms within the powder compact, spreads between the grains and induces particle rearrangement due to the liquid capillary forces. Rearrangement and densification occur by the movement of particles from their original positions to new positions with higher degree of space filling [37]. Good wettability and solubility of Si_3N_4 are essential and the overall densification is strongly affected by the amount and viscosity of liquid phase present, green density, wetting, sintering temperature and type of additives [37]. The rate of densification

follows $\Delta L/L_0 \approx \frac{1}{3}\Delta V/V_0 \approx t^{1+y}$ where ΔL and ΔV are the changes in length and volume, respectively. L_0 and V_0 correspond to the initial length and volume, respectively. t is time and the exponent of 1+y is slightly greater than 1 [37].

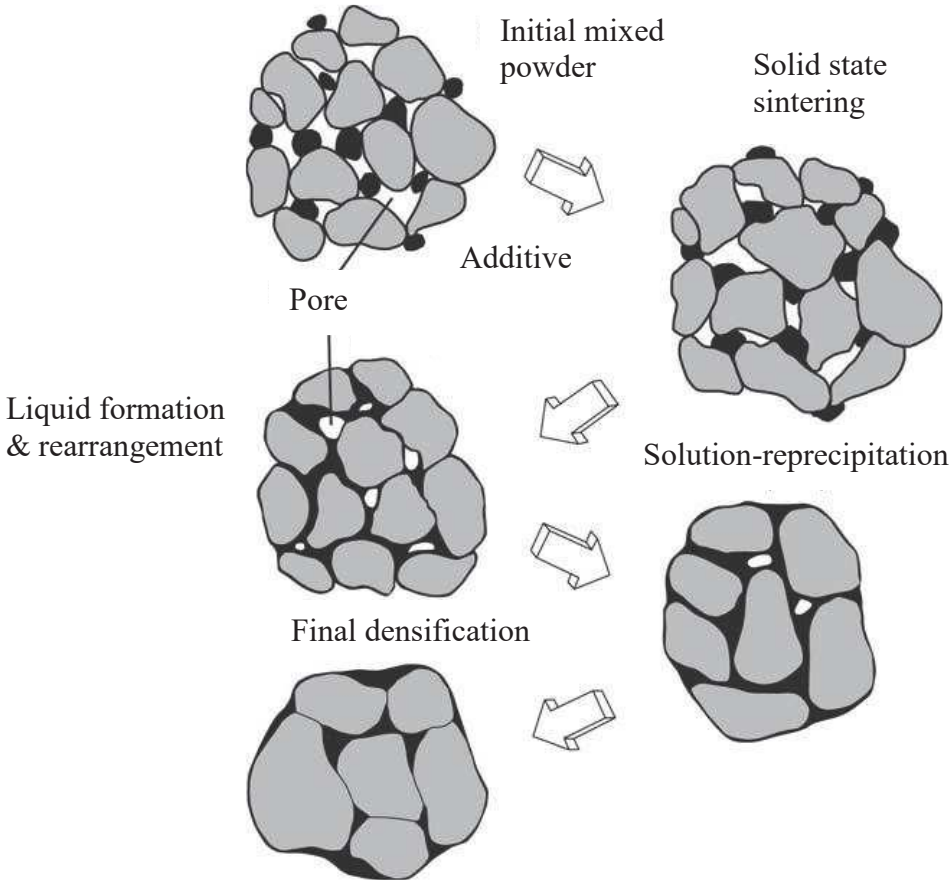

Fig. 2.16. Schematic illustration of the steps of LPS process [60]

In the second stage, solution-precipitation leads to further shrinkage and densification. This is induced by the capillary forces and the chemical potential gradient between points of contact and the area away from the contact points. This mechanism occurs by dissolution of atoms at the contact points and reprecipitation away from those areas. Simultaneously, grain growth occurs by dissolution of smaller particles and reprecipitation on coarser particles [37]. In this stage, shrinkage follows $\Delta V/V_0 \approx t^{1/n}$ where n is 3 when solution-precipitation is the rate-determining mechanism (e.g., in Si_3N_4-MgO system), while the value is 5 when diffusion through the liquid predominates (e.g., in Si_3N_4-Y_2O_3 system) [10].

By decreasing the free surface area through the pore filling mechanism and reduction of pore volume, shrinkage and significant densification occur during the LPS process [44]. The presence of liquid phase is essential for both densification and phase transformation. Although the pore filling mechanism is performed simultaneously with α → β-phase transformation, complete conversion to β-Si_3N_4 does not imply the full reduction of porosity [44]. Based on **Fig. 2.17**, particle-rearrangement is the fastest mechanism in the LPS process. By contrast, solution-reprecipitation and solid-state or skeleton sintering, which are respectively controlled by liquid phase and solid-state diffusion mechanisms, are comparatively slower.

Grain growth or particle coarsening is the dominant mechanism of stage III. The rigid skeleton impedes any further particle rearrangement and comparatively reduces the shrinkage and densification rates [37].

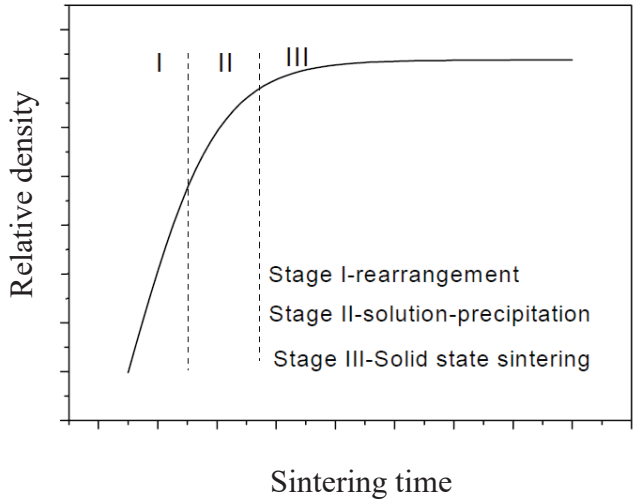

Fig. 2.17. Three stages of liquid-phase sintering [37]

Generally, near net-shaped large and complicated samples can be produced by a heating process which offers low shrinkage and little densification [45]. Addition of a small amount of carbon to the starting materials can lead to a further decrease in the overall linear shrinkage. This occurs by formation of SiC particles which bond together the Si_3N_4 grains and increases the resistance to particle rearrangement and inhibits large shrinkage [45]. In the absence of oxide additives, as illustrated in **Fig. 2.18**, commercial RBSN shows some shrinkage, while high purity silicon nitride ceramic shows negligible (0.2%) linear shrinkage. Unlike Al_2O_3 and CaO, the presence of silica

alone or Fe_2O_3 showed no significant effect on the sintering and shrinkage behaviour of this ceramic [57].

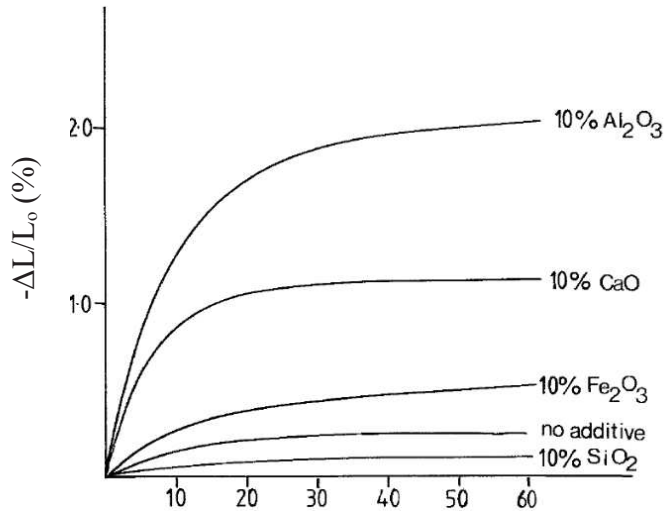

Fig. 2.18. Shrinkage of high purity silicon nitride in the presence of additives at 1750°C [57]

2.5.2. Microstructural Development of Heat-treated Si_3N_4 Ceramics

Phase transformation of α to β-Si_3N_4 is the other process occurring during LPS. Following nitriding, the microstructure is composed of α- and β-Si_3N_4; in the presence of a liquid phase at temperatures above 1410°C, all the remaining α-Si_3N_4 transforms into β-Si_3N_4 grains embedded in a glassy phase [37]. Under the heating condition of 1400-2000°C and 0.1 to 100 MPa N_2 pressure, α-Si_3N_4 is thermodynamically unstable and tends to transform to β-Si_3N_4, which is stable at all temperatures [9, 37]. The α → β-Si_3N_4 phase transformation requires a lattice reconstruction and requires the presence of a liquid during the solution-precipitation stage [10, 45]. In contrast, β → α-Si_3N_4 phase transformation is not thermodynamically feasible and has not been observed [37].

By lowering the activation energy of transformation to 405 kJ.mol^{-1}, the presence of a liquid phase is required for breaking six bonds (each bonding energy is ≈ 435 kJ.mol^{-1}) and remaking strong Si-N bonds [37]. This liquid could be pure silicon but at temperatures below 1410°C this phase does not exist. However, in the presence of silica, metal oxides or inter-metallic compounds such as $FeSi_2$, liquid formation can occur (e.g., $T_m \approx$ 1212°C) [9]. Oxide additives such as MgO, Y_2O_3,

Y_2O_3+Al_2O_3 and impurities like Al are the other sources of liquid phase formation [9]. When alpha phase is in contact with this phase, it dissolves and reacts with atomic nitrogen to form β-Si_3N_4 [9]. In heat-treated samples, β-phase is present as either original grains formed during the nitriding process or as produced during the post heat-treatment process by thermal transformation [47]. Accordingly, depending on the chemical composition of the ceramics at T< 1400°C, reprecipitation could occur: a) on the newly generated β-nuclei by super-saturation or b) on the pre-existing β-Si_3N_4 that coexist within the α-grains in the starting composition. Hence, different microstructures may develop [37].

The difference between grains' curvatures is the driving force for grain growth during the post-heat treatment. The growth kinetics of β-Si_3N_4 grains is described by **Eq. 2.29** where G is average grain size, G_0 is the initial grain size, k is the kinetic constant, t is the time and the exponent n is 3 for diffusion control reaction and 2 for interface-reaction control [37].

$$G^n - G_0^n = kt \qquad \textbf{Eq. 2.29}$$

After heat-treatment, the microstructure is composed of elongated β-grains with an aspect ratio (length-to-diameter) in the range of 5 to 10, which is controlled by the composition of the starting powder, type of additives and sintering parameters [37]. Compared to the Si_3N_4 prism planes, the basal planes are less stable but grow faster**.** This is because the attachment of a surface nucleus is energetically more favourable on the basal plane and this results in the formation of a rod-like grain morphology as shown in **Fig. 2.19** [37].

During the cooling process, liquid may disappear by either of the following routes:

1- Evaporation [37]
2- Incorporation into the solid phase and formation of a solid solution [37]
3- Crystallization of the liquid and/or formation of a glassy phase [37]

In the latter case, amorphous or crystalline secondary phases may precipitate at Si_3N_4 grain boundaries and triple junctions as shown in **Fig. 2.20** [37, 51]. The thickness of the inter-granular glassy phase is mainly affected by the types of additives [37]. Accumulation of this amorphous phase at grain boundaries and triple points has detrimental effects on the high temperature mechanical properties of silicon nitride and is the result of using large amounts of oxide additives

[47]. Hence, the microstructure of heat-treated silicon nitride is composed of β-Si_3N_4 and amorphous phases and the presence of some residual α-phase in the form of equiaxed grains is also feasible due to incomplete phase transformation [37].

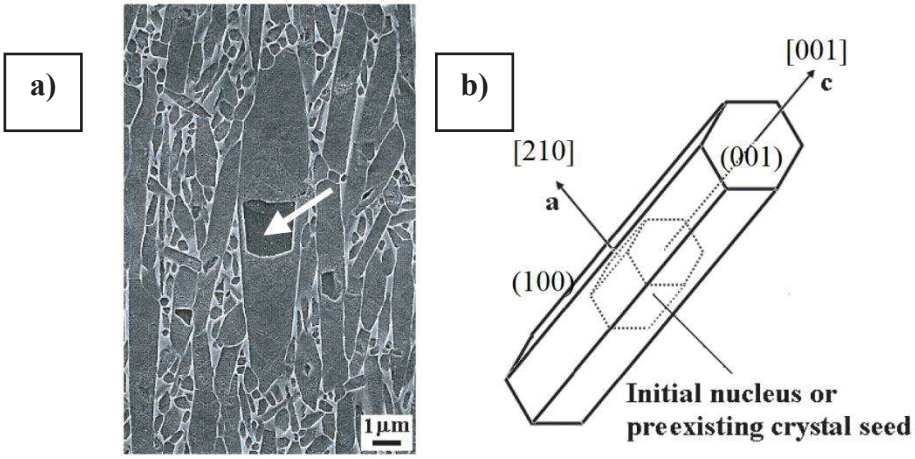

Fig. 2.19. Illustration of the growth of faceted β-Si_3N_4 grains from a pre-existing crystal seed, a) grain growth along the c-axis and from the initial seed particle and b) schematic illustration of the growth directions and crystal planes [61]

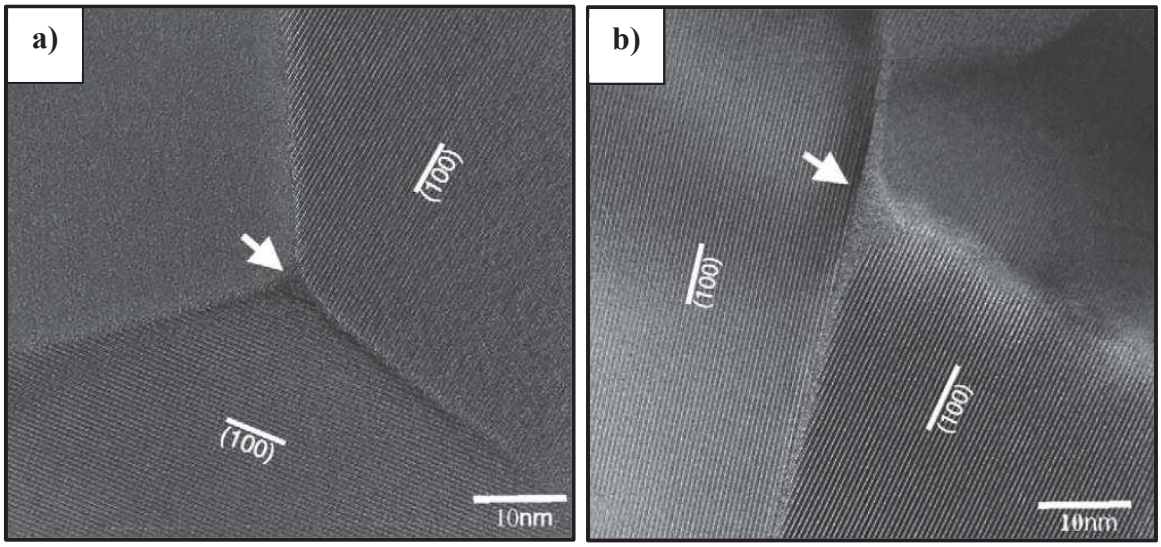

Fig. 2.20. TEM images of triple junctions of Si_3N_4 grains in RBSN ceramics using a) 6 wt.% Y_2O_3-2 wt.% Al_2O_3 and b) 6 wt.% Y_2O_3-2 wt.% MgO [51]

2.5.3. Role of Additives and Impurities on the Post Heat-treatment Process

In the production of a sintered structure, using oxide additives is a prerequisite of obtaining a fully dense microstructure [37], while in porous structures, these additives facilitate the phase transformation and particle consolidation. Relative density, phase ratio of α/β, grain size and grain aspect ratio are among the many properties which are affected by the type and amount of sintering aids [51]. By mixing the starting silicon powder with a low volume fraction of additives, sintering aids are incorporated into the structure of RBSN ceramics prior to the nitridation process [57].

Oxide or non-oxide aids such as BeO, AlN, Mg_3N_2, ZrN, ZrC, Al_2O_3+AlN and Y_2O_3+AlN, which form solid solutions with silicon nitride, have been used individually or in combination [37]. In contrast, MgO, Al_2O_3, La_2O_3, Nd_2O_3, Yb_2O_3, Y_2O_3, CeO_2, ZrO_2, Li_2O and $MgAl_2O_4$ are among the many additives which have been used in binary or ternary systems with no solid solution formation [62].

At elevated temperatures, the SiO_2 layer reacts with sintering additives and impurities and produces a low temperature melting point silicate liquid via **Eq. 2.30**. This phase wets the surface of RBSN grains, penetrates the grain boundaries, dissolves α-Si_3N_4, initiates the sintering mechanism and precipitates β-phase [37, 57]. During the cooling process, the liquid solidifies either as amorphous or partially crystalline silicate phase at the grain-boundary [37].

$$\alpha\text{-}Si_3N_4 + SiO_2 + \text{additives} + \text{impurities} \rightarrow \beta\text{-}Si_3N_4 + \text{amorphous/crystalline phase [37]} \quad \textbf{Eq. 2.30}$$

The concentration of silica on the surface of particles, the amount of α-Si_3N_4 dissolved in the liquid and the content and type of additives or impurities determine the melting point and viscosity of the resulting liquid phase [37]. For instance, the eutectic temperature in the binary rare earth oxide – silica (RE_2O_3-SiO_2) systems is increased based on the following order: Nd_2O_3-SiO_2 (1600°C) < La_2O_3-SiO_2 (1625°C) < Yb_2O_3-SiO_2 (1650°C) < Y_2O_3-SiO_2 (1660°C) [62]. The presence of impurities or nitrogen gas decreases the eutectic temperature [37] and with the addition of Si_3N_4 to the above system, the nominal eutectic temperatures are reduced as follows: Nd_2O_3-SiO_2 (1500°C), La_2O_3-SiO_2 (1500°C), Yb_2O_3-SiO_2 (1550°C), Y_2O_3-SiO_2 (1550°C) [62].

Additives tend to agglomerate during the process and agglomeration within the ceramic matrix may lead to the formation of large voids surrounded by dense regions [57]. Therefore, properties

of heat-treated ceramics can be also correlated to the thorough mixing and distribution of additives within the matrix particles [57]. It has been observed that good additive distribution is as important as their value, and a good distribution of additives within the silicon compact leads to an enhanced shrinkage [57]. Particle size of additives could also affect the distribution of liquid phase within the matrix, so that additives of large particle size would lead to the preferential formation of Si_3N_4 with an abnormally large grain size around the oxide additive-rich regions due to the uneven distribution of particles [63]. Therefore, the amount and rate of densification, the morphology of β-microstructure developed after the heating, the characteristics of the grain-boundary phase and thus the high-temperature mechanical properties of ceramics are greatly controlled by the nature and characteristics of the introduced oxide additives [37].

In the production of Si_3N_4, various sintering aids may be used for a) densification, b) $\alpha \rightarrow \beta$ phase transformation and c) anisotropic β-Si_3N_4 grain growth [62]. A functionality triangle map has been plotted by Plucknett et al. in **Fig. 2.21,** which assigns a specific role to each individual additive during sintering of silicon nitride ceramics. Those additives that sit in the middle of the triangle, contribute equally to all the three functions, while those which sit at the corners contribute to only one role and others are positioned based on the weights of their contributions to multiple functions [62].

Single sintering aids such as oxides of the lanthanide or Group III elements (e.g. La_2O_3, Nd_2O_3, Yb_2O_3, etc) are among the rare earth oxides (RE_2O_3) which are typically used to facilitate $\alpha \rightarrow \beta$ phase transformation [62]. In multiple component additive systems, phase transformation occurs at much lower temperatures compared to single additive systems [62]. Thus, a single RE_2O_3 has minimal beneficial effect on densification and does not allow significant particle rearrangement. In this case, by formation of a high viscosity oxynitride glass phase, sintering is controlled by diffusion and densification and is retarded [62]. To densify such compositions, hot pressing, hot-isostatic pressing, and gas-pressure sintering must be applied [62].

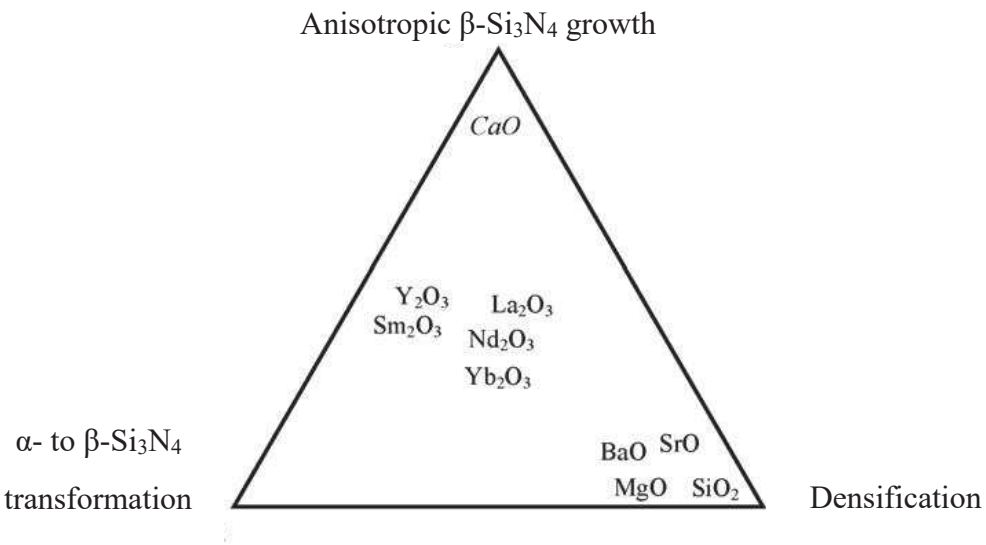

Fig. 2.21. Functionality map showing the effect of individual sintering aids during sintering of Si_3N_4 ceramics [62]

In contrast with rare-earth oxides which have high melting points and low densification, alkali and alkaline-earth oxides such as MgO and CaO have low melting points and due to the low viscosity of their liquids, can enhance the solution-diffusion-precipitation mechanism [37]. It has been observed that CaO significantly decreases the glass viscosity and increases the rate of densification [62]. However, as illustrated in **Fig. 2.21**, this oxide contributes to anisotropic β-grain growth and promotes debonding of the grains in dense Si_3N_4 ceramics [62]. Therefore, the initial aim of adding CaO to the silicon nitride system is in promoting anisotropic grain growth [62]. In contrast, Yb_2O_3 encourages the formation of granular grains rather than anisotropic growth due to the preferential attachment of Si and N to the prism plane surfaces [62].

For densification of Si_3N_4, MgO is one of the most commonly used aids which reacts with SiO_2 to form liquid eutectic at 1543°C [56]. In combination with MgO or Al_2O_3, Y_2O_3 has been extensively used for the fabrication of dense silicon nitride ceramics (99% of theoretical density) composed of elongated β-grains [64]. However, the Y_2O_3-MgO system has a lower melting point and lower viscosity than those of Y_2O_3-Al_2O_3. Therefore, RBSN sample in the presence of the former oxide systems has demonstrated higher degrees of nitridation and relative density, while lower extents of phase transformation and β/α-phase ratio [51].

2.5.4. Role of Powder Bed on the Post Heat-treatment Process

The technique of using a powder bed has been adopted and used in many processes that deal with high temperatures. While the effect of powder bed on microstructural properties of RBSN grains is still lacking, there are a few studies which have focused on the effect of powder bed on the densification, weight loss and shrinkage of the heat treated Si_3N_4 samples [34, 56, 65, 66].

During heating, the density is changed by a number of processes including loss and gain of weight [57] and loss of porosity [57]. The presence of impurities such as O_2, H_2O or CO in the atmosphere is an important factor which leads to decomposition of Si_3N_4. Pressure vessel's walls serve as large surface area substrates to adsorb water between running cycles and water molecules may be desorbed from the inner surfaces during heating [57]. However, thermal decomposition of Si_3N_4 by direct sublimation above 1500°C is the major factor which leads to considerable weight losses through the reaction: Si_3N_4 (s) → Si (g) + N_2 [34, 35]. Powder bed technology and N_2 gas over-pressurizing (e.g., P= 1.4 MPa) are effective in preventing Si_3N_4 thermal decomposition [57]. To slow down this dissociation, the compacted sample can be immersed in a powder bed of appropriate composition which is usually composed of silicon nitride, boron nitride and the same proportion of oxide additives as added to the base ceramic [34]. Therefore, in addition to inhibiting the decomposition of Si_3N_4, this process stops the loss of oxide additives by volatilization [34]. Consequently, inhibiting volatilization, reducing weight loss and keeping the microstructure uniform, are considered as the main role of the powder bed [65].

The effects of MgO on the properties of RBSN have been studied by multiple researchers. Although magnesia is a well-known refractory oxide, it is highly volatile at temperature above 1400°C and shows remarkable mobility at high sintering temperatures. Besides, in a reducing atmosphere in the presence of H_2O, the formation of volatile hydroxides such as MgOH and $Mg(OH)_2$ increases the mobility of MgO. In addition to the mixing approach which is a common method in most studies, additives may be introduced into the RBSN as soluble salts or by vapor diffusion from a powder bed [56]. This oxide has been added to commercial RBSN ceramic by infiltrations of saturated aqueous magnesium nitrate under vacuum, followed by a calcination step at 500°C. In a vacuum, the rate of vapor transport away from a surface is controlled by the rate of

evaporation-condensation, while under 1 atm. gas pressure it is controlled by the gaseous phase diffusion of magnesia away from the source [56, 57, 66].

Sintering and linear shrinkage of silicon nitride at atmospheric pressure has been observed by embedding the RBSN compact in a powder bed mixture containing MgO [34]. Impregnation has been carried out by adding magnesia (10 wt.%) to the powder bed as a source of magnesia [56]. An increase in magnesium content of RBSN samples with annealing time (**Fig. 2.22-a**) and annealing temperature (**Fig. 2.22-b**) has been observed based on the impregnation experiments [56].

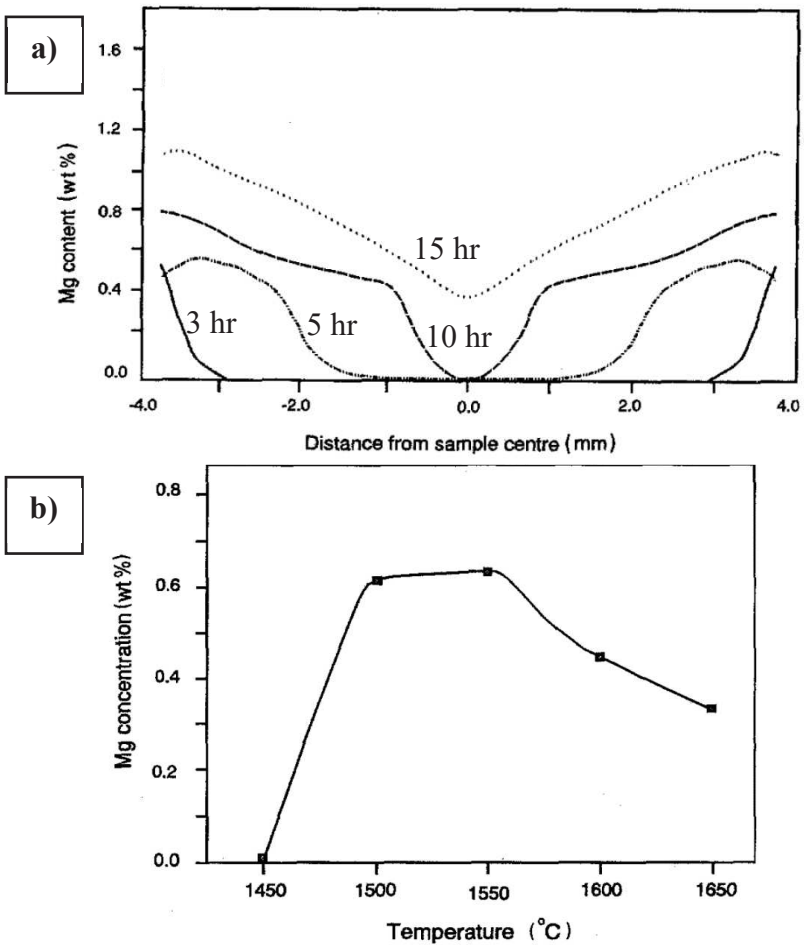

Fig. 2.22. Magnesium concentration a) across RBSN sample at 1450°C after various annealing time and b) at sample centres and at various annealing temperature after 5 hr [56]

Using an electron microprobe analyser, the obtained magnesium profiles have illustrated that almost 2 wt.% magnesia has been transported into the compact allowing it to achieve the densification of 93% of theoretical [56].

As shown in **Fig. 2.23** in the absence of MgO in the powder bed, the content of MgO added as sintering aid to the silicon nitride compact has been decreased by volatilization at high temperature [34]. Initially, a rapid decrease in the content of MgO was observed while after several hours, loss of MgO was greatly impeded. This could be due to reaching the vapor pressure equilibrium in the powder bed or by densification and the formation of closed pores [34]. Almost complete loss of MgO has been also observed by a laser microspectral analysis on the surface of a sintered sample in **Fig. 2.24.** This is explained by the high vapor pressure of MgO at elevated temperatures, e.g., 10^{-4} Torr at 1600°C [34].

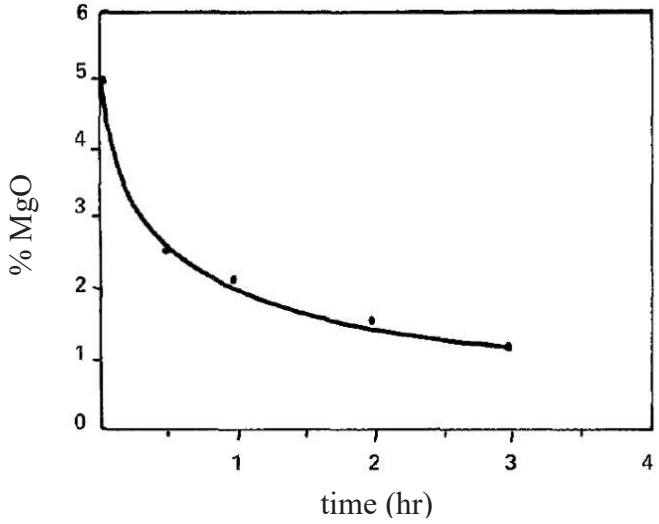

Fig. 2.23. Content of MgO in Si_3N_4 sample sintered at 1800°C for various time [34]

2.6. Pore Structures and Pore Characteristics

Foams are widely applied in engineering fields for lightweight components, refractory materials, catalysts, industrial absorbents and filtration membranes [67, 68]. In general description, *foam* refers to solids with pores, cavities, voids or channels, therefore any materials which contains cavities or pores may be considered porous, but the structure of pores can be quite complex and have various morphologies as shown in **Fig. 2.25** [67]. For instance, surface roughness which appears in **Fig. 2.25-g** generally is not considered as a pore unless the depth is more than its width

[67]. The shape and size of pores have significant influence on the response of the materials to an external or internal stress [69]. To understand the relationship between processing, microstructure and mechanical properties of porous structures, a good understanding of pore morphologies is essential and to avoid any ambiguity in describing the pores structure, a number of useful terms must be defined [67].

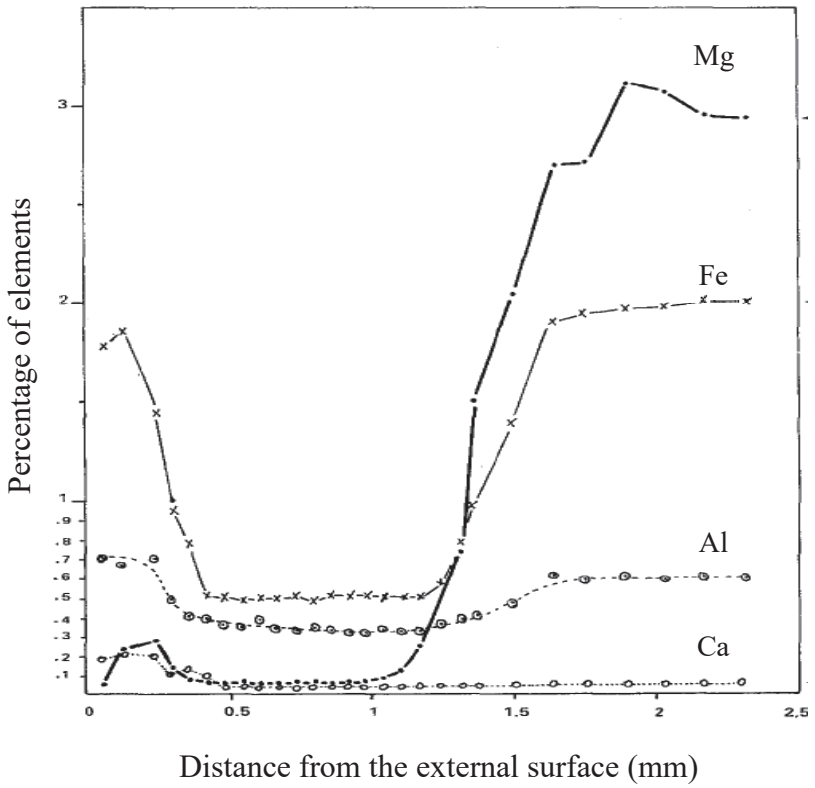

Fig. 2.24. Concentration profile of Mg versus distance in a sintered Si_3N_4 sample [34]

True density (and true volume) refers to the density (and volume) of materials when excluding pores and voids, while apparent density (and apparent volume) refers to density (and volume) of materials including pores and voids [67]. *Closed pores*, *blind pores* and *through pores* are the three classifications of pores based on their accessibility [70]. Closed pores are totally isolated from their neighbours, **Fig. 2.25-a**, and closed porosity is the volume of closed pores to the apparent volume [67]. These pores are inactive in fluid flow and adsorption of gases but effective in altering bulk density, mechanical strength and thermal conductivity of solids [67]. In contrast, open pores are interconnected, and open porosity is the volume of open pores to the apparent volume [67]. Open pores are either accessible from one direction which are called *blind pores* (**Fig. 2.25-b** and

f) or have continuous channels of communications with neighbours through two ends, which are called *through pores* (**Fig. 2.25-c**, **d** and **e**).

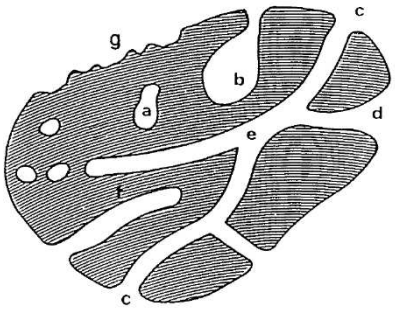

Fig. 2.25. Schematic illustration of various pores [67]

Physical properties such as density, thermal conductivity and strength, as well as chemical reactivity and foam interactions with gases and liquids are affected by the characteristics of pores [67]. Porous solids may have pores of various origins and sizes in the range of several nano-meters to several tens of microns [3]. Structures with macropores are applied in thermal insulation, biomedicine scaffolds, oxygen transport, filtration membranes and solid oxide fuel cells [71] and ceramics with high porosity are applied in filtration membranes, catalysts and sensors [72]. The control of pore structure and porosity content has a great importance in the design of porous materials [67], and the ability to describe the behaviour of porous solids in response to an external stimuli is important as it enables one to modify the microstructure of materials to specific requirements [69].

All the structural features, e.g., pore size, pore size distribution, porosity, interconnectivity and pore morphology, are highly dependent on the fabrication process [73]. Strength is usually decreased by increasing the total pore volume, therefore maintaining high strength may degrade other functional properties related to the morphological parameters such as pore size, morphology and tortuosity [71]. Therefore, the performance of these materials depends closely on their porosity and pore structure which can be controlled by fabrication techniques and conditions [73].

2.7. Mechanical Properties of Porous Si_3N_4 Ceramics

The strength of ceramic foams is one of the most important parameters which determines whether the solid can be applied for a specific function or not. Mechanical properties have great importance

especially in ultra-high porous structures as compressive strength is significantly reduced by the increase of porosity [68]. While some parameters such as nitriding temperature indirectly alter the strength of RBSN foams, others such as pore morphology, porosity content, compositions and grain morphology directly affect the mechanical performance and must be considered. Therefore, a well-designed microstructure is required to get a solid with a low number of defects and good mechanical properties.

2.7.1. Pore Characteristics

Depending on the applications being considered, foams with different pore characteristics might be required. Generally, a structure with uniform and closed pores and no defects exhibits good strength [68] while ceramics with large pores have low mechanical strength and are suitable as gas combustion mediums, catalyst supports and biomedical implants [74]. Level of porosity is the first and the most important parameter which affects the foam strength and may even result in foam collapse during the fabrication process. **Fig. 2.26** shows that the flexural strength of porous RBSN decreases exponentially as its porosity level increases and eventually reaches ≈ 1 MPa at ≈ 83 vol.% porosity [25].

2.7.2. Phase Composition of Silicon Nitride Ceramics

Strength of silicon nitride ceramics is also a function of composition, e.g., amount of unreacted silicon, composition of the glassy phase, and α/β-Si_3N_4 ratio. The presence of glassy phase is severely detrimental to the high temperature mechanical strength of the ceramic and therefore, it is ideal to decrease the content of silica prior to sintering and densification [9].

Phase composition after nitridation has an important role on the strength of samples as high alpha content provides better sinterability and improves toughness. The toughening effect of rod-like grains is enhanced by increasing the grain diameter which causes crack deflection and bridging [51]. Additionally, the amount of β-Si_3N_4 grains in the nitrided sample greatly influences the size of heat-treated grains. Since β-Si_3N_4 grains act as nuclei for β-Si_3N_4 formation, the size of the β-rods increases during post sintering [47]. It has been reported that a microstructure with a bimodal grain size distribution with fine and coarse structures has markedly improved mechanical properties [58].

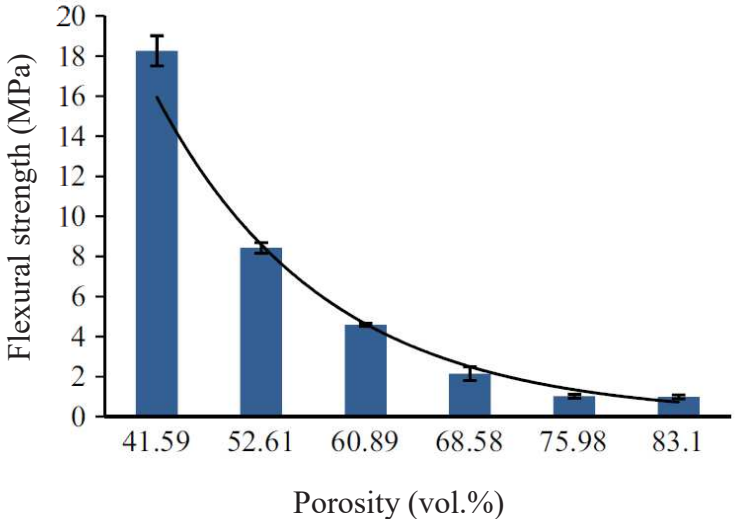

Fig. 2.26. Flexural strength versus the porosity level in porous RBSN ceramics [25]

Cracks and dislocations improve the nitridation of the silicon compact while a low degree of nitridation and residual silicon have detrimental effects on the fracture toughness and significantly reduce the mechanical properties of the sample. Molten phases formed during nitriding also result in large voids and defect formation, which are detrimental to the high temperature strength [51, 58].

2.7.3. Grain Morphology and Aspect Ratio

Another parameter that influences the strength is the grain size and aspect ratio of the phases present. Two common approaches in the production of samples with enhanced mechanical performances are: a) addition of a second phase such as SiC whiskers, SiC platelet, ZrO_2 or TiN particles which act as reinforcements by crack deflection, microcracking and crack bridging, but also b) self-reinforcement of Si_3N_4 bodies by microstructural control [58].

Ceramic composites, such as zirconia-toughened ceramics, exhibit good mechanical properties due to their optimized composition [68]. By introducing zirconia phase in an alumina matrix, ultralight alumina/zirconia foams with porosity of ≈ 95-96 vol %, compressive strengths of ≈ 0 .77-1.52 MPa and closed pore structure have been obtained [68]. Although the porosity of this material was

quite high, the strength was due to the stabilized alumina/zirconia foam, uniformly distributed zirconia in the cell wall, closed pore structure, and thin and uniform-thickness cell walls [68].

In the second approach, the mechanical properties of porous Si_3N_4 are affected by grain morphologies, grain size, glassy phase composition and internal defects [58]. Kawai has illustrated that interlocked columnar β-Si_3N_4 grains possess enhanced flexural strength compared to equi-axed grains [75]. Rod-like β-Si_3N_4 grains with enhanced interlocking show superior properties both at high and low temperature including high strength, high thermal shock resistance and high strain and damage tolerance. A high aspect ratio of fine grains increases grain interlocking, reduces the possibility of intergranular defects and thus increases the strength [45, 47]. Silicon nitride whiskers, which randomly grow in the pore cavities, might also alter the strength of sample. It has been reported that these grains do not contribute to the formation of solid struts and may decrease the strength of porous body [25]. In spite of many studies on the strengthening mechanism of elongated grains with high aspect ratio [46], the role of whiskers on the mechanical performance of highly porous Si_3N_4 structures is still not clear and well-understood.

2.8. Fabrication of Porous Ceramics

Ceramic foams such as alumina, zirconia, silica, titania, and silicon nitride are classes of lightweight inorganic materials which have low bulk density and are chemically, mechanically and thermally stable under harsh conditions [46, 68]. A combination of high permeability, remarkable chemical stability and excellent thermal stability, low thermal conductivity, biocompatibility, and good mechanical stability governs the widespread application of these materials [71].

Compared to other ceramic foams, porous silicon nitride has drawn attention due to its low dielectric constant, low oxidation and corrosion resistance and superior mechanical properties at high temperature [39]. Si_3N_4 foams have been used as gas/liquid filters, catalyst supports, acoustic absorbents, separation membranes, microwave-transparent components and bone scaffolds and more recently have become attractive for electromagnetic wave penetrating materials to reduce the dielectric constant and loss [73, 76-78].

A great deal of effort has been expended in the development and fabrication of porous ceramics with various methods, especially in the last two decades [79]. To fabricate ceramic foams with

tailored properties a variety of methods have been used such as carbothermal reduction of SiO_2 [72, 80], cold isostatic pressing [76], partial sintering of silicon nitride, sacrificial template method, adding pore-forming agents, direct foaming [73], freeze casting or ice-templating [71, 76], tape casting [46], gel-casting, combustion synthesis and replica techniques. Each method presents its own advantages and disadvantages. Some of these processes are expensive as they require high temperatures or expensive starting powders. Low levels of porosity, lack of pore interconnectivity, high cost of the post-sintering machining steps, inhomogeneity and low strength of the structure, complexity of the fabrication technique, toxicity of the materials, poor rheological properties of powder particles, high sintering temperatures (e.g., 1900°C), large amounts of sintering aids and high linear shrinkage (e.g., 15-20% [23]) are some of the other issues and difficulties which could be involved in these techniques. More explanation on the details of various fabrication procedures is provided in the following discussions.

2.8.1. Carbothermal Nitridation of Silica

In the presence of oxide additives and carbon black, and under nitrogen pressure of ≈ 0.6 MPa, porous β-Si_3N_4 ceramic was obtained at T >1600°C by carbothermal nitridation of SiO_2 via **Eq. 2.31** [72, 80].

$$3SiO_2 + 6C + 2N_2 \rightarrow Si_3N_4 + 6CO \qquad \textbf{Eq. 2.31}$$

Large dimensional change, ≈ 16% linear shrinkage and the need for using expensive high-quality α-Si_3N_4 seeds to control the microstructural and mechanical properties are some of the disadvantages of this technique [80].

By addition of α-Si_3N_4 seeds, α-Si_3N_4 was developed at low sintering temperatures while at T> 1700°C the formation of β-Si_3N_4 with fibrous microstructure was obtained [72]. The presence of Si_3N_4 seeds also led to the formation of a fine microstructure as shown in **Fig. 2.27-b** compared to the one in the seed-free sample, which is composed of only coarse equiaxed Si_3N_4 grains with small aspect ratio, **Fig. 2.27-a** [72].

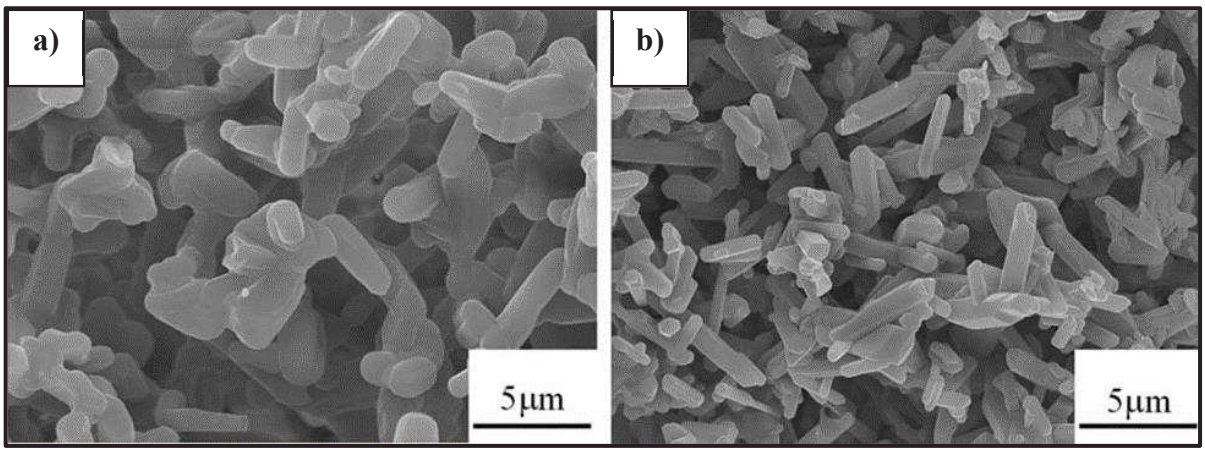

Fig. 2.27. SEM micrographs of porous Si_3N_4 produced by carbothermal reduction of silica in the presence of a) 5 wt.% Y_2O_3 and b) 5 wt.% Y_2O_3 and 5 wt.% Si_3N_4 seeds [72]

2.8.2. Cold Isostatic Pressing

In the presence of a binder (e.g., polyvinyl alcohol, PVA), cold isostatic pressing has been used for the fabrication of a porous Si_3N_4 structure with different pore structures [76]. The pore structure and bulk density can be controlled by changing the applied pressure. For instance, burning out the PVA particles and applying pressures of 2 and 20 MPa led to the formation of a monomodal pore structure (**Fig. 2.28**) with pores in the range of ≈ 1 μm diameter. Small pore size, low content of open porosity and high tortuosity led to a low permeability in these porous structures [76].

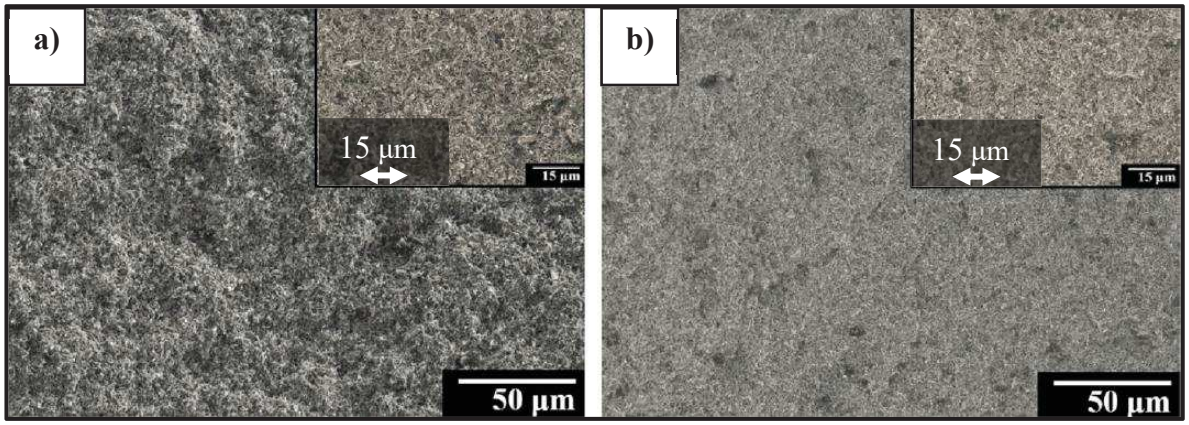

Fig. 2.28. SEM micrographs of porous samples prepared by cold isostatic pressing under a) 2 MPa and b) 20 MPa pressure [76]

2.8.3. Partial Sintering

By sintering the powder compacts to a certain degree of densification, fabrication of porous ceramics is feasible via partial sintering. For non-oxide ceramics such as Si_3N_4, SiC and SiAlON, by adjusting the amount and type of the sintering aids and sintering conditions such as time and temperature, partial sintering is used as a common, cost-effective and simple process for the fabrication of porous ceramics [79, 81]. For instance, porosities of 10 to 20 vol.% with strengths of 200 to 300 MPa have been achieved using the partial sintering method. Decreasing the sintering aid content increased the porosity content to ≈ 40-50 vol.%, while reducing the mechanical strength to < 50 MPa [77, 78]. Nevertheless, the porosity content obtained via this method is relatively low (< 60 vol.%), pores are fine and pore distribution is usually random and inhomogeneous. Therefore, there is a limited control over the microstructural properties of the foam and obtaining high permeability is not feasible by this method [78, 79, 81].

2.8.4. Placeholder Method

Adding fugitive substances into the initial ceramic mixtures is called the *placeholder method* and can be combined with various fabrication techniques such as partial sintering or pressureless sintering of silicon nitride powder. This process leads to the production of porous β-Si_3N_4 ceramics with macro-porosity and enhanced permeability [81]. To form a cellular structure, high temperature decomposable materials such as: graphite and coal ash, H_3PO_4, urea ($CO(NH_2)_2$) [17], benzoic acid balls [16], methyl methacrylate (MMA), poly (methyl methacrylate) (PMMA) [11, 18], polystyrene (PS), plastic particles, starch, sawdust, shell flour, long fibers such as thread, metal wires and organic whiskers may be added to the starting powder and are burned out to form pores [3, 81]. To completely eliminate the pore forming agents, this method requires a post heat treatment process which is generally difficult and considered as a drawback, especially since the presence of residual impurities and carbon in the system is very common [77].

In other cases, non-volatile materials such as KCl [17], ammonium carbonate, ammonium bicarbonate and ammonium chloride have been used to produce pores after which the material is soaked in water to dissolve the residual agent [3].

By adjusting the sintering temperature, content and type of pore former agents, porosity, pore size distribution and morphology of pores can be controlled [77]. As an example, via a pressureless sintering method and by using α-Si_3N_4 and phosphoric acid (H_3PO_4), porous Si_3N_4 ceramics with porosities of 46.5 vol.% and 60 vol.% and bending strength of 90 and 110 MPa are formed at 1000 and 1200℃, respectively. **Fig. 2.29-a** and **b** illustrate the relatively spherical morphology of pores obtained by this method [77].

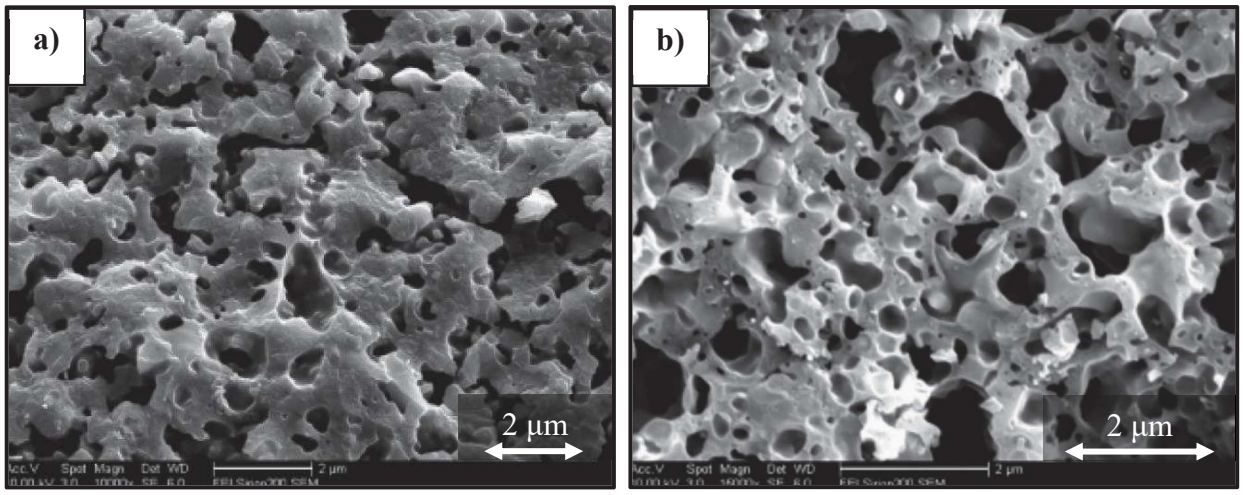

Fig. 2.29. SEM images of porous silicon nitride ceramics in the presence of 50 vol.% H_3PO_4 and at sintering temperatures of a) 1000℃ and b) 1200℃ [77]

In contrast, using starch as the pore former agent led to the formation of irregular pores, as shown in **Fig. 2.30-a** [79] and using fugitive organic whiskers led to the formation of uniform rod-like pores with random directions, **Fig. 2.30-b** [81]. Fly ash cenosphere balls resulted in the formation of perfectly spherical and large pores with fine inter-particle pores of < 1μm, as shown in **Fig. 2.31-a** to **c**. Beside acting as pore former agents, these balls could melt become a sintering aid and densify the structure at 1780℃ [78].

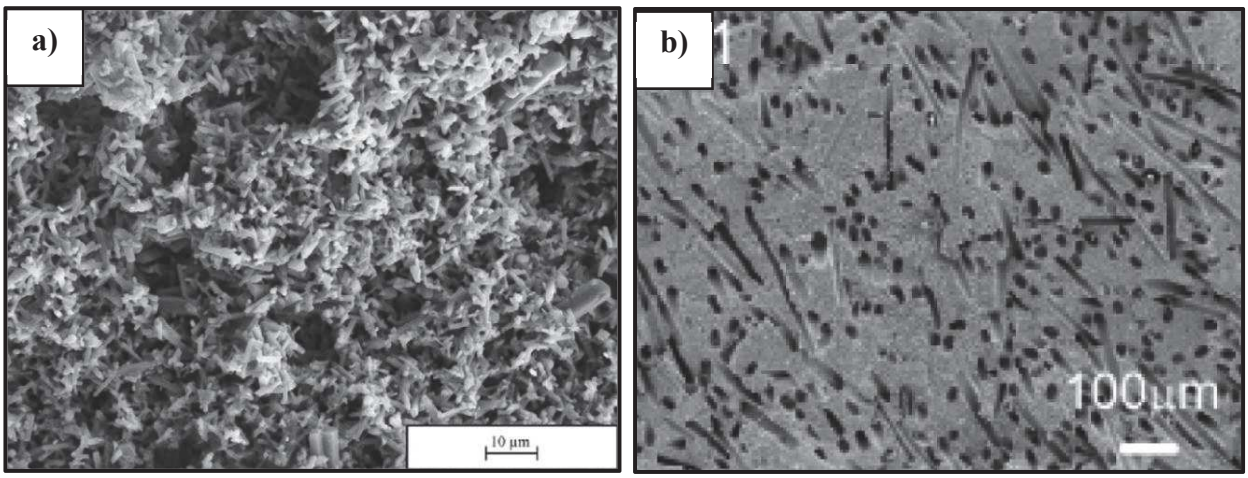

Fig. 2.30. SEM micrographs of porous Si_3N_4 ceramics using a) starch [79] and b) fugitive organic whiskers [81] as pore former agents

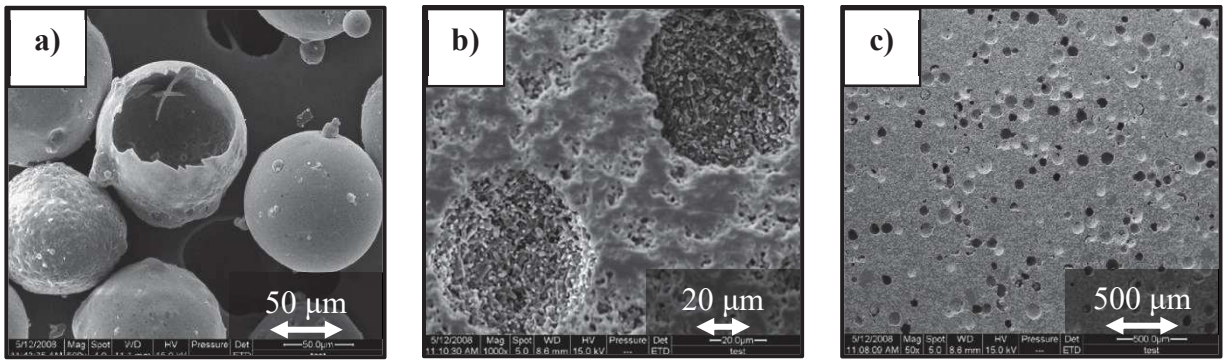

Fig. 2.31. SEM micrographs of a) Fly ash cenosphere balls, b and c) small pores and spherical holes in matrix [78]

2.8.5. Direct Foaming

In the fabrication of pores with either open or closed structure, as shown in **Fig. 2.32**, the direct foaming method is convenient, cheap and effective [68, 73, 82]. This process involves direct incorporation of gas into the ceramic suspension and can lead to the fabrication of highly porous foams [68].

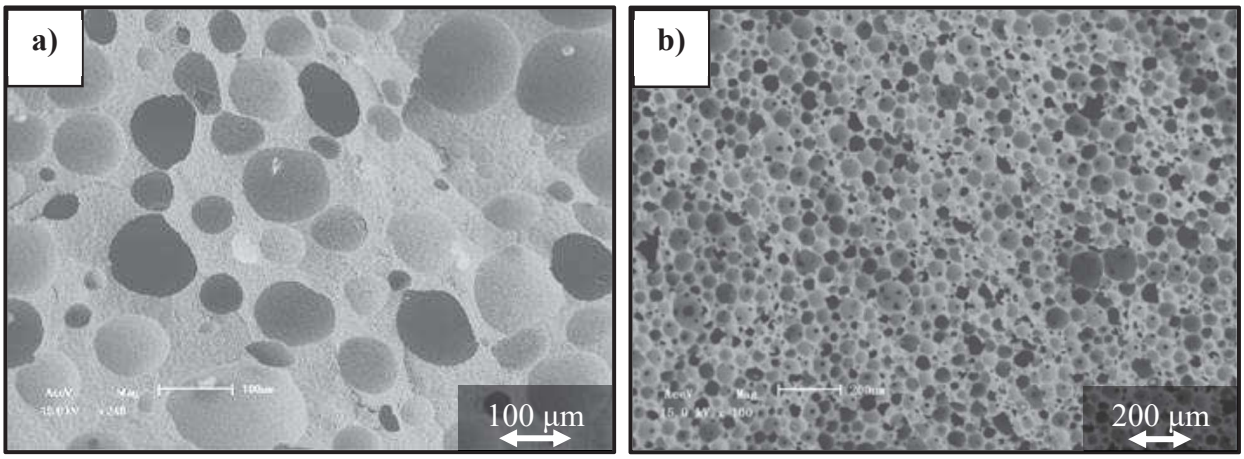

Fig. 2.32. SEM microstructure of porous Si_3N_4 foams produced by direct foaming, a) closed-cell structure and b) open-cell structure [82]

For the fabrication of high-performance homogenous porous structures, the stabilization of air bubbles is crucial as wet foams are thermodynamically unstable [73, 82]. This is mainly because of the high overall free energy of the system which is introduced by the large air-water interfacial area [82]. Therefore, the ultra-stable wet foams could be fabricated only by hydrophobic particles since they can enhance the strength of liquid films by adsorbing at the air-bubble interface [73]. Consequently, surfactant as foam stabilizer must be used in this method.

For the fabrication of silicon nitride foams using commercial α-Si_3N_4 particles, short and long chain surfactants have been used as the modifier [73]. However, the stability of wet foams and bubbles introduced into a ceramic suspension are higher for short-chain surfactants compared to those produced by long-chain surfactants [82]. Long-chains surfactants have low capacity for energy adsorption at the gas-liquid interface and the resultant wet foams may collapse within a few minutes after foaming [82].

Recently, Zhongpei Du et al. has fabricated porous silicon nitride foams using short chain surfactant n-propyl gallate (PG) [73]. In the absence of PG, the contact angle was 15^o, showing that the raw particles were hydrophilic. By improving the hydrophobicity of particles and foamability of wet foams, higher PG content increased the contact angle of particles and thus improved the stability of the bubbles and pores, shown in **Fig. 2.33** [73]. 1 wt.% PG foam stabilizer led to the formation of irregular large pores with closed structure due to the insufficient

hydrophobicity of the particles. The highest hydrophobicity achieved in the presence of 3 wt.% surfactant, increased the contact angle to 63◦ and led to the formation of regular spherical pores with 100 to 400 μm diameter [73].

Solid content and rotating speeds are the other effective parameters controlling the morphology and mechanical strength of this technique. For instance, by increasing the solid content from 20 vol.% to 30 vol.%, the porosity content decreased from ≈ 96 vol.% to ≈ 93 vol.%, and the compressive strength increased from 0.37 MPa to 2.6 MPa [73].

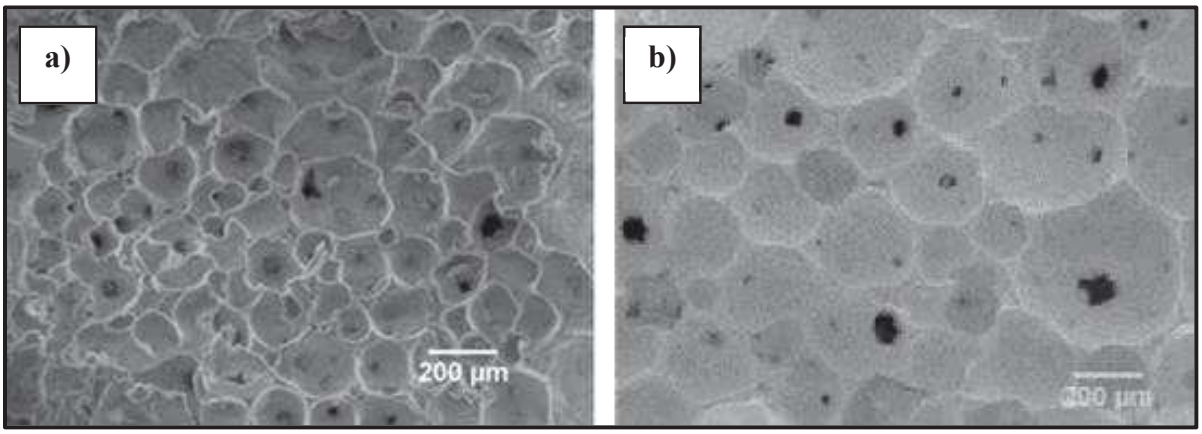

Fig. 2.33. SEM micrographs of porous Si_3N_4 foams fabricated via direct foaming method using a) 1 wt.% surfactant and b) 3 wt.% surfactant [73]

2.8.6. Ice-templating Technique

The *ice-templating* technique takes advantage of the growth of ice crystals to template colloidal suspensions. This process is based on freezing of the starting colloidal suspension, then segregation of particles by the solidification front and growing ice crystals. This is followed by removal of the frozen solvent, leaving sublimated crystals and pores which are replicas of the ice crystals. Eventually, heating is performed to consolidate and densify the structure in the presence of sintering additives [71].

Fig. 2.34-a and **b** show the typical anisotropic lamellar structure of pores obtained in ice-templated samples when water was used as a solvent. Freezing rate and solids loading are the most important features controlling the pore size and porosity content. For instance, by adjusting the solids loading from 50 wt.% to 65 wt.%, total pore volume has been altered between ≈ 69 vol.% to ≈ 52 vol.%.

It is also possible to control the morphology and size of pores using various solvents (e.g., water, camphene, TBA, cyclohexane) or by the aid of the additives such as glycerol, polystyrene or sucrose [71]. It was observed that cyclohexane nuclei, which solidify at 6.5°C and earlier than water, could stop the growth of ice crystals [76]. Consequently, pore size was decreased as ice crystals could not push away or pass through the solid cyclohexane nuclei [76]. This technique is called emulsion-ice templating and due to the inhibition of ice crystal growth results in the formation of irregular pore morphology (**Fig. 2.34-b**) instead of aligned pore structure (**Fig. 2.34-a**) [76]. Both samples showed bimodal pore size distribution, with pore sizes ranging from 0.83-17.28 μm [76].

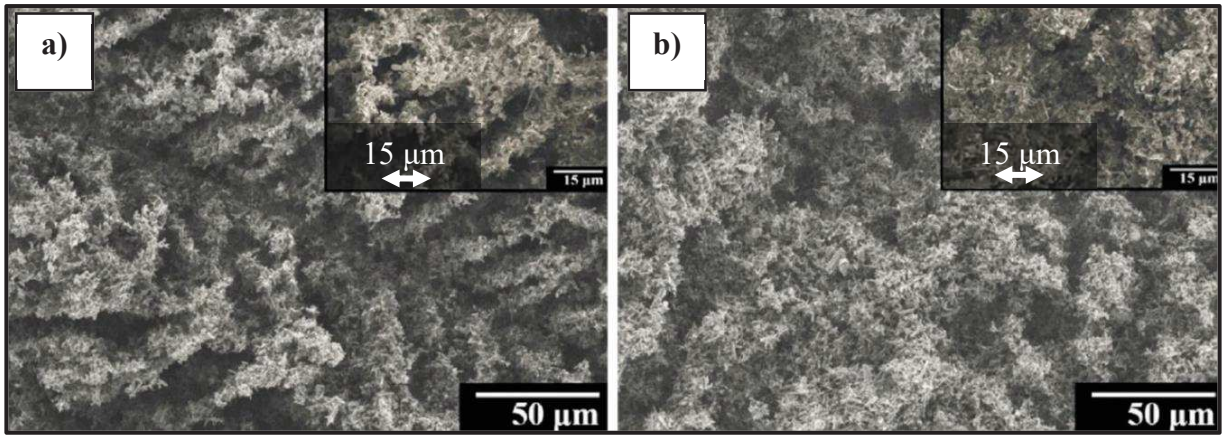

Fig. 2.34. SEM micrographs of porous Si_3N_4 produced by a) ice-template technique and b) emulsion-ice templating [76]

In addition to freezing rate (see **Fig. 2.35-a** and -**b**), additives such as zirconium acetate are effective in modifying the morphology of pores. Using zirconium acetate, the structure of pores is altered from the typical lamellar structure with preferential orientation into a honeycomb-like structure (**Fig. 2.35-c**) [71]. Additionally, using organic burn-out pore formers combined with this method seems to be a successful approach to fabricate isotropic pores homogeneously dispersed in the microstructure. As illustrated in **Fig. 2.35-d**, this combination led to the remarkably broader pore size distribution compared to the pores in ice-template technique [71].

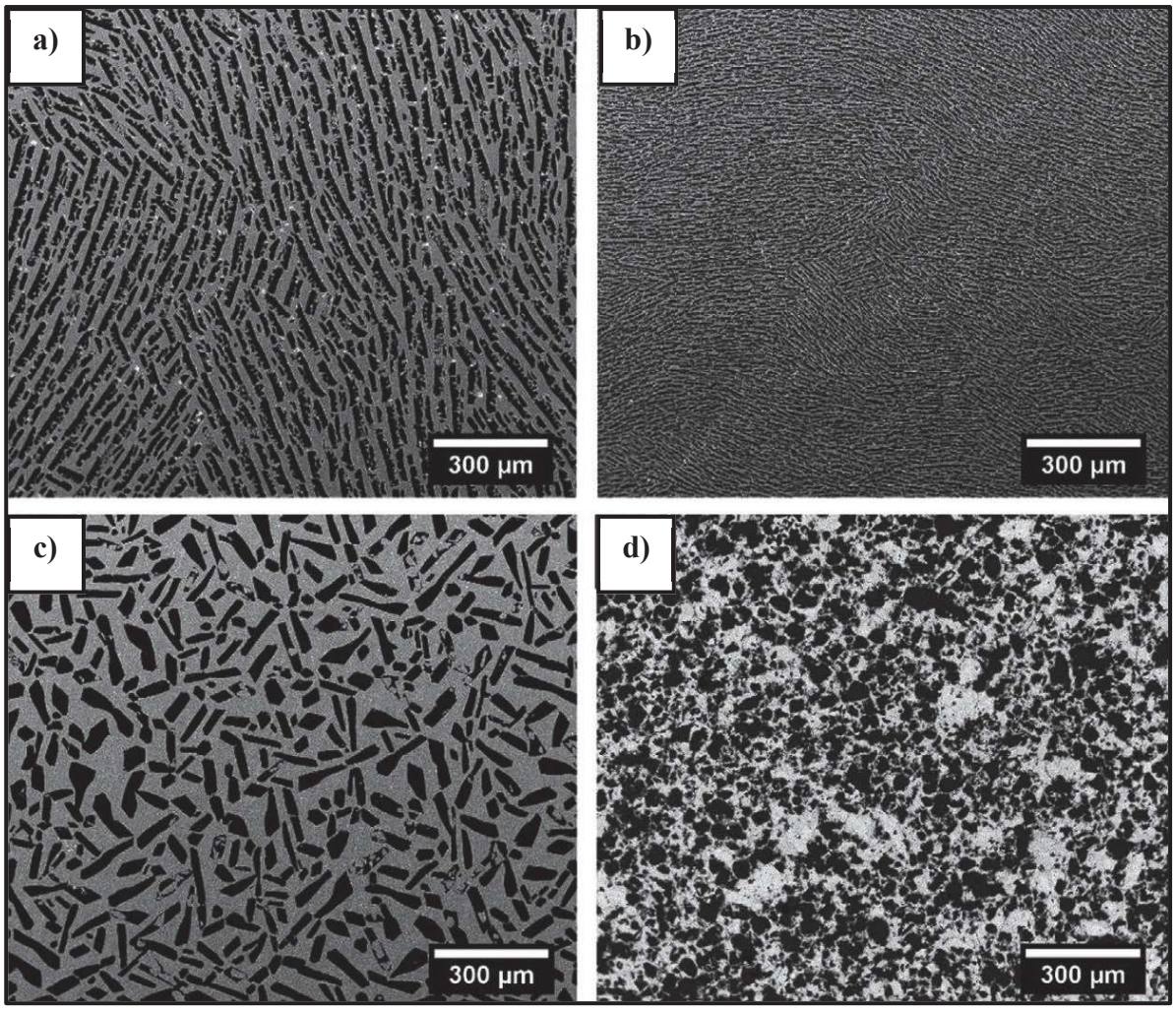

Fig. 2.35. Microstructure of pores produced with ice-template technique: a) frozen at 2°C min^{-1}, b) frozen at 25°C min^{-1}, c) frozen at 2°C min^{-1} with zirconium acetate and d) using pore former agents [71]

2.8.7. Tape Casting Technique

Si_3N_4 membranes with porosity of < 66 vol.% have been produced by tape casting of silicon slurry and calcination at 1300°C in flowing NH_3 gas. Via vapor-liquid-solid growth mechanism, this process leads to the formation of α-whiskers (**Fig. 2.36**) with sizes of 30–80 nm in diameter and pores of 0.1 to 1.0 µm. This sample showed bending strength of 34 MPa which is suitable for membrane distillation and separation of fresh water [46].

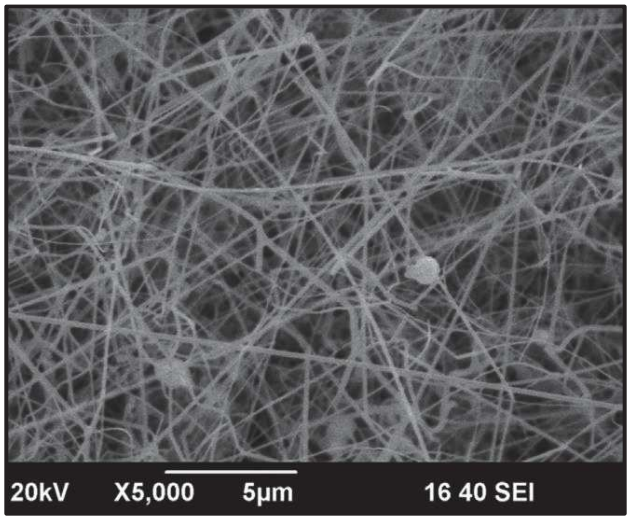

Fig. 2.36. SEM image of the α-Si_3N_4 membrane produced by tape casting of silicon slurry and calcination at 1300℃ for 5 hr [46]

2.8.8. Gel-casting

Gel-casting is a wet forming process based on concepts derived from traditional ceramic processing and polymer chemistry and is used to produce near-net-shape ceramic parts with large size and complex shape. Machinability of the green body with high strength is a notable advantage of gel casting compared to other techniques. Excellent homogeneity, low shrinkage (≈ 3%), high yield and high strength of green bodies are some of the unique advantageous of this method which make it suitable for the production of ceramic parts from more than a dozen different compositions including Si_3N_4, Al_2O_3, SiC, $MgAl_2O_4$ spinel and ZrO_2-mullite [83-92].

By means of making concentrated homogeneous suspensions with low viscosity, ceramic powders are mixed with liquids which consist of monomers for forming chain and cross-linked structure. By in-situ polymerization of organic monomers, a three-dimensional network structure is generated which homogenously distributes particles in slurries that immobilizes the starting powder particles to create a gelled part [39, 83, 93].

To prepare a stable and castable suspension, water-soluble organic monomers are essential components of the gel casting system which dissolves in a premix solution [84]. Monomers can only form linear polymer chains by a single double bond while a crosslinker has at least two double bonds which link polymer molecules to form a gel and network structure [94]. Acrylamide (AM)

is the most commonly used gelling agent and performs efficiently in gel casting of a high strength green body, but it has been found to have neurotoxic effects [39, 86]. Methacrylamide (MAM), N,N'-methylenebisacrylamide (MBAM), 2-hydroxyethyl methacrylate (HEMA) and methacrylic acid (MAA) are examples of low-toxicity monomers, and agarose, gelatine, agar, starch, chitosan, and sodium alginate are some non-toxic gelling materials [39, 83, 90, 94]. However, agarose and gelatine are expensive and the green bodies resulting from both low-toxic and non-toxic gelling materials suffer from low mechanical strength, thus are not suitable for any post machining step [39, 90]. Despite the high toxicity of these materials, using acrylamide ($C_2H_3CONH_2$) as a monomer and N,N'-methylenebisacrylamide ($(C_2H_3CONH)_2CH_2$) as branch former cross-linker is preferred and is used very extensively [84, 85].

Defects such as agglomerates and air bubbles decrease the performance of the final products [94] therefore to break down agglomerates and achieve homogeneous slurries, pH adjustment, degassing and milling are some of the typical steps used in this fabrication technique. Initiator (e.g., ammonium persulphate, APS, $(NH_4)_2S_2O_8$), catalyst (e.g., N,N,N',N' tetramethylethylenediamine, TEMED, $C_6H_{16}N_2$) and free radical polymerization additives are the other rheological agents which play a significant role in accelerating the polymerization and setting the suspension [94]. While a long setting time is ideal for degassing and casting processes, it should be short enough to avoid particle sedimentation. It was observed that gelation time and initiator content has an inverse correlation; therefore, by increasing the content of initiator, the setting time and therefore particle sedimentation and segregation can be reduced [19].

Then, the slurry is poured into a mould with desired shape and heated to obtain a green body with a network structure [94]. Polymerization usually takes place in the temperature range of 30-80°C during which the suspension is consolidated and forms a green body [93]. The resulting cross-linked polymer is an elastic hydrogel which serves as a binder to carry particles [84].

After demoulding and machining, heating the wet green bodies to remove solvents and burn out the monomers are the subsequent steps, and are accompanied with shrinkage, weight loss and possible warpage. By evaporation during the process of drying, liquid is removed; meanwhile, the distance between particles is decreased and internal stress and non-uniform shrinkage might occur,

Fig. 2.37. To stop severe warpage and cracking, fast drying must be hindered and to decrease the drying rate and weight loss, materials are maintained in a moist atmosphere [85, 94].

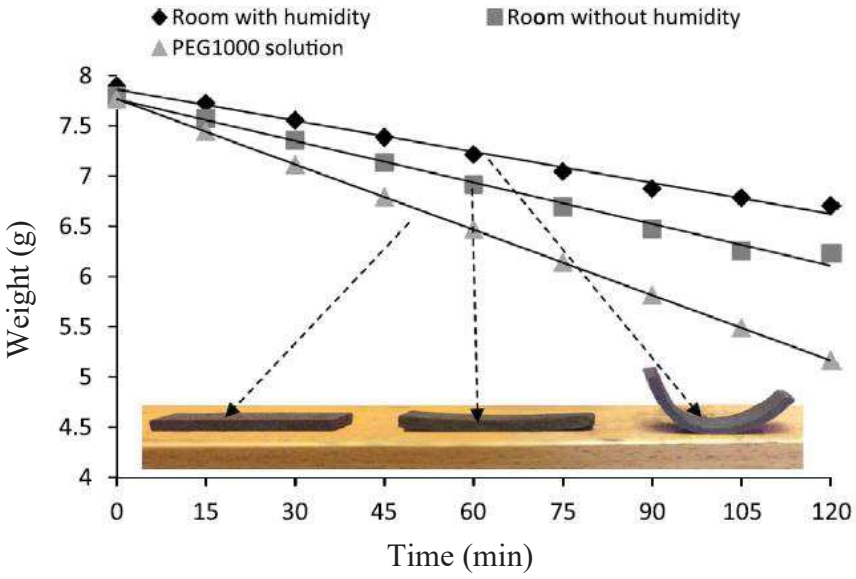

Fig. 2.37. Changes in green sample weight during different drying methods [85]

2.8.8.1. Gel-casting of α-silicon Nitride

Gel casting of α-silicon nitride has been applied to obtained both porous and dense structures [86, 93]. However, poor rheological properties and inconsistency of Si_3N_4 suspensions makes this process challenging and undesirable [95]. In combination with sintering aids such as Al_2O_3 and Y_2O_3, pressureless sintering may be performed to consolidate the structure and obtain the final β-Si_3N_4 parts [93, 94]. By altering the concentration of the ceramic slurry and solids loading, the porosity content, microstructure and mechanical properties can be tailored. For instance, dense silicon nitride structures have been obtained in the presence of 52 vol.% solids loading [86], **Fig. 2.38-a**. By decreasing the solids loading to 30 vol.%, porous Si_3N_4 with a porosity of ≈ 36-57 vol.% was obtained, **Fig. 2.38-b.** Low porosity, anisotropic growth of β-grains and good grain interlocking lead to high flexural strengths in the range of 108-235 MPa [93].

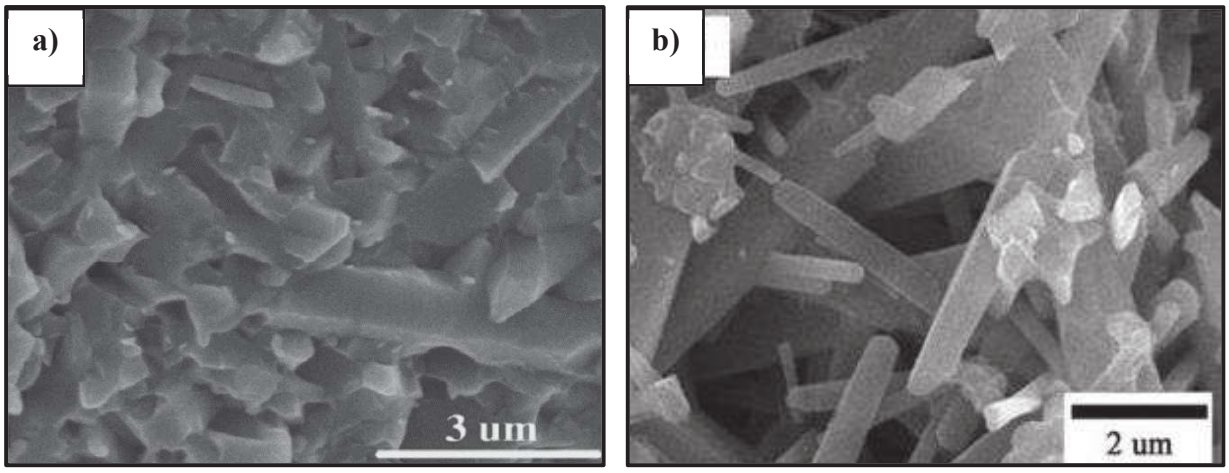

Fig. 2.38. Microstructures of Si_3N_4 ceramics prepared by gel casting: a) dense structure with 52 vol.% solid loading [86] and b) porous structure with 30 vol.% solid loading [93]

2.8.8.2. Gel-casting of Silicon

To produce porous silicon nitride components but eliminate the issues of working with Si_3N_4 powder, gel casting of silicon powder may be applied [19]. By employing a pore-forming agent and altering the concentration of the ceramic slurry and solids loading the porosity content, microstructure and mechanical properties can be tailored. To minimize the flows developed during the gel casting and to increase the stability and fluidity of the suspension and strength of the green body, the volume of gel casting agents, the suspension's pH, mixing time and solids loading should be carefully controlled. Rheological behaviour of silicon and silicon-polymer suspensions have been studied and gel casting parameters have been optimized [19, 84, 85].

The intensity of silicon surface oxidation and therefore the release of hydrogen gas is strongly controlled by the suspension's pH (**Eq. 2.32** to **Eq. 2.34**) [85]. It was observed that with respect to the surface chemistry of silicon particles, to increase the suspension stability, a strong repulsion between the particles must be produced which occurs at pH of 6, 8.5 and 10. However, to minimize the amount of hydrogen generated in an aqueous system which causes uncontrolled porosity, the pH must be set at lower than 9, in which case the silica layer serves as a stable protective coating around silicon particles and thus the reaction is stopped. The optimum pH value for a silicon and PMMA suspension at which the suspension has both the highest stability and the lowest hydrogen release is 8.5 [19].

$Si\ (s) + 2H_2O\ (l) \rightarrow SiO_2\ (s) + 2H_2\ (g)$ [85] **Eq. 2.32**

$SiOH + H^+\ (aq) \leftrightarrow SiOH_2^+\ (pH< 7)$ [85] **Eq. 2.33**

$SiOH + OH^-\ (aq) \leftrightarrow SiO^- + H_2O\ (pH> 7)$ [85] **Eq. 2.34**

The monomer content and monomer/cross-linker ratio affect the sample green-strength, distortion and warpage. Moreover, high monomer content makes the polymer burn out step more complex, increases sample homogeneity whilst lowering defects and consequently giving higher strength, as shown in **Fig. 2.39-a**. A high ratio of monomer/cross-linker leads to incomplete polymerization and a low ratio leads to increase in the length of the bridges linking polyacrylamide chains. Therefore, the highest cross-linking density and strength were obtained when the ratio of monomer/cross-linker was between 15 to 20, as shown in **Fig. 2.39-b** [19].

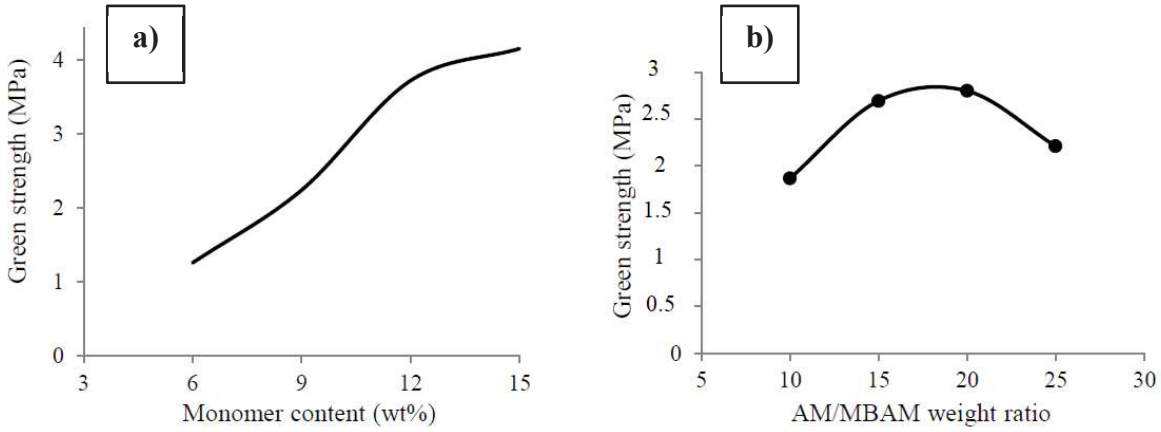

Fig. 2.39. Green strengths of the gel-cast samples versus a) monomer content and b) monomer/cross-linker ratio in the premix solution [19]

2.8.9. Reaction Bonding Combined with Gel Casting and Sacrificial Template Techniques

Since 2008, several attempts have been made to fabricate highly porous silicon nitride components via the reaction bonding process [11, 16-18, 82]. To produce silicon powder compacts with sacrificial agents and other additives, mostly dry-processing techniques and in particular uniaxial pressing have been performed [11, 16-18, 47]. However, due to poor particle packing and poor particle distribution, this process leads to production of inhomogeneous closed-structure foams with porosity of < 60 vol.% and microstructural defects, as shown in **Fig. 2.40**.

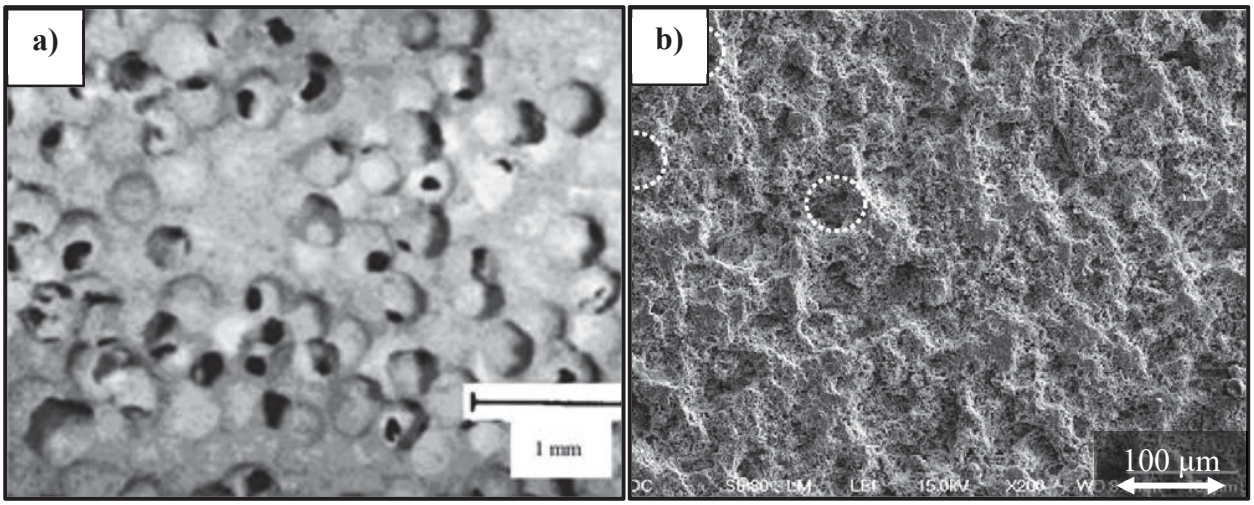

Fig. 2.40. SEM micrographs of porous RBSN prepared by uniaxial pressing of a) Si-Benzoic acid powder mixture, porosity of the foam is 53 vol.% [16] and b) Si-PMMA powder mixture, porosity of the foam is 48.5 vol.% [11]

By using polymethylmethacrylate (PMMA) beads as pore-forming agents and a combination of the sacrificial template technique and gel-casting, followed by reaction bonding, porous silicon nitride bodies with high levels of porosity have been fabricated [19] and the flowchart for this fabrication procedure is shown in **Fig. 2.41**.

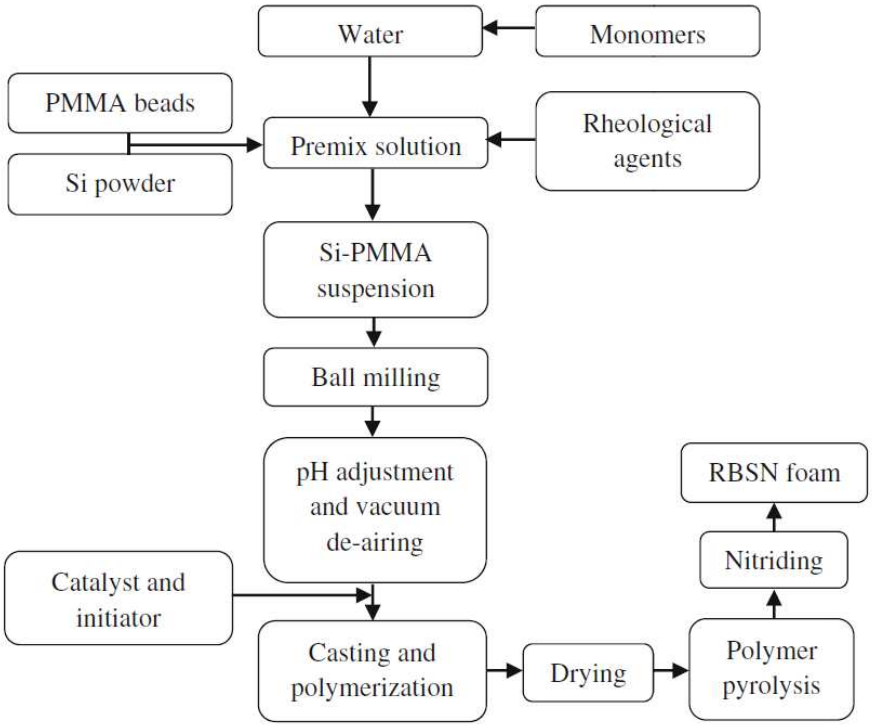

Fig. 2.41. Porous RBSN fabrication via combination of sacrificial template technique, gel-casting and reaction bonding process [23]

The ability to tailor porosity and enhance the homogeneity and strength of the porous structure through the optimization of fabrication parameters are the main advantages of this combination. Using different rheological agents and monomers leads to a stable and homogenized Si-PMMA suspension which is then cast, polymerized, dried and pyrolyzed to produce the cellular silicon structure. By heating the green compact, the continuous network of the PMMA beads and other polymers are burnt-out and an open silicon structure with a high level of porosity is formed. The burn out temperature for this system is 525°C which was slightly higher than the decomposition temperature of monomers and PMMA. However, the PMMA burn-out process is not environmentally friendly and in order to avoid structural defects such as cracks, the heating process should be very slow which is time-consuming [96].

By controlling the content of PMMA beads and the monomers, the porosity level of the foam has been increased up to 87 vol.%. The resultant open structure with high levels of porosity leads to full nitridation within a few hours, which enables the production of large bodies and complex

microstructures [19]. However, during nitridation of porous RBSN fabricated via wet processing, whiskers form as the dominant microstructure as shown in **Fig. 2.42.**

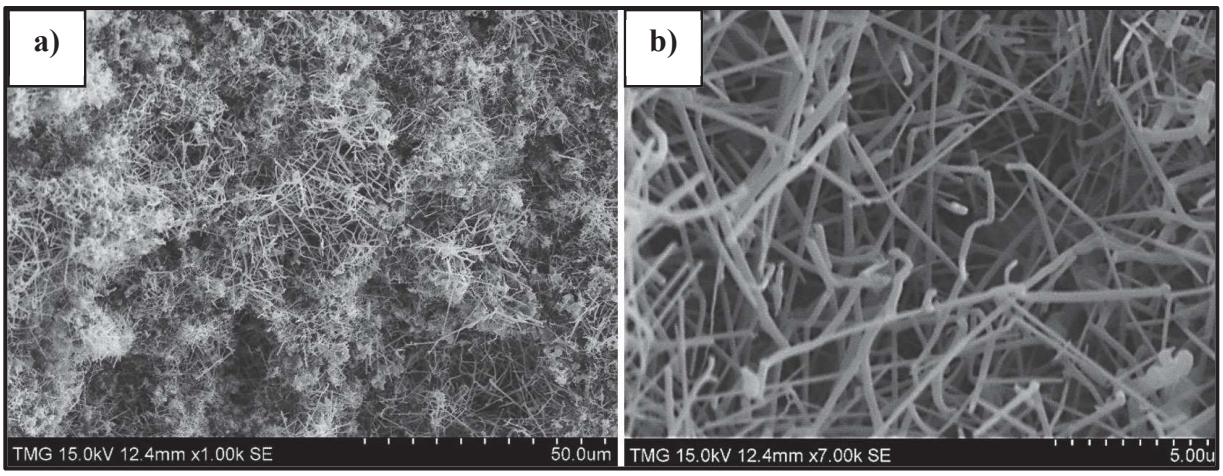

Fig. 2.42. Formation of whiskers in porous Si_3N_4 structure [19]

As was discussed before, α-Si_3N_4 whisker formation is based on the reactions between SiO gases and nitrogen. The high degree of porosity in this structure results in high surface area which provides large free spaces for whiskers to form and grow. The presence of iron and hydrogen in the system also encourages the gaseous phase reactions and enhances the formation of whiskers [23, 25]. In contrast, addition of small amounts of MgO prevented whisker formation during nitridation as shown in **Fig. 2.43-a**. The influence of Y_2O_3-Al_2O_3 on the microstructural properties of the Si_3N_4 foam has also been investigated but revealed that this combination was not effective in stopping whisker formation, **Fig. 2.43-b** [33]. However, after heat-treatment at 1700°C for 2 hr, the microstructure of the RBSN with either MgO or Y_2O_3-Al_2O_3 was completely whisker-free (**Fig. 2.43-c** and **d**) [33]. The mechanisms of these morphology changes in the highly porous silicon nitride bodies have not been studied and require further investigation.

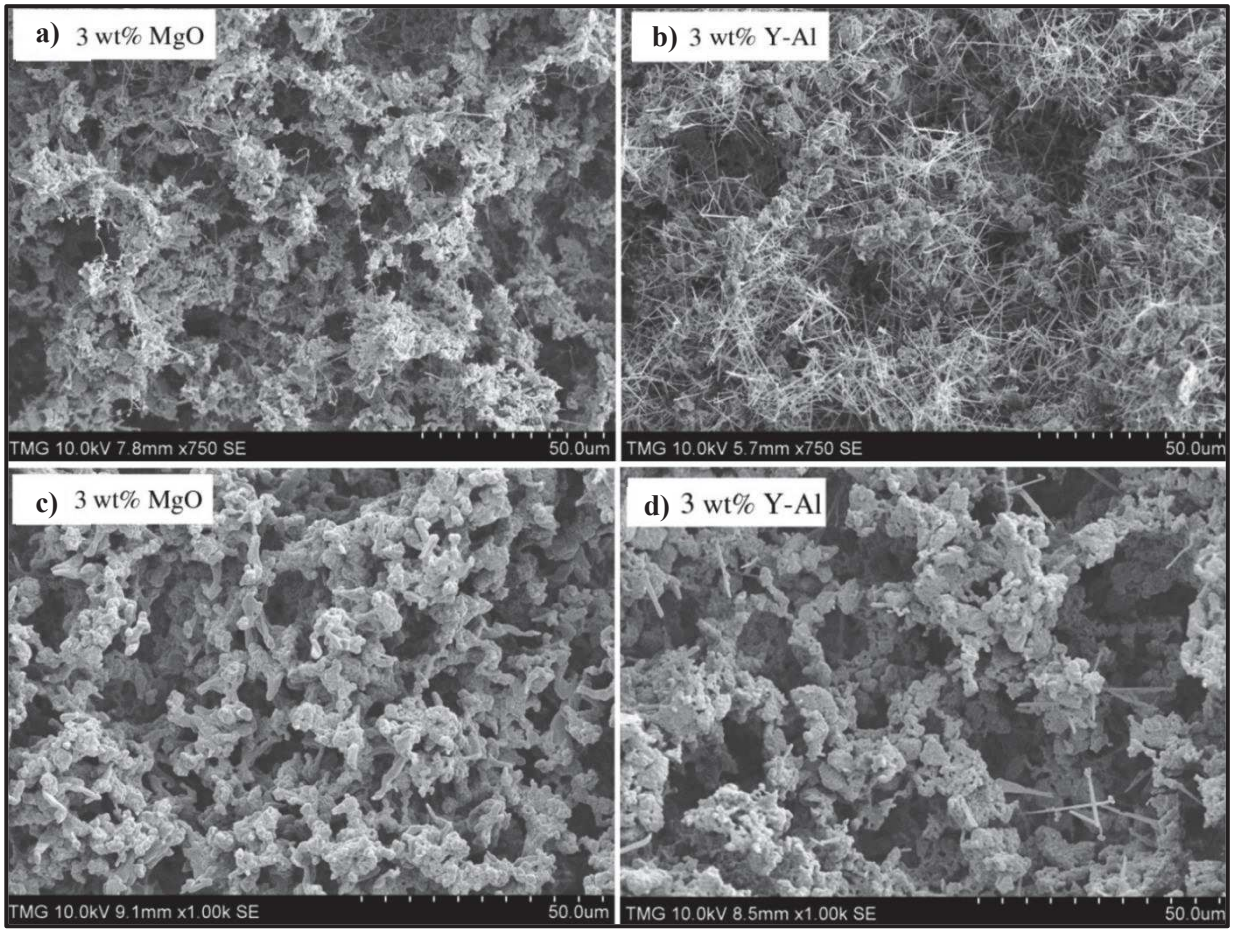

Fig. 2.43. Influence of 3 wt.% (a, and c) MgO and (b, and d) Y_2O_3-Al_2O_3 on the microstructure of the porous RBSN after nitriding at 1425°C and post heat-treatment at 1700°C, respectively [33]

Chapter 3. Formation Mechanism of Porous Reaction-bonded Silicon Nitride with Interconnected Pores in the Presence of MgO

Raheleh Nikonam M. [a,] *, Martin D. Pugh [a], Robin A.L. Drew [a]

[a] Department of Mechanical, Industrial and Aerospace Engineering, Concordia University, Montreal, CANADA, H3G 1M8

*corresponding author: r_nikona@encs.concordia.ca

This article has been published in the Journal of the European Ceramic Society 39 (2019) 915-927, https://doi.org/10.1016/j.jeurceramsoc.2018.10.032

Abstract

In porous reaction bonded silicon nitride, whiskers normally grow in globular clusters as the dominant morphology and deteriorate the pore interconnectivity. However, the ceramic microstructure was significantly transformed with the addition of MgO; specifically, the morphology was modified to a combination of matte and hexagonal grains. Microstructural observation along with thermodynamic studies suggest that MgO interfered with the presence and nitridation of SiO (g). Consequently, rather than being involved in the whiskers' formation, surface silica instead reacted with volatile MgO to form intermediate products. Through these reactions, whisker formation was blocked, and a porous interconnected structure formed which was confirmed by 3D tomography. After heat-treatment at 1700°C, β-Si_3N_4 crystallized in a glassy matrix containing magnesium. Resulting samples had an open-pore structure with porosity of 74-84 vol. %, and density of 0.48-0.75 g.cm^{-3}. Combination of high porosity and pore size of < 40 μm led to compressive strengths of 1.1 to 1.6 MPa.

Key words:

Silicon nitride; Reaction mechanism; Whiskers; Magnesium oxide; Pore morphology

3.1. Introduction

According to Gibson and Ashby, porous structures represent a class of materials where a continuous network of the solid skeleton forms the edges and faces of pores. Exhibiting a special combination of high surface area, low density, low specific heat and high thermal insulation makes them widely applicable in various industrial fields [97, 98]. As porous structures can be quite complex, both application and performance of these materials are determined by the characteristics of their pores, i.e. texture, size, distribution and interconnectivity. For applications in tissue engineering scaffolds, environmental filters, forced convection heat-exchangers for electronics devices and aerospace fluid storage tanks, open pores are favored which make the structure permeable. Channel interconnectivity is the key factor allowing the uninterrupted flow of fluid through a membrane. In addition, at a constant porosity, both permeability and flow rate of a porous media are controlled by channel diameter. To target the applications where transport of high temperature fluids is required, the possibility of being able to design the porous ceramic structure is crucial [18, 47, 99-103].

By offering excellent thermal shock resistance and mechano-chemical stability, the high temperature capability of porous silicon nitride (Si_3N_4) to 1700°C makes this ceramic an attractive candidate for molten metal and exhaust particulate filters [11]. In production of cellular Si_3N_4, there have been several successful manufacturing techniques, e.g. aqueous gel-casting [104], spray-dried method [105], protein foaming [106], sacrificial template [18, 107], emulsions, and replication of polymer foams [98]. However, the significant disadvantages of these processes are high cost of the starting silicon nitride powder and difficulty with machining of the final components which have limited their widespread usage. By maintaining the original dimensions, reaction bonding of silicon nitride (RBSN) is an easy and economical process that enables fabrication of complex shapes with low shrinkage of ±0.1 % and inherent porosity of ≈ 20 % [11, 18, 41]. In this method, elemental silicon of any physical condition can react with nitrogen in the temperature range of 1250°C to 1450°C. Additionally, the silicon dioxide layer, which naturally exists on the surface of silicon, will contribute to the nitriding reaction by generating silicon monoxide gas. As an interesting feature, the nature of the nitriding reaction can alter the grain growth, crystallographic structure (α or β), and the resultant morphology of the RBSN grains, i.e., matte, hexagonal or whisker [21, 41, 46, 47, 108].

As a reinforcing material for ceramic, glass or metal matrix composites, silicon nitride whiskers have received wide attention, mostly because of their high specific modulus, high specific strength, fracture toughness, and enhanced wear resistance. Having the advantage of better mechanical performance, the fracture toughness of whisker-reinforced composites depend on the whisker characteristics, i.e., radius, length, strength and elastic modulus [109-111]. However, whisker agglomerates often cause an inhomogeneous structure and hinder further improvement of fracture toughness and mechanical properties [112]. In addition to the toughening potential of whiskers, simultaneously they affect the pore characteristics in a porous structure.

Homogenously dispersed SiC whiskers in a porous alumina substrate can enhance the filtering efficiency of particles by hindering their flow and by providing a large specific surface area as an absorption site [113]. However, as permeability is related to the open porosity and pore size, whiskers grow into void spaces and as the pore size decreases, the permeability reduces continuously [26, 51, 114, 115].

In the production of highly porous RBSN structures, pore-forming agents, e.g. polymer beads were employed as sacrificial templates [11-19]. Using this method, despite a homogenous distribution of pores and a controllable range of porosity, the production of a highly porous structure with a designed pore shape has been a challenge as the high free surface area leads to the formation of whisker agglomerates occupying the precursor cavities. While struts were composed of matte and hexagonal grains, whisker clusters grow within the pores, and thus, a suitably permeable porous body could not be obtained [19]. Therefore, a well understood mechanism is required to be able to control the formation of whiskers during the in situ nitridation of silicon.

The α structure of silicon nitride, which is thermodynamically unstable, forms equiaxed matte grain, whereas β-hexagonal exhibits elongated stable grains. Many studies have determined that through reaction with surface silica at temperatures between 1700°C to 1900°C, oxide additives promote the α- to β-Si_3N_4 phase transformation by nucleation and grain growth in the solution-precipitation stage of liquid-phase sintering (LPS). In combination with various oxides such as La_2O_3, Y_2O_3 and Yb_2O_3, MgO has been typically used as a Si_3N_4 sintering aid with the main function of densification. Given the favorable integration of the LPS process and inexpensive nitriding reaction, it has been of special interest to study post-sintered RBSN ceramics and the

influence of sintering aids on the nitriding behavior of silicon particles. With various melting points and viscosities of eutectic melts, therefore, different microstructures of post-sintered bodies are expected. In addition, as these additives may be included in the starting silicon before nitriding, an effect on the nitridation behavior and thus phase transformation, reaction rate and grain morphology is very likely [11, 41, 47, 116]. For instance, compared to the Al_2O_3-Y_2O_3 system, MgO-Y_2O_3 additions have been shown to increase the relative density, α/α+β phase ratio and percent nitridation of the post-sintered bodies [51]. Grain morphology and whisker formation in RBSN ceramics have also been affected by adding MgO, unlike Al_2O_3-Y_2O_3 additions [33]. Most of these investigations, however, were carried out on low porosity samples, and studies focused on the interaction of these additives on the nitriding reaction are quite limited [11, 33, 47]. Besides, no detailed information is available concerning the influence of MgO on the mechanism of grain morphology modification.

To achieve a more precise control over the pore shape and interconnectivity of channels in porous RBSN, the objective of the current research was to study the nitriding reaction mechanism, crystallization and pore morphology modification in the presence of MgO. Using sequential nitriding, the migration of elements, phase formation, and reaction mechanism were clarified and then substantiated using available thermodynamic data obtained from FactSage package software. The resultant ceramic composition and microstructure were characterized via XRD, SEM-EDX and 3D tomography analysis. Subsequently, the porosity, density, linear shrinkage, weight loss and compressive strength of the porous bodies were measured as a function of oxide content.

3.2. Experimental Procedure

3.2.1. Sample Preparation

The fabrication method used in this study was based on a published work where the reaction-bonding process has been combined with gel casting and a sacrificial template using polymer microbeads [19]. A uniform slurry was formed by dispersing silicon powder (99.995 %, 8 microns, ABCR) and PMMA beads (Microbeads, 10-40 μm) in deionized water with the weight ratio of Si: PMMA: H_2O of 16: 44: 40. Various contents of MgO powder (> 99 % purity, -325 mesh, Sigma-Aldrich) up to 12 wt. % of the resulting Si_3N_4 were then added. Using a monomer, cross-linker and gel-casting rheological agents, a uniform slurry was achieved at pH of 8.5, which was then

cast and heated to complete the polymerization step. The porous silicon structure was created by polymer burn-out at 525°C for 2 hr of the demoulded dried bar. To produce porous RBSN, nitriding was carried out in a high purity nitrogen atmosphere (99.999 % purity, $O_2 < 2$ ppm, $H_2O < 3$ ppm, THC < 0.5 ppm). Microstructural changes and phase transformation of samples during the nitriding process were investigated with a sequential heating process up to 1425°C. The dwell time at this temperature was 4 hr, whereas at lower temperatures samples were heated for 10 min. A further heat-treatment step at 1700°C for 2 hr was then performed by immersing samples in a powder bed comprising Si_3N_4, BN and MgO powder. The latter minimized thermal decomposition of the ceramic body and loss of MgO by creating a local gas equilibrium.

3.2.2. Characterization of the Samples

To determine the phase transformation during heat-treatment, X-ray diffractometry (XRD; X'Pert Pro, Panalytical) was carried out using CuKα radiation on the crushed samples. Identification of phases was achieved by comparing the diffraction pattern of the samples with JCPDS standard cards. According to the equation by Gazzara and Messier, the percentage of α- and β-Si_3N_4 can be evaluated by comparing the diffraction intensities of (101) and (210) reflections for the β-phase, and (102) and (201) reflections for α-phase [117].

Scanning electron microscopy (SEM, Hitachi, S-3400 N) was used to study the morphology and interconnectivity of the porous structure. Au-coated fracture surfaces of samples were studied under high vacuum with 5-15 kV and 40-50 mA imaging conditions. X-ray micro-tomography (SkyScan 1172, camera pixel of 3 μm) was performed on a 3×3×12 mm^3 sintered sample to obtain a three-dimensional image of the porous body.

In addition to the conventional SEM imaging, EDX mapping and point analysis (Oxford Instruments, Wave Model) were performed to identify elements and detect their distributions on the polished surface. For this, a low viscosity, slow-curing epoxy resin was used to infiltrate the pore volume inside a vacuum chamber. The surface of the sample was then ground and polished with different diamond pastes down to 0.5 μm for microscopic observation.

Using Archimedes' technique, ASTM C373-88 standard, the density and porosity of samples were measured. Linear shrinkage and weight loss were calculated for eight identically processed

samples. Cylindrical samples with the aspect ratio of ≈ 1.3 (height of 15 mm and diameter of 11 mm) were subjected to uniaxial compression testing using an Instron-3382 machine. Data were recorded at 0.4 sec intervals during testing with a pre-test crosshead velocity of 0.5 $mm.sec^{-1}$ and a test crosshead velocity of 0.5 $mm.min^{-1}$. The strengths presented are the average values of five individual tests.

3.3. Results and Discussion

3.3.1. Nitridation Process

Prior to the nitriding reaction, the dried bodies were heated to 525°C for 2 hr in order to burn-out the polymer beads and reveal a porous silicon structure. SEM micrographs of fracture surfaces of dried and pyrolysed samples are shown in **Fig. 3.1**.

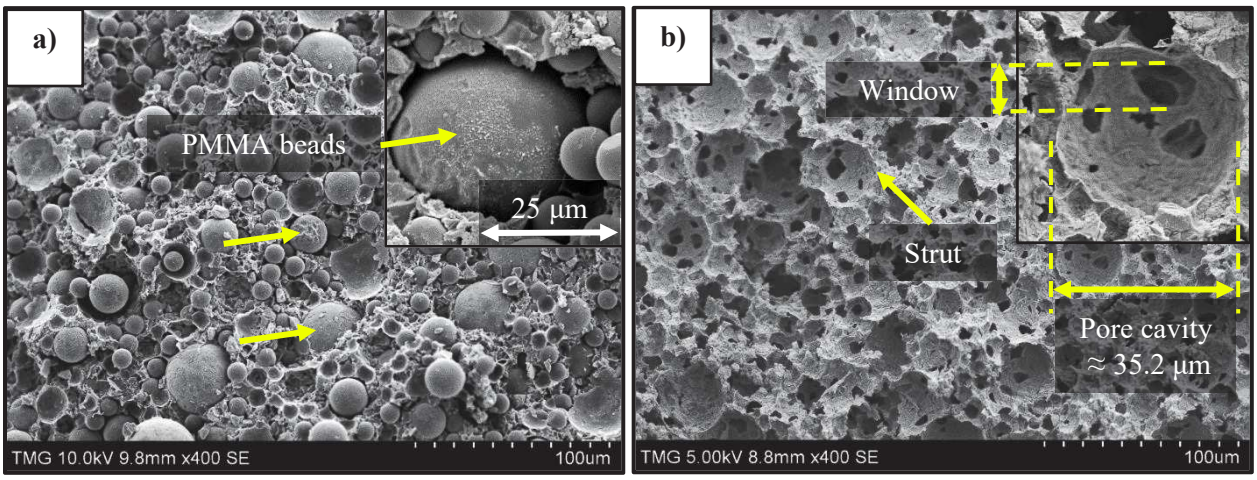

Fig. 3.1. SEM micrographs of a) as dried precursor containing polymer beads and b) after pyrolysis

Polymer burn-out during the pyrolysis step led to the formation of a porous structure with uniform pore distribution. With **Fig. 3.1-b** originating from the uniform structure of the dried body, **Fig. 3.1-a** microstructure indicates that the PMMA beads did not aggregate during suspension preparation. SEM observation revealed that the porous structure of the pyrolysed samples with and without MgO were essentially the same at this stage. Spherical pores connected with one another through more or less semi-circular windows on the strut's walls created a 3D interconnected structure. Pore size distribution in this sample was a function of the polymer particle size, i.e., 10,

20 and 40 µm; however, due to the pyrolysis linear shrinkage, a slight shift to smaller values are generally expected.

3.3.1.1. Whiskers Formation in the Absence of MgO

Grain morphologies of the nitrided samples with no additive are presented in **Fig. 3.2**. Along with formation of whiskers as the dominant morphology, some matte and hexagonal grains were observed in minor amounts. The α-matte deposits as small grains when Si vapor reacts with nitrogen through a gaseous phase reaction and continues by evaporation-condensation or diffusion of Si atoms to the nucleation sites. In contrast, the elongated β-Si_3N_4 hexagonal grains mainly grow when nitrogen diffuses in liquid or solid Si [41].

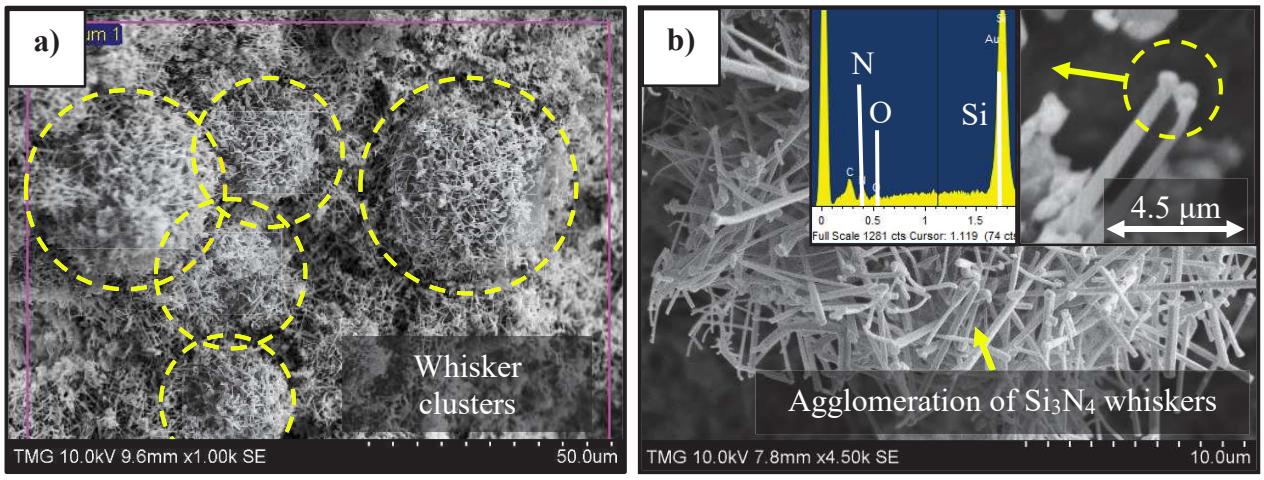

Fig. 3.2. SEM of fracture surface at two different magnifications illustrating the blocked pores with silicon nitride whiskers

Fig. 3.2-a, and **-b** revealed that silicon nitride whiskers were randomly elongated in different directions and formed spherical clusters occupying pore cavities. Most of these grains were quite straight, short and polyhedral in cross-section, which suggests they are potentially β-silicon nitride [118]. Some of them were characterized by the presence of small beads on their tips that were found to contain Si (61 wt. %), N (33 wt. %) and O (6 wt.%), based on EDX microanalysis. This was evidence that silicon nitride whisker growth proceeded through a vapor-liquid-solid (VLS) mechanism: where nitrogen and silicon monoxide gas species dissolve in a liquid droplet. The chemical composition of the starting silicon powder listed in **Table 3.1** revealed the presence of impurities, which usually form low viscosity melts, especially compounds of iron and aluminum.

The presence of these beads on growing whiskers suggests that the growth process was probably incomplete, and the whiskers would have grown further given more time at temperature [41, 119, 120].

Table 3.1. Chemical compositions of the starting silicon

Element	Si	C	O	Fe	Al	Ca
Value (%)	100.000	< 0.1	1.3	0.001	< 0.001	0.0003

An oxygen impurity of 1.3 wt. % in the starting silicon (**Table 3.1**) can be assumed to be mostly in the form of native surface silica. In the Si-O system, the stability region of different silicon oxides is a function of temperature and oxygen partial pressure in the ambient atmosphere, so by decreasing pO_2/p^{θ} at high temperature, SiO_2 becomes unstable and SiO vapor is generated [55]. In this regard, despite the positive ΔG° of **Eq. 3.1,** at high temperature and an oxygen partial pressure below the critical amount, reduction of surface silica on silicon becomes feasible. Considering that nitriding occurred under an atmosphere of 99.999 % purity nitrogen gas, the pO_2 would have been lower than 10^{-5} atm. This low oxygen content could enhance the partial pressure of SiO at the oxide-silicon interface and supply volatile SiO gaseous species for the formation of silicon nitride whiskers according to **Eq. 3.2** [11, 55, 119].

$SiO_2\,(g) + Si\,(s) \leftrightarrow 2SiO\,(g)$ **Eq. 3.1**

$\Delta G^{\circ} = -328.1\times10^{-3}T + 595.4$ kJ. mol^{-1} (867-1412℃)

$\Delta G^{\circ} = -292.8\times10^{-3}T + 545.9$ kJ. mol^{-1} (1412-1465℃)

$3\,SiO\,(g) + 2\,N_2\,(g) \leftrightarrow Si_3N_4\,(s) + 3/2\,O_2$ **Eq. 3.2**

$\Delta G^{\circ} = 619.8 \times 10^{-3}T - 354.7$ kJ. mol^{-1}

With the evaporation rate of 10^{-6} kg.m^{-2}.sec^{-1}, the vapor pressure of silicon would be of the order of 10^{-7} atm at 1350℃ [21]. Furthermore, considering that a high degree of porosity should promote silicon vaporization, the oxygen generated from the nitriding reaction zone would lead to the active oxidation of silicon, and thus, an increased partial pressure of SiO species via **Eq. 3.3**. Accordingly, the re-oxidation cycle accelerated whisker formation, which blocked the open pore volume. As nitriding through the gaseous phase reaction between SiO and N_2 proceeds at a much faster rate than that involving Si vapor, correspondingly whisker formation occurs prior to the

formation of matte or hexagonal grains [21, 41, 55]. ΔG° of reactions were calculated using the "Reaction" module in FactSage 6.4 package software.

$Si\ (g) + 0.5O_2\ (g) \leftrightarrow SiO\ (g)$ **Eq. 3.3**

$\Delta G^{\circ} = -82.4\times10^{-3}T - 125.1$ kJ. mol^{-1} (25-1412°C)

3.3.1.2. Morphology Modification in the Presence of MgO

With the dominant microstructure of matte and hexagonal grains, SEM images in **Fig. 3.3** show that the addition of MgO in the starting silicon significantly reduced whisker formation. It seems that the open pore structure in **Fig. 3.3-a** and **-c** allows whiskers to become more elongated compared to **Fig. 3.2-a,** where the available space for grain growth was more constrained and the length of whiskers is observed to be shorter. By increasing the amount of MgO to 9 wt. %, gradually the magnitude of whisker formation decreased. At 12 wt. % MgO, almost no whiskers were evident, and all the silicon nitride was either in the form of matte or hexagonal grains. With significant MgO present (**Fig. 3.3-g**) the pore morphology and characteristics were completely different compared to no additive, **Fig. 3.3-h**. The pores became regular and spherical with diameters less than 40 μm instead of irregularly shaped whisker-blocked pores. The open versus blocked-pore morphology is even more obvious on their polished cross-sections shown in **Fig. 3.4**. Based on the contrast between dark regions (resin) and light regions (ceramic), pore cavities, whiskers and solid struts can be distinguished. For the same nitriding time, the unfilled cavities in the sample with no additive show the whisker-blocked pore structure, diminishing the structure's permeability. Whereas with 12 wt.% MgO, the pore structure appears entirely whisker-free and interconnected which allowed the resin to completely infiltrate the microstructure and fill the cavities.

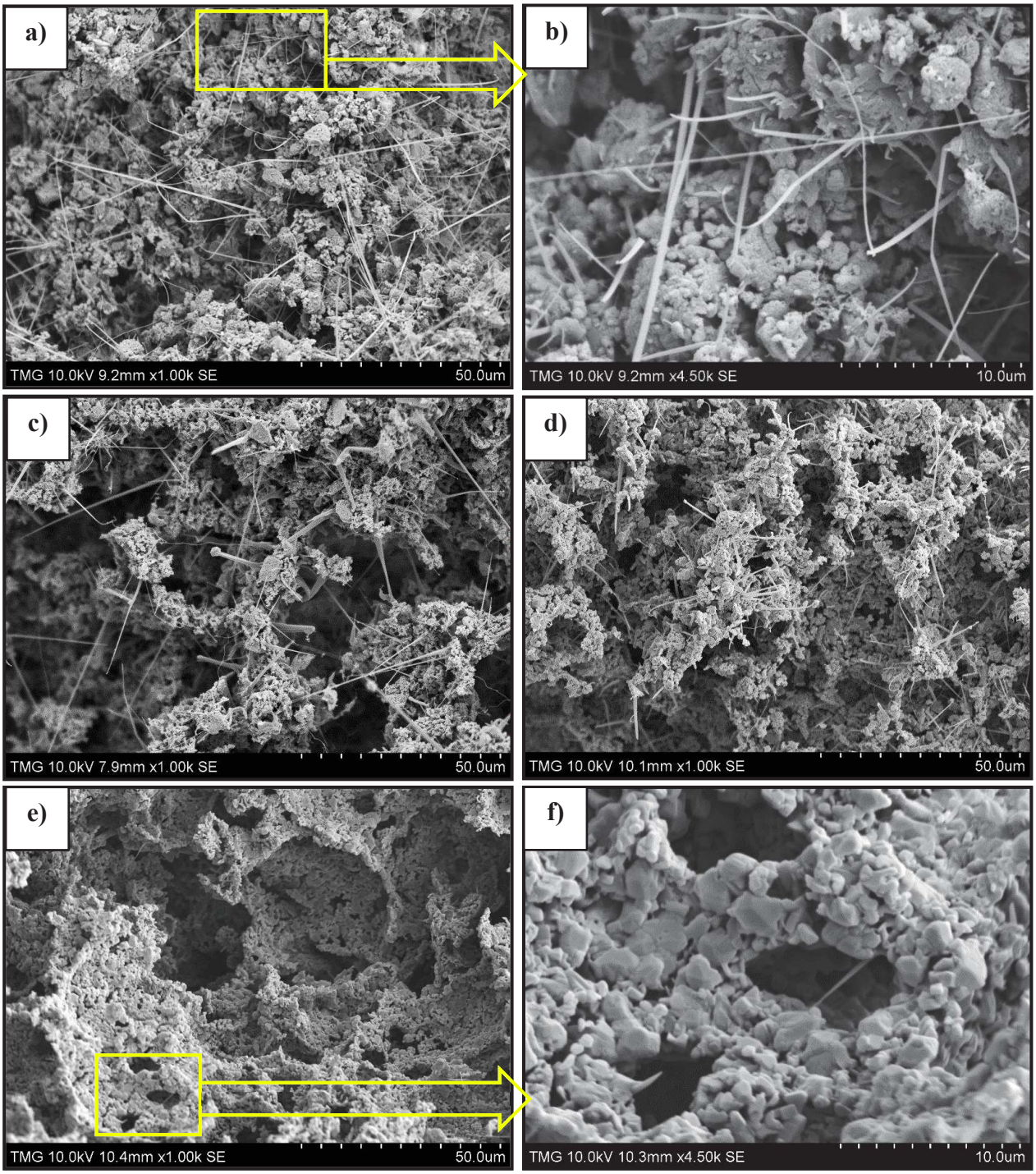
a)
TMG 10.0kV 9.2mm x1.00k SE
50.0um
b)
TMG 10.0kV 9.2mm x4.50k SE
10.0um
c)
TMG 10.0kV 7.9mm x1.00k SE
50.0um
d)
TMG 10.0kV 10.1mm x1.00k SE
50.0um
e)
TMG 10.0kV 10.4mm x1.00k SE
50.0um
f)
TMG 10.0kV 10.3mm x4.50k SE
10.0um

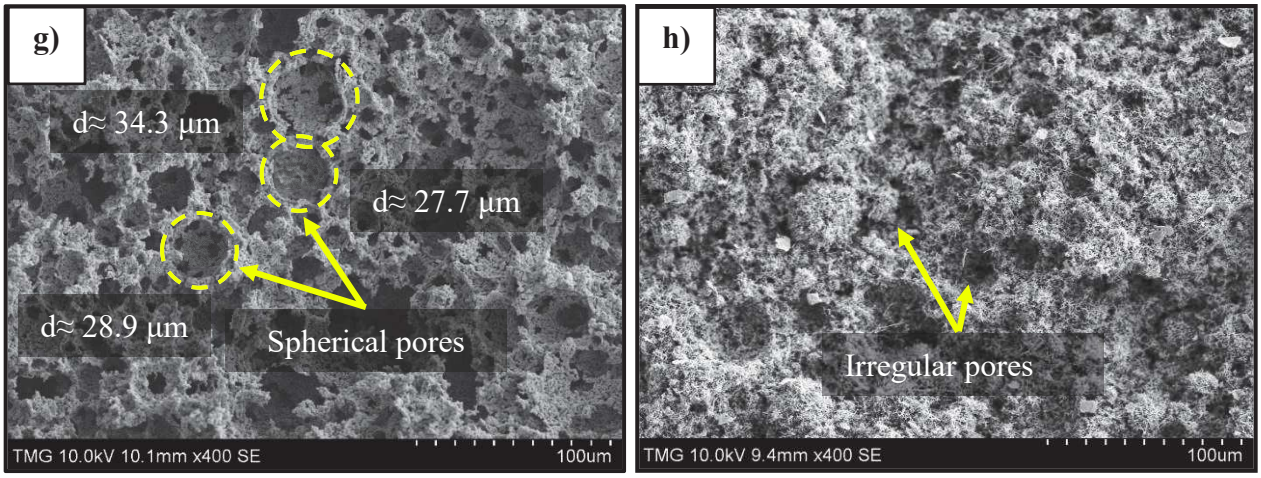

Fig. 3.3. SEM of fracture surfaces illustrating the pore structures in the presence of different MgO contents nitrided at 1425℃; a and b) 3% MgO, c) 6% MgO, d) 9% MgO, and e, f and g) 12% MgO, and compared to h) 0% Mg

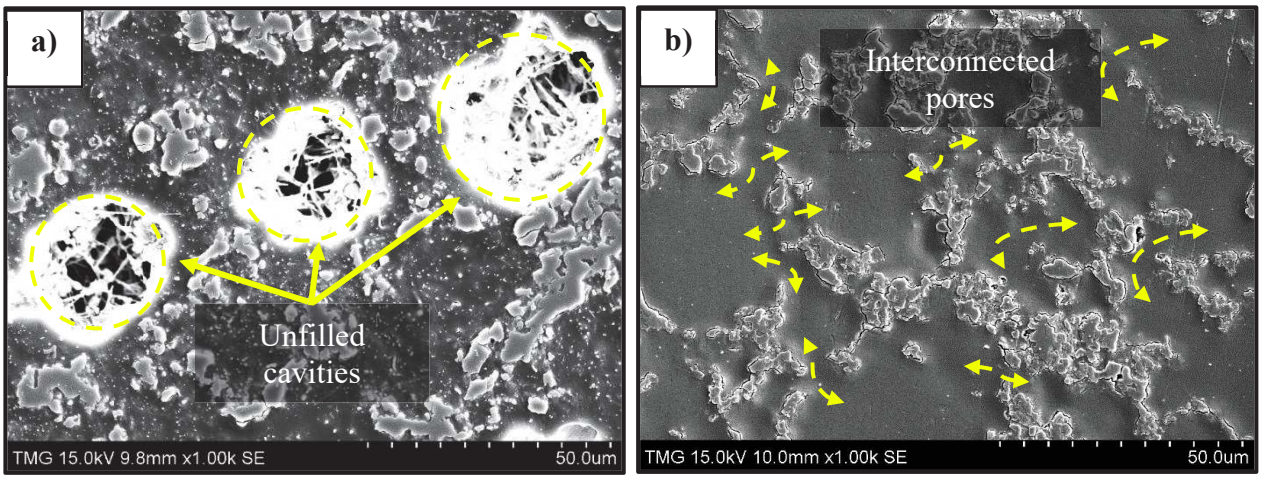

Fig. 3.4. Polished resin-infiltrated cross-sections showing the pore structures in silicon nitride containing a) 0% MgO and b) 12% MgO

Fig. 3.5 and **Table 3.2** show, respectively, the XRD patterns and relative phase ratios of the nitrided samples with different contents of MgO. After heating for 4 hr, nitridation was complete as no residual silicon was detected in the nitrided samples. N_2 gas could easily have diffused into the interior region of the porous Si body through the permeable pore channels. In such an open porous network the nitriding reaction proceeds very quickly compared to conventional RBSN

structures with low porosity, which can take several days of heating for full nitridation depending on component size [41].

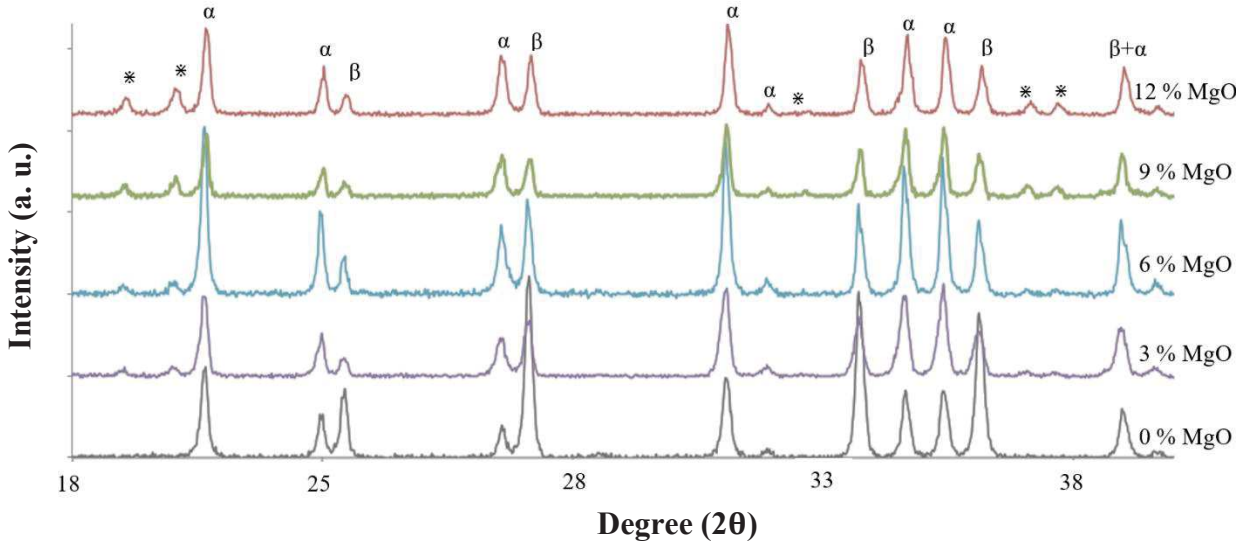

Fig. 3.5. XRD patterns of material nitrided at 1425°C with 0, 3, 6, 9 and 12% MgO (α, β *and* $*$ show peaks corresponding to α-Si_3N_4, β-Si_3N_4 and Si_2N_2O, respectively)

Table 3.2. Phase fractions and α/β-Si_3N_4 phase ratio obtained by XRD from samples containing different MgO contents and nitrided at 1425°C

MgO content	wt. %			
	α-Si_3N_4	β-Si_3N_4	α/β-Si_3N_4	Si_2N_2O
0% MgO	30.8	69.2	0.4	0
3% MgO	60.4	34.7	1.7	4.9
6% MgO	56.5	34.2	1.6	9.3
9% MgO	51.8	35.4	1.4	12.8
12% MgO	51.6	33.6	1.5	14.8

Table 3.2 shows that, along with both the α and β polymorphs of Si_3N_4, minor amounts of silicon oxynitride (Si_2N_2O) formed when MgO was added. The α-Si_3N_4 content was higher in all MgO-containing samples compared to those comprising no MgO and indicates preferential formation of the α-phase. Considering that in the MgO-SiO_2 system the first eutectic liquid forms at a somewhat higher temperature (1543-1557°C) than the nitriding temperature, we can assume that the α/β-

phase ratio was not due to liquid formation. While the less stable α-phase is known to dissolve oxygen, β-silicon nitride contains no oxygen [21, 41]. Therefore, an increased presence of oxygen in the system originating from the oxide additive promoted the preferential formation of α-phase. To define the role of this oxide in the microstructural changes of the porous RBSN, samples contain 12 wt.% MgO were sequentially heated up to a temperature of 1700℃.

The XRD results and phase compositions presented in **Fig. 3.6** and **Table 3.3** revealed that Si and MgO were the only crystalline phases detected in the sample after the pyrolysis step. By heating the porous silicon body to 1100℃, some minor peaks between 2θ of 20˚ to 45˚ were present which corresponded to ≈ 3 wt. % Forsterite, Mg_2SiO_4 as well as residual MgO.

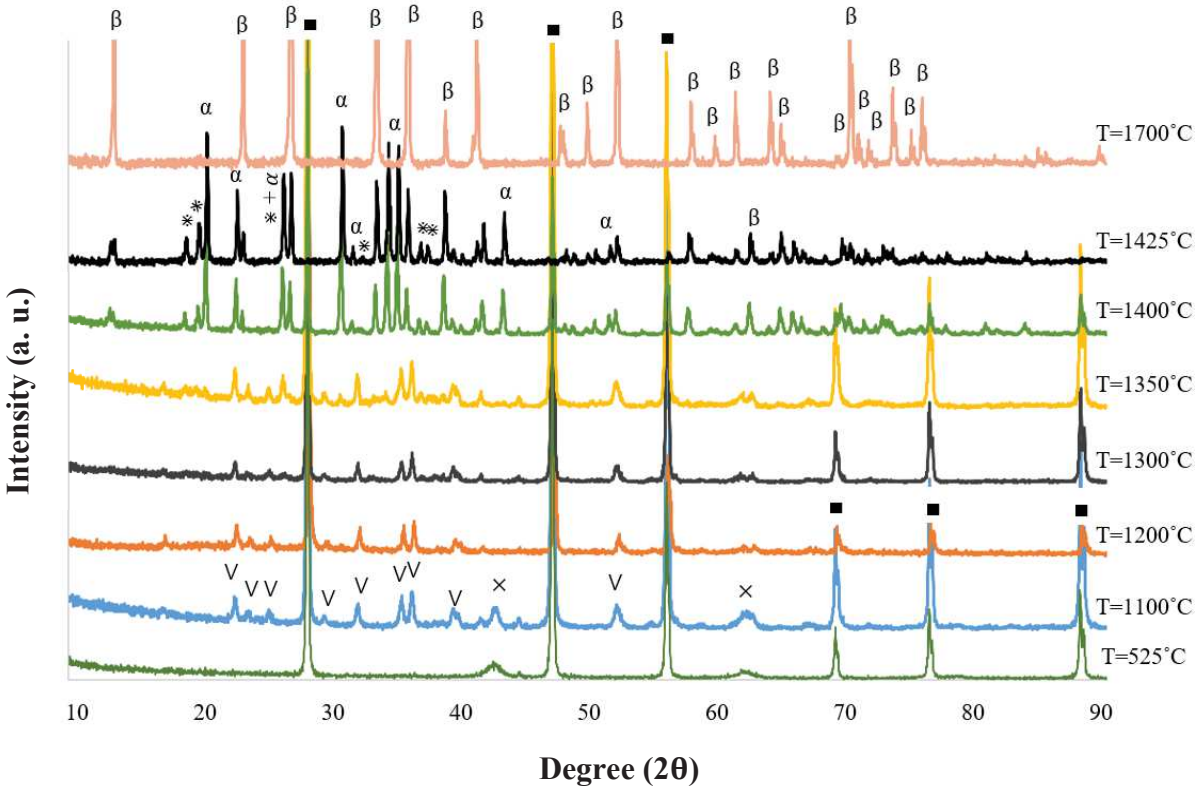

Fig. 3.6. XRD patterns of samples containing 12% MgO heat-treated at 525, 1100, 1200, 1300, 1350, 1400, 1425 and 1700℃ (α, β , $*$, $\vee$, $\times$ and ■ show peaks corresponded to α-Si_3N_4, β-Si_3N_4, Si_2N_2O, Mg_2SiO_4, MgO and Si, respectively)

Table 3.3. Phase fractions and α/β-Si_3N_4 phase ratio obtained for samples containing 12% MgO and heat-treated at different temperatures

Heat-treatment temperature	wt. %						
	Si	MgO	Mg_2SiO_4	Si_2N_2O	α-Si_3N_4	β-Si_3N_4	α/β-Si_3N_4
T= 525°C	97.5	2.5	0	0	0	0	0
T= 1100°C	95	2	3	0	0	0	0
T= 1200°C	91.0	0	9	0	0	0	0
T= 1300°C	94.0	0	4.0	2.0	0	0	0
T= 1350°C	90.5	0	4.0	2.5	2.3	0.6	3.8
T= 1400°C	49.4	0	1.5	7.4	29.2	12.5	2.3
T= 1425°C	0	0	0	14.8	51.6	33.6	1.5
T= 1700°C	0	0	0	0	0	100	0

At 1200°C, while the Mg_2SiO_4 peaks intensified up to a maximum of ≈ 9 wt. % content, crystalline MgO was no longer detected. Experimentally Mg_2SiO_4 can be formed at temperatures between 1000°C and 1400°C by reaction between solid or gaseous MgO (g, s) and native surface SiO_2 present on the surface of silicon particles [121]. Thermodynamic data in **Eq. 3.4** confirms that this reaction can involve either gaseous or solid MgO, both of which have large negative ΔG°.

$$2MgO\,(g, s) + SiO_2\,(s) \rightarrow Mg_2SiO_4\,(s) \qquad \textbf{Eq. 3.4}$$

$$\Delta G^{\circ}_g = 368.9 \times 10^{-3}\,T - 10^{+3}\ kJ.\ mol^{-1}\ (866\text{-}1465°C)$$

$$\Delta G^{\circ}_s = 62.4 \times 10^{-3}\,T - 100.5\ kJ.\ mol^{-1}\ (800\text{-}1465°C)$$

However, with MgO vapor present, the reaction is much more thermodynamically favorable. In an experiment where porous silicon (without additive) was placed on MgO powder during nitridation, it is revealed in **Fig. 3.7** that the formation of whiskers was stopped. Indeed, a similar microstructure is observed in **Fig. 3.3-g** (12% MgO addition), in which the pore cavities became entirely spherical and whisker-free. This both confirms that MgO is highly volatile at elevated temperature and also that it interfered with the nitriding reaction to change the microstructure and morphology of the porous Si_3N_4.

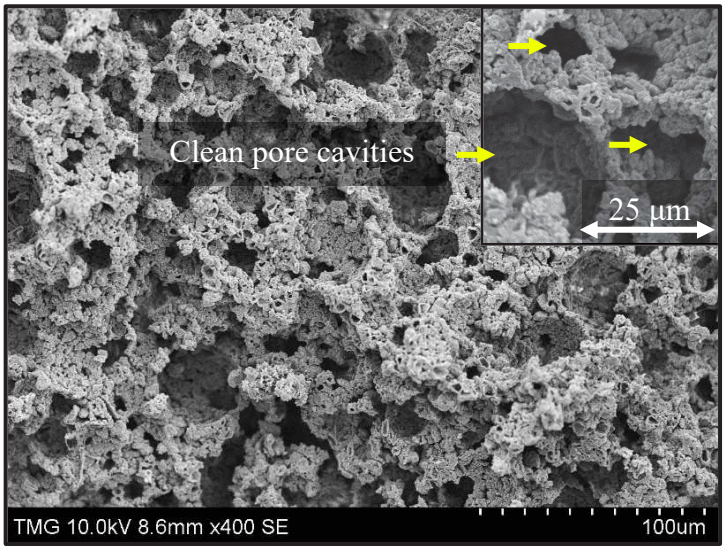

Fig. 3.7. SEM micrograph of pure silicon precursor nitrided on top of MgO powder bed

In addition, a relatively uniform elemental distribution of Mg and O around the Si particles shown in **Fig. 3.8** suggests that magnesium silicate formed predominantly through reaction of an Mg-containing gaseous phase rather than that of a solid phase. Aside from the elevated temperature, the high surface area and levels of porosity would enhance the vaporization rate. Accordingly, Mg-containing vapor migrated to the silica-rich surface and reacted to form Mg_2SiO_4 [56, 122, 123]. The protective SiO_2 layer acting as a "sink" for magnesium, reacted with gaseous magnesium oxide rather than with the silicon and hence SiO gas formation was suppressed. It is worth noting that under neutral and reducing atmospheres, along with molecular MgO, the major vapor species in thermodynamic equilibrium with solid MgO are reported to be O_2 (g) and Mg (g) [124]. Therefore, we can expect that with vaporization of MgO, the local oxygen vapor pressure in the pore volume would increase and alter the partial pressure of the SiO in the very early stage of nitriding. This is also in agreement with the higher α-Si_3N_4 content in samples containing MgO compared to that of silicon nitride with 0% MgO (**Table 3.1**) since small amounts of oxygen to the reaction zone are reported to alter the α/β-Si_3N_4 ratio [22].

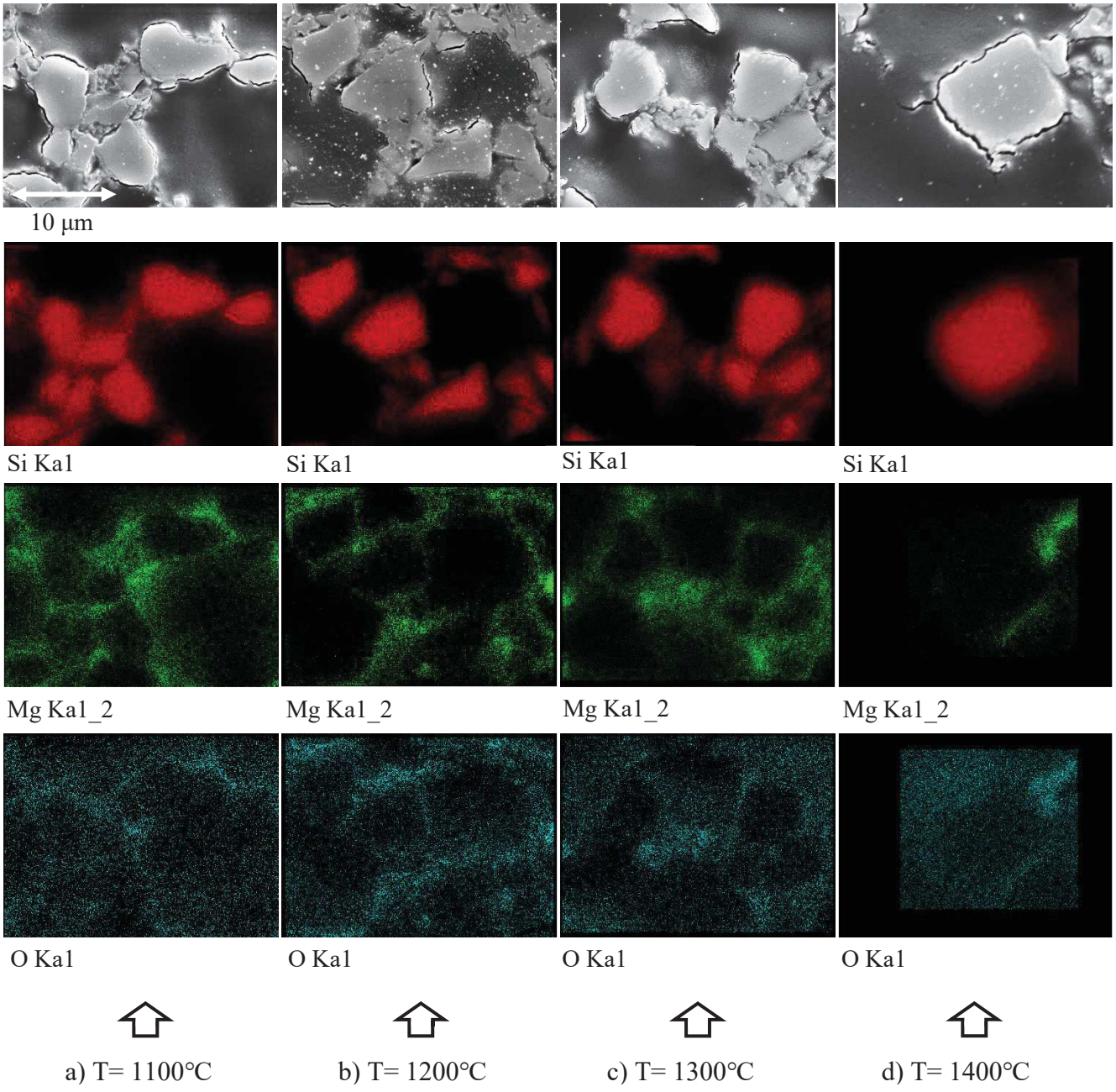

Fig. 3.8. EDX mapping of 12% MgO addition to the porous silicon precursor and nitrided at different temperatures (note Mg and O segregation on the particle surfaces)

The XRD pattern of samples with 12% MgO additions showed the formation of both α- and β-Si_3N_4 at 1350°C with α being the dominant phase. As the temperature was increased to 1425°C, the α/β ratio decreased and is attributed to the melting of silicon and formation of more β phase. After 4 hr heating, Si_2N_2O coexisted along with silicon nitride up to an amount of ≈ 15 wt. %. Unfortunately, due to the similar elemental contrast of these two phases and the limited resolution of the EDX system, microstructural distinction between Si_3N_4 and Si_2N_2O phases was not possible.

Formation of Si_2N_2O has been reported at temperatures ≥ 1700°C due to oxidation of Si_3N_4 [125-128]. In the current work, Si_2N_2O formed at a lower temperature, just prior to any silicon nitride formation and confirmed that oxidation of Si_3N_4 was not involved in the development of this phase. On the other hand, the appearance of Si_2N_2O coincided with a simultaneous decrease in magnesium silicate content when MgO was present. Therefore, by decomposition of Mg_2SiO_4, as an intermediate phase through reaction with nitrogen, formation of Si_2N_2O was initiated and enhanced by the presence of oxygen. The calculated Gibbs free energy for this reaction described in **Eq. 3.5** gives a very large negative ΔG°, indicating that this reaction is very thermodynamically favorable. Further formation of Si_2N_2O could have occurred through oxidation of silicon due to the increased local pO_2 [55].

$$Mg_2SiO_4\,(s) + 3Si\,(s) + 2N_2\,(g) \rightarrow 2Si_2N_2O\,(s) + 2MgO\,(s, g) \qquad \textbf{Eq. 3.5}$$

$$\Delta G^{\circ} = 371.8T - 745 \times 10^{+3}\ kJ.\ mol^{-1}\ (640\text{-}1414°C)$$

Based on these observations, in the presence of MgO, a decrease in whisker formation was found to coincide with an increase in Mg_2SiO_4 and Si_2N_2O contents. This favored the formation of equiaxed grains of Si_3N_4 rather than whiskers. Given the fact that the Si_3N_4 morphology is closely related to the gaseous partial pressure of the various species present, MgO changed the partial pressure of the reactants, thus modifying the grain morphology to a mixture of matte and hexagonal grains. Consequently this created an open and interconnected porous microstructure.

3.3.2. High Temperature Heat-treatment

3.3.2.1. Effect on Microstructure

When MgO-containing nitrided samples were further heated to 1700°C for 2 hr, the only detectable crystalline phase was β-Si_3N_4. Consequently, it is proposed that silicon oxynitride, remaining after

nitriding, contributed to liquid phase formation and enabled complete α- to β-Si_3N_4 phase transformation. **Fig. 3.9** presents the overall microstructural evolution during heat-treatment from the silicon precursor shown in **Fig. 3.9-a**, to the final β-Si_3N_4 microstructure in **Fig. 3.9-d**. It is clear from **Fig. 3.9-b** that the nitriding reaction initiated at the surface of the Si and progressed inwards by diffusion of nitrogen. Once a nitride layer covered the surface of the silicon particles, further nitridation depended on the diffusion of nitrogen through the surface silicon nitride layer [41]. Fully nitrided grains, observed in **Fig. 3.9-c,** were a combination of α- and β-phase. The elongated β-Si_3N_4 grains in **Fig. 3.9-d** developed during liquid phase transformation. XRD pattern of the sample in **Fig. 3.6** confirmed that the only phase present in this structure was β-Si_3N_4.

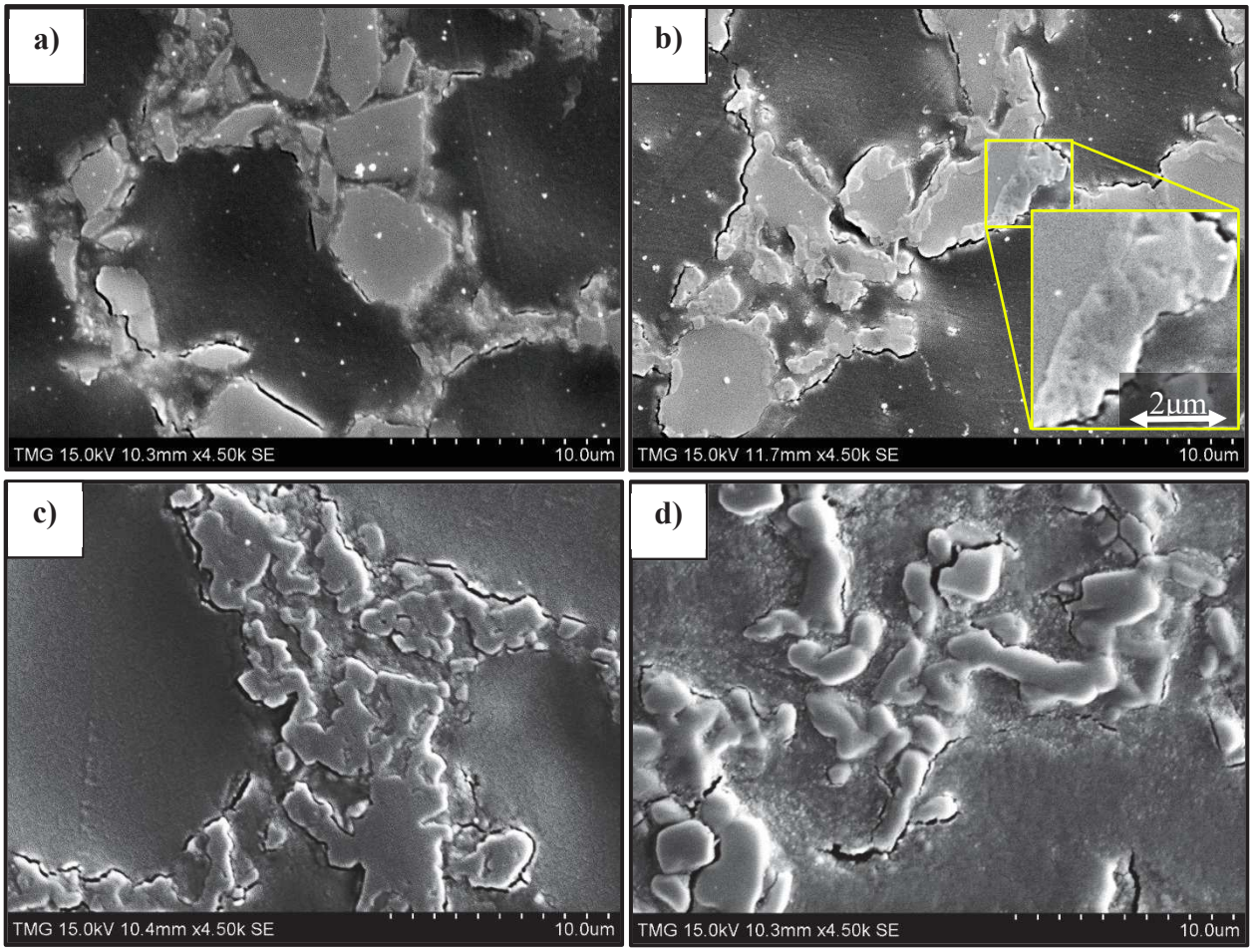

Fig. 3.9. Microstructural development and grain growth of the Si precursor containing 12% MgO after heat-treatment at different temperatures: a) 1100°C, b) 1400°C, c) 1425°C and d) 1700°C

SEM micrographs of MgO-containing samples in **Fig. 3.10** shows that after heat-treatment at 1700°C, the β phase precipitated as elongated hexagonal grains. In samples containing 3 % MgO, local supersaturation led to abnormal grain growth in abundant regions of liquid phase. Low content of sintering additives resulted in the formation of grains with various sizes and thus, an inhomogeneous microstructure, as shown in **Fig. 3.10-a** and **-b**. By increasing the MgO content and Si_2N_2O phase ratio, the amount of liquid phase became high enough that the low viscosity melt migrated to the boundaries and suppressed the abnormal grain growth. Hence, with homogenous distribution of liquid phase during the heat-treatment process, grain growth occurred in multiple regions and fine β-Si_3N_4 with uniform size distribution were precipitated in the 6 % MgO samples. From 9 wt. % to 12 wt. % MgO, while the length of the rod-like grains remained relatively constant indicating negligible grain growth on the β-basal plane (001), grain coarsening occurred mainly on the prismatic planes (100). Grains with the maximum length of 6 μm were surrounded by glassy phase as indicated by arrows in **Fig. 3.10-g**. The results of EDX analysis of this figure showed the presence of magnesium, nitrogen and oxygen in the form of an Mg-Si-O-N oxynitride amorphous phase.

X-ray micro-tomography was used as a non-destructive analysis to visualize and characterize the porosity of the heat-treated structure. Through the LPS process, all whiskers vanished, and the precipitated hexagonal β-grains formed the struts in the resulting porous microstructure.

The interconnected pore network of 12 wt. % MgO samples was observed in 2D cross-sections of eight sequential slices cut through z axis (**Fig. 3.11**). Furthermore, 3D construction images of thin layers with a thickness of 116 μm, illustrate a continuous network of pore channels interconnected in three-dimensional space (**Fig. 3.12**). The pores were relatively uniform and completely whisker-free; consequently, a porous structure with high interconnectivity was obtained.

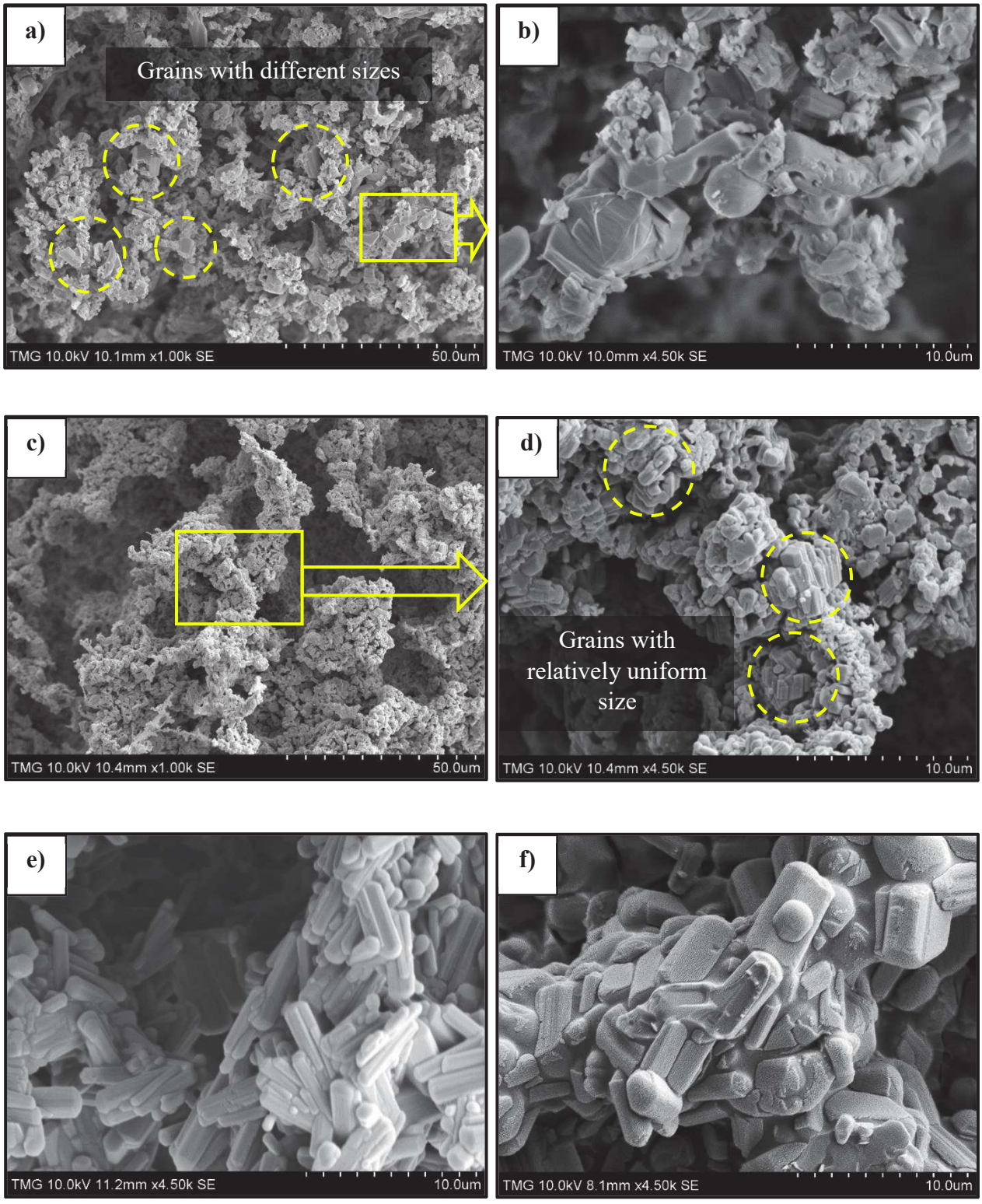
a)
Grains with different sizes
TMG 10.0kV 10.1mm x1.00k SE
50.0um
b)
TMG 10.0kV 10.0mm x4.50k SE
10.0um
c)
TMG 10.0kV 10.4mm x1.00k SE
50.0um
d)
Grains with relatively uniform size
TMG 10.0kV 10.4mm x4.50k SE
10.0um
e)
TMG 10.0kV 11.2mm x4.50k SE
10.0um
f)
TMG 10.0kV 8.1mm x4.50k SE
10.0um

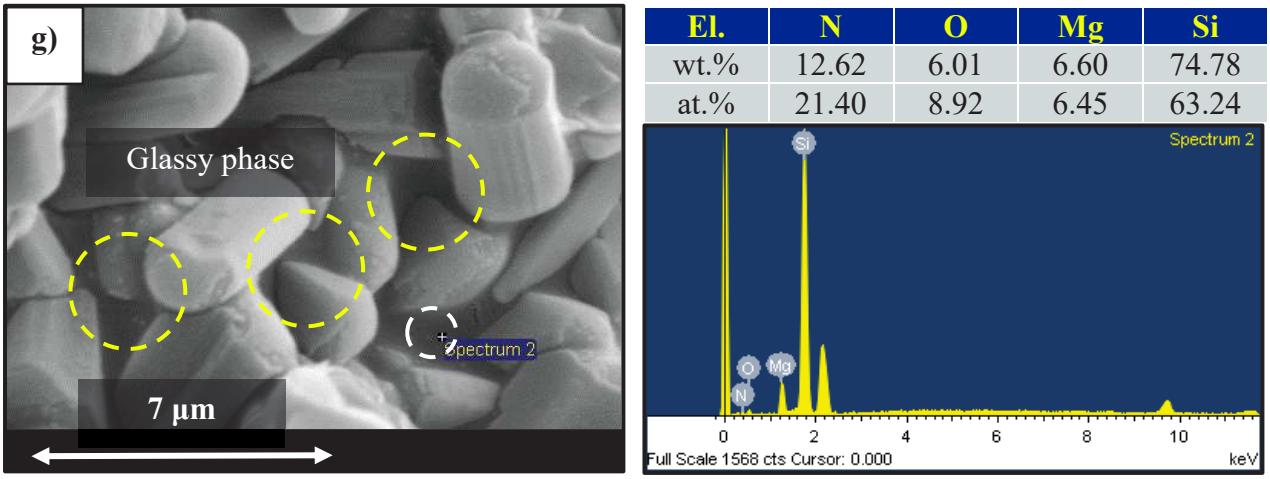

Fig. 3.10. SEM micrographs of various MgO precursor contents heat-treated at 1700°C: a and b) 3% MgO, c and d) 6% MgO, e) 9% MgO, f) 12% MgO and g) shows glassy phase and EDX spectrum of (f)

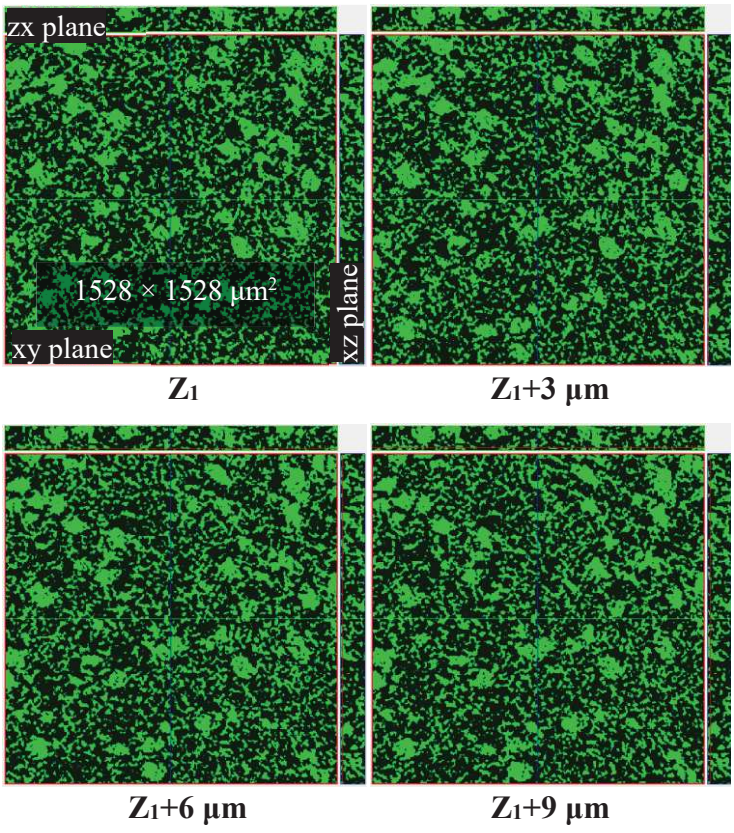

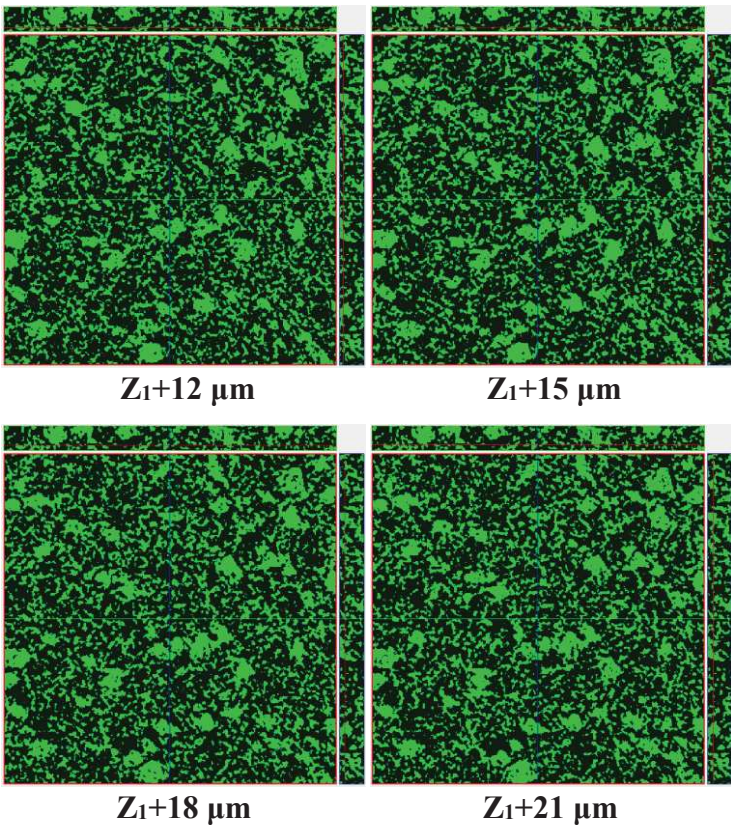

Fig. 3.11. Slice images of xyz planes for eight sequential slices of porous silicon nitride containing 12% MgO (green region shows the solid body and black areas are pores)

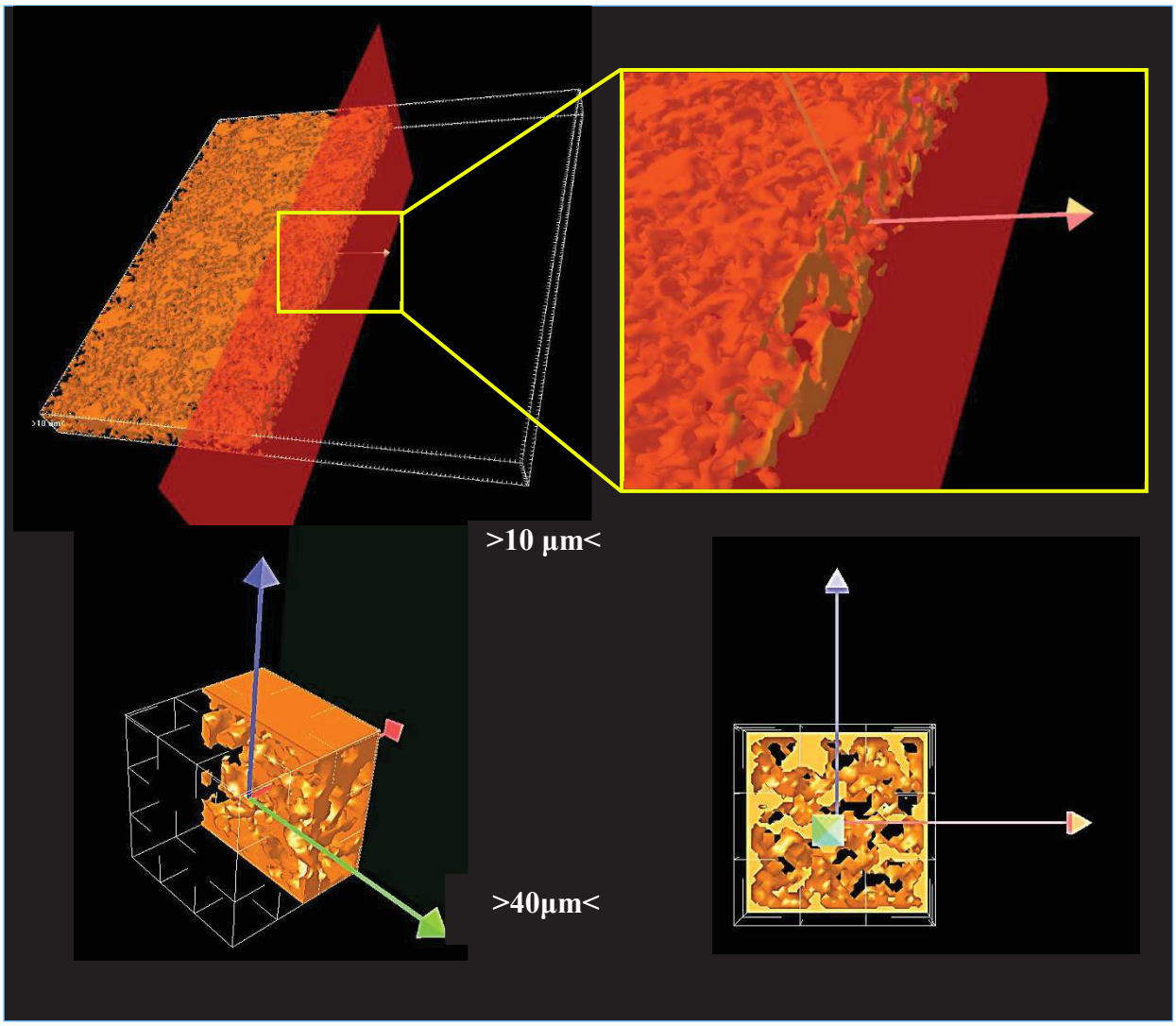

Fig. 3.12. 3D reconstruction images of porous silicon nitride ceramic (orange region shows the solid body)

3.3.2.2. Properties of the Porous Samples

The weight losses and linear shrinkages obtained as a function of additive content are plotted in **Fig. 3.13.** Thermal decomposition of Si_3N_4 and evaporation of MgO were the main sources of weight loss which can be controlled by the contents of liquid phase and partial pressure of MgO in the ambient atmosphere. Therefore, from 0 to 9% MgO, weight loss was increased as liquid phase formation was enhanced with higher additive contents. However, the sudden drop at 12

wt.% MgO is explained by the high partial pressure of volatile MgO diffusing from the powder bed, which could be high enough in the local atmosphere to effectively suppress oxide loss.

The smallest shrinkage (0.4%) was found with 3% MgO content, whereas the highest shrinkage (1.6%) occurred in the case of 12% MgO owing to the presence of more liquid phase. Particle size and shape, type and amount of oxide additives are the main factors governing the shrinkage and densification behavior during heat-treatment at this temperature. In typical LPS, if the amount of low viscosity liquid phase is high enough, the liquid penetrates between the grains and induces the first stage of shrinkage by grain rearrangement. Later, through solution-precipitation and densification, further shrinkage is observed. In post-sintering of RBSN, however, the particle rearrangement would not occur as bonding between nitrided grains hinder the effect of capillary forces. This leads to the low shrinkage of all samples indicating that the dimensions of the nitrided bodies remained virtually unchanged during heat-treatment at 1700°C. By increasing the oxygen content of the system, originating from MgO, silica or Si_2N_2O, accumulation of liquid phase could result in some particle rearrangement and enhanced shrinkage through solution of α-phase and neck junctions [41, 47]. The overall LPS shrinkage results in a decrease in porosity and thus some densification. **Fig. 3.14** shows the bulk density and apparent porosity for 12% MgO samples heat-treated at 1700ºC is ≈ 74 vol.% and 0.75 $g.cm^{-3}$ compared to ≈ 81 vol.% porosity and 0.53 $g.cm^{-3}$ density for as-nitrided samples. Therefore, the post-nitriding heat-treatment step in the presence of MgO led to the some densification and a slight decrease in porosity. However, for lower MgO contents a different trend was observed: for 6% MgO addition, the porosity was ≈ 84 vol. %, and the bulk density decreased to ≈ 0.48 $g.cm^{-3}$ and is attributed to MgO evaporation. However, at higher MgO content, lower porosity and a denser structure was achieved due to the densification promoted by liquid phase formation.

3.3.2.3. Compression Testing

Compression tests were carried out on samples heat-treated at 1700°C and the results are presented as a function of oxide content in **Fig. 3.15**. As strength is closely related to microstructure, the high porosity content of samples led to the relatively low compressive strengths. Low-magnification SEM micrographs of samples contain 6 and 12 wt.% MgO show the differences in their cellular structures. The highest porosity content, 6% MgO, showed a compressive strength of

≈ 1.1 MPa whereas with enhanced shrinkage and a lower porosity of 74 vol.%, the 12% MgO samples led to a higher strength of ≈ 1.6 MPa. These values are comparable with those reported for cellular Si_3N_4 structures fabricated for biomedical applications [101]. In the latter case, interconnected large pores and high porosity are considered suitable for tissue in-growth and nutrition delivery [101]. The compression testing data are in good agreement with the microstructures of samples; therefore, we can assume that in the current study, the high porosity content was the main factor limiting the compressive strength. In addition to the influence of porosity, one should consider the differences in pore size distribution of samples, especially the fact that pores are major flaws in any porous structure and the maximum and mean pore size highly affect the mechanical properties of samples. Although the amount and size of polymer beads were essentially the same for all samples; with different MgO content, samples experienced various linear shrinkage; thus, resulting in different pore size distribution.

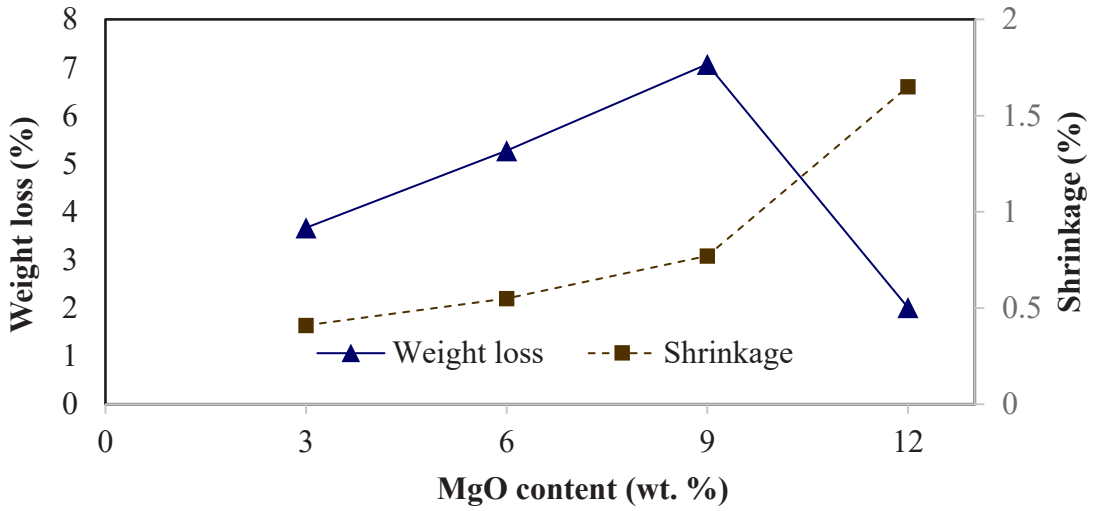

Fig. 3.13. Linear shrinkage and weight loss vs MgO content for samples heat-treated at 1700°C

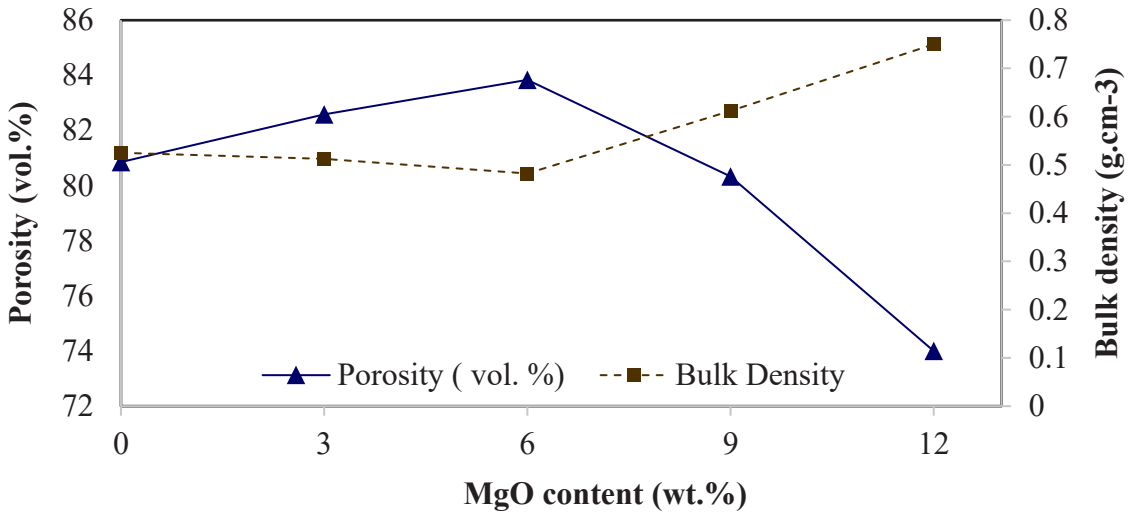

Fig. 3.14. Porosity and density variation vs MgO content after heat-treatment at 1700°C

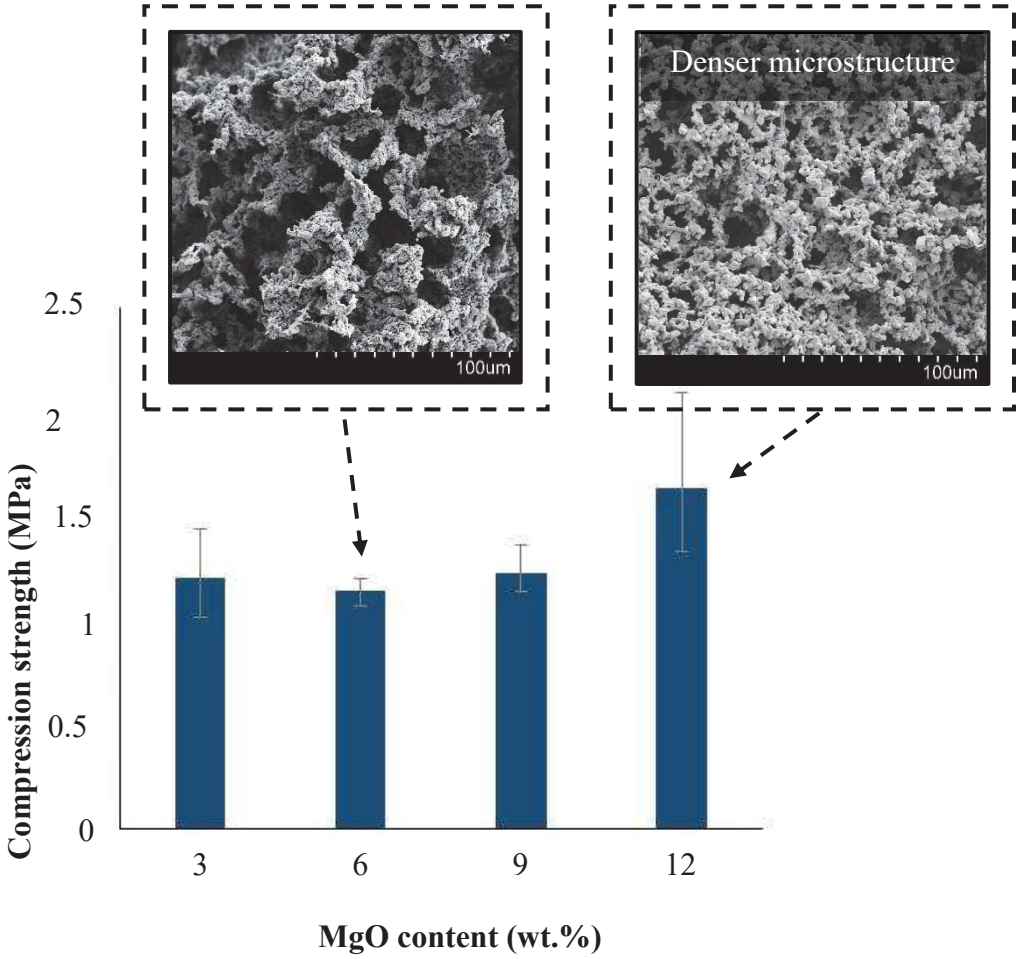

Fig. 3.15. Compression strength of samples vs MgO content heat-treated at 1700°C

3.4. Conclusion

The formation and morphology change of highly porous RBSN structure was investigated in the presence of MgO. Quantitative and visual comparisons showed a strong correlation between the ceramic's composition and morphology of grains. In the presence of MgO, Mg_2SiO_4 formed as an intermediate phase predominantly via a gaseous phase reaction between MgO and surface silica. At higher temperature, with a concurrent decrease in the content of Mg_2SiO_4, Si_2N_2O formed and coexisted with α-Si_3N_4 at 1425°C. This mechanism significantly altered the dominant reaction, simultaneously modifies the grains morphology to fine equiaxed grains and enhances the pore channel interconnectivity. From 0 to 12 wt.% MgO, the α/β-phase ratio significantly increased from ≈ 0.4 to ≈ 1.5. Low content of MgO restrained whisker growth and led to the formation of sintered grains with relatively bimodal size distributions. No whiskers appeared with 12 wt.% MgO content during the nitriding process and coarse sintered grains with a uniform size distribution formed in a highly porous interconnected structure. X-Ray tomography confirmed that the pore network extended continuously and homogeneously throughout the microstructure. Upon heat-treatment up to 1700°C, Si_2N_2O disappeared by its incorporation into a liquid phase out of which β-Si_3N_4 formed. Upon cooling to room temperature, the liquid became a glassy phase and contained magnesium, oxygen and nitrogen. The resulting material showed a high porosity of 74-84 vol.% and density of 0.48-0.75 $g.cm^{-3}$ with a mean compression strength of between 1.1 to 1.6 MPa, with the highest porosity displaying the weakest strengths.

Chapter 4. Microstructural Evolution Mechanism of Porous Reaction Bonded Silicon Nitride Ceramics Heat-treated in Two Powder Beds

Raheleh Nikonam M.[a,*], Martin D. Pugh[a], Robin A.L. Drew[a]

[a] Department of Mechanical, Industrial and Aerospace Engineering, Concordia University, Montreal, CANADA, H3G 1M8

*corresponding author: r_nikona@encs.concordia.ca.

This article has been published in Ceramics International 45 (2019) 21986-21997, https://doi.org/10.1016/j.ceramint.2019.07.213

Abstract

Porous Si_3N_4 with various grain morphologies was prepared by direct nitriding of silicon powder and subjected to heat-treatment while embedded in a Si_3N_4 powder bed. The influence of MgO, added either to the starting silicon or to the powder bed, on the microstructural transformation and morphology of pores at temperatures between 1425°C and 1700°C are discussed. In the presence of MgO, α-Si_3N_4 grains with equiaxed morphology resulted in an interconnected microstructure with spherical pores. By contrast, in the absence of MgO, an α-whisker-dominant microstructure resulted in pores of various morphologies. During the post heat-treatment process, the α-whiskers gradually vanished, and grains recrystallized as very fine β-Si_3N_4 rods. Consequently, pores became spherical, large and whisker-free. In agreement with the results of SEM-EDX along with XRD analysis, the observed morphology transition and full phase transformation occurred by vapor phase transport of MgO from the powder bed and a subsequent solution-precipitation mechanism. The presence of volatile MgO in the powder bed caused a substantial decrease in weight losses, while enhancing β phase formation, grain coarsening and linear shrinkage. The development of coarse β-rods from α-matte grains in a Si-Mg-O-N glassy phase was related to the presence of substantial liquid phase during the growth mechanism. Compared to the granular morphology, whiskers with high aspect ratio gave rise to a high sintering driving force and led to a maximum value of ≈ 2% linear shrinkage and porosity of ≈ 30 vol.%. Consequently, this ceramic exhibited the highest compressive strength of ≈ 10 MPa.

Key words:

α-Si_3N_4 whiskers; Equiaxed grains; Powder bed; Magnesium oxide; Vapor phase transportation

4.1. Introduction

The good combination of high thermal shock resistance, wear resistance and low friction coefficient have placed porous silicon nitride (Si_3N_4) among the most highly desirable refractory ceramics for the production of microwave–transparent components, membrane supports, catalyst carriers or liquid/gas filters [39, 40, 76]. Compared with other preparation methods such as aqueous gel casting [39], cold isostatic pressing, freeze-casting [76], and direct foaming [73], reaction bonding of silicon nitride (RBSN) has been widely investigated and applied in the production of porous Si_3N_4, which is attributed to its simplicity, low cost and near net-shaped products (≈ 0.1% size change) [41, 129-131]. In combination with gel casting and a sacrificial template technique, reaction bonding has led to the fabrication of highly porous Si_3N_4 samples (up to 87 vol.%) with an open-cell structure [19]. However, controlling the microstructure present in RBSN is rather critical as the nitriding reaction is simultaneously influenced by several processing parameters [44, 52, 54]. Observations on the variation of RBSN microstructure depending on the presence of native or added impurities led to the development of a novel approach, which modifies the characteristics of the ceramic when employing appropriate additives [13, 47, 51, 57, 132]. By altering the nitriding mechanisms, for instance, additives have been employed to fabricate a microstructure with granular α-matte grains with increased channel interconnectivity [133], or fine needle-like crystals (called whiskers) with enhanced filtration efficiency [26] and bending strength [25].

As a prerequisite of liquid phase sintering (LPS), the presence of oxide impurities also results in the formation of a eutectic melt, which accelerates mass transport and the sintering kinetics of silicon nitride through a fast diffusion path. This encourages high temperature phase transformation, β-Si_3N_4 rod formation and consolidation of the structure [60, 64, 93]. Since the 1950s, many studies have been performed on the effect of LPS parameters (e.g., temperature, time, and type of additives) on morphological and physical properties of Si_3N_4 based ceramics [11, 63, 116, 134, 135], however only a few studies focused on the role of a powder bed acting on the LPS process. In order to slow down dissociation of Si_3N_4 and to offset high temperature decomposition

in a post-nitriding heat-treatment process, a powder bed of appropriate composition is required. Hence, the composition of the powder bed plays a significant role in providing a suitable partial pressure, reducing the ceramic weight losses and keeping the microstructure uniform [34, 35, 65, 66].

Whereas introducing oxide additives along with liquid phase sintering may allow the production of RBSN with various controlled microstructures, a perfect mixing and distribution of these particles within the matrix powder, is difficult (if not impossible) to obtain, and thus additive agglomeration, incomplete nitridation or lack of homogeneity in the microstructure lowers the performance of a porous body [56, 136]. In addition to the conventional mixing approach, vapor phase transport from external sources such as a powder bed could be another effective route to introduce oxide additives into the microstructure [34, 56]. Immersing porous Si_3N_4 ceramic with a high surface area into a powder bed containing volatile species may alter the resultant RBSN microstructure. Magnesia has a high vapor pressure at T≥ 1400°C and appears to be a suitable candidate [34, 56]. Accordingly, powder bed technology may be adopted as a post heat-treatment approach: not only to inhibit the volatilization, but also to enable the modification of the microstructure and properties of a fully nitrided porous Si_3N_4 containing no additive.

The main objective of this research was to study the impact of powder bed compositions on the morphology and microstructural transitions of heat-treated porous RBSN grains. Samples (with and without MgO) were prepared by reaction bonding and ensuing heat-treatment up to 1700°C to obtain a porous Si_3N_4. These were subsequently exposed to MgO from a powder bed. Phase formation and $\alpha \rightarrow \beta$-Si_3N_4 phase transformation resulting from heat-treatment were investigated by X-ray diffraction. Pore morphology and microstructural transformation were studied by SEM analysis equipped with EDX. Additionally, the influence of sample composition and microstructure on the linear shrinkage, weight loss, porosity and compressive strength were determined. This investigation will aid the understanding of the microstructural development mechanisms of heat-treated porous RBSN with MgO present either in the ceramic body or in the surrounding powder bed.

4.2. Experimental Procedure

Prior to the post heat-treatment process, porous silicon samples were prepared by a place-holder method described previously [19]. Using high purity silicon powder (99.995%, -8 μm, ABCR, Fe impurity content= 0.001%) and PMMA beads (10, 20 and 40 μm, Microbeads), a premixed solution was prepared in deionized water with the Si: PMMA: H_2O ratio of 16: 44: 40. Organic monomers, i.e. acrylamide (AM) and N,N'-methylenebisacrylamide (MBAM), as the main components of the gel-casting process along with initiator and catalyst, were added to facilitate polymerization.

Two sets of reaction bonded Si_3N_4 samples, with and without MgO, were prepared and were labeled as "RBSN" and "MgO-RBSN", respectively. To obtain samples containing additive, MgO (> 99% trace metals basis, -325 mesh, Sigma-Aldrich) was added to the slurry with a ratio of 12 wt.% of the final Si_3N_4 mass. After milling and degassing under vacuum, the suspension was cast in silicone rubber moulds, polymerized at 50°C and then dried at 120°C for 5 hr. The porous bodies were prepared by heating the dried samples for 2 hr at 525°C and subsequently nitrided for 4 hr at 1425°C under flowing ultra-high purity nitrogen (99.999%) at atmospheric pressure. To decrease the temperature gradient within the thickness of the sample due to the exothermic nature of the nitriding reaction and to minimize local melting of silicon at temperatures above 1410°C (melting point of Si), slow heating rates have been applied, i.e., 10°C min^{-1} to 1350°C and 0.5°C min^{-1} to 1425°C.

Subsequently, samples were immersed in a powder bed and placed in a BN container. With the weight ratio of 1:1, this mixture was composed of Si_3N_4 powder (grade M11 higher purity, ABCR) and BN powder (Industrial grade powder, COMBAT) and labelled as "SN". To determine the effects of powder bed composition on microstructural variations of samples, MgO was added to the former mixture. This powder bed was labeled "MgO-SN", the composition of which contains MgO/Si_3N_4 with the weight ratio of 0.12:1. Finally, porous samples were sequentially heat-treated at 1700°C under 1 atm. nitrogen gas for holding times of 10 min. and 2 hr. The notification "MgO-RBSN heat-treated in SN" for example stands for a heat-treated porous sample which contains MgO only in the starting silicon powder and none in the surrounding powder bed.

Crystalline phase identification and quantification were performed by powder X-ray diffraction analysis (XRD; X'Pert Pro, Panalytical). Data was collected from the crushed samples with an accelerating voltage of 40 kV and anode current of 45 mA. The equation of $I\% = \frac{Ii}{\sum Ii}$ was used for phase quantification, where I_i is the peak height of phase i [137]. Relative amounts of the different nitrided phases were determined quantitatively based on the intensities of (101) and (210) diffraction peaks for β-Si_3N_4 phase, along with the intensities of (210) and (102) peaks for the α-Si_3N_4 phase. Scanning electron microscopy (SEM, Hitachi, S-3400 N) equipped with energy-dispersive analysis (EDX, Oxford Instruments, Wave Model) was used to characterize microstructures. Under high vacuum with 5-15 kV and 40-50 mA imaging conditions, Au-Pd coated surfaces were studied after fracturing. Cylindrical specimens with dimensions of d≈ 14.28 mm and h≈ 20 mm have been used to determine the characteristics of porous ceramics. Average heat-treatment linear shrinkage and mass changes (which could be attributed to the compositional changes, decompositions and volatilization of materials) were determined for seven porous Si_3N_4 samples. The average porosity of the heat-treated ceramics was determined by Archimedes' technique, ASTM C373-88 standard. The strength of the porous heat-treated ceramics was measured using Instron tester (Model 3382) at a constant crosshead speed of 0.5 mm min^{-1} and under uniaxial compressive loading.

4.3. Results and Discussion

4.3.1. Microstructural Observations of MgO-RBSN Samples

In order to facilitate the understanding of the microstructural variations in MgO-RBSN and RBSN, the results have been organized into two separate sections with the microstructures of MgO-RBSN being discussed first.

To fabricate porous MgO-RBSN, magnesia was added to the starting silicon powder and the reaction bonding carried out at 1425℃. During the nitriding, the grain morphology and phase ratio can be controlled by several factors, especially oxygen content and type of additives [20]. In the presence of MgO, Si_3N_4 with granular morphology formed which led to the porous interconnected microstructure with clean spherical pores (**Fig. 4.1-a** and **-b**). X-ray diffraction patterns in **Fig. 4.2-a** and **Table 4.1** identified the presence of Si_2N_2O, and Si_3N_4 with the α/β phase ratio of 1.5. Formation of the α-rich microstructure and silicon oxynitride phase are both attributed to the

variation in the ratio of pO_2/pN_2 in the surrounding atmosphere. At elevated temperature, the content of MgO, Mg, and O_2 vapor species would increase under a neutral atmosphere [124]. Accordingly, at T≥ 1400°C, the partial pressure of oxygen in the ambient gas was enhanced by the evaporation and decomposition of MgO, leading to the development of a microstructure composed of α-matte grains with an equiaxed morphology. Furthermore, Si_2N_2O was favored in the presence of the high partial pressure of oxygen [55, 124, 133].

After formation of sufficient liquid (typically 5 to 15 vol.%) combined with particle rearrangement, LPS proceeds at 1600-1800°C through the concurrent mechanisms of solution-precipitation and grain growth [60]. α-matte subsequently dissolves, and β-hexagonal rods precipitate according to the reaction: $\alpha\text{-}Si_3N_4 + SiO_2 + MgO \rightarrow \beta\text{-}Si_3N_4$ + Si-Mg-O-N glassy phase. However, the microstructures of MgO-RBSN heat-treated at 1700°C for 2 hr in a SN powder bed, presented in **Fig. 4.1-c** and **-d,** revealed the lack of grain growth and incomplete LPS, leading to a very fine-grained microstructure. Although a decrease in α/β phase ratio from 1.5 to 0.15 was observed in **Fig. 4.2-b** and **Table 4.1**, illustrating partial phase transformation, this reaction was incomplete and confirmed by the presence of 13.5 wt.% untransformed α-phase.

To study the influence of powder bed composition, MgO was included in the SN powder bed and heat-treatment was performed for 2 hr at 1700°C. Compared to the microstructures of samples heat-treated in SN alone (**Fig. 4.1-c** and **-d**), formation of coarse interlocked hexagonal-grains with an aspect ratio of ≈ 6 (**Fig. 4.1-e** and **-f**) illustrates significant grain coarsening. XRD analysis in **Fig. 4.2-c** and **Table 4.1** revealed the presence of $\beta\text{-}Si_3N_4$ only and so a complete transformation of α- to $\beta\text{-}Si_3N_4$ phase occurred.

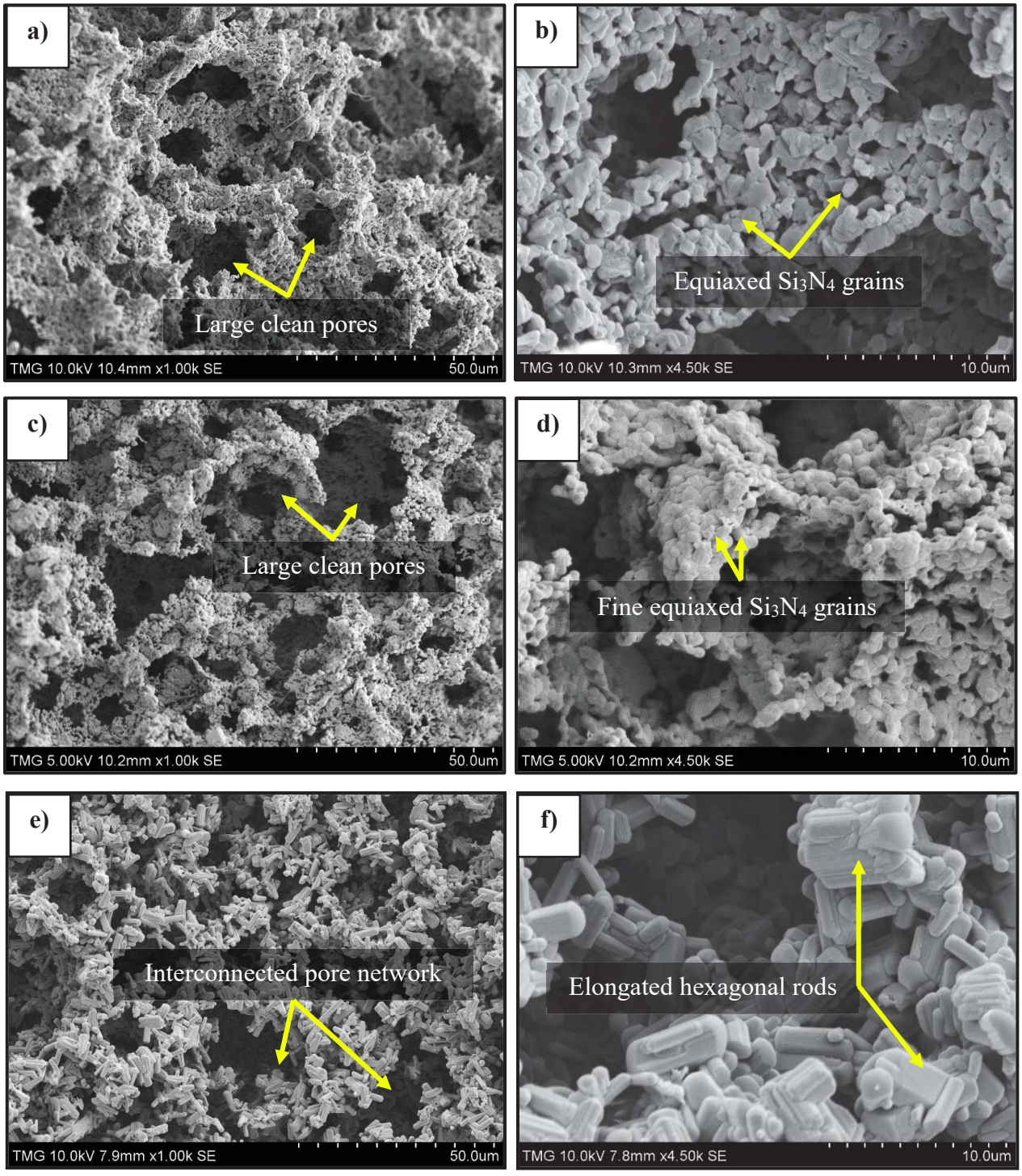

Fig. 4.1. SEM micrographs of various samples: a) and b) MgO-RBSN nitrided at 1425°C for 4 hr, c) and d) MgO-RBSN heat-treated at 1700°C for 2 hr in SN powder bed, e) and f) MgO-RBSN heat-treated at 1700°C for 2 hr in MgO-SN powder bed

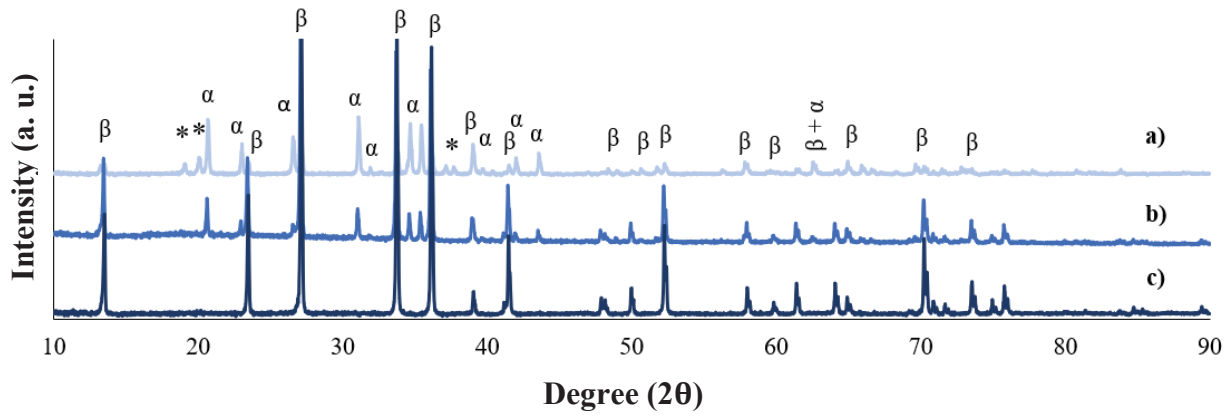

Fig. 4.2. XRD patterns of a) MgO-RBSN nitrided at 1425°C for 4 hr, b) MgO-RBSN heat-treated at 1700°C for 2 hr in SN powder bed and c) MgO-RBSN heat-treated at 1700°C for 2 hr in MgO-SN powder bed (α, β and * show peaks corresponding to α-Si_3N_4, β-Si_3N_4 and Si_2N_2O, respectively)

Table 4.1. Phase fractions and α/β-Si_3N_4 phase ratio of MgO-RBSN samples

Sample	Temp. (°C)	Dwell time (min)	Si_2N_2O	α-Si_3N_4	β-Si_3N_4	α/β-Si_3N_4
			wt.%			
MgO-RBSN	T= 1425	t= 240	14.8	51.6	33.6	1.5
MgO-RBSN heat-treated in SN	T= 1700	t= 120	0	13.5	86.7	0.15
MgO-RBSN heat-treated in MgO-SN	T= 1500	t= 10	0	17.8	82.2	0.21
	T= 1600	t= 10	0	13.8	86.2	0.16
	T= 1700	t= 10	0	0	100.0	0.00
	T= 1700	t= 120	0	0	100.0	0.00

The SEM micrographs of heat-treated MgO-RBSN samples in MgO-SN powder bed (**Fig. 4.3**) illustrate the microstructural development and phase transformation with temperature and exhibit a quite different morphology compared to the as-nitrided grains. For example, **Fig. 4.3-a** and **-b** reveal nucleation of fine equiaxed grains at 1500°C. These β-nuclei formed mainly because of the presence of impurities introduced from the starting silicon powder (i.e., O (≈ 1.3%), Fe (≈ 0.001%),

Al (< 0.001%) and C (< 0.1%) as reported by the manufacturer) which favored the formation of low-melting eutectics at T≤ 1500°C. Although in $MgO\text{-}SiO_2$ binary phase diagram the first eutectic liquid forms at T≈ 1543(50)°C [56], the presence of nitrogen gas and traces of impurities, notably Fe, could slightly lower the eutectic temperature [42]. The coexistence of about 82 wt.% β-Si_3N_4 with residual α-Si_3N_4 at this temperature results from the partial phase transformation and is illustrated in **Fig. 4.4** and **Table 4.1.**

At 1600°C, the content of α-phase, since it is a metastable phase, was reduced and the α/β-Si_3N_4 phase ratio decreased from 0.21 to 0.16 (**Fig. 4.4** and **Table 4.1**). Since the solution-precipitation process occurs by diffusion of dissolved species in the silicate liquid [41], increasing both the temperature and dwell time favors phase transformation and morphology modification. The presence of rods of various sizes suggests a grain growth mechanism which was proceeded by dissolution of fine rods and precipitation of coarse ones. Grain growth proceeded along both the c-axis and perpendicular to the prism planes (**Fig. 4.3-c** and **-d**). However, due to the continuous and faster growth kinetics of β-grains in the [001] direction compared to slower growth in the [210] direction, anisotropic angular grains with hexagonal morphology were formed [61, 138, 139]. Growth striations in **Fig. 4.5** seem to be evidence of the gradual precipitation, growth and coarsening mechanism of hexagonal crystals from the supersaturated liquid phase.

By increasing the temperature to 1700°C, the liquid-phase viscosity would decrease and its volume fraction increase, which led to complete phase transformation (**Fig. 4.4** and **Table 4.1**) and precipitation of elongated β-grains (**Fig. 4.3-e** and **-f**). The results of EDX analysis presented in **Fig. 4.3-f** and **Table 4.2** show the presence of high concentrations of magnesium and oxygen in the Si-Mg-O-N oxynitride glass. By extending the duration to 2 hr, the amount of liquid phase decreased by grain coarsening (**Fig. 4.1-f**), and, upon cooling, an amorphous thin layer of oxynitride glass containing Mg solidified and was heterogeneously distributed between the individual grains [140]. β-Si_3N_4 produced the struts of a porous structure and resulted in the formation of the highly interconnected pore channels.

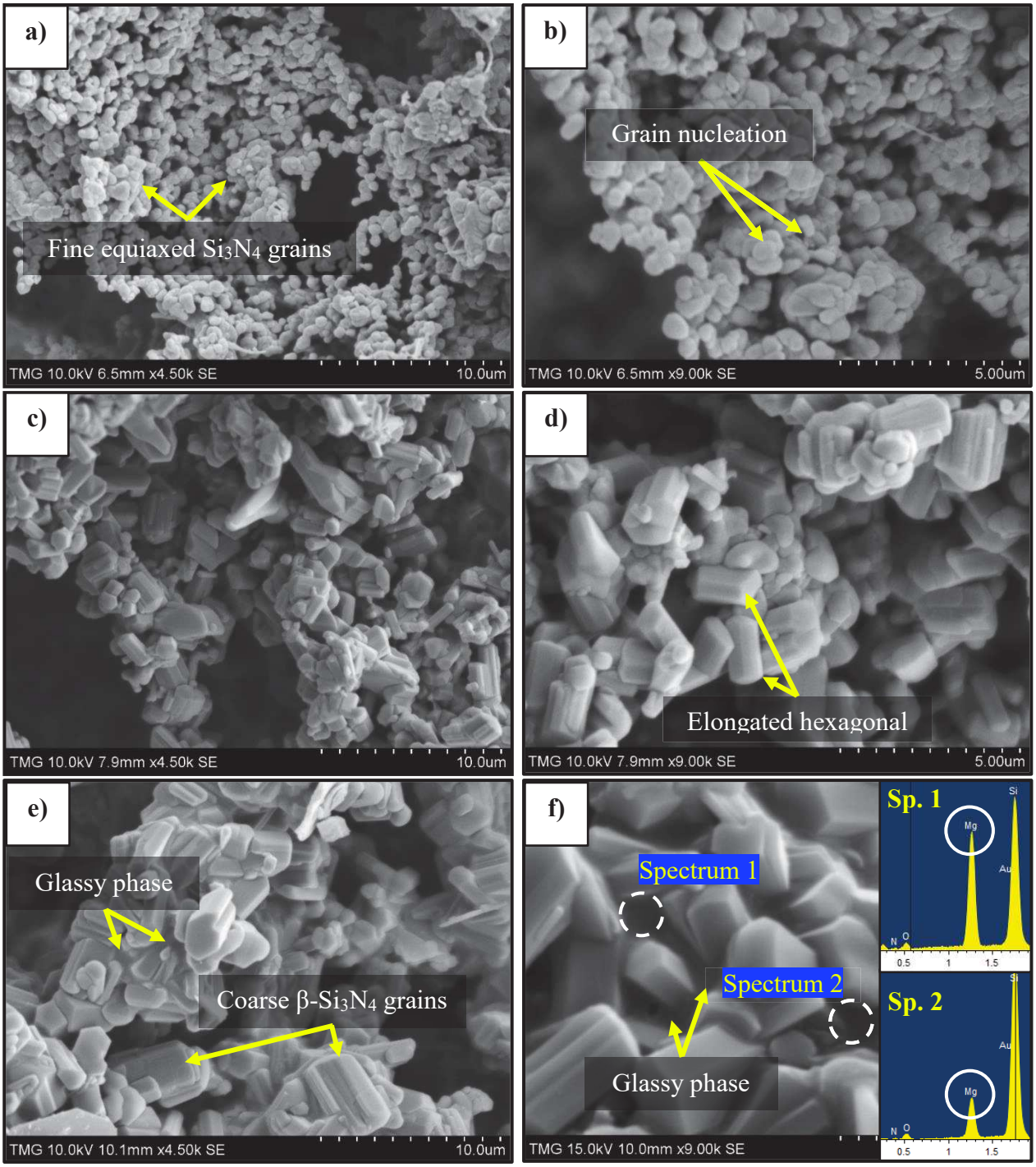

Fig. 4.3. SEM micrographs of heat-treated MgO-RBSN grains in MgO-SN powder bed at different temperatures for 10 min: a) and b) T= 1500°C, c) and d) T= 1600°C, e) and f) T= 1700°C

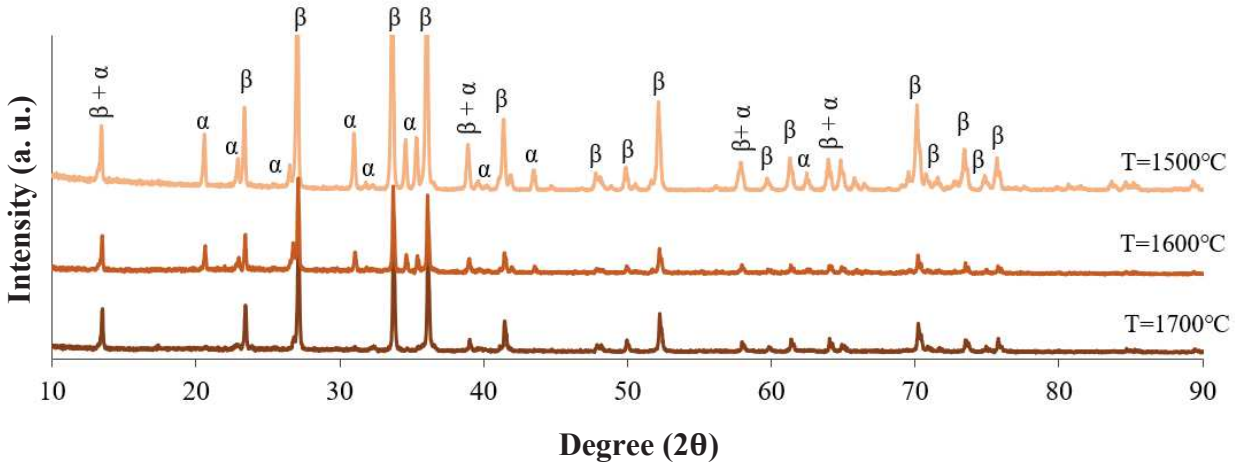

Fig. 4.4. XRD patterns of MgO-RBSN samples heat-treated in MgO-SN powder bed at different temperatures for 10 min (α and β show peaks corresponding to α- and β-Si_3N_4, respectively)

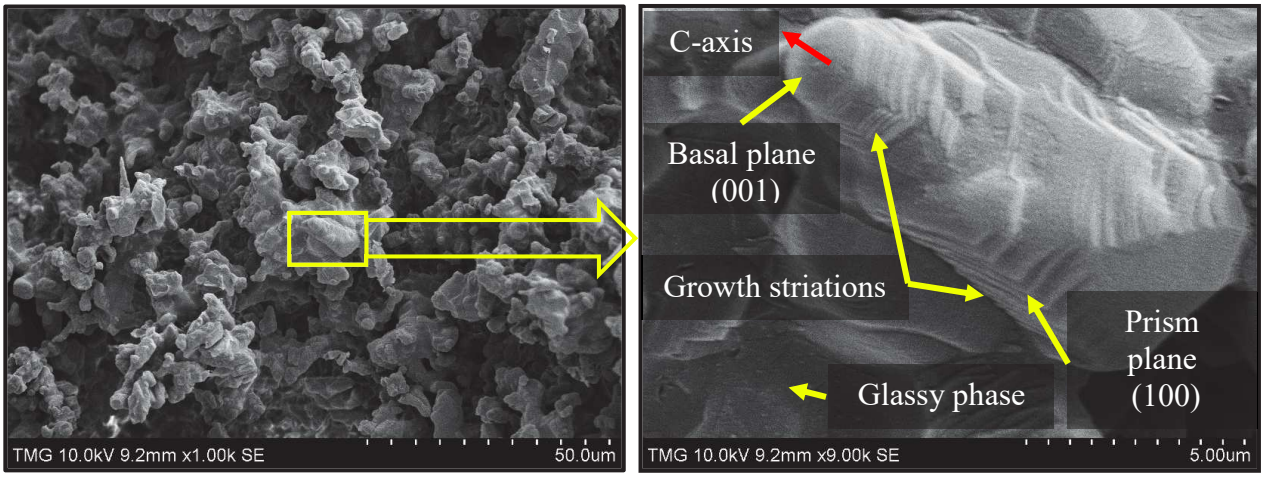

Fig. 4.5. Hexagonal striations illustrating the gradual precipitation, growth and coarsening mechanism of a rod-like crystals

Table 4.2. Results of EDX analysis

Spectrum	N K	O K	Mg K	Si K
	wt.%			
Fig. 4.3-f, Sp. 1	5.78	7.84	30.46	55.92
Fig. 4.3-f, Sp. 2	7.31	9.11	12.31	71.28
Fig. 4.6-a	27.96	2.40	---	69.64

Fig. 4.6-f	20.61	1.67	1.28	76.45
Fig. 4.8-e	28.59	3.33	0.46	67.62
Fig. 4.8-f	20.96	2.54	0.35	76.14
Fig. 4.11	2.29	49.10	21.90	26.23

4.3.2. Microstructural Observations of RBSN Samples

RBSN samples were prepared and heat-treated in a powder bed with and without MgO and then characterized by SEM-EDX and XRD. **Fig. 4.6-a** and **b** show that by excluding MgO from the starting powder, the microstructure of the porous sample is predominantly whiskers creating pores of various shapes. As microspheres with 10-40 µm diameters were employed as space holder/pore forming agents, large pores with spherical morphology were expected. Nevertheless, in ultra-pure nitrogen atmosphere, the dominant SiO (g) nitriding reaction by the vapor-liquid-solid (VLS) mechanism led to the formation of fine pores only with whiskers growing into the former large pores [20, 133]. The result of EDX analysis in **Fig. 4.6-a** and **Table 4.2** confirmed the co-existence of oxygen (≈ 2.40 wt.%) with silicon (≈ 69.64 wt.%) and nitrogen (≈ 27.96 wt.%) which suggests the formation of liquid puddles and dissolution of nitrogen and SiO gas for the growth of whiskers via LPS. Observation at higher magnification (**Fig. 4.6-b**) shows that the pore volume is blocked with elongated whiskers of various lengths (≤ 27 µm) and diameters (≤ 1 µm).

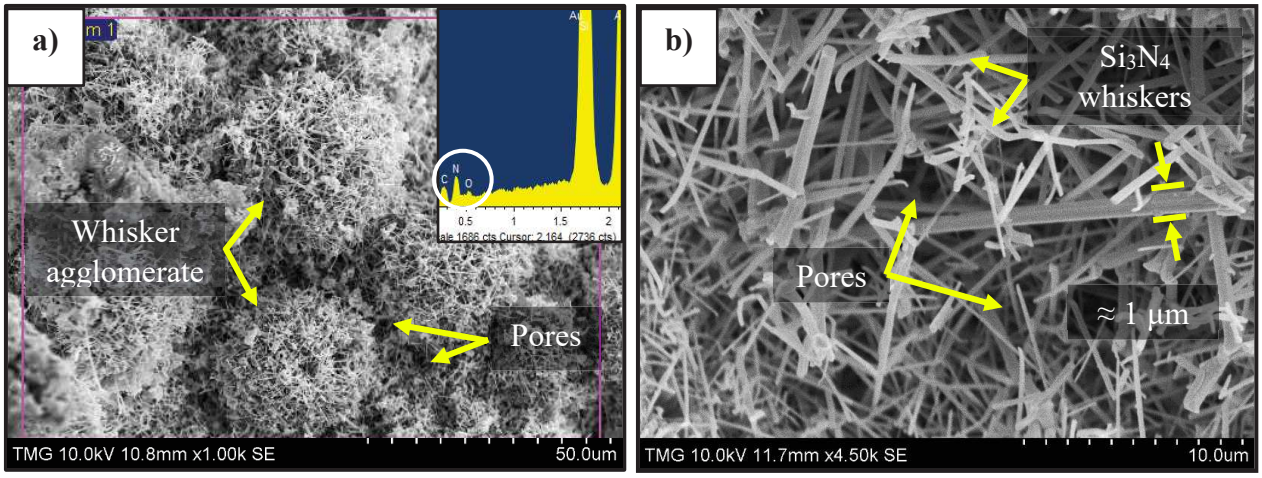

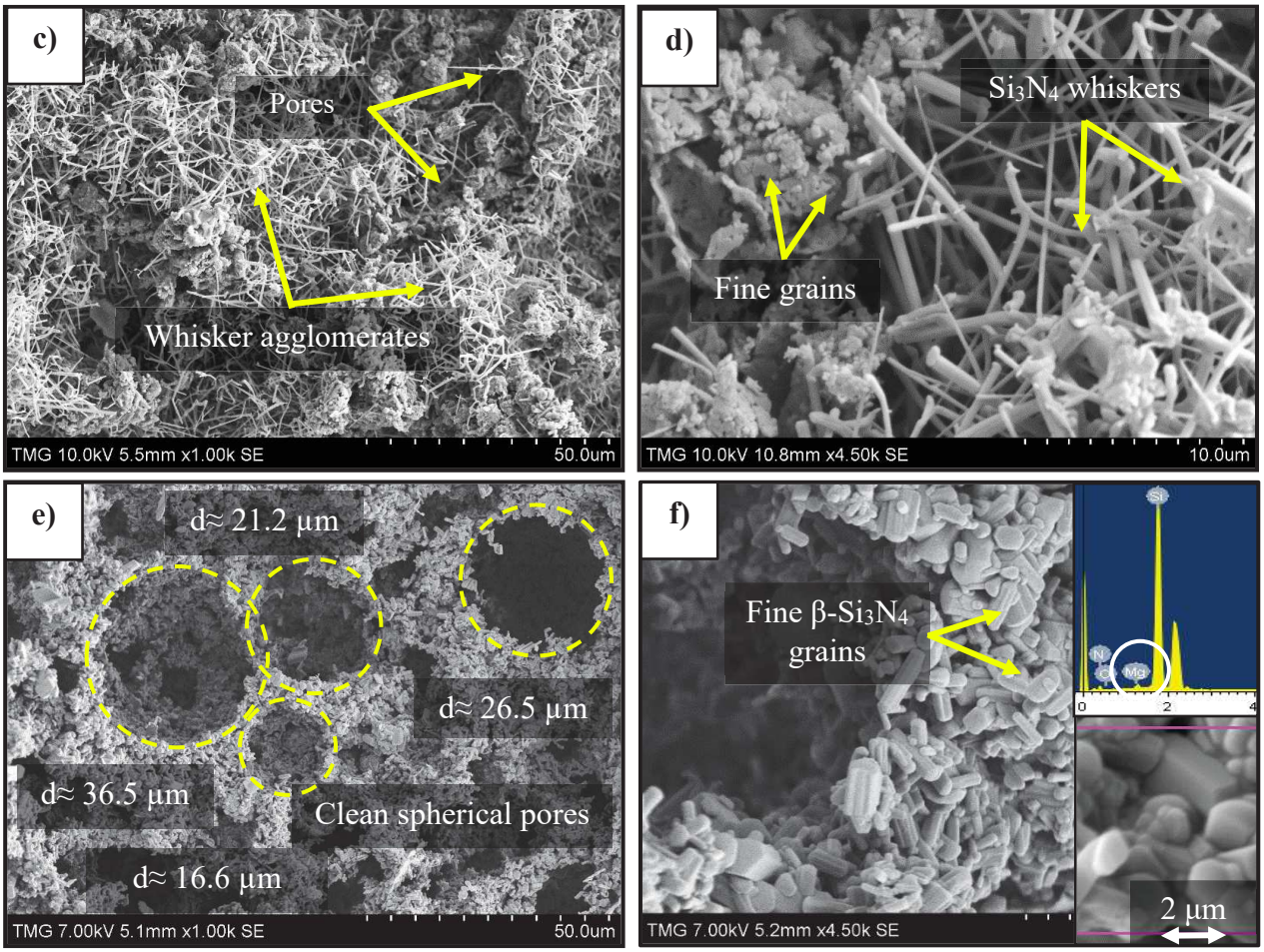

Fig. 4.6. SEM micrographs of various samples: a) and b) RBSN nitrided at 1425°C for 4 hr, c) and d) RBSN heat-treated at 1700°C for 2 hr in SN powder bed, e) and f) RBSN heat-treated at 1700°C for 2 hr in MgO-SN powder bed

The XRD analysis shown in **Fig. 4.7-a** and **Table 4.3** revealed the formation of 100% crystalline Si_3N_4 with the α-phase content of ≈ 27 wt.% and the α/β-Si_3N_4 phase ratio of ≈ 0.36. Although at temperature above 1410°C (melting point of silicon) liquid phase formation is accelerated and formation of β-Si_3N_4 as the dominant crystalline phase is encouraged [36], in the current research, complete nitridation of silicon and the formation of 100% silicon nitride product was not hindered. Local melting of silicon and incomplete nitridation mainly occur at high heating rate and in silicon compacts with relatively low porosity and especially in regions of accumulated oxide impurities [52]. It is worth mentioning that unlike dense and large silicon compacts which need long nitridation procedures (≥ 72 hr) [19, 41], in this open-pore cellular structure with high pore interconnectivity and high purity (99.995%), full nitridation of silicon occurred at 1425°C within

a few hours and no residual silicon was remained after 4 hr heating, as was confirmed by the XRD analysis in **Fig. 4.2** and **4.7**.

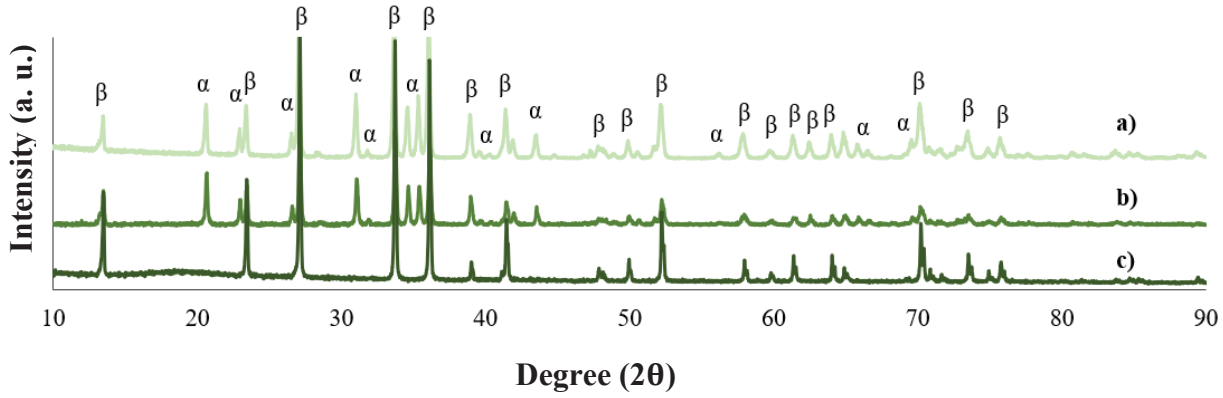

Fig. 4.7. XRD patterns of a) RBSN nitrided at 1425°C for 4 hr, b) RBSN heat-treated at 1700°C for 2 hr in SN powder bed and c) RBSN heat-treated at 1700°C for 2 hr in MgO-SN powder bed (α and β show peaks corresponding to α- and β-Si_3N_4, respectively)

The grain morphologies and the pore network structures of the RBSN heat-treated in SN powder bed are presented in **Fig. 4.6-c** and **d.** No major microstructural changes occurred upon heat-treatment, and the whisker and pore morphologies appear similar to those prior to heat-treatment. Only, occasionally, a lower whisker content was observed associated with fine equiaxed grains (**Fig. 4.6-d**). X-ray diffraction patterns presented in **Fig. 4.7-b** and **Table 4.3** show the presence of less α-Si_3N_4 with a slightly lower α/β-Si_3N_4 phase ratio and this is attributed to some liquid formation promoting partial phase transformation resulting from impurities introduced from the starting materials.

In contrast, porous RBSN samples produced in an MgO-SN powder bed (**Fig. 4.6-e** and **-f**) revealed an abnormal microstructural transition after heat-treatment. The morphologies of grains and pores changed drastically due to the elimination of the whiskers, creation of large whisker-free pores (**Fig. 4.6-e**, d< 40 μm), and precipitation of fine hexagonal β-rods (**Fig. 4.6-f** and **4.7-c**). However, no morphology change was observed in samples heat-treated in the same powder bed at 1300°C for 2 hr (**Fig. 4.8-a**) or at 1425°C for 10 min (**Fig. 4.8-b**). These observations suggest that the presence of MgO in the powder bed, high temperature heat-treatment and prolonged heating times were the three main factors favoring the morphological modification of whiskers.

At 1500℃ and 1600℃, **Fig. 4.8-c** and **-d**, which is close to the lowest eutectic point in the MgO-SiO_2 system, only a slight change in the morphology of whiskers was observed. In addition, at 1600℃ and 1700℃, the EDX analysis in **Fig. 4.8-e** and **-f** and **Table 4.2** detected the presence of Mg in the microstructure after 10 min heat-treatment. Considering that no MgO was added directly to the RBSN but knowing that magnesia has high vapor pressure at T≥ 1400℃, e.g., 10^{-4} Torr (≈ 1.3×10^{-6} atm) at 1600℃ [34, 56], the only explanation for the observed microstructural change must be the diffusion of MgO from the powder bed into the porous RBSN. Vapor phase transport of MgO through evaporation, diffusion away from its source, and condensation into the compact has been reported previously in the literature [34, 56]. Accordingly, with an inter-diffusion coefficient (D_{MgO}^{N2}) of 1.5×10^{-4} m^2 s^{-1} at 1550℃ at atmospheric pressure, the chance of a chemical reaction between silica and magnesia vapor is controlled by a) the diffusion rate of vapor species from their source through the nitrogen gas, b) the amount of surface silica in the RBSN and c) the temperature [56]. Therefore, after 2 hr heating in the MgO-SN powder bed, the content of Mg detected by EDX analysis increased to 1.28 wt.%, see **Fig. 4.6-f** and **Table 4.2**. Considering the accuracy limitation of EDX analysis for high porosity samples, the actual content of the deposited MgO could be even higher. Therefore, based on the microstructural evidence, MgO was introduced into the highly porous heat-treated RBSN structure by a vapor phase diffusion mechanism, which provided the driving force for α to β phase transformation and created a microstructure with spherical pores and open cavities (**Fig. 4.6-e**).

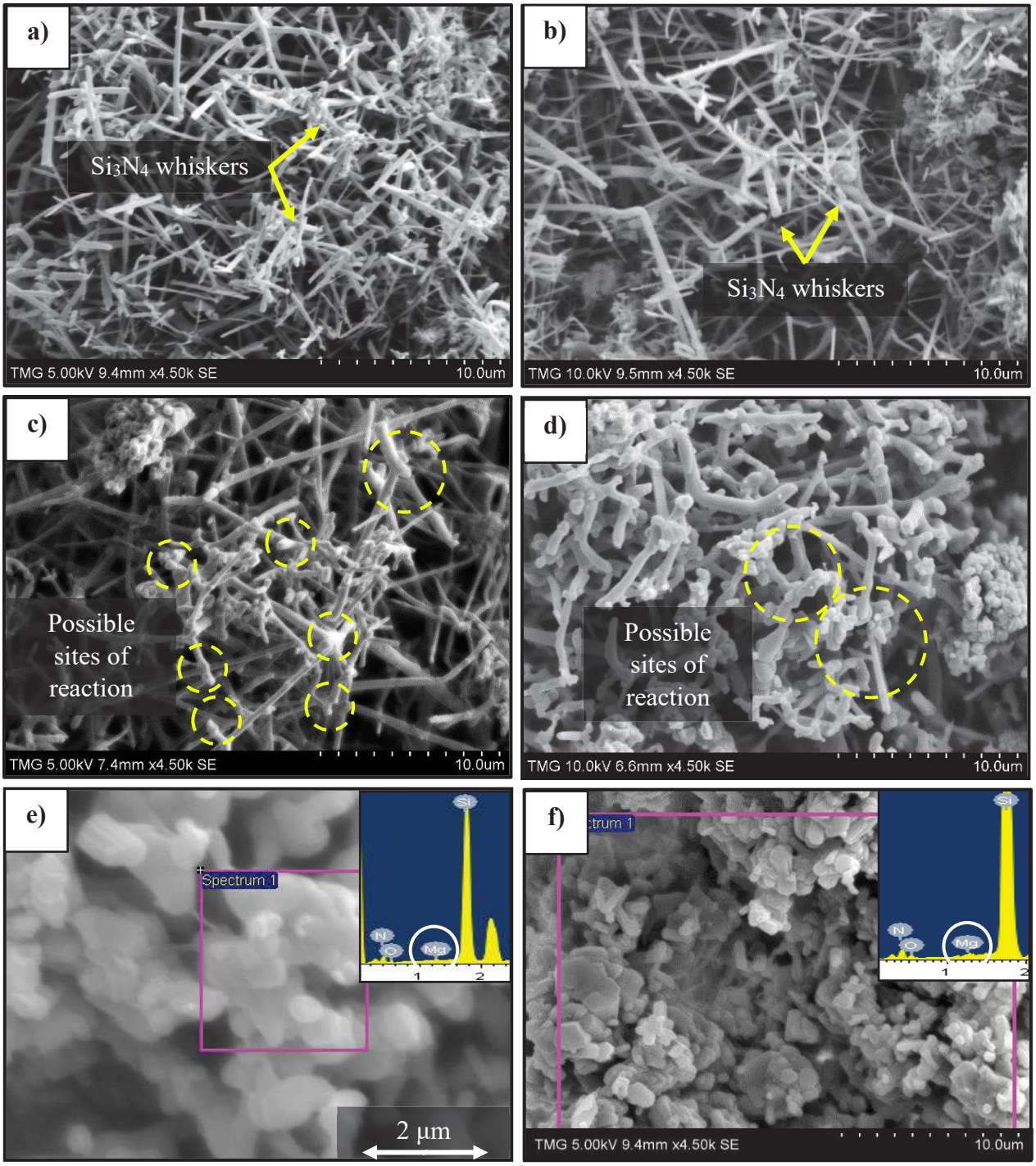

Fig. 4.8. SEM micrographs of heat-treated RBSN grains in MgO-SN powder bed for different temperatures and dwell times: a) T= 1300°C and t= 2 hr, b) T= 1425°C and t= 10 min, c) T= 1500°C and t= 10 min, d) and e) T= 1600°C and t= 10 min, and f) T= 1700°C and t= 10 min

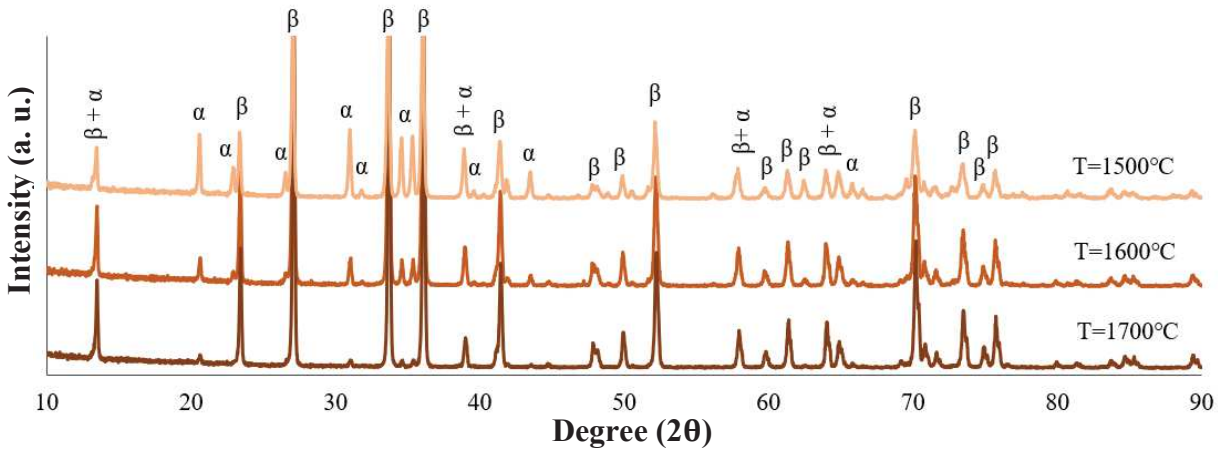

Fig. 4.9. XRD patterns of RBSN samples heat-treated in MgO-SN powder bed at different temperatures for 10 min (α and β show peaks corresponding to α- and β-Si_3N_4, respectively)

With a gradual decrease in α/β-Si_3N_4 phase ratio (**Fig. 4.9** and **Table 4.3**), the β-Si_3N_4 phase content was enhanced with increasing temperature. Furthermore, high surface area per unit volume of whiskers played a very critical role in accelerating the phase transformation and morphology change from α-whiskers to fully β-hexagonal rods. This is mainly explained by the fact that reducing the particle size gives rise to a higher content of surface silica and hence liquid phase [58], simultaneously increasing the Gibbs free energy of the system which enhances the sintering activity [34, 141].

While α-whiskers had a smooth surface and small cross-sectional area prior to phase transformation, the presence of small beads at the end of whiskers and bumps along the length of whiskers shown in **Fig. 4.8-c** and **-d** suggests VLS reaction sites. Therefore, with the gradual morphological transition (**Fig. 4.10-a** to **-c**), the α-whiskers to β-rods microstructural transformation reaction initiated at ≈ 1500°C, grains dissolved and fused together at ≈ 1600°C and re-precipitated as elongated β-hexagonal grains at ≈ 1700°C, showing a progressive coarsening mechanism associated with increase in temperature and heating time.

Based on the observed microstructures, beta grains in samples containing MgO both in the starting silicon and in the powder bed (**Fig. 4.1-f**) were coarser compared to those containing MgO only in the starting silicon (**Fig. 4.1-d**) or just in the powder bed (**Fig. 4.6-f**). The presence of high content of pre-existing β-crystals which coexist with the α-phase in the composition of RBSN (≈ 73 wt.%

β-Si_3N_4) led to the formation of a fine-grained microstructure in **Fig. 4.6-f**. When magnesia was only available in the starting silicon and not in the surrounding powder bed (MgO-RBSN heat-treated in SN powder bed, **Fig. 4.1-d**), a large fraction of that MgO could well be lost by evaporation; consequently, phase transformation and grain elongation were incomplete. In addition to the EDX analysis results shown in **Table 4.2**, deposition of a considerable amount of crystalline $MgSiO_3$, shown in **Fig. 4.11**, confirmed the high vapor pressure of MgO during heat-treatment. This deposition was also observed on the water-cooled furnace insulators after running several heating cycles under ultra-high purity nitrogen.

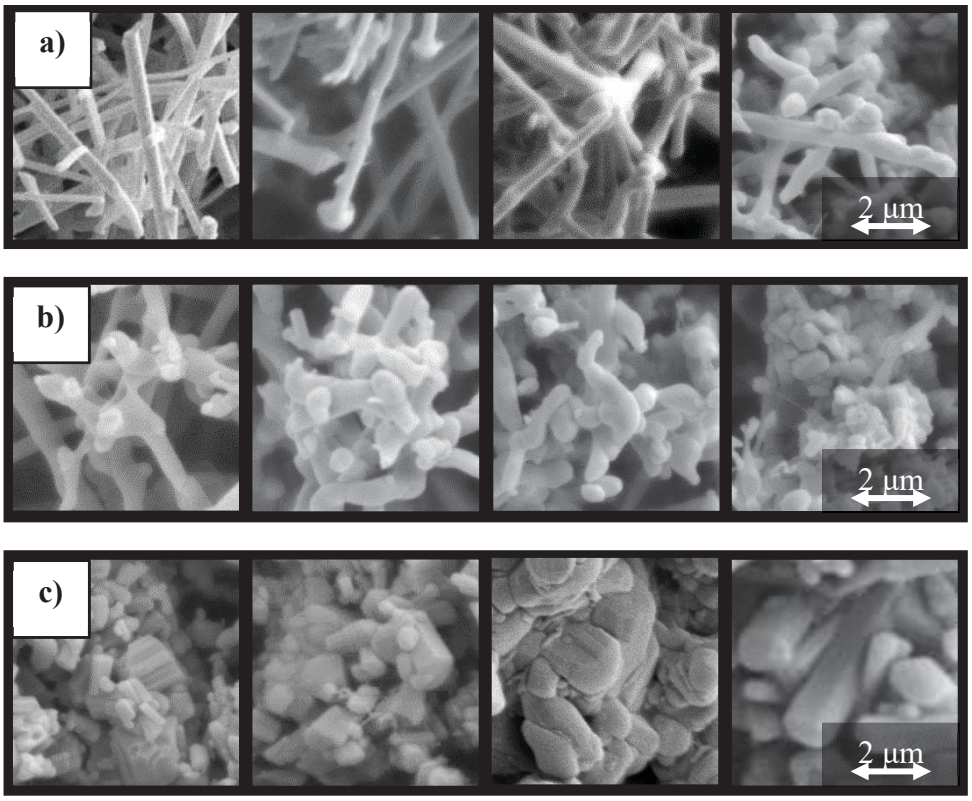

Fig. 4.10. Morphology development from whiskers to hexagonal grains: a) initiation of the reaction, b) solution and nucleation, c) precipitation and grain growth with increasing the heating temperature and time

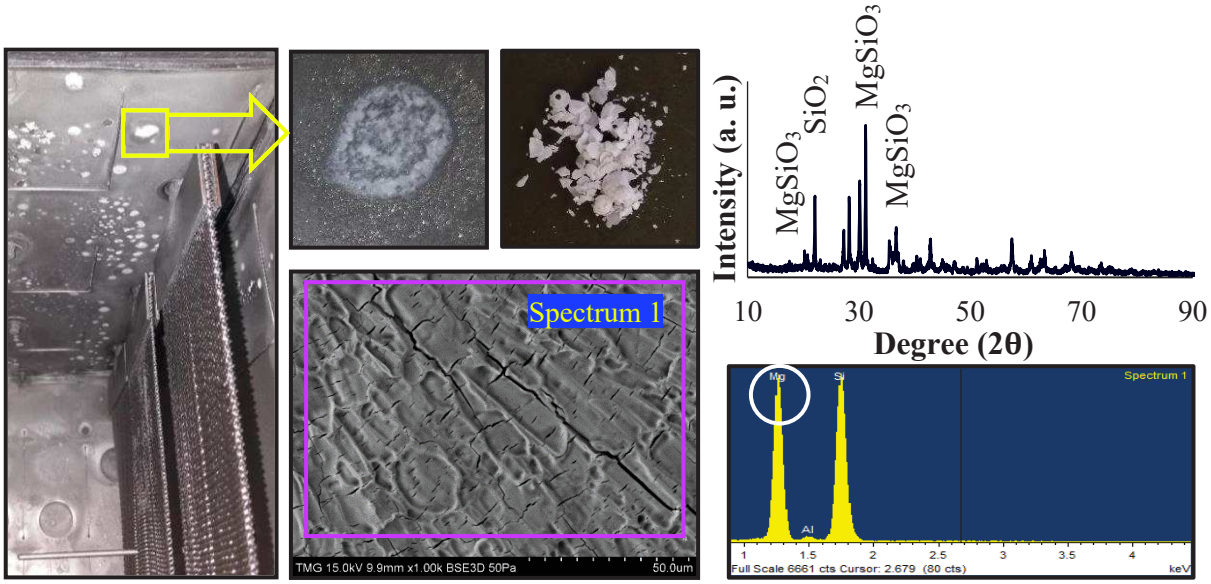

Fig. 4.11. XRD and EDX analyses showing the deposition of MgO-containing phase on the water-cooled furnace insulators

Table 4.3. Phase fractions and α/β-Si_3N_4 phase ratio of RBSN samples

Sample	Temp. (°C)	Dwell time (min)	α-Si_3N_4	β-Si_3N_4	α/β-Si_3N_4
			wt.%		
RBSN	T= 1425	t= 10	27.0	73.0	0.36
RBSN heat-treated in SN	T= 1700	t= 120	26.0	74.0	0.35
RBSN heat-treated in MgO-SN	T= 1500	t= 10	24.1	75.9	0.31
	T= 1600	t= 10	8.0	92.0	0.08
	T= 1700	t= 10	1.7	98.2	0.01
	T= 1700	t= 120	0.0	100.0	0.00

4.3.3. Linear Shrinkage and Weight Losses During Heat-treatment

To illustrate how the presence of MgO in the starting silicon and/or the powder bed affects the properties of the porous heat-treated samples, the average linear shrinkages and changes of mass are plotted in **Fig. 4.12** and **4.13**, respectively. The differences in the shrinkage of samples embedded in powder bed with or without magnesia showed the impact of powder bed composition

on the high temperature densification behavior. The lowest linear shrinkage of ≈ 0.4% corresponds to RBSN heat-treated in a SN powder bed. This almost negligible shrinkage is attributed to mostly solid-state reactions.

During LPS, when early liquid forms, densification starts through two stages of particle rearrangement and solution-precipitation [142]. The contact flattening and the pore filling are the two main theories explaining LPS densification [37]. Upon adding MgO to the starting silicon (MgO-RBSN) and heating to 1700°C, a eutectic melt formed, and shrinkage increased to ≈ 1.2%. Shrinkage was further enhanced to ≈ 1.5% when MgO was also introduced into the powder bed, since MgO vapor suppressed the decomposition and loss of liquid. The most significant densification, however, occurred in RBSN sample embedded in MgO-SN powder bed, which is in agreement with the microstructural observations. Meanwhile the driving force for sintering and shrinkage is by lowering the free surface area and energy of the system, the samples with finer silicon nitride particles experienced the highest shrinkage. With fine needle whiskers, a greater driving force would have been generated [42], which created the maximum shrinkage of ≈ 2%.

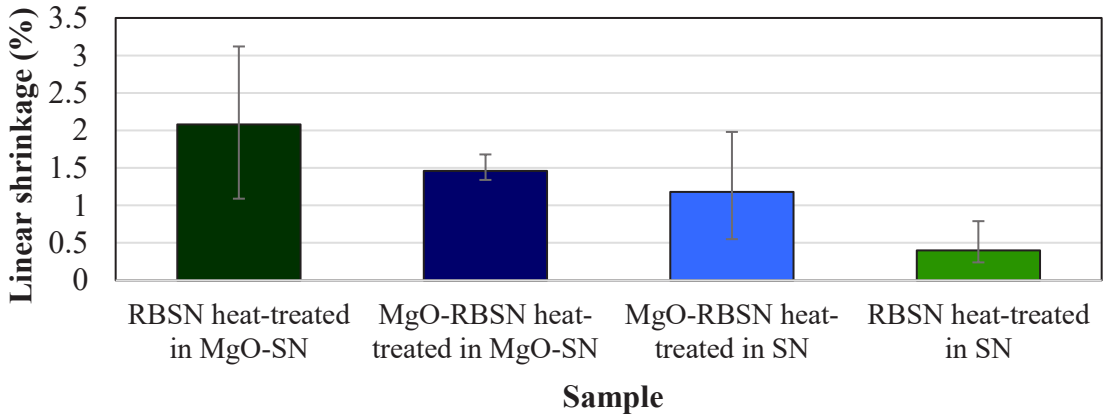

Fig. 4.12. Linear shrinkages of heat-treated samples

Mass changes shown in **Fig. 4.13** were generally negative and caused by thermal decomposition and evaporation of volatile species [42, 143]. Therefore, for RBSN embedded in a SN powder bed, the average weight loss of ≈ 1.7 wt.% arose as a result of decomposition of $Si_3N_4 \rightarrow 3Si + 2N_2\uparrow$ at 1700°C [34]. However, RBSN ceramics heat-treated in MgO-SN powder bed showed the lowest weight loss with an average of ≈ 0.4 wt.%. This negligible amount suggested that the weight loss by Si_3N_4 decomposition was possibly compensated by vapor phase diffusion from the powder bed

and some oxidation which subsequently decreased the overall weight losses. This is in agreement with the linear shrinkage and the SEM-EDX observations of the heat-treated RBSN samples. Upon addition of magnesia to the starting silicon, the weight loss of MgO-RBSN generally increased by liquid eutectic formation and thermal decomposition. The high vapor pressure of MgO at this temperature suggests that the observed weight loss was not entirely due to the thermal decomposition of silicon nitride. Hence evaporation and decomposition of MgO partially contributes to the weight loss [34] up to the maximum of ≈ 3 wt.%.

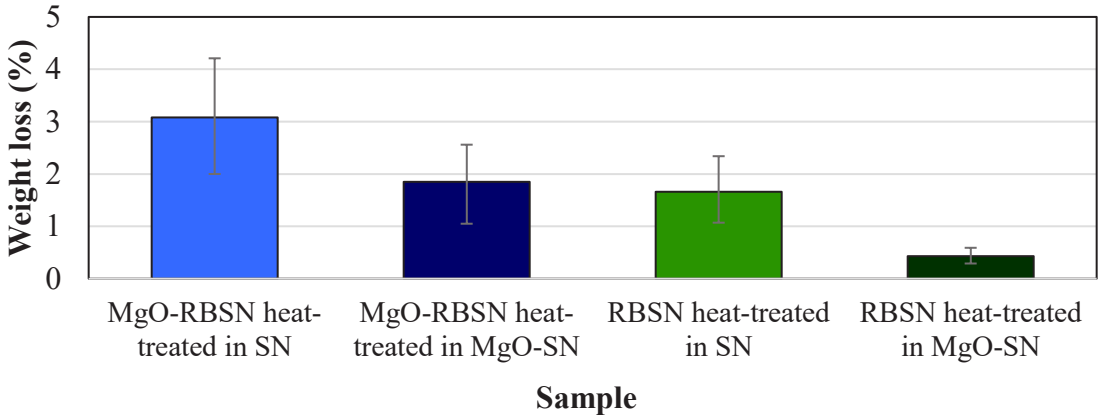

Fig. 4.13. Weight losses of heat-treated samples

4.3.4. Porosity and Compressive Strength Measurements

Porosity measurements and compression tests were carried out on porous ceramics heat-treated in various powder beds at 1700°C for 2 hr and the results are illustrated in **Fig. 4.14** and **4.15**, respectively. It is clearly apparent in **Fig. 4.14** that samples which have been heat-treated in MgO-SN powder bed demonstrate lower porosity compared to those heat-treated in SN-only powder bed. A decrease in the porosity content in this case can be attributed to the presence of MgO in the powder bed and would confirm that diffusion of MgO vapor from the powder bed had occurred during the heat-treatment process, as discussed previously. This would enhance the liquid phase formation during the LPS mechanism and thus increase the densification and linear shrinkage as observed in **Fig. 4.12**. The difference in the porosity content for samples heat-treated in two different powder beds became even more pronounced in RBSN ceramics as compared to MgO-RBSN. In the presence of eutectic liquid phase, in addition to the sintering process, phase transformation and precipitation of β-phase are accelerated [58]. Accordingly, microstructural

transition from elongated whiskers to fine hexagonal grains during the heat-treatment process led to a high linear shrinkage (≈ 2%) and resulted in a high densification and a low porosity content (≈ 30 vol.%).

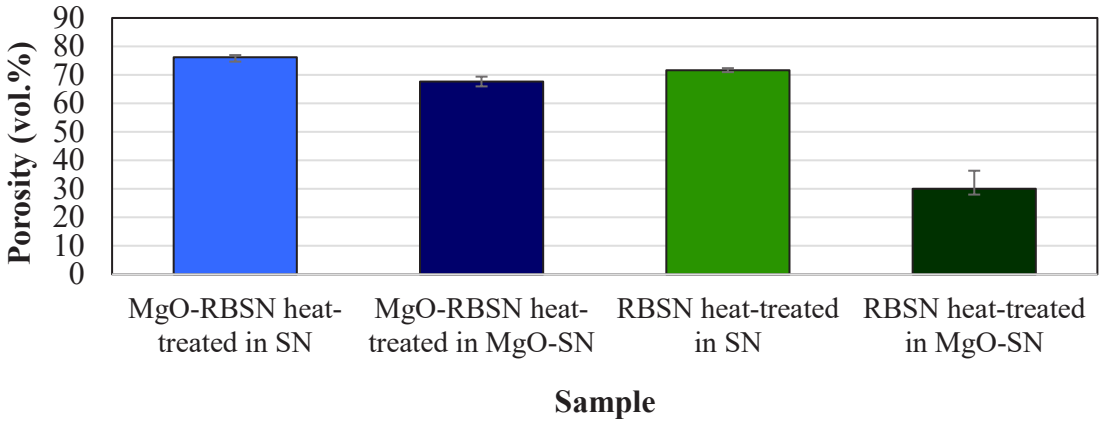

Fig. 4.14. Porosities of heat-treated samples

It is widely acknowledged that in porous structures, mechanical strength is increased as the porosity content decreases. Accordingly, based on **Fig. 4.15**, with variation of porosity, the samples generally had compressive strengths of ≤ 10 MPa and the strength reached the highest value at the lowest porosity content, i.e., 30 vol.%.

Additionally, the mechanical properties of porous Si_3N_4 would be affected by grain morphologies, so that whiskers with high aspect ratio can act as reinforcements and increase the strength by crack bridging or crack deflection [58, 111]. Consequently, in ceramics with porosity of ≥ 67 vol.%, mechanical strength was below 2.5 MPa when the microstructure was dominantly granular grains, whereas strength has been enhanced to ≈ 4.1 MPa when elongated whiskers grew in the microstructure (RBSN heat-treated in SN). These results suggest that the post heat-treatment process in the presence of MgO could potentially be used to control the microstructure of porous reaction bonded silicon nitride ceramics which is critically important in improving the strength and the performance of the structures.

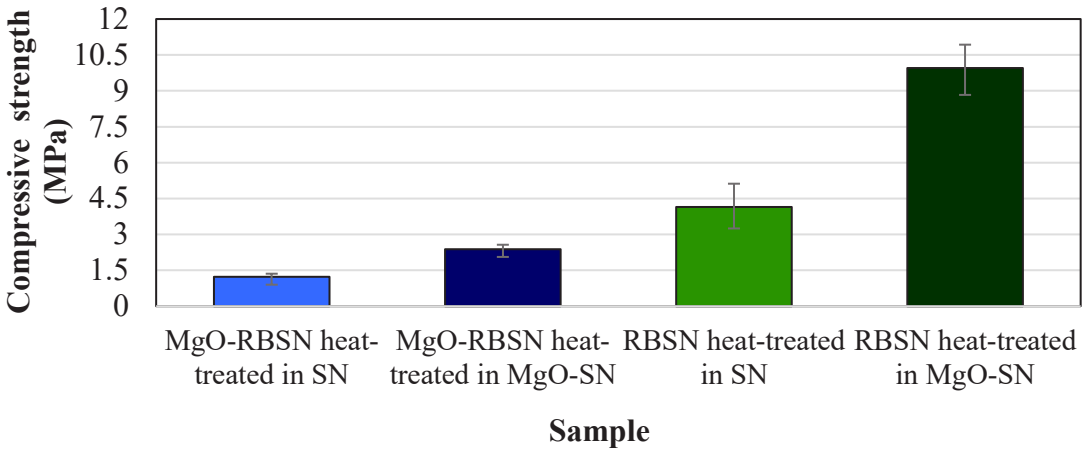

Fig. 4.15. Compressive strengths of heat-treated samples

4.4. Conclusion

The effect of MgO additions to the starting silicon powder or to the powder bed on the microstructural transition of porous RBSN was studied. In the presence of MgO in the starting silicon, a porous structure with granular α-matte and clean spherical pores was obtained. However, excluding MgO from the starting silicon, the ceramic exhibited a microstructure composed of interconnected α-Si_3N_4 whiskers.

Unlike for the case of a simple SN powder bed, when samples were heat-treated in a MgO-SN powder bed, α-whiskers gradually dissolved at ≈ 1500°C and re-precipitated as fine β-grains at ≈ 1700°C, which created clean, spherical and large pores. The results of SEM-EDX observations along with XRD analysis suggested that the observed microstructural transitions were due to the vapor phase transport of MgO from the powder bed which coincided with a gradual decrease in α/β-Si_3N_4 phase ratio and corresponding grain growth. Hexagonal grains coarsened significantly when MgO was introduced both into the starting silicon and into the powder bed. Otherwise, very fine-grained microstructures with homogeneous grain size were formed.

The linear shrinkage and densification increased upon the heat-treatment of samples embedded in a MgO-SN powder bed, especially in the presence of whiskers with high aspect ratio which led to approximately 2% shrinkage. This sample showed the lowest weight losses and porosity possibly due to the diffusion of vapor species from the powder bed.

The compressive strength of the heat-treated ceramics with porosity varying from ≈ 30 vol.% to ≈ 76 vol.% was ≤ 10 MPa. The specimens heat-treated in powder bed containing MgO exhibited lower porosity and thus higher strength than those heat-treated in SN powder bed alone. Additionally, in highly porous ceramics, the presence of Si_3N_4 whiskers resulted in a self-reinforced microstructure with strength of ≈ 4.1 MPa.

These observations confirmed that the microstructure of Si_3N_4 grains and pores, the liquid phase sintering process and the resultant properties were highly sensitive to the composition of the surrounding powder bed and suggest that powder bed technology can be adopted as a post heat-treatment approach to modify the microstructure of porous RBSN containing no additive.

Chapter 5. Pore Structure, Porosity and Compressive Strength of Highly Porous Reaction Bonded Silicon Nitride Ceramics with Various Grain Morphologies

Raheleh Nikonam M.[a,*], Martin D. Pugh[a], Robin A.L. Drew[a]

[a] Department of Mechanical, Industrial and Aerospace Engineering, Concordia University, Montreal, CANADA, H3G 1M8

*corresponding author: r_nikona@encs.concordia.ca

This article has been published in the Journal of Materials Science, 55 (2020) 509-523, https://doi.org/10.1007/s10853-019-04078-3

Abstract

Complex characteristics of the pores and properties of porous reaction bonded Si_3N_4 have been investigated and correlated to the microstructure of Si_3N_4 grains. Porous ceramics with porosities of ≤ 75 vol.% and α-Si_3N_4 matte grains (α/β phase ratio of 1.5) or α-Si_3N_4 whiskers (α/β phase ratio of 0.36) were prepared by in-situ nitridation of silicon powder. To obtain various microstructures by α→β-phase transformation and grain morphology modification, samples were heat-treated at 1700°C while embedded in a Si_3N_4 powder bed containing MgO. By the growth of α-matte or β-Si_3N_4 grains on the pore walls, highly interconnected structures with spherical cavities and unimodal pore size distributions resulted with d_{50}≈ 8.8 μm and ≈ 6.5 μm, respectively. In contrast, α-whiskers grew inside the pore cavities, thus complex and irregular inter-particle pores appeared which generated an extra peak near d_{50}≈ 1 μm forming a bimodal pore size distribution. Compared to the α-matte grains, α-whiskers densified upon heat-treatment and produced a large drop in porosity, which resulted in a structure with less interconnectivity. As a consequence of growth of fine β-rods, pore walls became relatively smooth and whisker-free, thus inter-cluster channels were modified to spherical cavities with d_{50}≈ 3.7 μm. Samples exhibiting networked whiskers and fine pores, or low porosity demonstrated higher compressive strength than the interconnected structures with spherical cavities.

Key words:

Si_3N_4 grain morphology; Pore structure; Pore size distribution; Porosity; Compressive strength

5.1. Introduction

Porous silicon nitride (Si_3N_4) ceramics have been employed in a wide range of applications, especially when high thermal insulation, chemical inertness, high permeability or lightweight are required [144, 145]. Examples of applications are diesel particulate filter (DPF), water purification, catalyst and membrane support, wave-transparent materials, acoustic absorbent, refractory linings and bio-implants [73, 108, 146, 147]. To possess the required properties for a particular application, the microstructural characteristics of porous Si_3N_4 need to be carefully designed as the performance of a cellular body is closely correlated to the geometric features of grains, pore shape, size and volume, as well as channel interconnectivity and mechanical strength [71, 73, 146, 148]. For instance in bone scaffolds, large pores, that is to say of diameters of 50-500 μm, and porosities of 40-90 vol.% are beneficial as they provide free spaces for bone in-growth and vascularization [40, 100, 149-151]. In contrast, cellular materials with pores of diameters of 1-15 μm and porosities of 30-45 vol.% have shown sufficient mechanical strength to be suitable candidates for ceramic membrane supports [152]. Fine pores having diameters of 0.1-1 μm and 0.1-10 μm are of interest as freshwater membranes and hot gas filters, respectively [46, 153, 154]. In ceramic-metal composites, interconnectivity of the ceramic and metal phases are essential [155, 156] and in battery electrodes or aerospace fluid storage tanks continuous transport of fluids through the pore channels and advancement of reactions are required [103]. Those will be guaranteed by a structure providing: high interconnectivity, high porosity and pores with appropriate dimensions [157, 158]. Accordingly, to meet the stringent target requirements, the ability to design and customize the microstructural characteristics of porous Si_3N_4 is vital.

Depending on the application being considered, several processing routes such as combustion, aqueous gel casting, cold isostatic pressing and freeze-casting have been recently employed in the production of foams [39, 76, 159]; however developing an economical, tightly controlled fabrication process that simultaneously satisfies all requirements has so far been extremely challenging. Direct nitridation of Si powder is a reliable and cost-effective route for the mass production of porous reaction-bonded silicon nitride (RBSN) [53]. Altering the fabrication conditions or using oxides additives in a post heat-treatment process leads to the formation of α- and β-Si_3N_4 grains with hexagonal structure and with various morphologies [20, 22, 36, 41, 62]. Post sintering of MgO-containing Si_3N_4, for instance, has been extensively applied in the

production of β-Si_3N_4 with enhanced grains interlocking [51, 62, 64]. Along with the traditional powder mixing technology, magnesia has been introduced to the RBSN microstructure via vapor phase transport from a surrounding Si_3N_4 powder bed. High temperature and high vapor pressure of this additive ensures mobility and diffusion of magnesia which is then followed by a reaction with protective natural silica at $T_e \approx$ 1548°C favouring densification [34, 56, 160]. In order to fabricate a porous structure having macro-pores, adding fugitive organic pore-forming agents such as spherical-shaped polymethyl methacrylate beads (PMMA) combined with gel casting process are practical solutions [3, 19, 161-163]. By employing this technique, density can be as low as 0.4 g cm^{-3} [19], therefore grain morphology, porosity, density and pore size should be precisely controlled as they play a crucial role in governing the mechanical response [75, 164].

Study of the fabrication and designing of porous reaction bonded based silicon nitride ceramics, especially in combination with post heat-treatment, has received increasing attention. Nevertheless, many investigations focused on the effect of fabrication variables on the grain formation mechanisms [133, 160], porosity content or foam strength [7, 11, 16-18, 47]. In most of these studies, the complex microstructure of pores was neglected and no detailed investigation of the relationship between RBSN grain morphology and pore size distribution or pore morphology was reported.

The principle objective of the current study was to clarify the influence of Si_3N_4 grain microstructure on variations of pore structure, morphology and size, as well as porosity, density and compressive strength of porous reaction bonded Si_3N_4 ceramics. To fabricate porous samples with potential applications in environmental filters, membrane supports and ceramic infiltrated metal composites, PMMA pore formers with particle size of < 40 μm have been applied. Various distinct microstructures were obtained by the use of MgO as an oxide additive, direct nitridation of silicon powder at 1425°C, and a post heat-treatment process at 1700°C while samples were embedded in a powder bed. In this work, the morphology of grains and the α/β phase ratio were correlated to the structure and morphology of pores using XRD, TGA and SEM analyses. Pore size distribution, porosity, density and weight loss were determined by mercury intrusion porosimetry (MIP), Archimedes' technique and mass measurements. Interconnectivity of channels was observed using non-destructive X-ray computed tomography (micro-CT) and strength of cylindrical samples were measured in compression and correlated to the samples' properties.

5.2. Sample Preparation and Characterization

We have followed the fabrication method described in literature [19] where acrylamide (AM, $C_2H_3CONH_2$, Sigma-Aldrich) as the monomer, and N,N'-methylenebisacrylamide (MBAM, $(C_2H_3CONH_2)_2CH_2$, Sigma-Aldrich) as the crosslinker, along with DS001 (Polymer Innovations Inc.) as the dispersant, and Poly(acrylamide) (PAM, Acros Organics, M.W. = 5,000,000 6,000,000) as the binder were used. DF002 (Polymer Innovations Inc.) was added as the antifoaming agent to stop formation of any air bubble. PMMA beads (Microbeads) of three particle sizes, 10, 20 and 40 μm, was used in the same weight proportions as space holder. The beads were very smooth and almost perfectly spherical and were dispersed in DI water along with silicon powder (99.995%, -8 μm, ABCR) with the weight ratio of PMMA: Si: H_2O equal to 44: 16: 40. To fabricate porous RBSN samples with magnesia (labeled as MgO-RBSN), 12 wt.% MgO powder (> 99% trace metals basis, -325 mesh, Sigma-Aldrich) was added to the suspension. To decrease hydrogen release and silicon oxidation through $Si\ (s) + 2H_2O\ (l) \rightarrow SiO_2\ (s) + 2H_2\ (g)$ and also to increase the stability of the suspension, pH was adjusted to 8.5 using 1N NH_4OH and HNO_3, whereupon a strong repulsion between particles exists [19]. Then, the solution was mixed thoroughly by milling, the pH was readjusted, and the suspension was de-aired under vacuum to remove any air bubbles. Ammonium persulfate (APS, $(NH_4)_2S_2O_8$, Sigma-Aldrich) and N,N,N',N'-tetramethylethylenediamine (TEMED, $C_6H_{16}N_2$, Sigma-Aldrich) were added afterwards as the free radical initiator and catalyst, respectively. The slurry was then cast into cylindrical molds (d≈ 14.28 mm and h≈ 20 mm), left at 50°C for 3 hr to polymerize and then demolded and dried at 120°C for 5 hr. Polymer and binder burn out occurred by heating the samples at 525°C for 2 hr. Porous samples were nitrided for 4 hr under flowing ultra-high purity nitrogen (99.999%, O_2< 2ppm, H_2O< 3ppm, THC< 0.5 ppm) at a temperature of 1425°C. To prepare a powder bed containing MgO, (labeled as "MgO-SN"), 12 wt.% magnesia was added to a 1:1 weight ratio silicon nitride-boron nitride mixture ("SN" powder bed). Subsequently, samples were embedded in a SN or MgO-SN powder bed and were heat-treated at 1700°C for 2 hr.

Phase compositions were identified by X-ray diffractometry (XRD; X'Pert Pro, PANalytical) using Cu Kα radiation at accelerating voltage of 40 kV and anode current of 45 mA. α/β-Si_3N_4 phase ratio was determined based on the ratio of $I_{\alpha(210)} + I_{\alpha(102)} / I_{\beta(101)} + I_{\beta(210)}$ where I is the height of different (hkl) peaks for α and β-Si_3N_4. Grains and pore morphologies were observed using

scanning electron microscopy (SEM, Hitachi, S-3400 N). Mercury intrusion porosimetry (MIP) was used to characterize the pore size distribution. Samples were placed in the pycnometer and permeated with mercury under increasing pressure. Maximum applied pressures for this analysis was 33 ksi (≈ 227 MPa) with the capacity of measuring up to 6 nm pores. The parameters in the Washburn equation for mercury surface tension and contact angle, ϕ were 0.48 N m^{-1} and 130˚, respectively. X-ray microtomography (SkyScan 1172, camera pixel of 3 μm) was used to characterize the interconnectivity of channels by reconstructing 3D images of a layer of 116 um thickness. Average porosity and density of five samples were measured based on Archimedes' technique, ASTM C373-88 standard. The average weight losses of heat-treated samples were measured using seven identical samples. The thermal degradation of samples was investigated by thermogravimetric analysis (TGA, Q50 V6.7) at a constant heating rate of 10℃ min^{-1} under pure nitrogen gas (99.99%) and up to its maximum temperature of 600℃. Cylindrical samples were tested in compression using an Instron-3382 Universal Testing machine at a constant crosshead speed of 0.5 mm min^{-1} until failure occurred. The relative quantity of impurities in the starting silicon and magnesium powder were determined with inductively coupled plasma mass spectrometry (ICP-MS) after digesting the powders in a mixture of HNO_3 and HCl with a relative ratio of 1:3 ratio at 110℃.

5.3. Results and Discussion

5.3.1. Morphology of the RBSN Grains

It is well known that the microstructure of reaction bonded Si_3N_4 can be a mixture of various grain types which is determined by the composition of the starting materials, synthesis process and heating temperature [22, 41]. The formation mechanisms of porous reaction bonded Si_3N_4 has been studied in detailed previously to illustrate grain developments at T ≥ 1250℃ into α and β structures via gaseous phase reaction and solid or liquid phase reaction, respectively [133]. As schematically illustrated in **Fig. 5.1a,** α-whiskers with high aspect ratio (> 25) [20] grow mainly inside the porosity or attached to other grains and occupy the pore cavities, while α-matte grains with irregular shape and various grain sizes deposit on pore walls and resulted in clean cavities (**Fig. 5.1b**)**.** Similar to α-matte, β-Si_3N_4 grains grow on pore walls but with the morphology of coarse elongated rods (**Fig. 5.1c**) or fine granular nuclei (**Fig. 5.1d**) [133]. The formation of the latter grains with relatively the same particle size occurs during the initial stages of the solution-

precipitation mechanism in the liquid phase sintering reaction and when β-rod formation is not yet initiated [160].

The SEM micrographs of Si_3N_4 resulting from a reaction bonding process at 1425°C and subsequent post heat-treatment at 1700°C in the presence and absence of MgO are summarized in **Fig. 5.2**. These microstructures along with the results of XRD analysis in **Fig. 5.3** and **Table 5.1** illustrate that the α-Si_3N_4 matte (**Fig. 5.2a**) with an α/β-Si_3N_4 ratio of 1.5 was the predominant grain morphology in the presence of MgO in the starting powder. In contrast, a microstructure with whiskers (**Fig. 5.2d**) and α/β-Si_3N_4 ratio of 0.36 was formed during direct nitridation of silicon powder when MgO was absent. MgO with its high vapor pressure at elevated temperatures increases the content of oxygen and, according to the relationship of $p(SiO)/p^\circ$ and $p(O_2)/p^\circ$ in the Si-O system, decreases the stability and content of SiO vapor species in the surrounding atmosphere [55, 124]. Both silicon vapour and oxygen impurity encourage the formation of α-matte grains and enhance the ratio of α/β-Si_3N_4 [133]. Accordingly, the former microstructure with higher α/β phase ratio was developed mainly by nitridation of Si (g) and in the presence of oxygen impurity generated from the oxide additive while the latter formed via a reaction between nitrogen and SiO (g) in ultra-pure nitrogen atmosphere [133]. No residual silicon was detected in any of the microstructures.

During post heat-treatment at T≥ 1450°C, mobility of MgO and subsequent diffusion from a powder bed into the porous RBSN microstructure was proven previously [34, 56, 160]. Through a reaction with surface SiO_2, MgO (present in the starting powder mixture or diffused from the powder bed) encourages liquid phase formation at 1700°C which dissolves α-Si_3N_4 and forms β-Si_3N_4 in the solution-precipitation stage of liquid phase sintering [160]. Similar to the growth of 100% β-rods from α-matte grains (**Fig. 5.2c**) when RBSN was heat-treated in MgO-SN powder bed, precipitation of 100% β-rods with dissolution of α-whiskers was observed (**Fig. 5.2f**). A slight decrease in the content of α-whiskers in **Fig. 5.2e** and **Fig. 5.3e** compared to those of **Fig. 5.2d** and **Fig. 5.3d** could be due to the presence of impurities forming a low temperature liquid eutectic and thus partial solution of α-whiskers. Accordingly, in the presence of MgO either in the starting powder mixture or in the powder bed, α→β-phase transformation and formation of β-grains at 1700°C was observed. As shown in **Fig. 5.2b** and **5.3b,** due to the presence of insufficient eutectic liquid phase, grain growth and full phase transformation did not occur in MgO-RBSN samples

heat-treated in SN powder bed: α-matte and fine β-nuclei (< 1 μm) coexisted in the microstructure and the α/β phase ratio was approximately 0.15. In contrast, 100% β-rods with coarse morphology and average aspect ratio of ≈ 2.74 formed in **Fig. 5.2c** when MgO was present both in the starting powder mixture and in the powder bed.

According to these observations, a combination of reaction bonding and post heat-treatment in the presence and absence of MgO led to the formation of α- and β-Si_3N_4 grains with various morphologies. For the comprehensive characterization of pores formed between these particles, which can range from sub-microns to tens of microns, classification of the observed pores is essential.

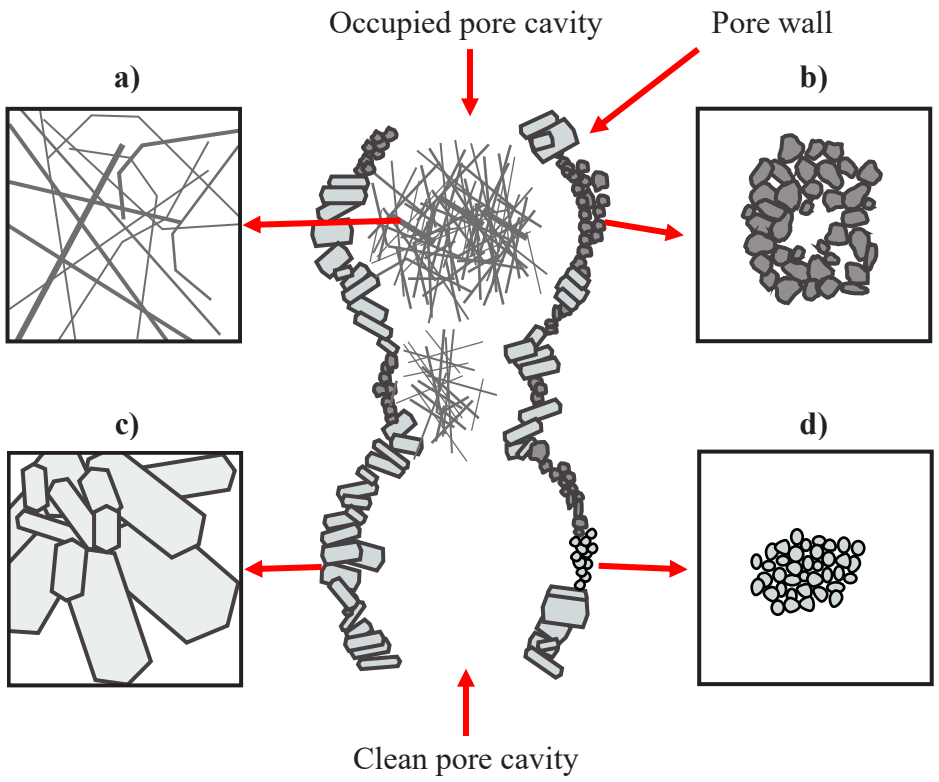

Fig. 5.1. Schematic illustration of reaction bonded Si3N4 grains grown inside the interconnected cavities or on the pore walls: a) α-Si_3N_4 whiskers, b) α-Si_3N_4 matte, c) β-Si_3N_4 rods, d) β-Si_3N_4 nuclei

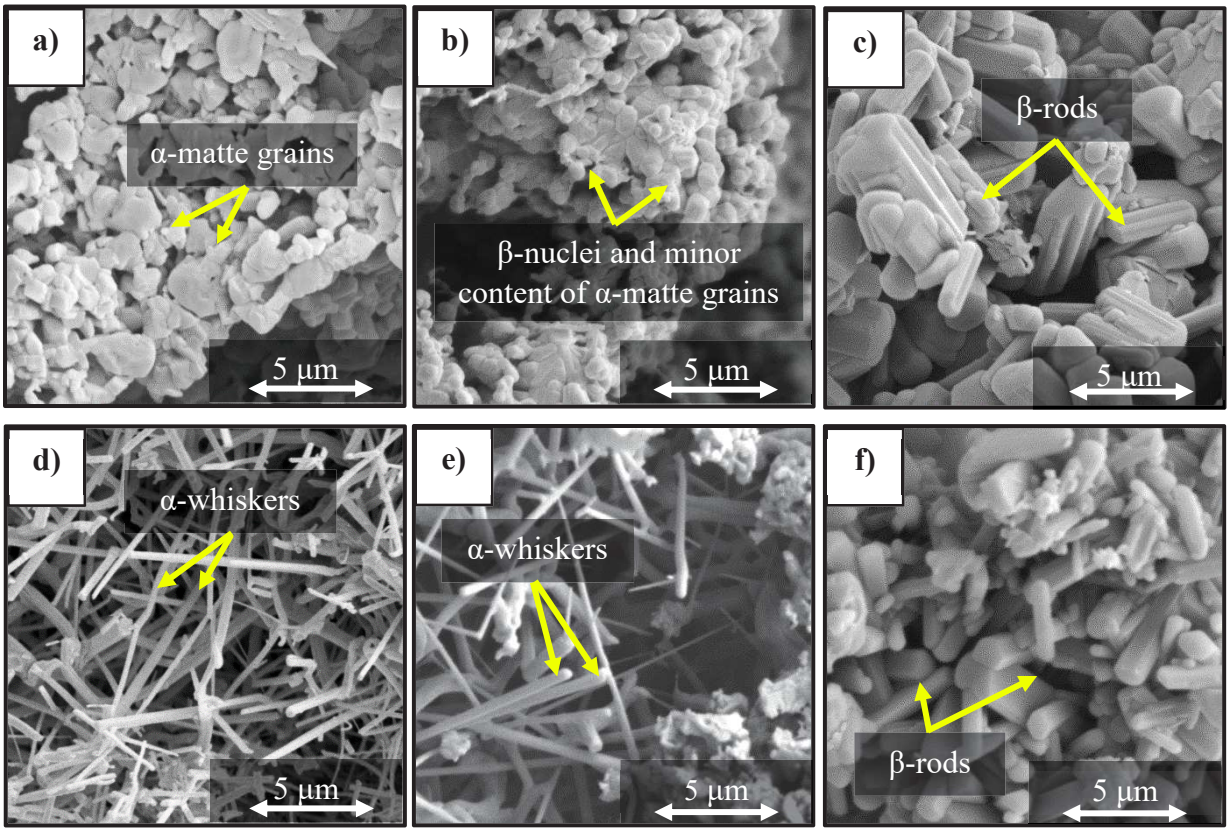

Fig. 5.2. SEM micrographs of porous samples demonstrating various grain morphologies in: a) MgO-RBSN, b) MgO-RBSN heat-treated in SN, c) MgO-RBSN heat-treated in MgO-SN, d) RBSN, e) RBSN heat-treated in SN, and f) RBSN heat-treated in MgO-SN

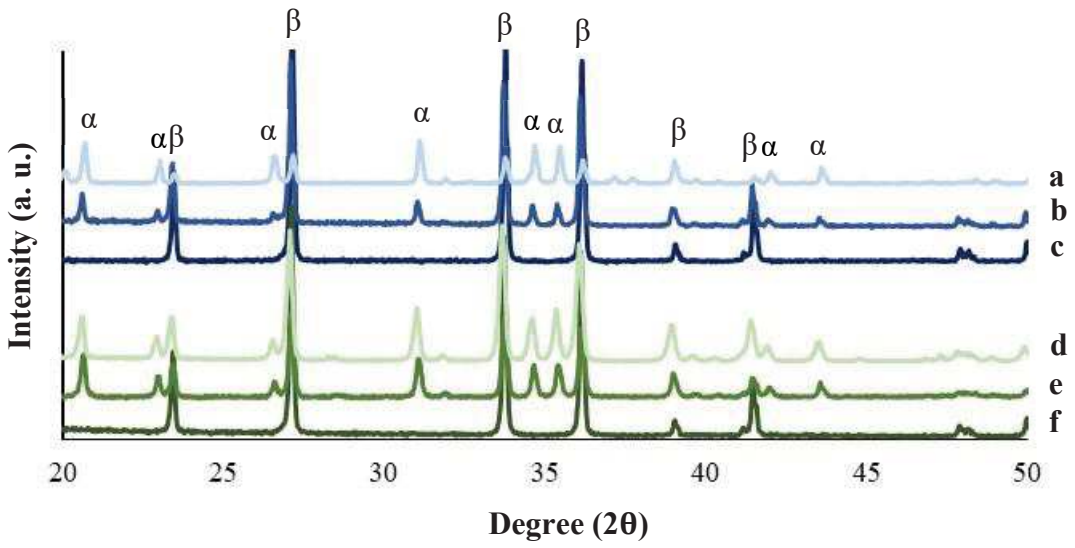

Fig. 5.3. XRD patterns of porous samples: a) MgO-RBSN, b) MgO-RBSN heat-treated in SN, c) MgO-RBSN heat-treated in MgO-SN, d) RBSN, e) RBSN heat-treated in SN, f) RBSN heat-treated in MgO-SN

Table 5.1. Characteristics of porous samples

Characteristics of samples	α/β-Si_3N_4 phase	Type of distribution	d_{50} (μm)	$\bar{d}$ (μm)	Peak (μm)	Standard deviation (μm)	Pore volume (ml g^{-1})	Porosity (vol.%)	Bulk Density (g cm^{-3})	Weight loss (wt. %)
MgO-RBSN	1.5	unimodal	8.88	13.8	9.06	23.76	0.98	75.17	0.73	NA
MgO-RBSN heat-treated in SN	0.15	unimodal	8.44	10.7	9.22	15.08	1.21	76.21	0.74	3.08
MgO-RBSN heat-treated in MgO-SN	0	unimodal	6.51	9.52	6.12	18.20	0.73	67.68	0.92	1.85
RBSN	0.36	bimodal	1.00	1.30	1.05, 7.24	0.63	0.86	73.82	0.81	NA
RBSN heat-treated in SN	0.35	bimodal	1.61	1.95	1.32, 2.69	0.88	0.77	71.65	0.88	1.66
RBSN heat-treated in MgO-SN	0	unimodal	3.79	3.40	4.78	1.93	0.29	30.05	1.03	0.43

5.3.2. Pore Formation and Classification

During reaction bonding process and the subsequent post heat-treatment, formation of pores occurs at different temperatures through various routes with the shapes and sizes that depend on the nature of the process. Several classifications of pores have been proposed in the literature based on their origin, shape, accessibility and size [8, 67, 165].

To study pore formation mechanism, thermal degradation behavior and weight loss of the dried sample containing MgO were studied by thermogravimetric (TGA) analysis and are presented in **Fig. 5.4a.** Under a nitrogen atmosphere, four weight loss steps were determined upon heating to 600°C. The first (12.43 wt.%) and the last (11.28 wt.%) weight losses were associated with the degradation of the polyacrylamide formed after polymerization of the gel-cast monomer [95].

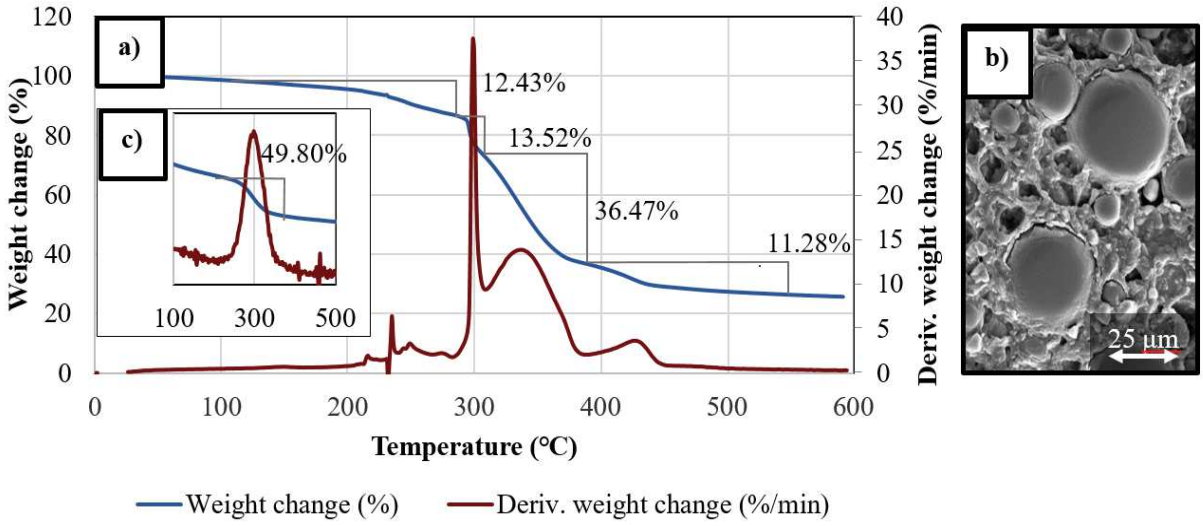

Fig. 5.4. a) Thermal decomposition curves of a sample containing MgO and polymers, b) SEM micrograph of the PMMA microspheres and silicon particles embedded in polyacrylamide matrix, and c) dehydration temperature of MgO powder absorbed ambient moisture

The SEM microstructure of the sample before pyrolysis in **Fig. 5.4b** illustrates the polyacrylamide network holding together the starting powders and the PMMA microspheres. With single-step degradation, a large weight loss (36.47 wt.%) initiated at 307°C is attributed to the decomposition of the PMMA beads and formation of the resultant precursor porous network [166]. A decrease in sample weight, starting at 277°C, was likely caused by decomposition of magnesium hydroxide formed during the suspension preparation and is more clearly observed in the derivative plot,

occurring at 300°C. **Fig. 5.4c** confirmed the presence of the same peak during the TGA analysis of the starting MgO powder that had become hydrated by absorption of ambient moisture. These degradation reactions, occurring at temperatures much lower than the nitriding temperature, led to the formation of the primary voids of several sizes that created an interconnected pore network.

Fig. 5.5 illustrates various pore morphologies arranged according to their size. All the pores having diameters of more than 50 nm are classified as macro-pores [8, 167]. **Fig. 5.5-a** shows the open-pore cellular structure of an MgO-RBSN sample containing nearly spherical cavities interconnected with one another. These macro-pores originated form the "subtractive" polymer-bead forming route [67] where space former PMMA was selectively removed by pyrolysis to create large spherical cavities linked together by small necks or fine inter-particle windows.

Compared to the spherical pores, inter-particles pores (**Fig. 5.5-b**) were irregular in shape, less in total volume and smaller in size (roughly less than 1 μm); therefore, they were expected to make a minor contribution to the total pore volume. Formation of fine pores with 80% smaller than 0.1 μm is typical of conventional reaction bonding occurs at temperatures of 1250-1450°C [21]. Inter-particle pores are thought to originate from the former silicon compact based on the particle size and shape, melting of silicon [21], condensation of vacancies [22], or direct vaporization of volatile species, e.g., silicon [22] and iron contamination [21].

Upon formation of whiskers, however, the pore structure became quite complex and rarely of uniform shape. **Fig. 5.5c** shows the inter-cluster channels formed between whisker agglomerates, which were likely first filled by mercury intrusion. Having smaller diameters compared to the inter-cluster channels, **Fig. 5.5d** illustrates the inter-particle pores. These irregular openings formed between whiskers have properties which are probably dependent on the content and the packing efficiency of needles.

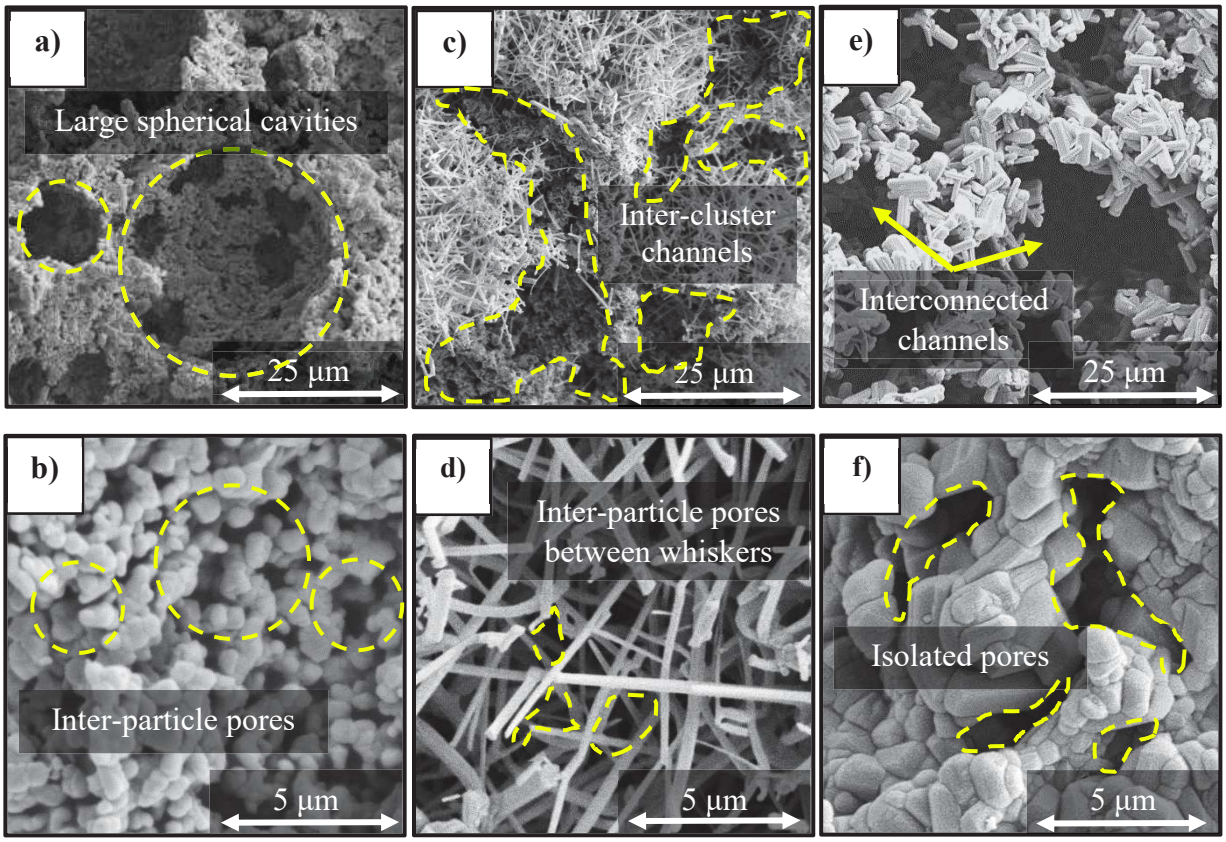

Fig. 5.5. Microstructure of the fracture surfaces of different pores: a) large spherical cavities, b) inter-particle pores, c) inter-cluster channels, d) inter-particle pores between whiskers, e) interconnected channels, and f) isolated pores

At the higher temperature of 1700°C, the pore configurations were significantly affected by heat-treatment in MgO-SN powder bed. **Fig. 5.5e** shows an interconnected structure of the heat-treated MgO-RBSN composed of open-pores. High permeability of the structure was ensured by the interconnectivity of macro-pores through large windows. This structure is better observed in **Fig. 5.6a** which shows formation of interconnected channels. The 3D reconstruction images in various sections (b: cross section, c: longitudinal section and d: oblique section) in **Fig. 5.6b** to **d** illustrate the permeable pores fully accessible from the surrounding.

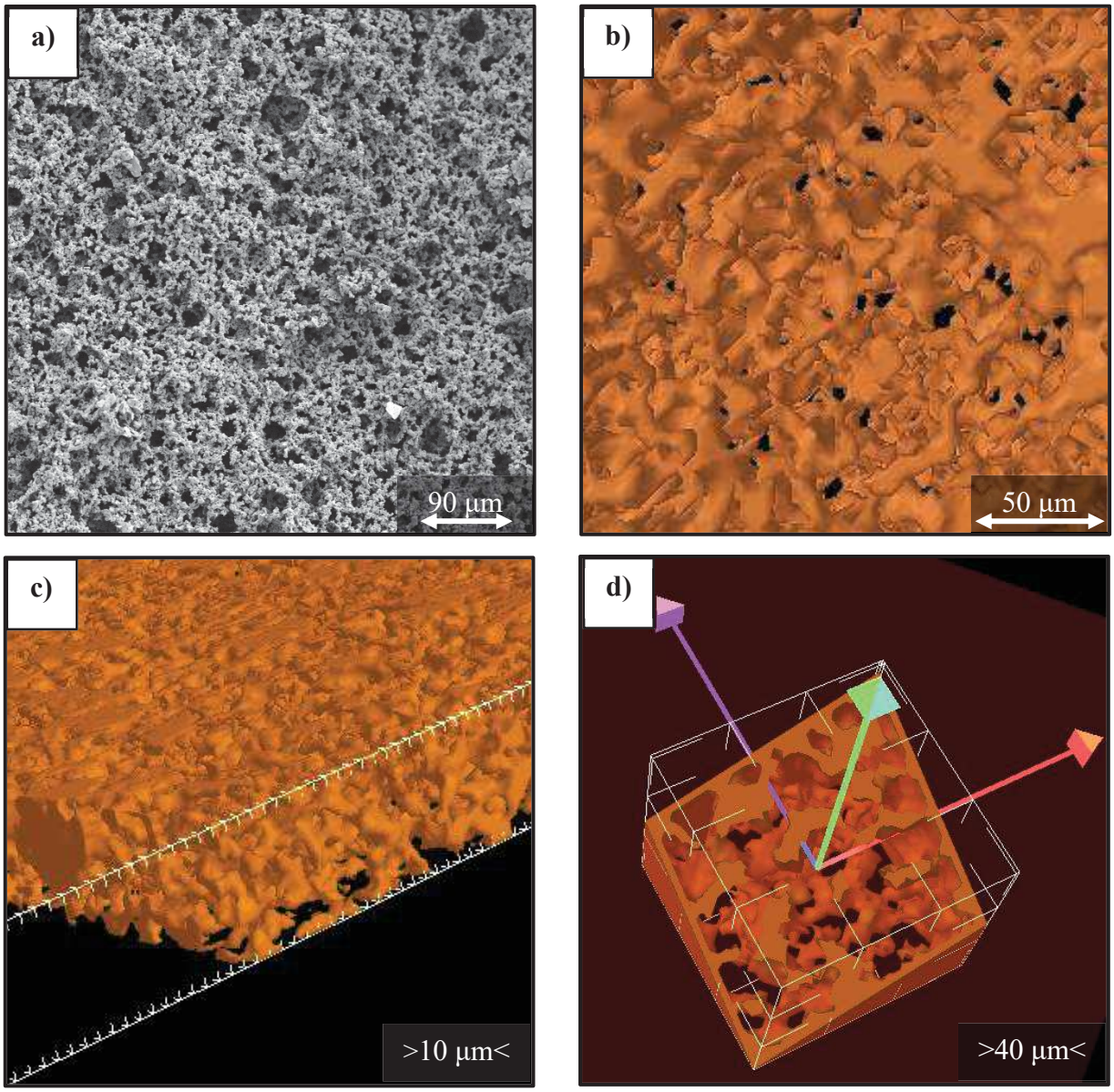

Fig. 5.6. a) SEM micrograph of pores constructing interconnected channels, b to d) the 3D reconstruction images of porous sample illustrating pore interconnectivity in: b) cross section, c) longitudinal section and d) oblique section of a layer of 116 µm thick

In contrast, heat-treatment of RBSN in MgO-SN powder bed resulted in the collapse of walls and formation of a microstructure with less interconnectivity, as shown in **Fig. 5.5f.** In this microstructure, fine pores are sparsely located at the inter-particle boundaries and appear to be only open at one end. With respect to high surface area and thus the high sinterability of whiskers,

this morphology formed by dissolution of α-whiskers and reprecipitation of fine β-rods, clogged some of the former open cavities and reduced the interconnectivity of the microstructure.

5.3.3. Characterization of Pores

To determine how the microstructure of pores correlates to the Si_3N_4 grain morphology, pore size distribution data of samples were measured by mercury porosimetry and the results are illustrated in **Fig. 5.7a** to **d**. With respect to the SEM micrographs in **Fig. 5.5**, pores would have filled with Hg when the applied pressure reached the required level for filling the largest neck entrances between them. Therefore, MIP data naturally illustrates smaller values than the actual internal pore size and is blind to closed pores that remain uncharacterized [168, 169].

Types of distributions and the values of median pore diameters (d_{50}, volume), mean diameters ($\bar{d}$), peaks in pore size distributions, pore volumes and standard deviations obtained from the MIP data are presented in **Table 5.1**. The corresponding data for porosity and density in this table was measured using Archimedes' method. A smaller standard deviation generates a narrow distribution of data, meaning that the pore sizes remained close to the mean; whereas a greater standard deviation shows a distribution with greater variability and a wider spread of the pore diameters. Morphology of pores appeared in the porous ceramics can be observed in **Fig. 5.8a** to **f**.

With the median pore diameter of 8.88 μm in **Fig. 5.7a** and **Table 5.1**, MgO-RBSN showed a density of 0.73 g cm^{-3}. Relative to RBSN, this sample had a wider pore size distribution, and a higher porosity and pore volume, namely, 75.17 vol.% and 0.98 ml g^{-1}, respectively. This was due to the formation of whisker-free cavities, shown in **Fig. 5.8a**, as well as loss of volatile materials or iron impurities by evaporation at elevated temperature. Iron compounds in the powder mixture might form a low melting point eutectic liquid, which encourages evaporation of volatile species and formation of fine pores. Using ICP analysis, the elemental composition of the starting silicon and magnesium oxide powders is listed in **Table 5.2** and confirmed the presence of minor impurities, notably iron in MgO powder.

In agreement with the SEM observations, after heating MgO-RBSN in a SN powder bed, the pore size distribution (**Fig. 5.7a**) and pore morphology (**Fig. 5.8b**) remained relatively constant. However, a slight increase in the porosity content to 76.21 vol.% and pore volume to the value of

1.2 ml g^{-1} (**Fig. 5.7b**) could be attributed to the decomposition and loss of MgO at 1700°C. An approximate 3 wt.% weight loss observed (**Table 5.1**) upon heating the MgO-RBSN sample in the SN powder bed confirmed the evaporation of volatile materials at 1700°C and was due to the absence of MgO in the surrounding atmosphere.

With a decrease in the median pore diameter to 6.51 μm, heat-treatment in the MgO-SN powder bed resulted in the densification, loss of porosity and pore volume to the values of 0.92 g cm^{-3}, 67.68 vol.% and 0.73 ml g^{-1}, respectively. This illustrates that morphology modification, β-grain growth and densification are accompanied by the partial elimination of pores and formation of a microstructure with smaller voids (**Fig. 5.8c**). Lower weight loss (≈ 1.85 wt.%, **Table 5.1**) during heat-treatment in the MgO-SN powder bed compared to the above case was due to the presence of MgO in the surrounding atmosphere which confirmed the important role of the powder bed chemical composition in preventing the thermal decomposition of materials.

Fig. 5.7c revealed that the formation of 3D-networked whiskers in RBSN sample shifted the pore size distribution graph to lower values and led to a median pore diameter of 1.00 μm. Having the lowest standard deviation, most of the pore sizes in this sample are grouped together near the mean diameter of 1.30 μm. Compared to the MgO-RBSN sample, the nitriding mechanism involving SiO gas species led to the formation of α-whiskers [20, 133] which restricted the pore channel volume (**Fig. 5.8d**) and decreased the porosity and the pore volume to 73.82 vol.% and 0.86 ml g^{-1}, respectively.

Meanwhile in the presence of whiskers, samples showed bimodal pore size distributions. In the absence of needle whiskers, unimodal pore size distributions were observed either before or after heat-treatment. This behavior illustrates the differences in the texture and grain morphology of various microstructures. Unlike samples with unimodal pore size distributions, those with bimodal pore size with diameters less than 1 μm made a significant contribution to the pore volume. According to the pore size distribution graphs, pores with diameters less than 1 μm occupied ≈ 53.84 vol.% in RBSN while only ≈ 4.40 vol.% in MgO-RBSN. This was manifested in an extra peak at 1.05 μm in the pore size distribution graph which corresponds to the inter-particle pores between whiskers. With a slight decrease in the content of whiskers, observed in **Fig. 5.2e**, high temperature heat-treatment in the SN powder bed increased the median pore diameter and shifted

the peak to 1.32 μm. In contrast, peaks appearing at higher values were associated with the inter-cluster channels between whisker agglomerates (**Fig. 5.5c** or **Fig. 5.8e**) or other openings with sizes dependent on the shrinkage level or the homogeneity of the microstructures. An approximate 1.66 wt.% weight loss was also observed due to the minor amount of liquid eutectic phase formation and thermal decomposition of heat-treated RBSN samples in the SN powder bed.

a) MgO-RBSN samples

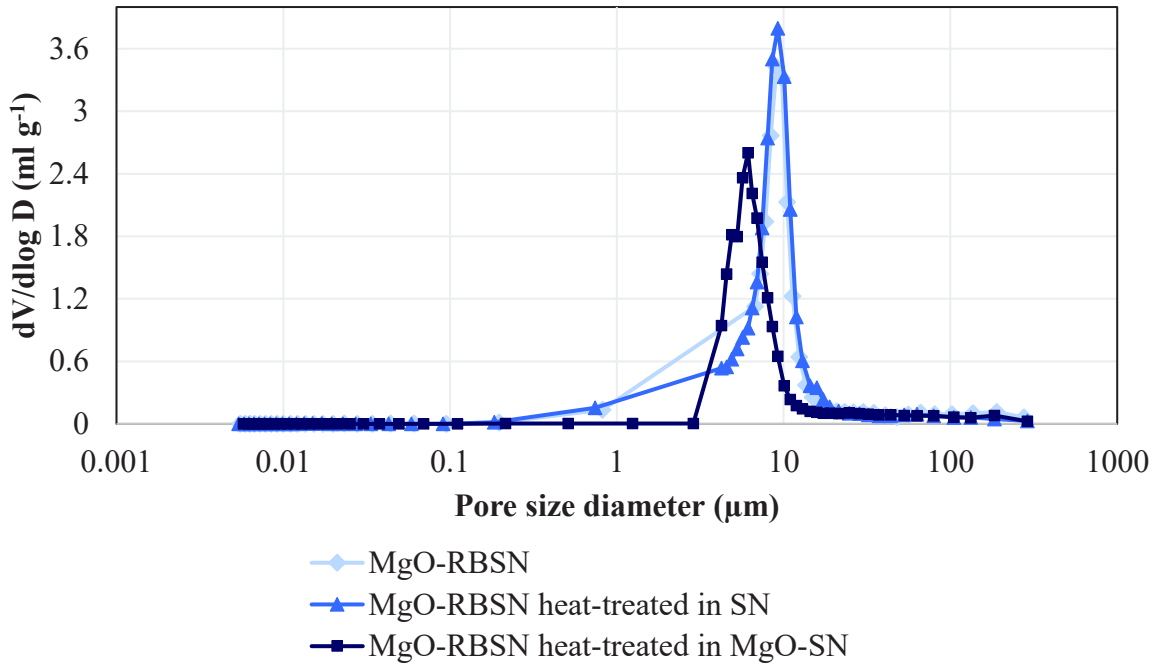

b) MgO-RBSN samples

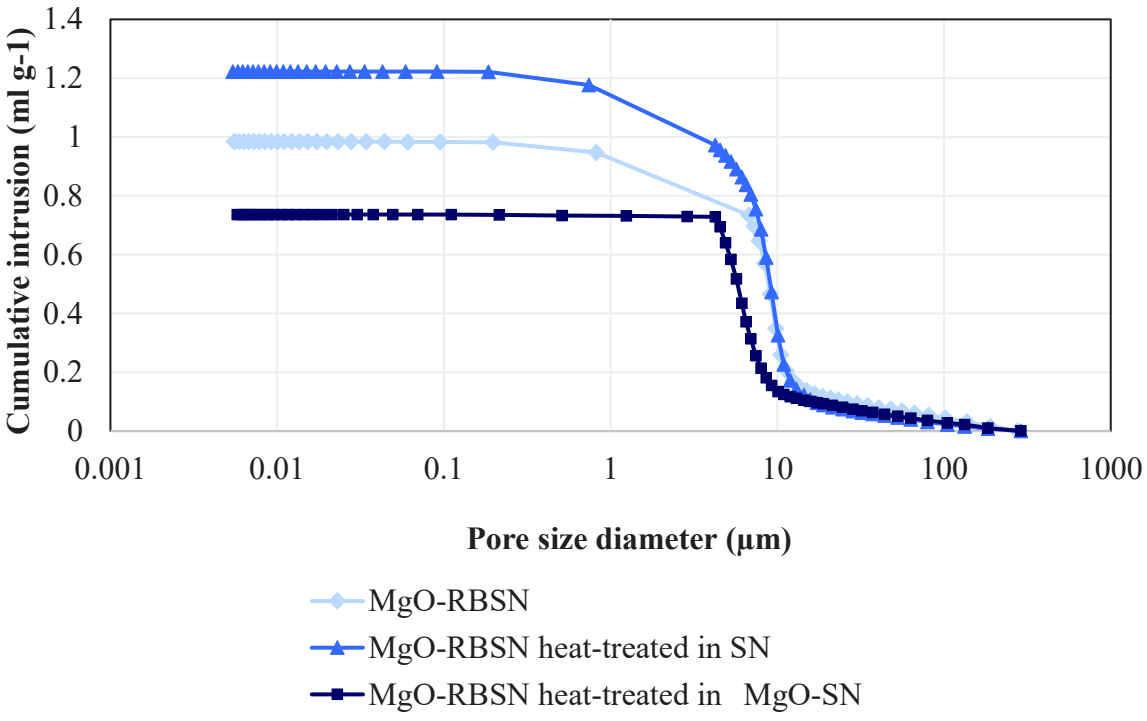

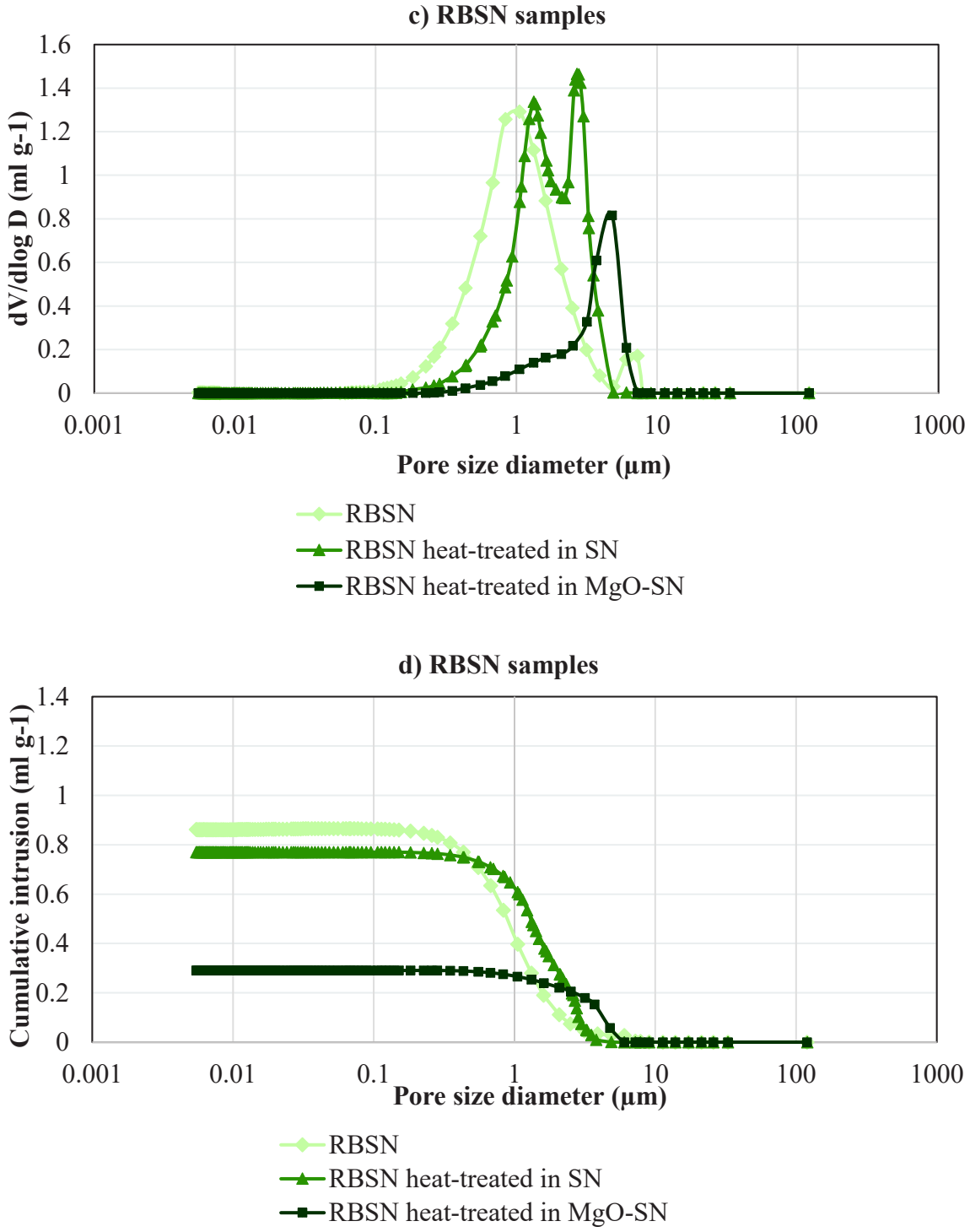

Fig. 5.7. Pore volume distributions (a and c) and changes of cumulative pore volumes (b and d) with pore size

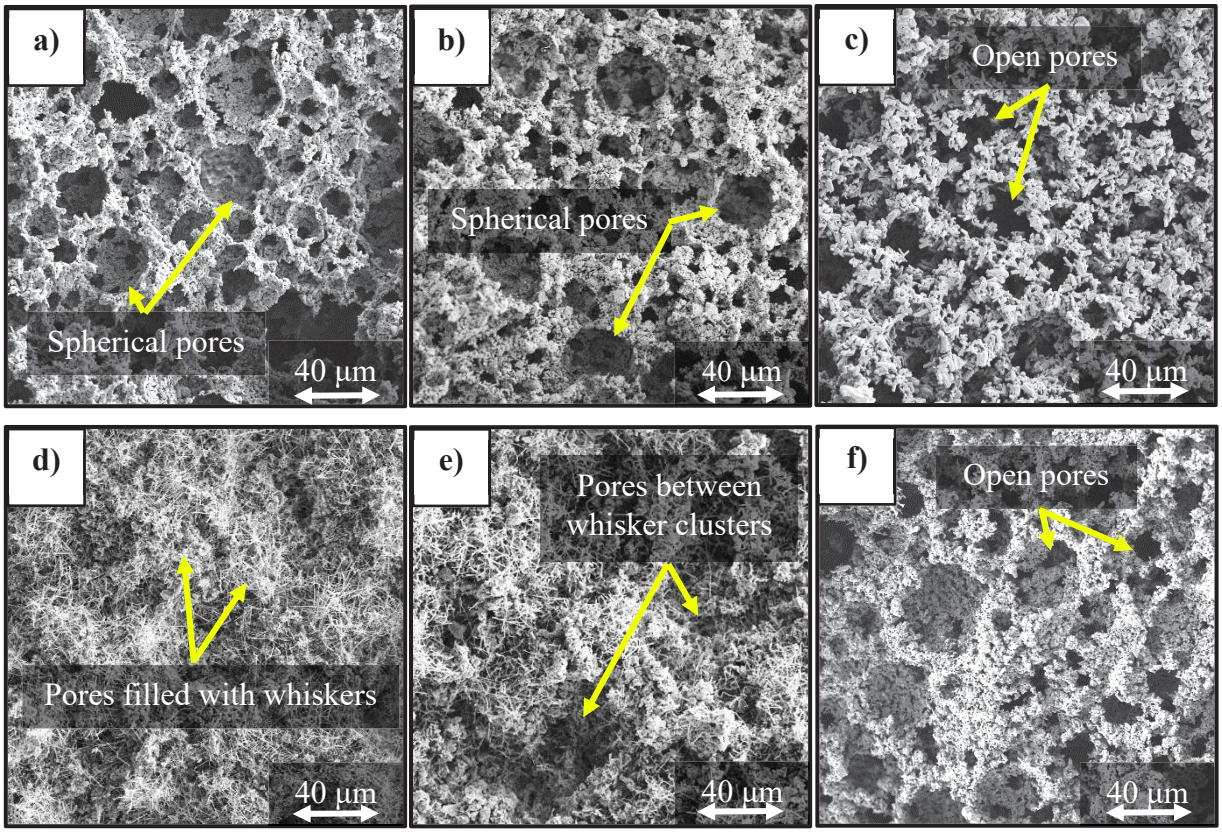

Fig. 5.8. SEM micrographs of porous samples demonstrating various pore morphologies in: a) MgO-RBSN, b) MgO-RBSN heat-treated in SN, c) MgO-RBSN heat-treated in MgO-SN, d) RBSN, e) RBSN heat-treated in SN, and f) RBSN heat-treated in MgO-SN

To confirm the role of whiskers on the formation of the extra peak associated with the inter-particle pores, MIP analysis was performed on a sample with a transitional microstructure. Having less whiskers dispersed between α-matte grains or β-Si_3N_4, this microstructure was achieved by adjusting the content of MgO in the starting powder (a selection between 0 to 12 wt.% MgO) [133]. SEM and MIP analyses are shown in **Fig. 5.9** and confirmed a lower content of whiskers in the microstructure. Hence the peak associated with the inter-particle pores at ≈ 1 µm tended to disappear, which changed the shape of the distribution from bimodal to unimodal.

Likewise, upon heat-treatment of RBSN in the MgO-SN powder bed, whiskers disappeared and recrystallized as 100% β-rods which resulted in the formation of large whisker-free cavities (**Fig. 5.8f**). Therefore, the peak associated with the inter-particle pores between whiskers disappeared in **Fig. 5.7c** causing the distribution to become unimodal. Smaller pores preferentially vanished at

the expense of bigger ones. The median pore diameter increased to 3.79 μm, while the volume of pores decreased to 0.29 ml g^{-1}, indicating a pore-coarsening mechanism [60]. Mobility and diffusion of MgO vapor from the MgO-SN powder bed to the porous RBSN samples not only led to significant microstructural modification, it also resulted in the lowest heat-treatment weight loss (≈ 0.43 wt.%). Having a huge surface area, fine whiskers sintered rapidly, and densification was enhanced; thus, the porosity reduced to ≈ 30 vol.%. The MIP analysis on samples heat-treated in the MgO-SN powder bed was repeated twice and very similar graphs were achieved confirming the repeatability of results. Therefore, with lower porosity content and smaller median pore diameter, this microstructure had a decreased interconnectivity [151] compared to the heat-treated MgO-RBSN samples.

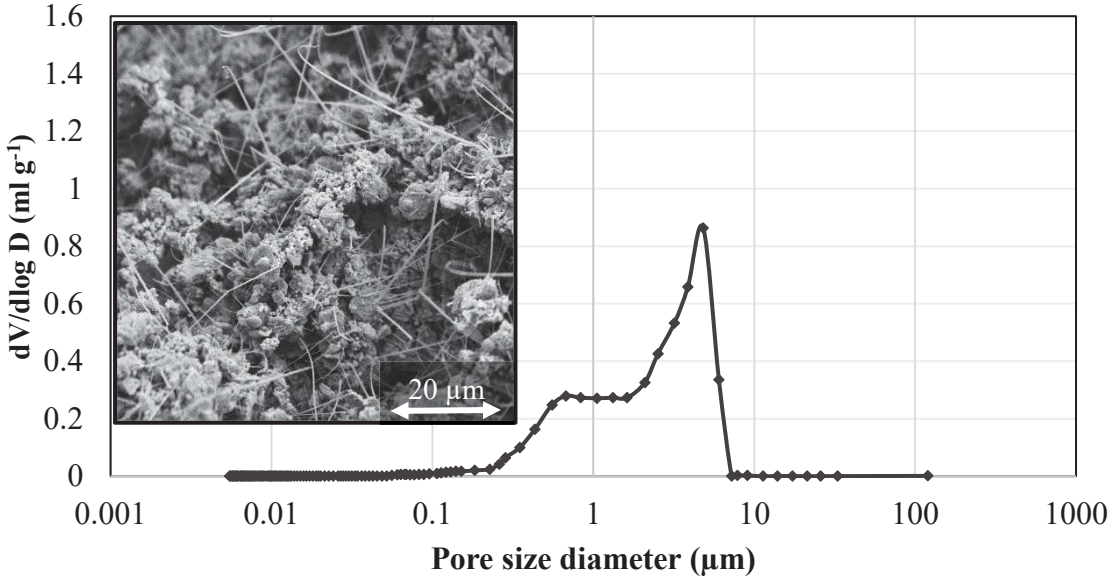

Fig. 5.9. SEM micrograph and pore size distribution of a sample with minor content of whiskers dispersed between α-matte or β-Si_3N_4 grains

Table 5.2. Impurity content of the starting Si and MgO powder

Element	Content in ppm	
	Si powder	MgO powder
Fe	2.826	872.578
Cr	0.277	5.721

Cu	0.175	0.103
Mn	0.040	131.303

5.3.4. Compressive Strength

Compression testing was carried out on samples before and after heat-treatment and the results are plotted in **Fig. 5.10**. Pores are considered to be critical defects and therefore the strengths of porous materials are determined by the size of the largest pores [8, 21, 41]. In MgO-RBSN samples containing large spherical pores (d_{50}≈ 8.88 μm), the compressive strength of samples was relatively low and around 1.1 MPa (**Fig. 5.10a**). With a post heat-treatment process in SN powder bed, no significant change occurred in the pore size distribution or morphology of grains, therefore relatively the same strength was obtained (**Fig. 5.10b**). In contrast, after the heat-treatment in the MgO-SN powder bed, shrinkage and densification triggered higher compressive strength (≈ 2.4 MPa in **Fig. 5.10c**). A strength of ≈ 7 MPa in RBSN in **Fig. 5.10d** suggested that the formation of 3D-networked whiskers with fine pores (d_{50}≈ 1 μm) resulted in a reinforced structure. However, heat-treatment of these samples in SN powder bed decreased the compressive strength to ≈ 4 MPa (**Fig. 5.10e**) and is assumed to be due to the lower content of whisker networks and presence of the slightly larger pores (d_{50}≈ 1.61 μm). Low content of porosity, small median pore diameter (d_{50}≈ 3.79 μm) and fine β-grains led to a compressive strength of ≈ 10 MPa for RBSN samples heat-treated in a MgO-SN powder bed (**Fig. 5.10f**). During heat-treatment in a MgO-SN powder bed, MgO-RBSN samples were affected by two opposing processes: shrinkage and thermal decomposition. Having bigger median pore diameter (d_{50}≈ 6.51 μm), higher porosity content and coarser β-grains produced lower compressive strength for MgO-RBSN (≈ 2.4 MPa) compared to RBSN samples (≈ 10 MPa). Based on these observations, it can be concluded that grain morphology, median pore diameter and porosity content were the key factors that greatly influenced the mechanical performance of the porous silicon nitride structures. Although it was impossible to separate the simultaneous contribution of each feature, the current study illustrates that microstructures with networked whiskers, smaller pore sizes, lower porosity, and fine β-grains showed relatively higher compressive strengths.

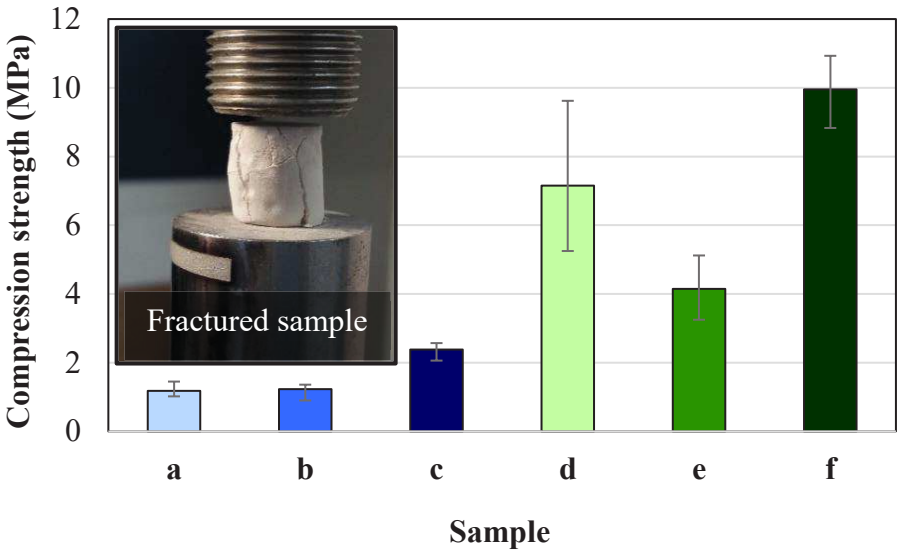

Fig. 5.10. Compressive strengths of different samples: a) MgO-RSBN, b) MgO-RBSN heat-treated in SN, c) MgO-RBSN heat-treated in MgO-SN, d) RBSN, e) RBSN heat-treated in SN, and f) RBSN heat-treated in MgO-SN

5.4. Conclusions

Porous Si_3N_4 ceramics with various α/β-phase ratios were fabricated by a reaction bonding combined with post heat-treatment. MgO was introduced into the starting silicon or to the surrounding powder bed to selectively tailor the morphology of grains. Microstructure of grains and pore formation mechanisms were studied and were correlated to the complex morphology of pores, pore size distribution, porosity, density, weight loss and compressive strengths of samples.

In the presence of MgO in the starting silicon, an interconnected porous structure with α-matte grains (α/β-phase ratio of 1.5), clean spherical pores, containing ≈ 75.1 vol.% porosity and a median pore diameter of ≈ 8.8 μm was obtained. Upon the heat-treatment, densification and grain growth in the MgO-containing powder bed, the pore sizes and porosity content decreased, and 100% β-rods formed. Having high channel interconnectivity, high porosity, and wide pore size distribution, these microstructures could be of an interest for ceramic-metal interpenetrating composites.

By excluding MgO from the starting silicon, α-whiskers (α/β-phase ratio of 0.36) hindered the pore volume and resulted in the formation of fine inter-particle pores along with inter-cluster

channels. With irregular shapes, the inter-particle pores between whiskers occupied a significant portion of the total pore volume which led to the formation of an extra peak at ≈ 1 μm in the pore size distribution. This caused the distribution to become bimodal. Due to the growth of whiskers in cavities, slightly lower porosity (≈ 73.8 vol.%) and a smaller median pore diameter (≈ 1.0 μm) were obtained in this microstructure. Having high porosity, complex pore structure and fine pores, whisker reinforced RBSN ceramics could be suitable for DPFs.

With a heat-treatment process in MgO-containing powder bed, α-whiskers vanished, and fine β-rods developed. This microstructure exhibited spherical clean pores with a median pore diameter of ≈ 3.79 μm. With porosity of ≈ 30 vol. % and enhanced mechanical strength this ceramic might be suitable for applications as membrane supports. Compared to α-matte grains, a high aspect ratio of α-whiskers caused a significant densification leading to the formation of a structure with less interconnectivity. Cavities were whisker-free and thus a unimodal pore size distribution was obtained. This morphology modification was not observed in a sample heat-treated in Si_3N_4 powder bed with no MgO.

Varying in the range of ≈ 1-10 MPa, the compressive strength of the porous ceramics was found to be a strong function of the sample microstructures. Samples with large interconnected spherical pores and coarse grains showed the lowest compressive strengths. On the contrary, low porosity, fine pores or 3D network of whiskers significantly reinforced the microstructures.

Chapter 6. A Comparative Study on Nitridation Mechanism and Microstructural Development of Porous Reaction Bonded Silicon Nitride in the Presence of CaO, MgO and Al_2O_3

Raheleh Nikonam M.[a,*], Martin D. Pugh[a], Robin A.L. Drew[a]

[a] Department of Mechanical, Industrial and Aerospace Engineering, Concordia University, Montreal, CANADA, H3G 1M8

*corresponding author: r_nikona@encs.concordia.ca

This article has been submitted to the Journal of Asian Ceramic Societies (Sept. 2019)

Abstract

During the in-situ nitridation of Si in the presence of CaO, MgO and Al_2O_3 formation of pores having various morphologies ranging from clean cavities to those fully occupied with whiskers indicated the possibility of different nitridation mechanisms operating. Experimental evidence suggested that, whereas the morphology of pores was controlled by nitridation of Si (g) in CaO-RBSN and SiO (g) in Al_2O_3-RBSN, a combination of these two reactions occurred during the nitridation of the MgO-RBSN. By inhibiting the growth of whiskers and maximizing the α/β ratio, the CaO addition led to the formation of matte grains creating clean spherical cavities with d< 40 μm and flexural strength of 0.8 MPa. In contrast, when using Al_2O_3 additions, a microstructure with a very low α/β ratio, fine inter-particle pores and 2.4 MPa flexural strength, reinforced with interlocking whiskers, was produced. The highest porosity (85%) and the lowest strength (0.3 MPa) occurred in the MgO-RBSN, which was composed of both matte grains and fine whiskers. Local supersaturation and low content of β-nuclei led to the formation of anisotropic β-grains with a bimodal microstructure in heat-treated CaO-RBSN while a unimodal microstructure was observed in heat-treated MgO-RBSN. No porosity loss or β-grain growth occurred in the heat-treated Al_2O_3-RBSN.

Key words:

Nitriding mechanism; Grain microstructure; Pore morphology; Microstructural evolution; Calcium oxide

6.1. Introduction

Porous silicon nitride (Si_3N_4) has a great potential to act as cell adhesion substrates, hot fluid filters, bioreactors, catalyst supports and heat insulators. Low density, chemical and thermal stability and a very high degree of heat, oxidation and corrosion resistance are among the remarkable performance of this ceramic [45, 73, 170, 171]. While in practice fabrication of porous silicon nitride may be applicable by partial sintering of α-Si_3N_4, widespread utilization of the prepared ceramic at elevated temperature has been limited by grain boundary sliding and subcritical crack growth [48, 77, 78, 172]. Alternatively, in situ nitridation of Si powder, firstly developed in the 1950s, has been applied to produce a porous structure in what has become to be known as reaction bonded Si_3N_4, or RBSN [21, 36].

Although any solid that contains pores may be regarded as a porous or cellular material, the complexity and variety of pore structure is based on its morphology, shape, size and accessibility, which has led to several pore classes being described in literature [67]. Open-pore morphology and high porosity (typically> 40 vol.%) are the important characteristics required for ceramic-metal composites, bone scaffold, separation membranes and filters as they provide high flow rate and channel interconnectivity [12, 18, 173]. In attempts to improve the porosity content and pore sizes above the ranges normally achieved in RBSN, that is to say 20-30 vol.% micro-porosity [10, 21], a variety of approaches have been developed [45, 73, 157]. The sacrificial template technique is one of the most important methods yielding a high porosity content with a tailored pore structure governed by adjusting the vol.% and morphology of fugitive substances [3, 17, 174]. For instance, spherical pores with ≈ 53 vol.% porosity and rod-like pores with ≈ 42 vol.% porosity have been developed using benzoic acid balls [16] and organic whiskers [175], respectively. Similarly, the shape and size of cavities can be affected by the morphology of the RBSN grains constructing the skeletal part [153, 176].

Besides the two morphologies of α-matte grains and elongated β-rods, Si_3N_4 may form whiskers randomly distributed throughout the pore channels [20, 22]. Many detailed studies have explained the growth mechanism of Si_3N_4 grains in porous RBSN [133, 160]; nevertheless, achieving a designed grain morphology and thus a controlled pore microstructure is the major challenge of this route as multiple processing variables are simultaneously involved [11, 44, 47, 58]. As an illustration, porosity provides more reactive area per unit mass and encourages surface reactions such as dissociation and silicon oxidation. This may affect both the amount of vapor species in cavities and thus gas-phase reactions, as well as the amount of surface silica and liquid-phase reactions [22, 177].

Apart from the processing conditions, there are several reports which have investigated the interactions of Si_3N_4 with oxide additives and the corresponding effects on the morphology of β-Si_3N_4 rods, their aspect ratio and strengths [37, 178]. Yet, these investigations mostly have focused on the performances of multi-components systems as Si_3N_4 sintering aids rather than as nitriding reaction modifiers. It must be remembered that the behavior of a single additive could be different from that of multi-components system. For example, use of systems such as MgO-Y_2O_3 [42], Al_2O_3-CaO [179], MgO-CaO-La_2O_3 [62] or CaO-Al_2O_3-SiO_2 [170], encourages low viscosity liquid phase formation and favors the liquid-phase sintering (LPS) process. However, the presence of liquid phase is not a prerequisite of nitriding. Knowing that the morphology and crystallinity of porous RBSN highly depend on gaseous-, solid- or liquid-phase reactions [10, 21], one may raise the question of whether a single oxide additive would interfere with nitriding reactions and would be effective in controlling the reaction pathway and the dominant grain morphology.

With emphasis on the relationships between the type of additive and the nitriding mechanism, the present work aims to develop highly porous RBSN with various grain morphologies. To examine the interaction of a single oxide additive with silicon and nitrogen gas, 10 and 15 mol.% of CaO, MgO or Al_2O_3 were introduced individually into the starting silicon while other processing variables remained constant. By separating the effects of various oxides, this work highlights the feasibility of designing porous RBSN microstructures in accordance with the starting powder's chemical composition. Interactions of the added oxides with surface silica, phase transformation, liquid phase formation and the presence of intermediate products up to 1700°C were studied.

Additionally, the corresponding effects on the microstructural development in terms of grain growth, porosity, density, linear shrinkages and flexural strengths were investigated.

6.2. Materials and Experimental Procedure

A detailed explanation of the porous RBSN fabrication process has been described previously [19]. Ceramics were prepared via gel casting using silicon (99.995%, D90= 7.7μm, ABCR), PMMA beads (10-40 μm, Microbeads) and DI water with the weight ratio of Si: PMMA: H_2O of 16: 44: 40. Acrylamide and N,N'-methylenbisacrylamide monomers and rheological agents were used to develop a homogenous and stable gel. CaO (99.95% metals basis, -20 mesh powder, Alfa Aesar), MgO (> 99% trace metals basis, -325 mesh powder, Sigma-Aldrich) and Al_2O_3 (> 99.5% trace metals basis, ≤ 10 μm, Sigma-Aldrich) were employed as oxide additives. **Table 6.1** shows the trace of impurities with contents of ≥ 10 ppm in these additives.

Table 6.1. Impurities with content of ≥ 10 ppm in the starting additive powders

Additive	values in ppm													
	Ca	Na	Fe	Al	B	Mn	Ga	Mg	Te	As	Ti	Zn	V	Ni
CaO	---	10	30	---	---	---	---	10	35	31	---	---	---	---
MgO	6404	40	1012	438	220	140	---	---	---	---	27	17	17	14
Al_2O_3	300	3000	225	---	18	---	110	50	---	---	40	15	---	---

10 and 15 mol.% of each oxide was added to the prepared solution. The slurries were molded, dried in air and subjected to pyrolysis at 525℃. Subsequently, the now porous silicon samples were heated at atmospheric pressure in an ultra-pure nitrogen gas (99.999 %, Air Liquide) containing a maximum of 2 ppm oxygen. Nitriding reactions were studied by heating the samples to temperatures between 1200℃ and 1425℃ for several minutes. Sample labelling was as follows: CaO-RBSN, MgO-RBSN and Al_2O_3-RBSN. The samples were then packed into powder beds composed of oxide additives, silicon nitride (Si_3N_4, grade M11 higher purity, ABCR) and boron nitride (BN, industrial powder, COMBAT) in which Si_3N_4 and BN were added in equal weight proportions. Post heat-treatment was carried out at 1700℃ for 2 and 4 hr.

Phase composition and transformation of the prepared ceramics were studied by X-ray diffraction analysis (XRD, X'Pert Pro, PANalytical) using CuKα radiation, λ= 1.54059 Å. The α/β-Si_3N_4

phase ratio was calculated based on the intensity of the (210) and (102) peaks for α-Si_3N_4, and (101) and (210) for β-Si_3N_4. To investigate the morphology of pores as well as microstructure and aspect ratio of grains, scanning electron microscopy (SEM, Hitachi, S-3400 N) equipped with energy dispersive X-ray spectroscopy (EDX, Oxford Instruments, Wave Model) was employed under high vacuum at 5-15 kV and 40-50 mA. Density and porosity of samples were measured using Archimedes' technique (ASTM C373-88 standard) and the results were presented as final values averaged over eight measurements. Linear shrinkages of samples have been measured based on the dimensional changes of four heat-treated samples. Three-point bending tests were carried out using three bar-like specimens with the dimensions of ≈ 30×7×7 mm^3. The span length of 20 mm, cross-head speed of 0.5 mm min^{-1}, and upper and lower shaft diameters of 5 mm and 2.5 mm, respectively, were used for this test.

6.3. Results and Discussion

To investigate the role of oxide additives on microstructural development, samples have been characterized based on SEM-EDX and X-ray diffractometry and for the purpose of clarity and simplicity, the observations will be discussed in two separate sections. The first part (**6.3.1**), presents the results of experimental data related to the nitriding mechanism and covers the interactions of oxide additives with silicon and N_2 at T≤ 1425°C. The second part (**6.3.2**) focuses on the interactions of the oxides with Si_3N_4 during the post heat-treatment process at 1700°C.

6.3.1. Reaction Mechanism and Microstructural Development During Nitriding

6.3.1.1. Al_2O_3-RBSN

Fig. 6.1a to **d** illustrate the morphology of Si_3N_4 grains formed in the presence of Al_2O_3. In reaction bonding, the morphology of grains and their growth rate critically depend on the reaction mechanism [22]. Considering the general theories stated in the literature; α-matte forms when nitridation of gaseous Si with molecular nitrogen occurs (**Eq. 6.1**) [21, 55], rods of β-Si_3N_4 nucleate via a reaction between solid or liquid Si with atomic nitrogen (**Eq. 6.2** and **6.3**) [21, 55], and α-whiskers are formed based on vapor-phase reaction between SiO and nitrogen (**Eq. 6.4**) [55, 108, 109, 119, 180].

$3Si\ (g) + 2N_2\ (g) \rightarrow Si_3N_4\ (s)$	$\Delta G^o = -2080 + 0.757T$ kJ. mol^{-1} [21]	**Eq. 6.1**
$3Si\ (l) + 2N_2\ (g) \rightarrow Si_3N_4\ (s)$	$\Delta G^o = -874 + 0.405T$ kJ. mol^{-1} [21]	**Eq. 6.2**
$3Si\ (s) + 2N_2\ (g) \rightarrow Si_3N_4\ (s)$	$\Delta G^o = -723 + 0.315T$ kJ. mol^{-1} [21]	**Eq. 6.3**
$3SiO\ (g) + 2N_2\ (g) \rightarrow Si_3N_4\ (s) + 1.5O_2\ (g)$	$\Delta G^o = -445 + 0.7676T$ kJ. mol^{-1} [55]	**Eq. 6.4**

Markedly, silica has a great influence on α-Si_3N_4 whisker formation as a proven supply of SiO vapor [109, 119, 120]. The overall content of this oxide, which occurs naturally on the surface of silicon particles, could be increased either by Si hydrolysis in water [181], or as a result of oxidation during the initial stage of reaction, T≈ 1250-1300°C [55]. Reduction of silica at elevated temperature via an oxide removal mechanism can then increase the silicon monoxide vapor pressure [21]. Under low $p(O_2)$ ($< 5\times10^{-3}$ atm), nitridation of silicon monoxide and thus formation of α-whiskers will continue by reduction of SiO_2 [52]. Development of a particular microstructure provides strong evidence about the reaction mechanism [20] and formation of whiskers in Al_2O_3-RBSN (10 mol.% Al_2O_3, **Fig. 6.1a** and **b**) revealed nitridation through SiO reaction. These whisker grains filled the pore cavities by growing inside the channels, resulting in the formation of pores with complex, irregular and random morphologies. This microstructure was even observed in the presence of a higher content of Al_2O_3 (15 mol.%) in **Fig. 6.1c** and **d**. Formation of reaction-bonded Si_3N_4 α-whiskers under ultra-high purity nitrogen gas has been observed in previous studies [46, 133] where a liquid puddle (impurity or catalyst) acts as a medium for the reaction to proceed [20, 182]. As proposed by Jennings et al. [20], whisker formation is thus promoted in less pure samples, which offers a higher chance of liquid phase formation. For this reason, the presence of surface silica in conjunction with silicon impurities such as Fe (**Table 6.1**) increased the possibility of whisker formation.

After 10 minutes at 1200°C, XRD analysis in **Fig. 6.2** and **Table 6.2**, show that strong peaks of Al_2O_3 still coexist with those of Si. Conversion of silicon to silicon nitride was initiated at ≈ 1350°C and proceeded rapidly so at 1400°C, after 10 min heating, almost 89 wt.% Si_3N_4 had already been formed. This could be due the fact that melting of silicon at ≈ 1410°C accelerates the liquid puddle formation as a preferred site for gaseous reactant dissolution and super-saturation [182]. Accordingly, as a low energy process, diffusion of nitrogen in the liquid melt allows the whisker crystals to grow quite fast [20]. After 2 hr heating at 1425°C, the nitridation has been completed with β-Si_3N_4 as the dominant phase. High nitriding temperatures (> 1410°C), high heating rates

and low oxygen content in the surrounding atmosphere all strongly encourage β-Si_3N_4 formation [22]. Under these conditions, atomic nitrogen with a Van der Waals radius of 1.5 Å is stable and can easily diffuse through the 1.5 Å diameter hexagonal tunnels along the *c* direction of the β-phase. Unlike the α-phase, these channels ensure the reaction progresses and enables higher diffusion rates of monoatomic nitrogen in polycrystalline β-phase [20-22]. Consequently, under ultra-high pure nitrogen gas, the α/β-Si_3N_4 ratio was almost negligible, i.e., 0.08, and formation of β-Si_3N_4 was favored over α-matte.

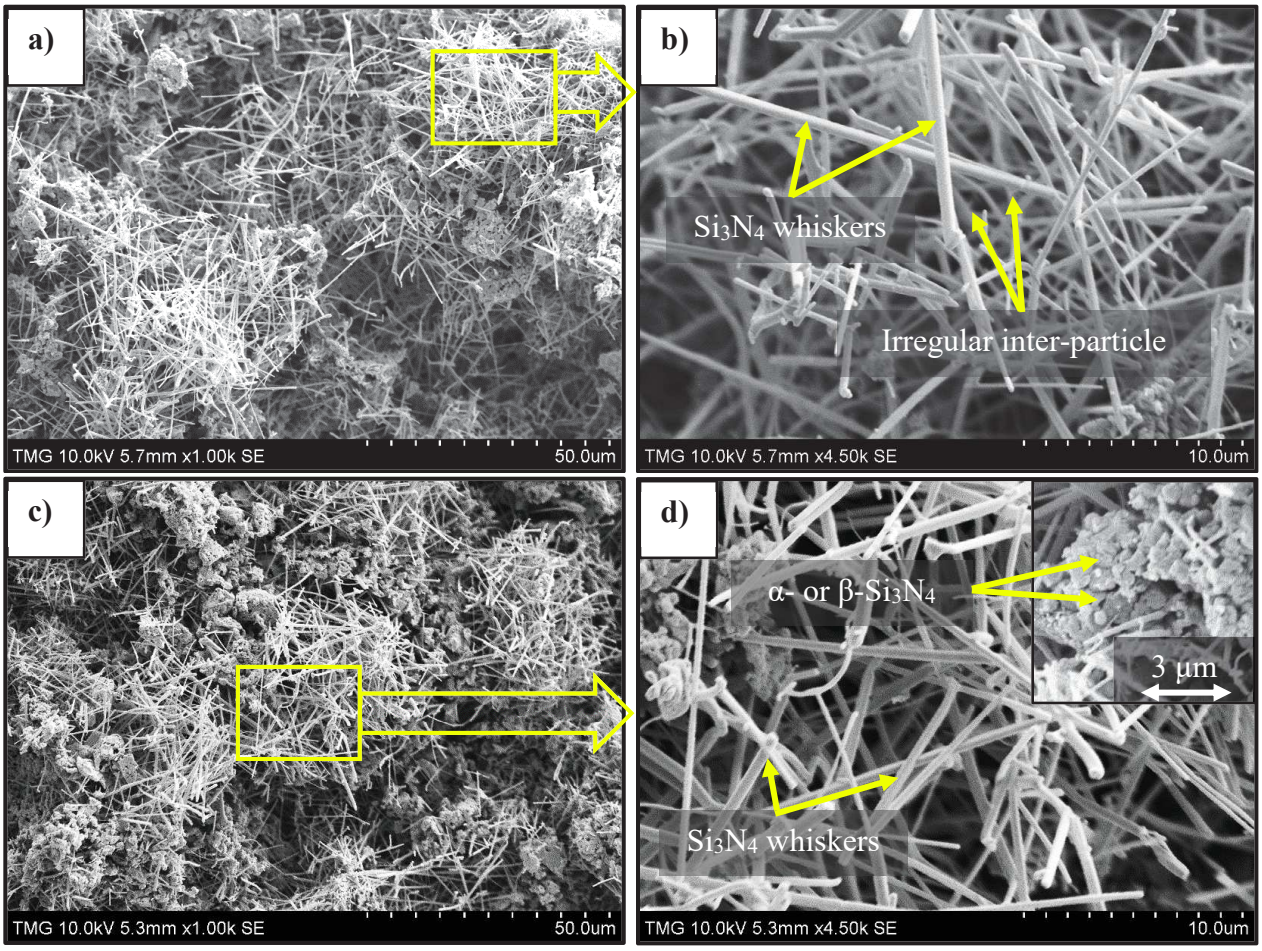

Fig. 6.1. SEM micrographs of samples containing Al_2O_3 nitrided at 1425°C for 2 hr, a) and b) 10 mol.% Al_2O_3 and c) and d) 15 mol.% Al_2O_3

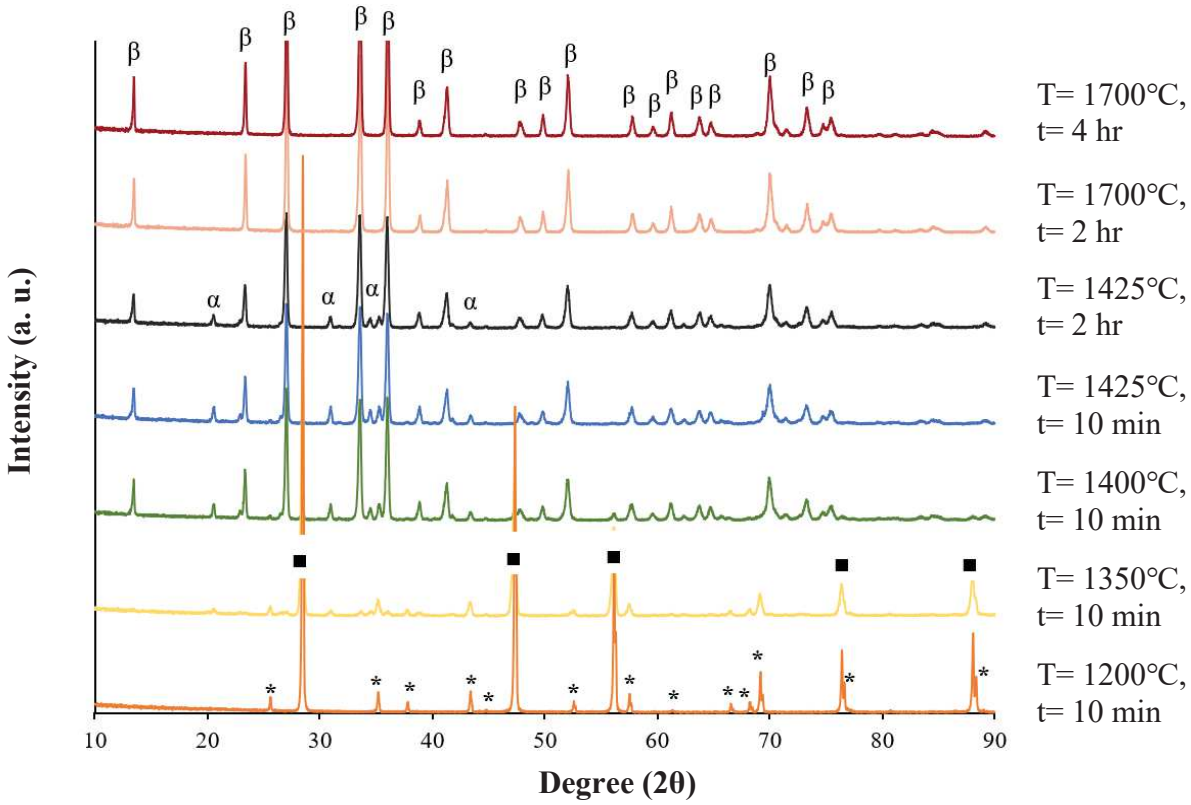

Fig. 6.2. XRD patterns of samples containing 15 mol.% Al_2O_3, heat-treated at various temperatures and heating durations (α, β , ∗ and ■ show peaks corresponded to α-Si_3N_4, β-Si_3N_4, Al_2O_3 and Si, respectively)

Table 6.2. Phase contents of samples containing 15 mol.% Al_2O_3

Heating conditions	wt.%				
	Si	Al_2O_3	α-Si_3N_4	β-Si_3N_4	α/β-Si_3N_4
T= 1200°C, t= 10 min	96.89	3.10	0.00	0.00	NA
T= 1350°C, t= 10 min	88.78	3.69	2.82	1.96	1.43
T= 1400°C, t= 10 min	9.34	1.74	7.94	80.96	0.09
T= 1425°C, t= 10 min	1.09	1.86	12.3	84.5	0.14

T= 1425°C, t= 2 hr	0.00	0.50	7.80	91.7	0.08
T= 1700°C, t= 2 and 4 hr	0.00	0.00	0.00	100.00	0.00

6.3.1.2. MgO-RBSN

Unlike Al_2O_3, in the presence of magnesia, the SEM images of MgO-RBSN in **Fig. 6.3a** to **d** illustrate the existence of various Si_3N_4 morphologies ranging from mainly α-matte to a minor content of fine whiskers and β-nuclei. By increasing the MgO content from 10 mol.% to 15 mol.%, comparatively the same morphology was observed in **Fig. 6.3c** and **d**. As indicated by the arrows, many inter-particle fine pores (**Fig. 6.3d**) as well as irregular-shaped large pores (**Fig. 6.3c**) exist. Growth of α-matte occurs by evaporation of Si and the resultant fine pores provide the required space for 22 vol.% expansion upon nitridation and so preserves the original dimensions of the sample relatively unchanged [20, 22].

High vapor pressure of MgO at elevated temperature has been reported under neutral atmosphere, which enhances the partial vapor pressure of oxygen due to dissociation of MgO [124]. Based on the stability region of SiO and SiO_2 in Si-O system [55], a higher oxygen content corresponds to a lower $p(SiO)/p^{\theta}$. Therefore, at a certain temperature, formation of solid SiO_2 would be favored if $p(O_2)/p^{\theta}$ is higher than the equilibrium content [22]. Therefore, the presence of oxygen would change the partial pressures of the vapor species in the surrounding atmosphere, the dominant nitriding reaction and thus affect the grain morphology.

The results of XRD analysis in **Fig. 6.4** and **Table 6.3** revealed the co-existence of Mg_2SiO_4 and Si_2N_2O as two intermediate products. Formation of a minor amount of Mg_2SiO_4 at 1200°C was probably due to a favorable reaction between surface silica and MgO vapor [121]. Moreover, Si_2N_2O formed at 1350°C as a result of silicon oxidation in a high oxygen content atmosphere [55]. Based on the XRD analysis, melting of silicon at T≈ 1410°C in the presence of impurities such as Fe and Al (**Table 6.1**) possibly decomposed or dissolved these intermediate phases at higher temperature.

It is worth noting that based on the results of XRD analysis, the amount of unreacted residual silicon in MgO-RBSN (**Table 6.3**) at each temperature was far greater than that of Al_2O_3-RBSN (**Table 6.2**). At 1200°C and 1350°C, no significant sign of nitridation was detected and at 1400°C almost 75 wt.% silicon remained unreacted. Compared to Al_2O_3-RBSN, the kinetically slower reaction in this system led to incomplete nitridation and the presence of residual silicon at 1425°C. Obviously, the gaseous reaction involving SiO vapor proceeds at a much faster rate than that involving Si vapor which proceeds by surface adsorption of nitrogen gas and nucleation of small crystals over available surfaces [21]. At the same time, the impenetrable SiO_2 layer separates nitrogen from the underlying silicon. Further evaporation of silicon must occur by escaping through fissures of the protective silica surface film, which normally retards the reaction by acting as a diffusion barrier [44].

Oxygen not only changes the partial pressure of the vapor species and discourages the reduction of silica, it can also easily remove active nitrogen by two sequential reactions: $N + O_2 \rightarrow NO + O$ and $N + NO \rightarrow N_2 + O$ [22, 41]. Jennings et al. suggested that oxygen could clog the hexagonal tunnels of β-phase, slowing down the overall kinetics and encourage the formation of energy-rich, oxygen-contaminated α-Si_3N_4 [20]. With considerably higher α-phase than that of the Al_2O_3-RBSN, MgO-RBSN showed an α/β-phase ratio of ≈ 1.75.

Formation of the α-rich microstructure with dominant matte grains suggested that the nitriding atmosphere was affected by the presence of MgO. The hypothesis is therefore proposed that by simultaneous nitridation of Si (g) and SiO (g), the presence of 10 or 15 mol.% MgO resulted in the formation of α-matte grains associated with low content of α-whiskers.

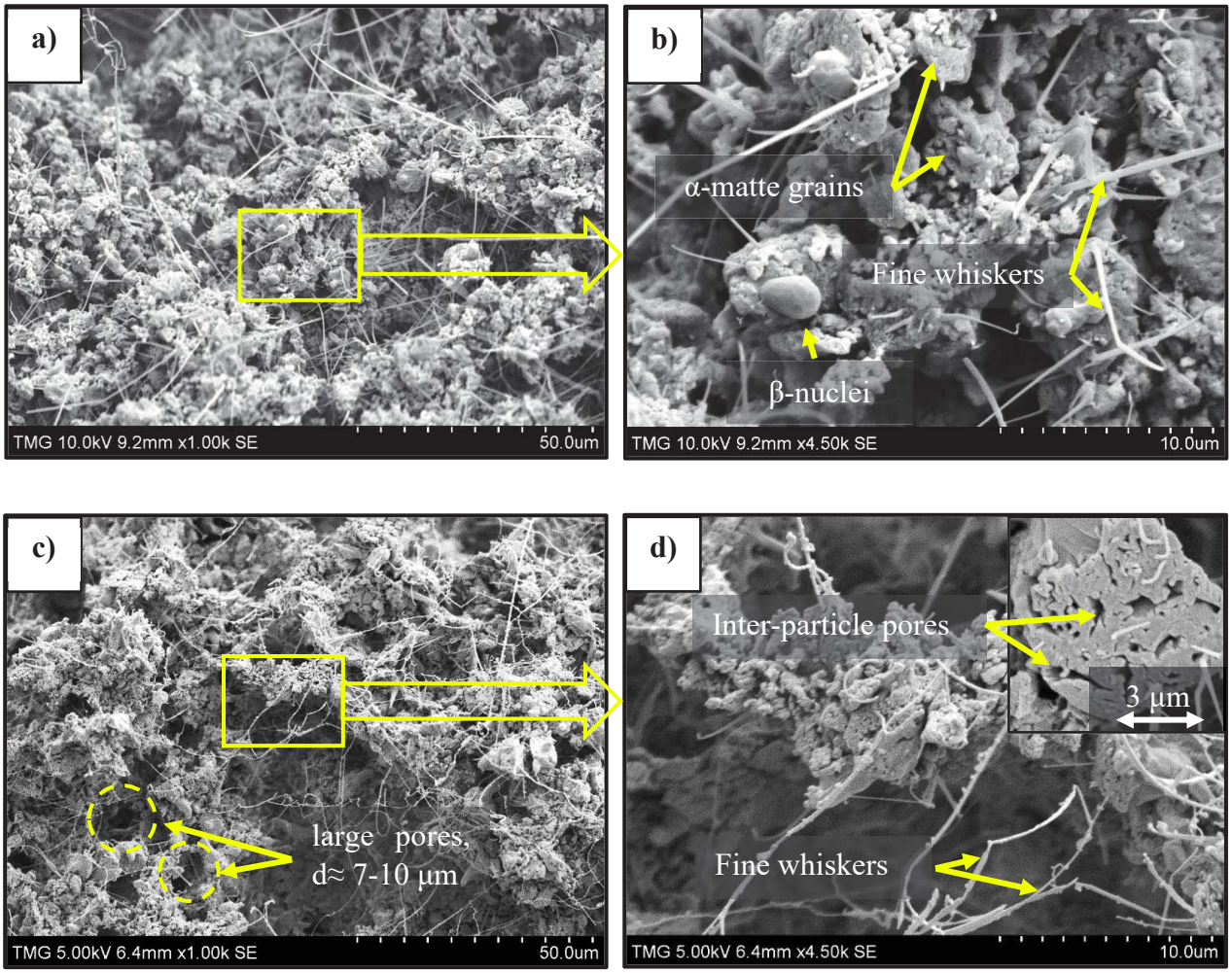

Fig. 6.3. SEM micrographs of samples containing MgO nitrided at 1425℃ for 2 hr, a) and b) 10 mol.% MgO, and c) and d) 15 mol.% MgO

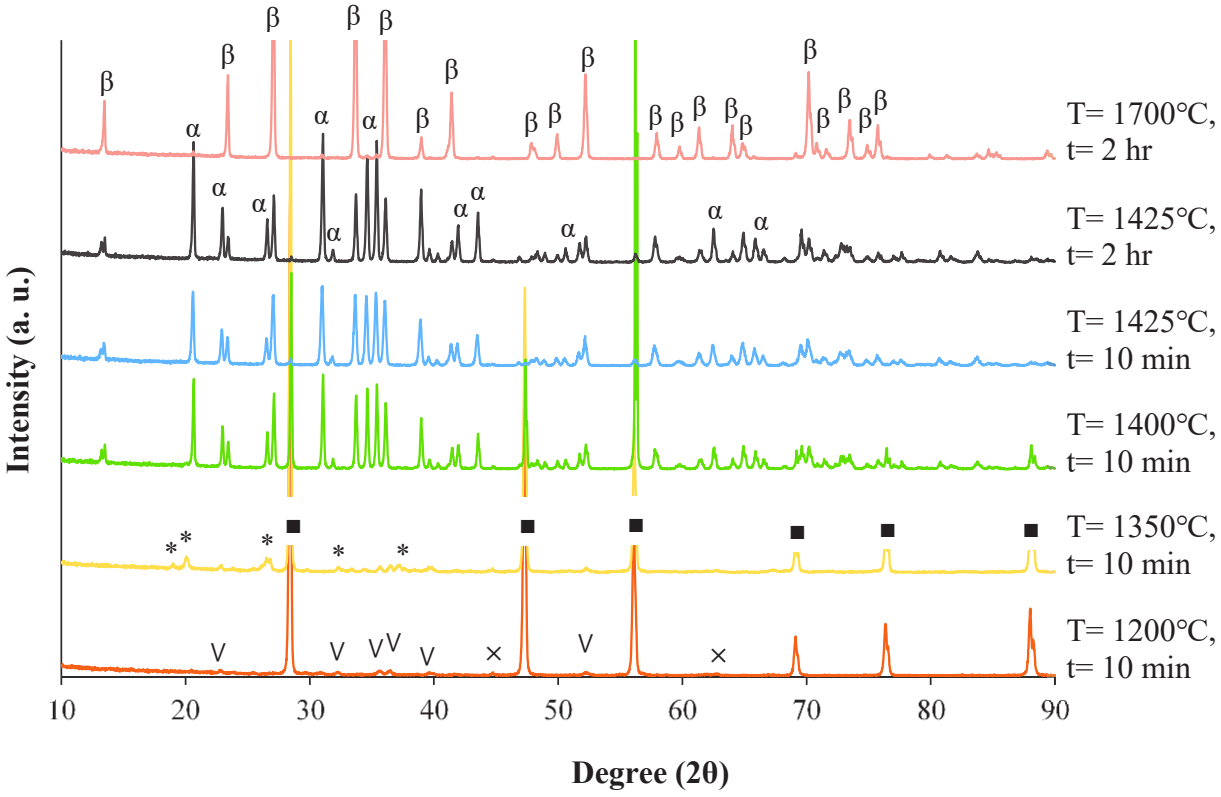

Fig. 6.4. XRD patterns of samples containing 15 mol.% magnesium oxide (α, β , ∗, ∨, × and ■ show peaks corresponded to α-Si_3N_4, β-Si_3N_4, Si_2N_2O, Mg_2SiO_4, MgO and Si, respectively)

Table 6.3. Phase contents of samples containing 15 mol.% MgO

Heating conditions	wt.%					
	Si	Mg_2SiO_4	Si_2N_2O	α-Si_3N_4	β-Si_3N_4	α/β-Si_3N_4
T= 1200°C, t= 10 min	99.23	0.77	0.00	0.00	0.00	---
T= 1350°C, t= 10 min	95.96	0.89	3.14	0.00	0.00	---
T= 1400°C, t= 10 min	75.04	0.00	0.89	13.21	10.84	1.66
T= 1425°C, t= 10 min	4.69	0.00	0.00	48.62	46.68	1.04
T= 1425°C, t= 2 hr	3.67	0.00	0.00	61.30	35.03	1.75
T= 1700°C, t= 2 hr	0.00	0.00	0.00	1.53	98.47	0.01

6.3.1.3. CaO-RBSN

Fig. 6.5 shows the SEM micrographs of CaO-RBSN after 2 hours of heating at 1425°C. In the presence of CaO, deposition of mainly α-matte grains led to the formation of more or less spherical pores**.** While the incorporation of 10 mol.% CaO (**Fig. 6.5a** and **b**) caused a significant difference in the morphology of grains, the presence of 15 mol.% CaO (**Fig. 6.5c** and **d**) entirely hindered whisker formation. An important observation here is that unlike Al_2O_3-RBSN, cavities were no longer filled with whiskers; therefore, highly interconnected channels with open spherical pores were fabricated.

The results of X-ray diffraction and phase compositions in **Fig. 6.6** and **Table 6.4** revealed the formation of various calcium silicates. At 1200°C, in addition to the strong Si peaks, a small amount of β-$CaSiO_3$ was detected. A solid-state reaction between CaO and SiO_2 at T> 900°C acts as a sink for the native surface silica and leads to the formation of $CaSiO_3$ [183, 184]. Thermodynamic data extracted from the "Reaction" module in FactSage 6.4 package software also

illustrated very high negative ΔG° for formation of $CaSiO_3$ via **Eq. 6.5**, e.g., -87.959 kJ. mol^{-1} at 1200℃.

$$CaO\,(s) + SiO_2\,(s) \rightarrow CaSiO_3\,(s) \quad \Delta G^{\circ} = -84.959\text{-}0.0025T \text{ kJ. mol}^{-1},\ T \approx 1125\text{-}1465℃ \quad \textbf{Eq. 6.5}$$

Phase transformation of $\beta \rightarrow \alpha$ and formation of α-$CaSiO_3$ has been previously observed at T> 1100℃ [183, 184]. Likewise, in the current study, when the heating temperature reached 1350℃, β-$CaSiO_3$ disappeared and α-$CaSiO_3$ formed.

At 1400℃, along with initiation of the nitriding reaction, X-ray diffraction confirmed the presence of ≈ 5 wt.% $CaSi_2O_2N_2$, which increased with heating temperature and time.

In the CaO-SiO_2 binary system, the first eutectic liquid forms at T≈ 1435℃, quite near the nitriding temperature, which could have been reduced by more than 100℃ in the presence of nitrogen and iron [37, 185]. To investigate the possibility of eutectic melt formation at 1425℃, the morphology of samples heat-treated for various time has been investigated. After 10 min heating, β-grains nucleated in the form of small polyhedrons (**Fig. 6.7a** and **b**). Although the formation of glassy phase (as a sign of liquid phase formation) was indiscernible by SEM in **Fig. 6.7a** and **b** or in **Fig. 6.5c** and **d**, by extending the heating time, SEM-EDX analysis in **Fig. 6.7c** to **f** confirmed the presence of Si-Ca-O-N glassy phase at grain boundaries. Based on the results of SEM along with XRD analysis in **Table 6.4**, with an increase in the content of $CaSi_2O_2N_2$, α-Si_3N_4 dissolved and β-peaks grew in Ca-containing glassy phase (**Fig. 6.7d**, L≈ 8.5 μm). Consequently, after 4 hr heating, the α/β phase ratio decreased while the content of $CaSi_2O_2N_2$ increased. Although under nitrogen atmosphere the formation of $CaSi_2O_2N_2$ has been reported via a solid-state reaction [186]; in the current study, formation of this phase coincided with the disappearance of $CaSiO_3$. It is inferred therefore that similar to the growth of β-Si_3N_4, the formation of $CaSi_2O_2N_2$ occurred via a liquid phase reaction.

Similar to MgO, under neutral atmosphere, vaporization and decomposition of CaO (s) has been reported at elevated temperature [124]. Therefore, it is postulated that generated oxygen would alter the vapor pressure of species in the surrounding atmosphere [55]. Oxygen impurity inhibits reaction of atomic N, maximizes the α/β-Si_3N_4 phase ratio and reduces the content of SiO vapor. Additionally, formation of intermediate phases (e.g., $CaSi_2O_2N_2$) possibly decreased the SiO vapor

content in CaO-RBSN system. This allows the formation of α-matte grains, a whisker-free microstructure with spherical cavities and an α/β phase ratio of 3.91. Since a porous microstructure composed of calcium silicate polymorphs and big interconnected pores have improved bioactivity and biocompatibility [185, 187], this material might be interesting in biomedical applications.

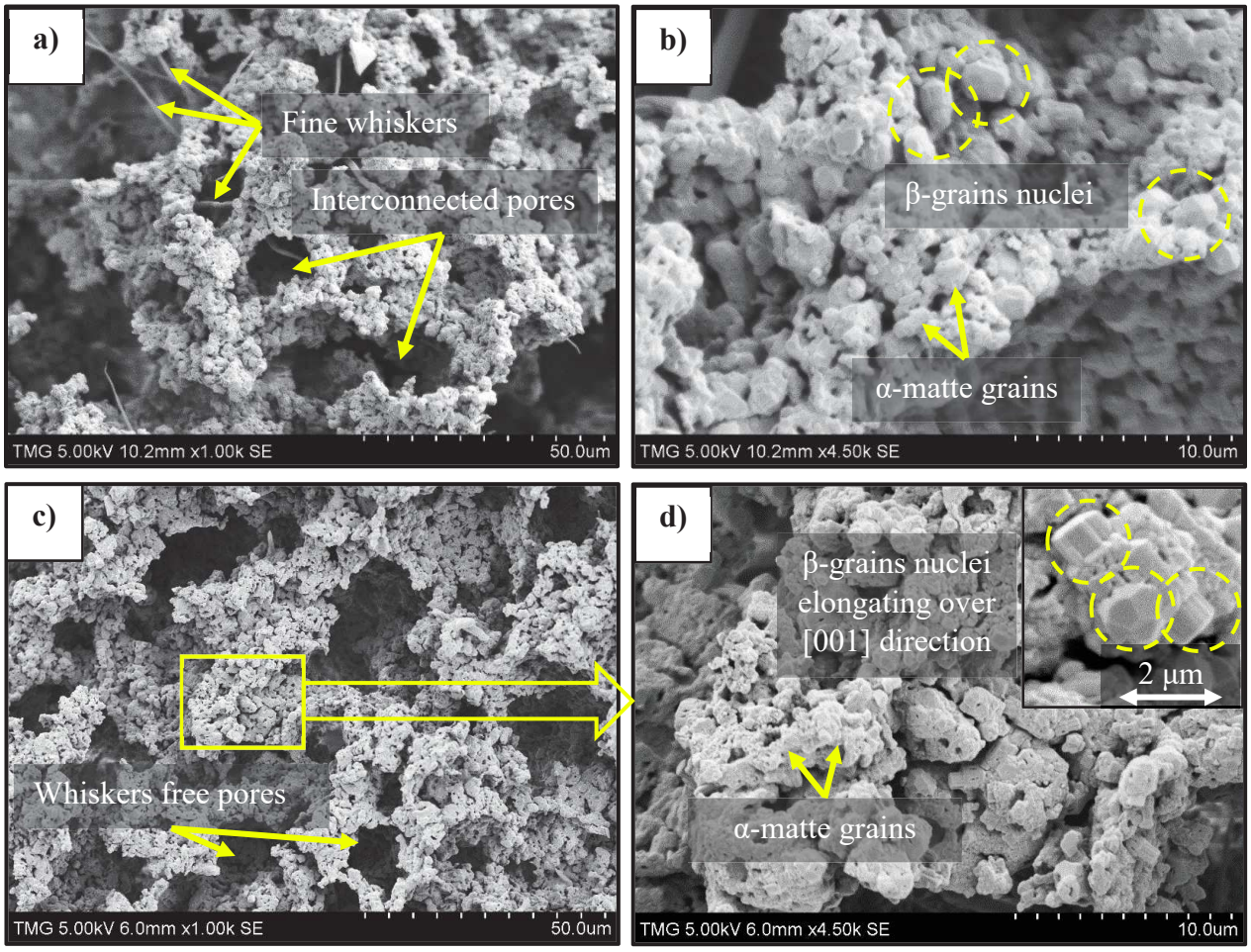

Fig. 6.5. SEM micrographs of samples containing CaO nitrided at 1425°C for 2 hr, a) and b) 10 mol.% CaO, c) and d) 15 mol.% CaO

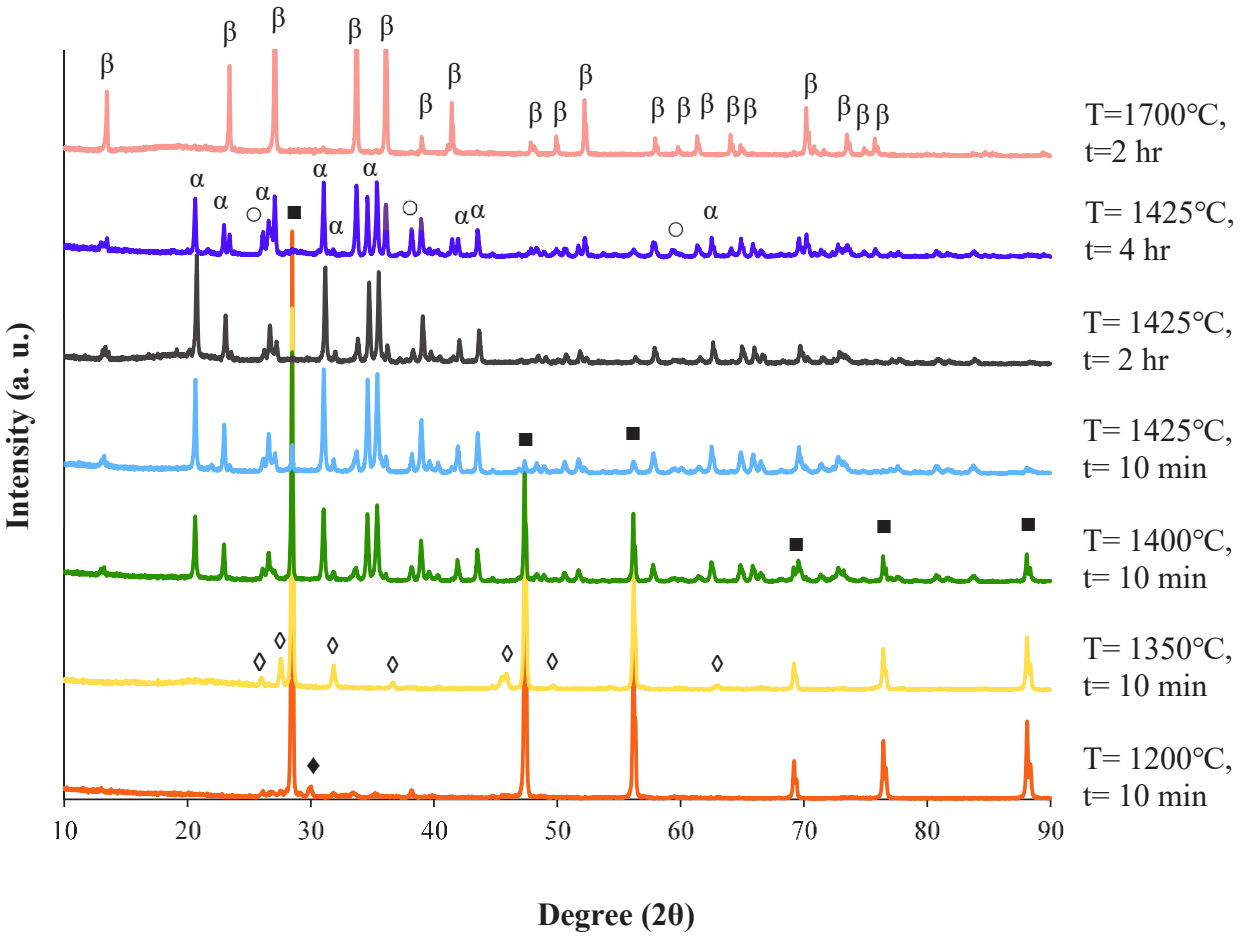

Fig. 6.6. XRD patterns of samples containing 15 mol.% calcium oxide (α, β , ◊, ♦, ○ and ■ show peaks corresponded to α-Si_3N_4, β-Si_3N_4, α-$CaSiO_3$, β-$CaSiO_3$, $CaSi_2N_2O_2$ and Si, respectively)

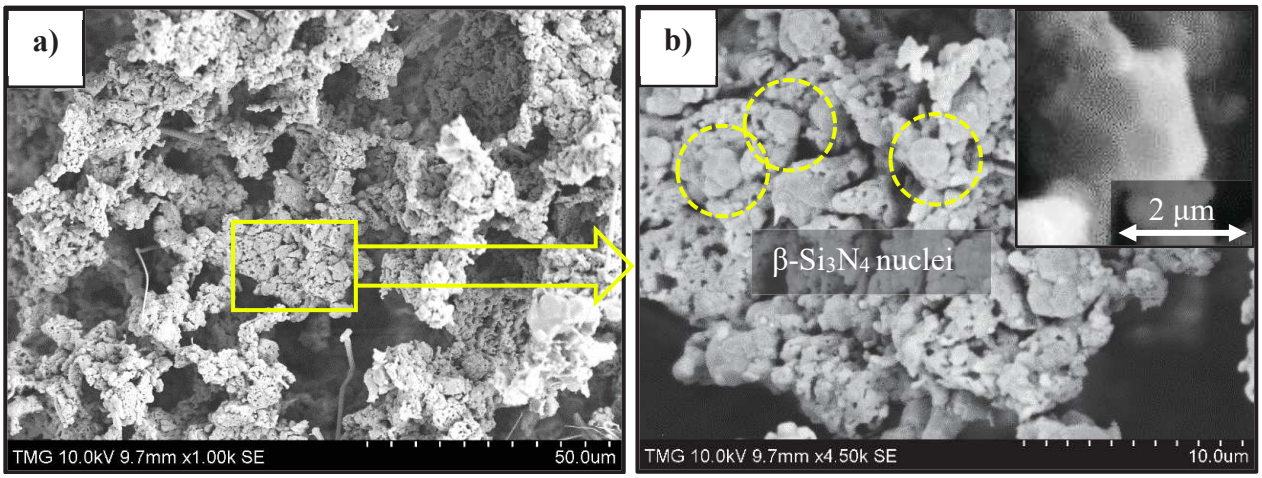

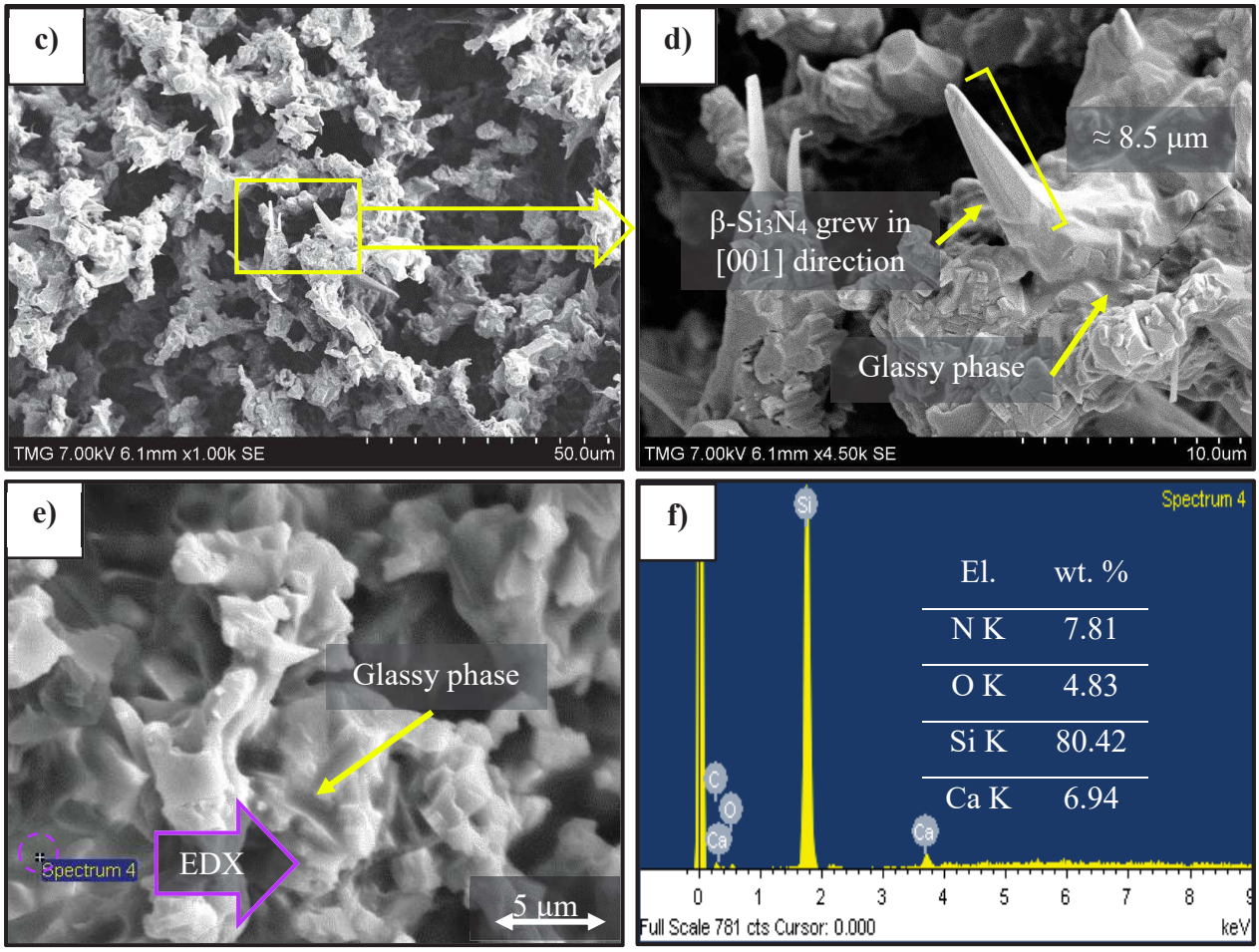

Fig. 6.7. SEM micrographs of samples containing 15 mol.% CaO nitrided at 1425°C for various time: a) and b) 10 min and c) to f) 4 hr

Table 6.4. Phase contents of samples containing 15 mol.% CaO

Heating conditions	wt.%					
	Si	$CaSiO_3$	$CaSi_2O_2N_2$	α-Si_3N_4	β-Si_3N_4	α/β-Si_3N_4
T= 1200°C, t= 10 min	97.70	2.30 (β-$CaSiO_3$)	0.00	0.00	0.00	---
T= 1350°C, t= 10 min	90.47	9.52 (α-$CaSiO_3$)	0.00	0.00	0.00	---
T= 1400°C, t= 10 min	62	0.00	5.06	29.16	3.78	7.71

T= 1425°C, t= 10 min	12.87	0.00	11.33	63.22	12.57	5.03
T= 1425°C, t= 2 hr	0.00	0.00	11.47	70.52	18.01	3.91
T= 1425°C, t= 4 hr	0.00	0.00	16.71	43.40	39.88	1.08
T= 1700°C, t= 2 hr	0.00	0.00	0.00	1.20	97.40	0.01

6.3.2. Microstructural Development During High Temperature Heat-treatment

6.3.2.1. Heat-treated Al_2O_3-RBSN

Fig. 6.8 illustrates the SEM micrographs of Al_2O_3-RBSN heat-treated at 1700°C. Compared to the microstructures in **Fig. 6.1c** and **d,** the content of whiskers has significantly decreased after 2 hr heat-treatment, **Fig. 6.8a** and **b.** This revealed the dissolution of the α-whiskers and precipitation of β-grains through LPS. The XRD pattern in **Fig. 6.2** and **Table 6.2** illustrates the presence of a single β-Si_3N_4 phase. Taking into the account that T_e in the Al_2O_3-SiO_2-Si_3N_4 system is ≈ 1470°C [37] and a very large amount of Al_2O_3 was added to the system (15 mol.% Al_2O_3 ≈ 11 wt.% Al_2O_3), no β-rod formation occurred. Obviously, the very low amount of α-phase in the original nitrided sample (≈ 7.8 wt.%) and thus the absence of enough liquid phase with sufficiently low viscosity halted the β-grain growth mechanism.

By increasing the heat-treatment holding time, still no β-grain growth occurred (**Fig. 6.8d**) while formation of a minor amount of coarse β-whiskers, perhaps composed of crystalline cores and an amorphous sheath containing the additive element [20], were observed in **Fig. 6.8e**. The presence of Al, possibly dissolved in an amorphous glassy phase, was confirmed by EDX in **Fig. 6.8f**. The results of XRD analysis illustrate the presence of β-Si_3N_4 as the single crystalline phase and no sign of β-SiAlON or Mullite ($Al_6Si_2O_{13}$) formation was detected during the heating procedures.

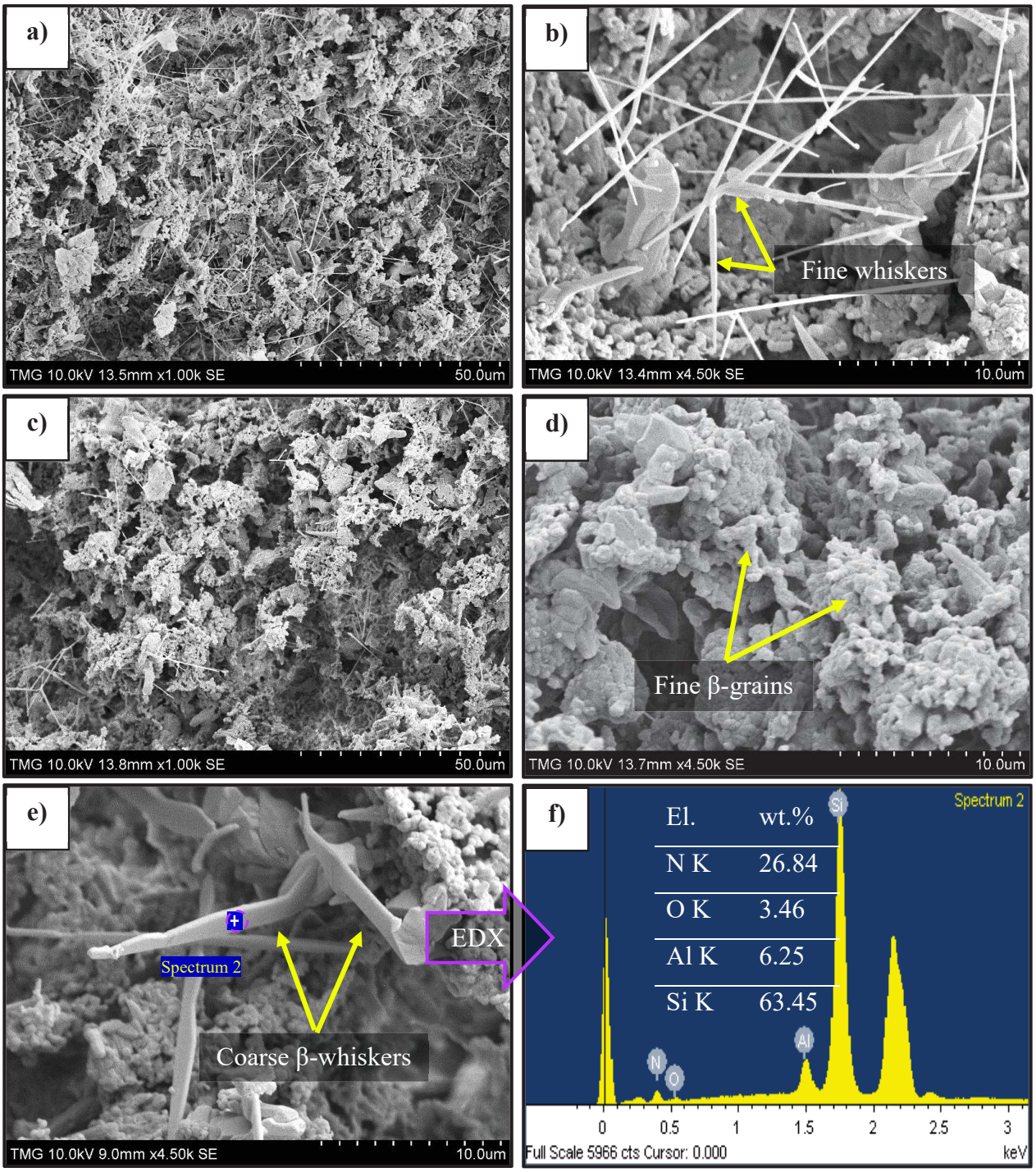

Fig. 6.8. SEM of fracture surfaces illustrating the morphology of silicon nitride grains in the presence of 15 mol.% Al_2O_3 heat-treated at 1700°C for various time, a) and b) 2 hr, c and d) 4 hr and e and f) growth of coarse β-whiskers

6.3.2.2. Heat-treated MgO-RBSN

Unlike Al_2O_3-RBSN, the SEM micrographs of heat-treated MgO-RBSN at 1700°C demonstrate the formation of beta-grains with no whiskers present in the structure as shown in **Fig. 6.9a** to **d**. This suggests that the fine whiskers observed in MgO-RBSN in **Fig. 6.3c** and **d** were α-Si_3N_4 but vanished during the LPS process. In MgO-SiO_2-Si_3N_4, liquid silicate forms at temperatures around 1390°C [37] which lowers the α → β phase transformation activation energy and accelerates β-grain growth through a solution-precipitation process [36, 188]. At 1700°C, XRD analysis in **Fig. 6.4** and **Table 6.3** confirmed the existence of β-grains as the dominant phase with almost 1.5 wt.% residual α-Si_3N_4.

Heat-treatment for 4 hr led to the formation of coarse elongated β-grains with a relatively unimodal microstructure (**Fig. 6.9c** and **d**). The aspect ratio of β-Si_3N_4 rods (**Fig. 6.10b**) was calculated based on the dimensions of almost a hundred grains from the SEM micrographs of fracture surfaces. Having relatively similar aspect ratio, **Fig. 6.10a** shows the length distribution (< 8 μm) and the width distribution (< 3 μm) of β-Si_3N_4 rods. Grain growth starts from the previously existing β-nucleus by dissolution of fine grains and phase transformation as the driving force. Hence the volume fraction and size of the initial β-grains control the microstructural development [139]. In the presence of ≈ 61 wt.% α-phase as well as ≈ 35 wt.% β-nuclei, a homogeneous microstructure with relatively similar grain size has developed after the 4 hr heat-treatment.

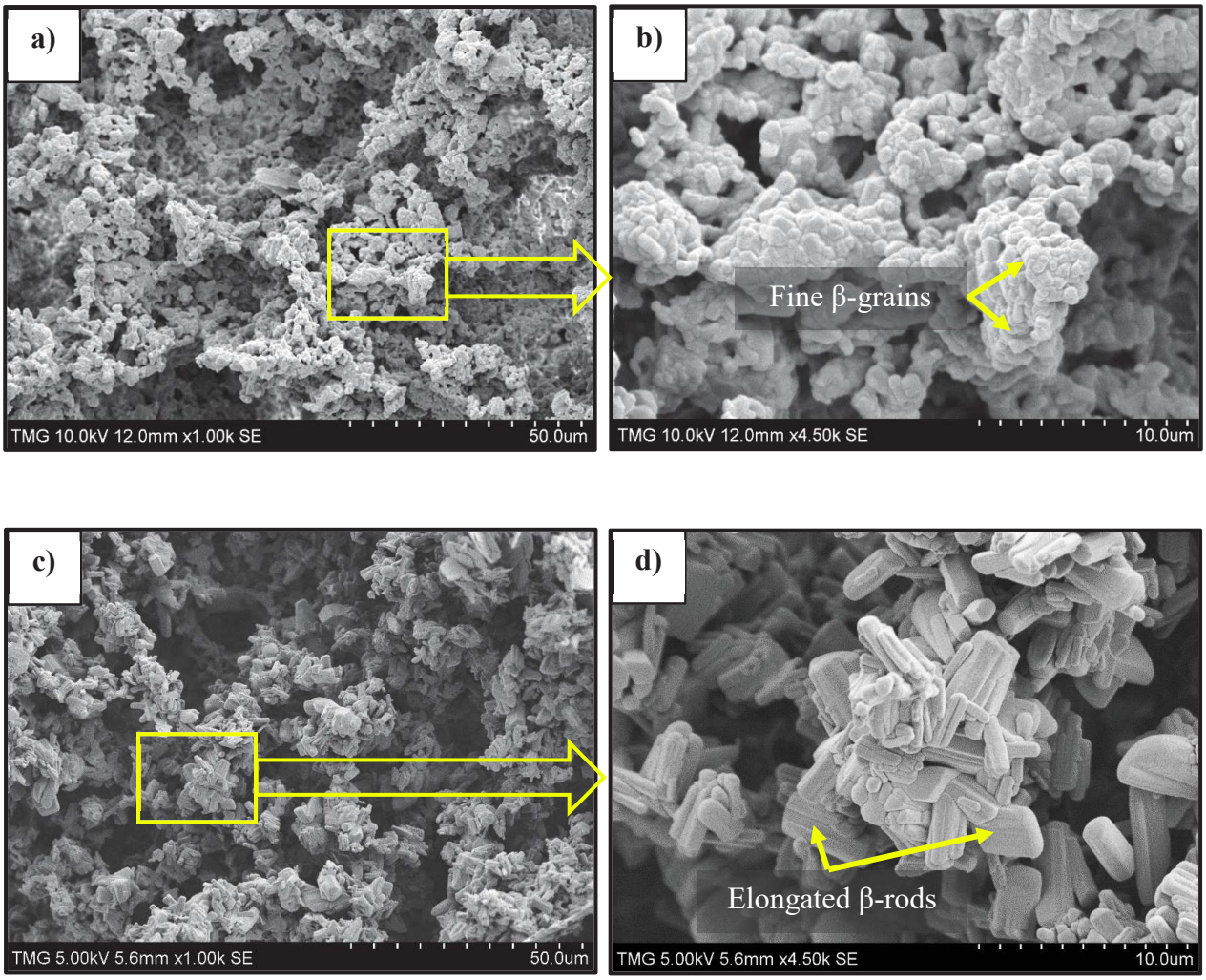

Fig. 6.9. SEM micrographs of samples containing 15 mol.% MgO heat-treated at 1700℃ for various time, a and b) 2 hr, c and d) 4 hr

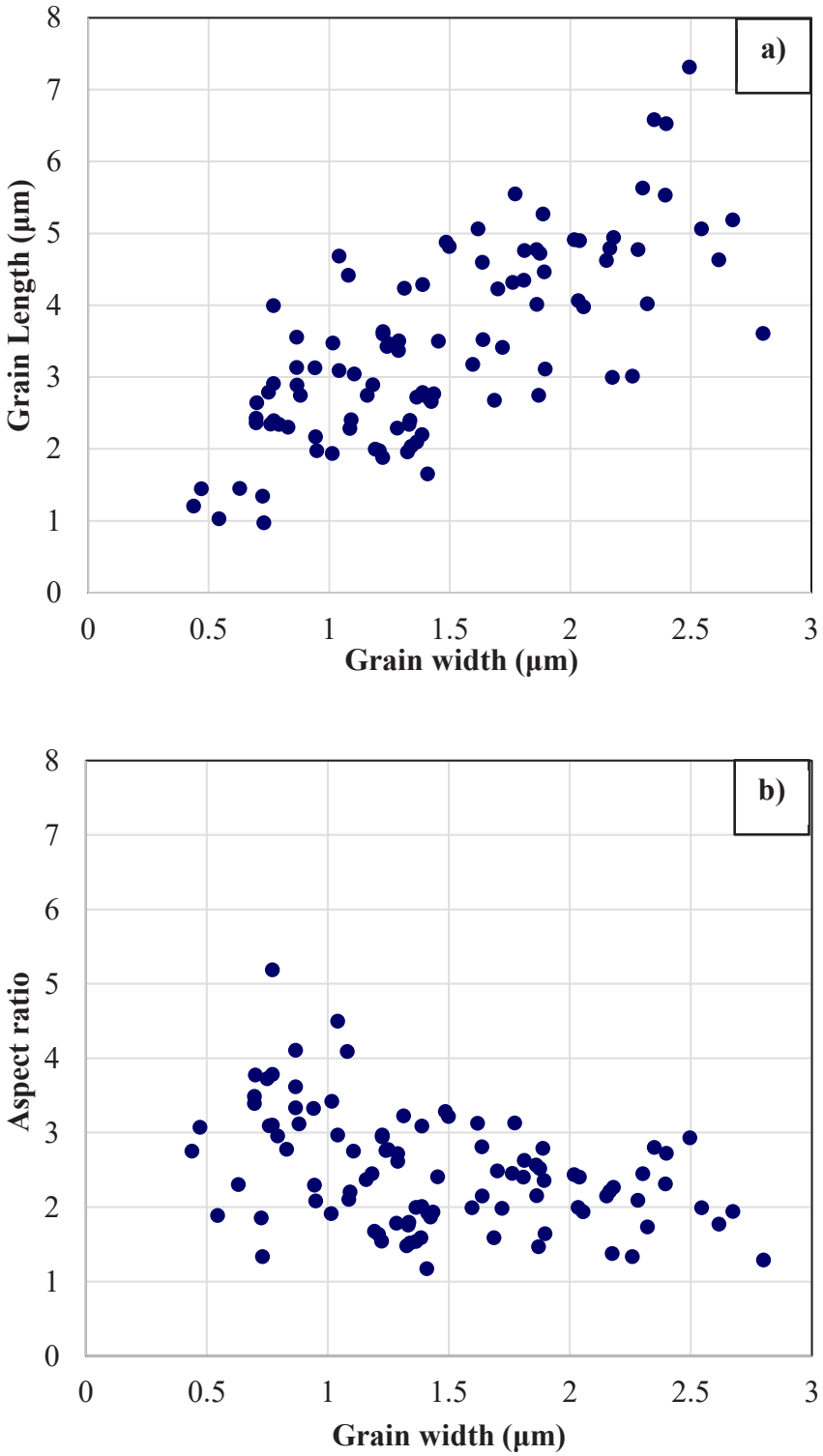

Fig. 6.10. a) The measured length-width distributions and b) the measured aspect ratio-width distributions of β-Si_3N_4 grains after 4 hr heat-treatment of MgO-RBSN

6.3.2.3. Heat-treated CaO-RBSN

Fig. 6.11 illustrates SEM micrographs of heat-treated CaO-RBSN at 1700℃. These figures demonstrate the formation of a bimodal microstructure due to the selective growth of large grains. Fine-grains clustered around highly elongated β-grains are embedded in an inter-granular Si-Ca-O-N amorphous phase (**Fig. 6.11d**). The development of a broad grain size distribution is evident in **Fig. 6.12**.

After a 2 hr heat-treatment (**Fig. 6.11a** to **c**), the reaction of α-Si_3N_4 with a eutectic phase led to the anisotropic grain growth and formation of β-rods with significant growth along the basal plane (001), controlled by diffusion mechanism, rather than growth normal to the prismatic plane (100) [189]. Based on the result of XRD (**Table 6.4**), a combination of ≈ 70 wt.% α-Si_3N_4 with ≈ 18 wt.% β-Si_3N_4 resulted in a small number of nuclei and a strong driving force for grain growth. In normal grain growth mechanisms, rapid consumption of liquid phase by coarse grains led to a shortage of liquid to feed the growth of fine nuclei [47]. In addition, inhomogeneous liquid phase distribution in the CaO-RBSN as a result of having coarse additive particles (particle size of CaO≈ -20 mesh while particle size of MgO≈ -325 mesh) led to the local super-saturation. Therefore, homogeneous nucleation and grain growth became difficult. After the 2 hr heat-treatment, formation of highly elongated needle-like grains with lengths up to 20 μm and very high aspect ratio (**Fig. 6.12**) are therefore attributed to the high super-saturation and the local inhomogeneity in the distribution of liquid phase [190, 191].

However, by increasing the dwelling time to 4 hr, a decrease in β-Si_3N_4 aspect ratios was observed in **Fig. 6.11e** and **f**. Due to a more uniform distribution of liquid phase along the grain boundaries, grain growth occurred simultaneously at multiple locations; the space was squeezed by further linear shrinkage and the growth of grains with high aspect ratio was hindered [62]. Evidence of growth hindrance by impingement with neighboring β-grains has been previously observed in similar porous samples [62]. This led to the formation of a bimodal microstructure with a broad grain size distribution and low aspect ratio (**Fig. 6.12**).

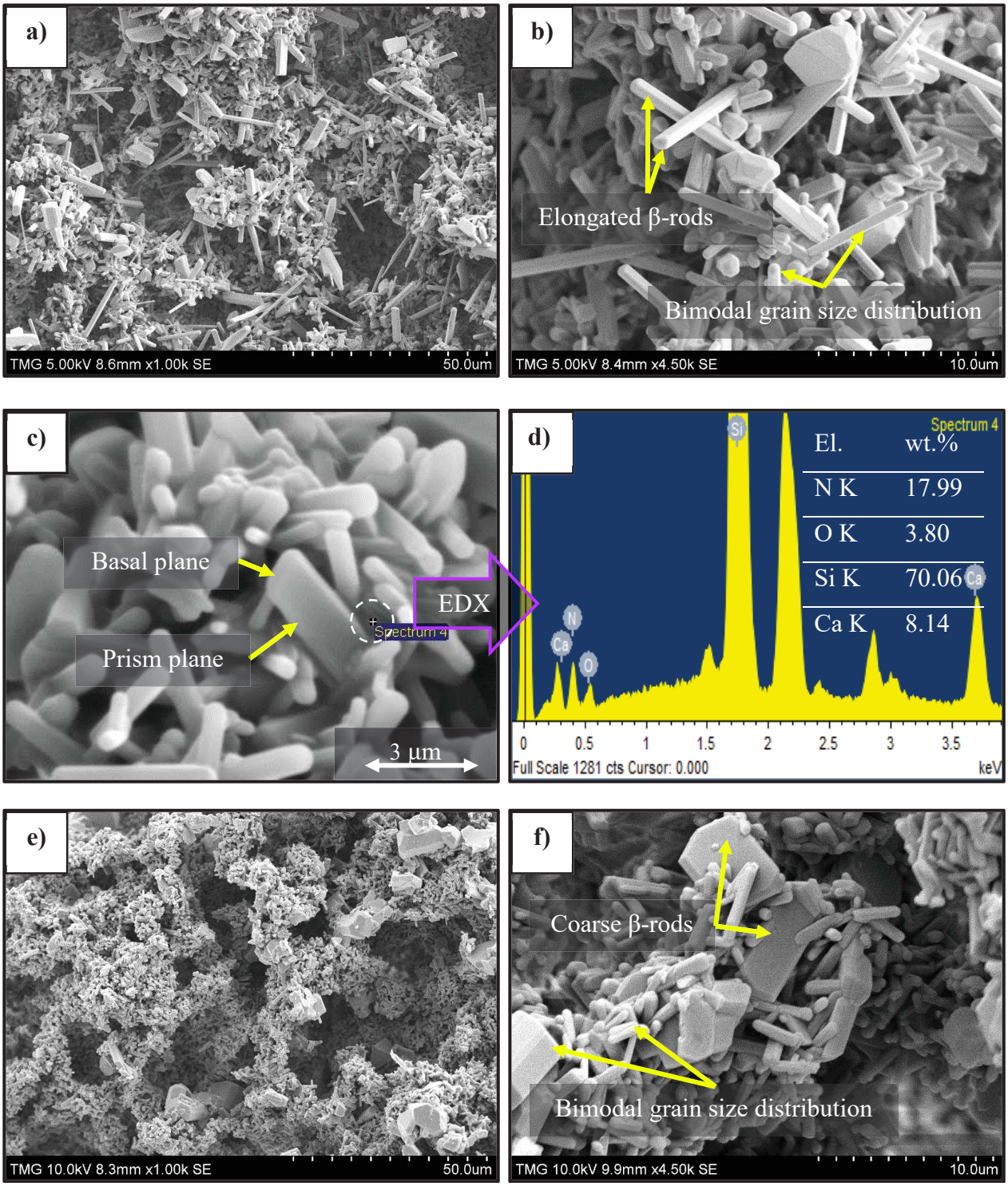

Fig. 6.11. SEM micrographs of samples containing 15 mol.% CaO heat-treated at 1700°C for various time, a), b) and c) 2 hr, e) and f) 4 hr. d) shows the EDX profile obtained from the micrograph in Fig.6.11c.

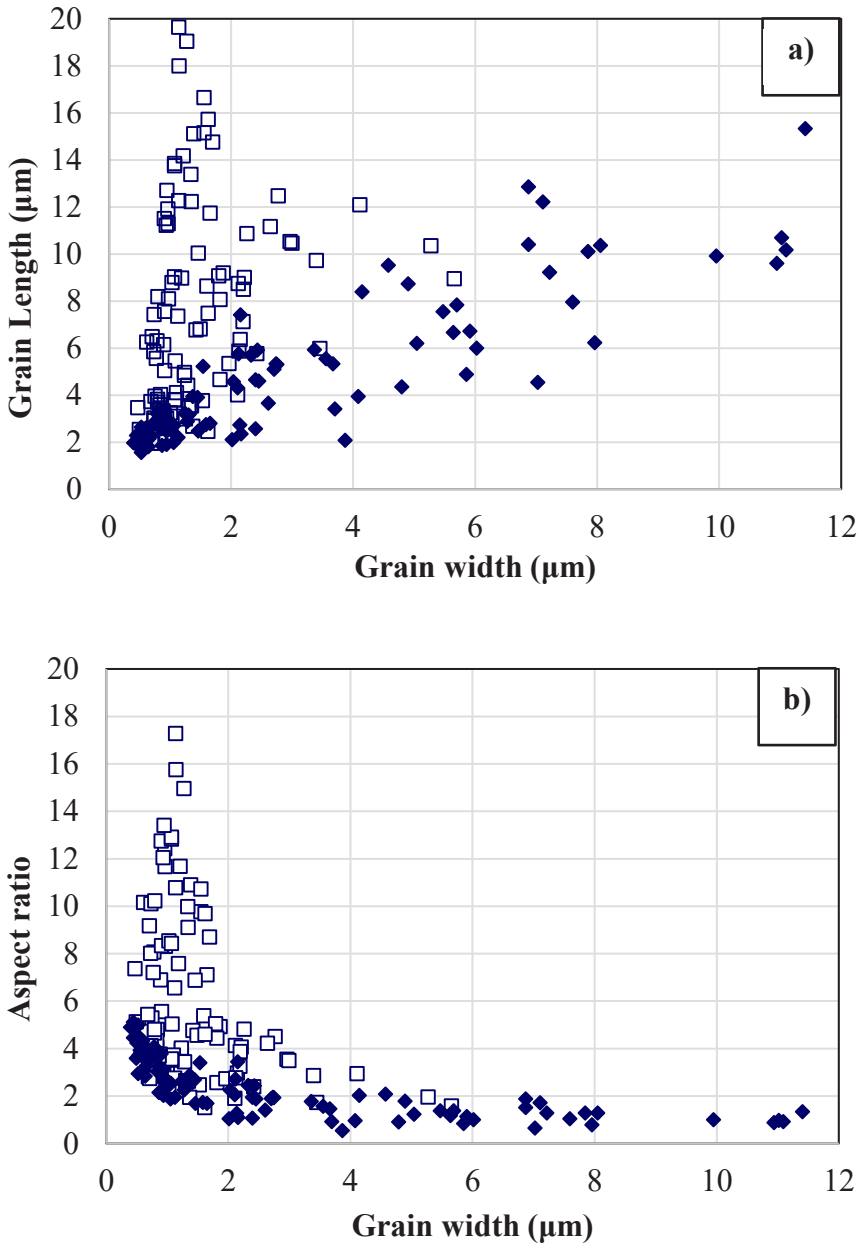

Fig. 6.12. a) The measured length-width distributions and b) the measured aspect ratio-width distributions of β-Si_3N_4 grains after 2 hr (□) and 4 hr (♦) heat-treatment of CaO-RBSN sample

6.3.3. Linear Shrinkage

The influence of phase composition on linear shrinkage during heat-treatment is shown in **Fig. 6.13.** In pressureless-sintering of Si_3N_4-based ceramics, a high viscosity liquid may promote α → β phase transformation but does not contribute significantly to particle rearrangement and

densification [62]. Similarly, the remarkably low shrinkage in Al_2O_3-RBSN after 2 or 4 hr heating could be attributed to the very low α/β-phase ratio and a high viscosity liquid phase formed during the heat-treatment, which impeded densification and led to only ≈ 0.4% shrinkage. Based on the average values in **Fig. 6.13**, when MgO was added to the system, low shrinkages, similar to that of the Al_2O_3-RBSN sample, occurred after 2 hr heating, however in the case of CaO addition shrinkage was ≈ 1%. The high α/β-phase ratio in CaO-RBSN provided a greater driving force for phase transformation which accelerated the densification [45, 62] and enhanced the linear shrinkage. Additionally, the formation of ≈ 11.5 wt.% $CaSi_2N_2O_2$ in the nitrided sample was desirable during densification by lowering the melting point and viscosity of liquid phase [186].

By extending the heating time to 4 hr a general increase in linear shrinkage was observed. After 4 hr heat-treatment, the overall linear shrinkage in MgO-RBSN (≈ 2.6%) was more than that of CaO-RBSN (≈ 1.6%). This could be attributed to the fact that in the CaO-SiO_2 binary system, formation of a liquid phase during nitriding is very likely ($T_e \leq$ 1435°C [37]) and thus LPS, partial shrinkage and particle rearrangement could have already started prior to the post heat-treatment. In contrast, in the MgO-SiO_2 binary system, the first liquid eutectic forms at higher temperature ($T_e \leq$ 1543°C [37]). Additionally, homogenous distribution of fine MgO particles could increase the extend of particle rearrangement. Phase transformation and grain growth simultaneously occurred in multiple regions instead of the locally dispersed liquid phase. Therefore, MgO-RBSN illustrated more shrinkage and uniform grains after 4 hr heat-treatment at 1700°C.

It is important to note that prior to the nitridation, we dealt with quite fragile and loose particle samples, therefore measuring the initial stages of shrinkage during the nitriding process was not feasible. Shrinkage further contributes to the decrease in porosity and densification of the structures.

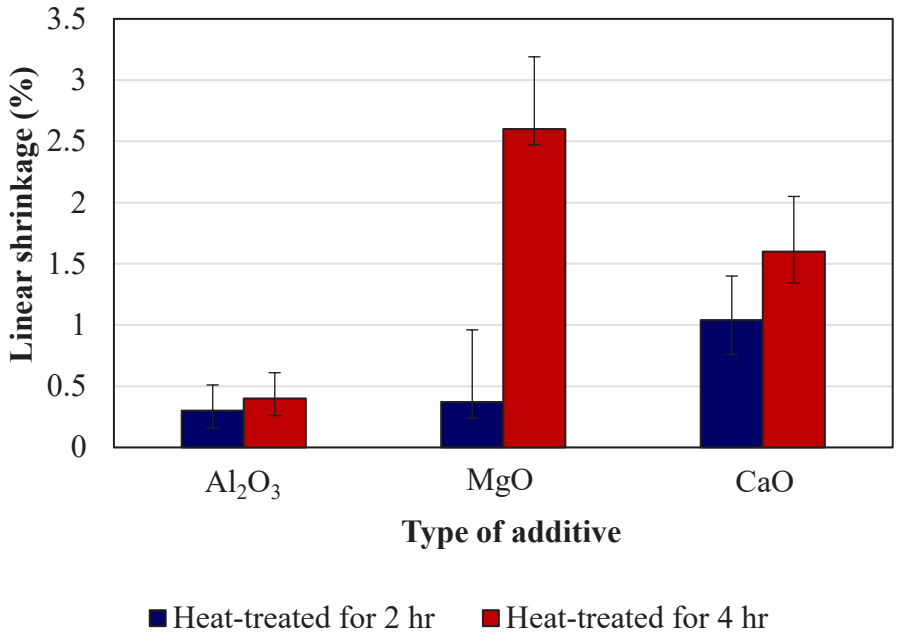

Fig. 6.13. Linear shrinkage after heat-treatment in the presence of different additives

6.3.1. Flexural Strength Results

Porous RBSN has been produced with various microstructures depending on the synthesis conditions and chemical compositions. A transition from a whisker-dominated microstructure with fine pores in Al_2O_3-RBSN to clean large pore cavities in CaO-RBSN is clearly apparent in **Fig. 6.16.** The results of average values for 3-point bending strength versus sample specifications are presented in **Table 6.5**. In porous brittle ceramics, pores are considered as the main defects lowering the flexural strength and this decreases exponentially with rise in porosity [47, 48, 193]. With the high porosity content of ≈ 78-85 vol.% and bulk density of ≈ 0.45-0.60 g. cm^{-3}, quite low flexural strengths were observed for all samples, roughly < 2.5 MPa, as shown in **Table 6.5**.

Owing to the microstructure composed of 3D interconnected whiskers, Al_2O_3-RBSN (**Fig. 6.16a**) illustrates a flexural strength of ≈ 2.42 MPa. This observation was in accordance with literature reporting the reinforcement potential of whiskers in porous ceramic matrices [194]. As no densification occurred during the heat-treatment, the strength decreased to ≈ 1.4 MPa due to the loss of interlocked whiskers (**Fig. 6.16b**).

MgO-RBSN has exhibited the lowest flexural strength (≈ 0.3 MPa). This sample was composed of high porosity (≈ 85 vol.%), low density (0.45 g cm^{-3}), ≈ 3.6 wt.% residual silicon, large pores and poorly-bonded matte grains (**Fig. 6.16c**). Unlike the 3D-interlocked whiskers in Al_2O_3-RBSN, a negligible content of fine and dispersed whiskers in MgO-RBSN did not increase grain interlocking. Even though the heat-treatment densification and full nitridation slightly improved the flexural strength, large pores and high porosity (**Fig. 6.16d**) led to a very weak microstructure.

By hindering the formation of whiskers, pores with large open cavities (e.g., 31 μm) and circle windows have been fabricated in CaO-RBSN (**Fig. 6.13e**). Having lower porosity (≈ 82 vol.%) compared to that of MgO-RBSN (≈ 85 vol.%), the flexural strength slightly increased. After a 4 hr heat-treatment, the porosity decreased (≈ 78 vol.%) and mechanical interlocking increased within the anisotropic grains (**Fig. 6.16f**). With crack bridging and crack deflection, therefore, rod-like β-Si_3N_4 grains stopped the propagation of cracks, reducing the possibility of inter-granular defects [47, 58] and consequently improving the flexural strength to ≈ 1.87 MPa. These observations illustrate that the strength of porous RBSN ceramics was simultaneously influenced by porosity and density, residual silicon, pore structure and grains morphology.

Table 6.5. Bending strengths of samples versus their specifications

Sample	Heating conditions		Flexural strength (MPa)	Porosity (vol.%)	Density (g cm^{-3})	Residual Si (wt.%)
	T (°C)	t (hr)				
Al_2O_3-RBSN	1425	2	2.42	80.89	0.58	0.00
Heat-treated Al_2O_3-RBSN	1700	4	1.40	81.49	0.59	0.00
MgO-RBSN	1425	2	0.30	85.11	0.45	3.67
Heat-treated MgO-RBSN	1700	4	0.44	82.61	0.52	0.00
CaO-RBSN	1425	2	0.84	82.26	0.53	0.00
Heat-treated CaO-RBSN	1700	4	1.87	78.67	0.59	0.00

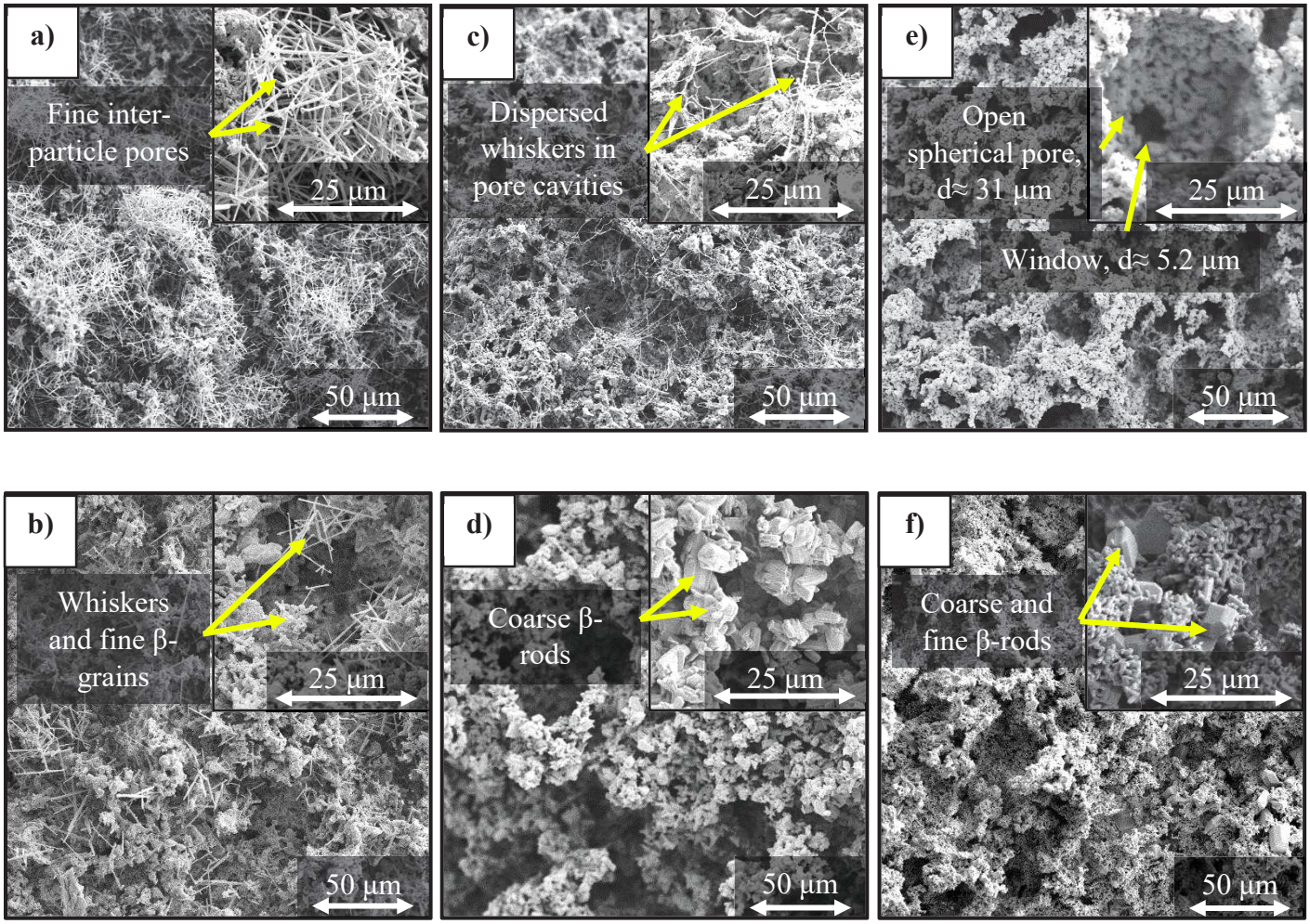

Fig. 6.16. Microstructures of pores in Si_3N_4 ceramics containing various oxides: a) Al_2O_3-RBSN, b) heat-treated Al_2O_3-RBSN, c) MgO-RBSN, d) heat-treated MgO-RBSN, e) CaO-RBSN and f) heat-treated CaO-RBSN

6.3.2. Porosity and Density of Porous Samples

The effect of additives on porosity and bulk density of nitrided and 4 hr heat-treated samples are shown in **Fig. 6.14** and **6.15**, respectively. The conversion of silicon to silicon nitride is accompanied by simultaneous structural changes and volume expansion. In this study, deducing information from mass changes during the heating process seemed impractical because of the complication of different factors occurring simultaneously, such as weight gains due to nitriding, formation of intermediate phases from other gases and weight loss by evaporation and decomposition.

In MgO-RBSN, in addition to the partial nitridation and residual silicon, lack of densification during the nitriding process led to the highest porosity (≈ 85 vol.%) and the lowest density (≈ 0.45 g cm^{-3}). Lamoreaux et al. has stated that between ≈ 10^{-15} and 0.2 atm oxygen partial pressure, the maximum vaporization rate of MgO at 1425°C is more than that of CaO and Al_2O_3 [124]. This illustrates that the high porosity of MgO-RBSN could be partly attributed to the high evaporation rate of MgO. In CaO-RBSN, possible eutectic formation and partial densification prior to the post heat-treatment led to a slightly lower porosity (≈ 82 vol.%) and a higher density (≈ 0.53 g cm^{-3}). Moreover, liquid-phase sintering densification occurred in the presence of MgO and CaO during the heat-treatment and reduced the porosity to the values of ≈ 82 vol.% and ≈ 78 vol.%, respectively.

Unlike the two above-discussed systems, Al_2O_3 has a low vapour-pressure at elevated temperature [124]; consequently produced a porosity of ≈ 80 vol.% and density of ≈ 0.6 g cm^{-3} in Al_2O_3-RBSN. In LPS, the final content of porosity is controlled by the two counteracting processes of shrinkage and bulk decomposition [192]. Accordingly, the slight increase in the porosity of heat-treated Al_2O_3-RBSN could be attributed to the thermal decomposition and loss of material at 1700°C which was not accounted for in the shrinkage and densification.

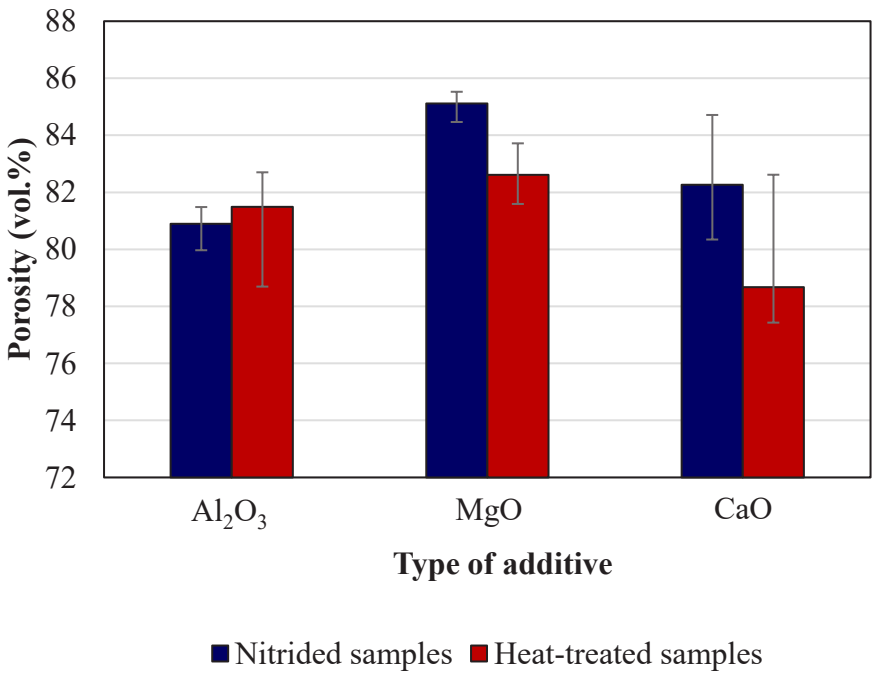

Fig. 6.14. Porosity of samples in the presence of different additives

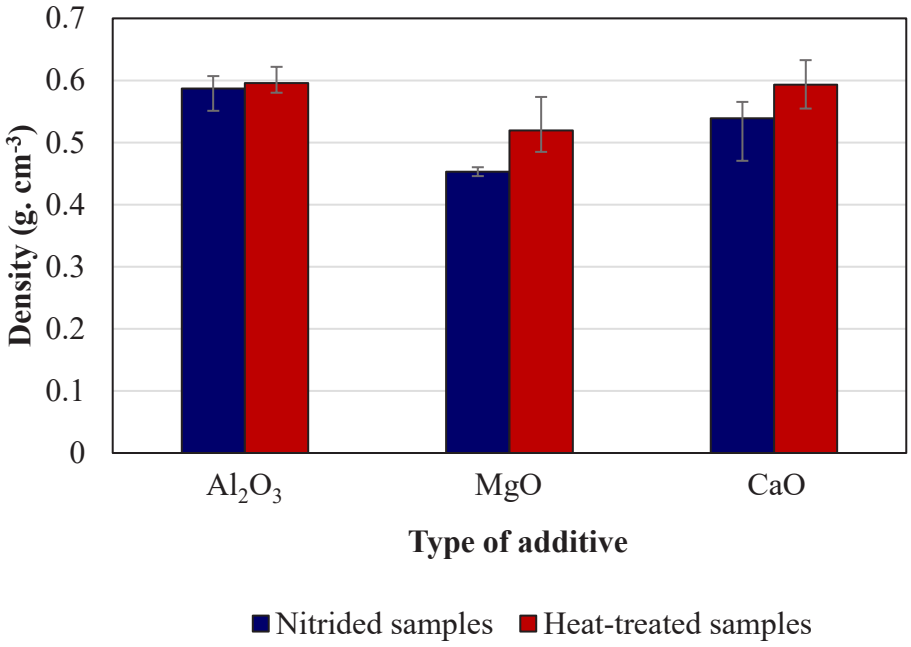

Fig. 6.15. Bulk density of samples in the presence of different additives

6.4. Conclusions

The aim of this study was to develop porous reaction bonded silicon nitride (RBSN) having various pore morphologies ranging from clean cavities to those fully occupied with whiskers. To control the nitriding mechanism, CaO, MgO and Al_2O_3 were used as oxide additives.

CaO additions impeded whisker formation and led to a drastic change in the microstructure by minimizing the content of whiskers and maximizing the α/β-phase ratio. α-matte grains and spherical pores (< 40 μm) with interconnected channels formed via nitridation of Si (g). The presence of significant content of α-Si_3N_4, formation of calcium silicates, a large driving force and inhomogeneous liquid phase distribution resulted in abnormal β-grain growth. At 1700°C, a bimodal microstructure with a wide grain-size distribution was developed. Heat-treatment densification led to the porosity of ≈ 78 vol.% and flexural strength of ≈ 1.8 MPa.

In contrast, a fast-gaseous reaction between SiO (g) and N_2 in the presence of Al_2O_3 led to the formation of whiskers in the pore structure. β-rich microstructure with fine grains was developed possibly due to the low content of generated oxygen and high stability of alumina at elevated

temperatures. The nitrided samples with interlocked whiskers and fine inter-particle pores showed an enhanced flexural strength (≈ 2.4 MPa). At 1700°C, α-whiskers disappeared, and porosity increased which decreased the mechanical interlocking and strength. Owing to the minor amount of liquid phase, this sample showed extremely low densification, low linear shrinkage and negligible grain growth.

For MgO-RBSN, a combination of Si (g) and SiO (g) nitridation led to the formation of α-matte grains with fine α-whiskers. A highly porous structure (≈ 85 vol.%) with minor unreacted silicon decreased the flexural strength to ≈ 0.3 MPa. At 1700°C, due to a homogenous liquid phase distribution and simultaneous grain growth at multiple locations, a unimodal microstructure with coarse β-grains and relatively similar aspect ratio were developed. This study illustrates that in reaction bonding of silicon powder, depending on the interactions of oxide additives with silicon and surface silica, nitridation mechanism can be altered to tailor the morphology of grains and pores, as well as the ratio of α/β-Si_3N_4.

Chapter 7. Conclusions and Future Work

7.1. Summary of Conclusions

This research aimed to develop porous RBSN ceramics with various microstructures and to investigate the roles of MgO, CaO and Al_2O_3 additives, temperature and powder bed on the properties of the resultant porous ceramic. In this thesis, porous silicon nitride ceramics have been fabricated based on a combination of gel-casting and sacrificial template techniques followed by nitriding and post heat-treatment. Mechanisms and thermodynamics of reactions, microstructural characteristics and evolutions, phase transformation, pore morphology, pore size distribution, interconnectivity and accessibility of pore channels, porosity and density, and mechanical strength of samples are some of the topics which are addressed in this study. The experimental results are summarized as follows:

As a result of a vapor-liquid-solid reaction between SiO in ultra-pure nitrogen gas, α-Si_3N_4 whiskers with high aspect ratio grew randomly in different directions, formed spherical clusters and blocked the pore cavities in RBSN samples. The nitriding mechanism and microstructural properties were studied in the presence of 0 to 12 wt.% MgO. It was observed that magnesia interfered with whisker formation and gradually modified the nitriding microstructure to a combination of α-matte grains and β-rods. Using thermodynamic data extracted from FactSage software, it was demonstrated that in an MgO-containing system, the mechanism of reactions was markedly altered in favor of Si (g) nitridation rather than that of SiO (g). At 3 wt.% MgO, a low content of whiskers was observed in pore cavities, whilst the full transition to α-matte and β-rods was achieved only in the presence of 12 wt.% MgO.

During the nitriding process, formation of granular Si_3N_4 in a porous sample containing no MgO but placed in an MgO-containing powder bed confirmed the high volatility of this oxide at elevated temperatures. The information obtained from the detailed microstructural analyses along with thermodynamic studies suggested that this morphology change could be due to the interference of MgO vapor with the presence and nitridation of SiO (g). Accordingly, instead of whisker formation, intermediate products, i.e., Si_2N_2O and Mg_2SiO_4, were identified through reaction between natural surface silica and volatile magnesia, producing an interconnected open-pore Si_3N_4 microstructure.

Compared to the sample with no additive, the α/β-Si_3N_4 phase ratio was higher in all MgO-containing samples. Both the formation of Si_2N_2O and the high α-Si_3N_4 content were attributed to the presence of oxygen in the system that originated from the added MgO. Consequently, at 1350°C, formation of α-rich Si_3N_4 microstructure was initiated from the surface of silicon grains and progressed inwards and was completed after 4 hr at 1425°C.

Full α- to β-Si_3N_4 phase transformation occurred at 1700°C after 2 hours of heating. Struts were composed of β-rods, which had precipitated in the Mg-Si-O-N oxynitride amorphous phase. A homogeneous microstructure with enhanced β-grain growth and uniform size distribution was obtained in the presence of 12 wt.% MgO.

In addition to SEM microscopy, resin-infiltrated systems, 2D cross-sections of sequential slices and 3D reconstruction images of MgO-RBSN samples confirmed the high interconnectivity of channels. Consequently, an open-pore structure with clean cavities and large pores of < 40 μm diameter increased the permeability and accessibility of channels in the porous MgO-RBSN structures.

Shrinkage and weight loss of samples during the heat-treatment were a function of MgO content. Liquid phase formation was increased by the presence of MgO which enhanced the shrinkage and grain coarsening. In contrast, high partial pressure of volatile MgO in the surrounding atmosphere and diffusion from the powder bed stopped the weight loss.

Porosity and density of heat-treated samples were controlled by both liquid phase formation and partial sintering, as well as decomposition and evaporation of volatile materials. Consequently, in the heat-treated MgO-RBSN samples, the combination of high porosity and low density led to a compressive strength between 1.1 and 1.6 MPa.

The effects of MgO-SN and SN powder beds on the morphological transition of grains and the α- to β-Si_3N_4 phase transformation were further investigated. Both RBSN and MgO-RBSN samples were embedded in powder beds of different compositions and heat-treated from 1425°C to 1700°C. Upon heat-treatment of RBSN samples in a powder bed containing MgO, α-whiskers occupying the pore volume gradually vanished and recrystallized as β-rods with a homogeneous grain size. With simultaneous grain growth, morphology modification was initiated at 1500°C and completed

at 1700°C. The results of SEM-EDX analysis along with XRD patterns suggested that the observed morphology modification occurred due to the transport of volatile MgO vapor from the powder bed to the porous structure and via liquid eutectic formation. This increased the linear shrinkage, densification and grain coarsening in both RBSN and MgO-RBSN samples while decreasing the ceramic weight loss and the α/β phase ratio. The lowest linear shrinkage of ≈ 0.4% was observed in RBSN samples heat-treated in an SN powder bed. In contrast, as a result of liquid phase formation and dissolution of α-whiskers with high aspect ratio and high sintering driving force, the highest shrinkage of ≈ 2% occurred in the RBSN samples heat-treated in an MgO-SN powder bed. Full phase transformation, β-grain growth and α-whiskers dissolution were not observed in samples heat-treated in a powder bed comprising just SN.

The role of MgO, grain morphology and microstructural transitions on the structure and morphology of pores, pore size distribution, porosity, density and compressive strength of samples were subsequently studied. Pores were classified based on their size, morphology, origin and accessibility. The presence of whiskers created fine, complex and irregular pores. Inter-particle pores between whiskers occupied around 53.8 vol.% of the total porosity and inter-cluster channels between whisker agglomerates caused larger openings in the microstructure. The pore size distribution graph was therefore bimodal with a peak near $d_{50} \approx 1$ μm, corresponding to the inter-particle pores.

In the presence of MgO in the powder bed, along with microstructural transitions from α-whiskers to β-rods, the structure of pores was modified to large, whisker-free and spherical cavities. Porosity was significantly decreased, and a structure with unimodal pore size distribution, less channel interconnectivity and clean cavities was formed.

The median pore diameters of 1.0 μm and 3.8 μm and porosity of 73.8 vol.% and 30.0 vol.% were measured in RBSN samples before and after heat-treatment in the MgO-SN powder bed, respectively. The median pore diameters of 8.8 μm and 6.5 μm and porosity of 75.1 vol.% and 67.6 vol.% were measured in MgO-RBSN samples before and after the heat-treatment in the MgO-SN powder bed, respectively.

Large pores and high porosity led to compressive strengths lower than 2.5 MPa, while 3D interconnected whiskers with fine pores or low porosity level led to the enhanced compressive strength, between ≈ 4 MPa and ≈ 10 MPa.

The effect of 10 and 15 mol.% CaO, MgO and Al_2O_3 additives on the reaction bonding of silicon, and the microstructural properties and flexural strength of porous RBSN samples were studied comparatively. Upon adding 15 mol.% (≈ 6 wt.%) CaO to the starting silicon, intermediate products formed, and whiskers were eliminated, producing an interconnected open-porous CaO-RBSN microstructure. The observations of high α-Si_3N_4 content and an α/β ratio of ≈ 3.9 with dominant matte grains in this sample suggest the nitridation of Si (g) through a reaction with molecular nitrogen. This mechanism could be attributed to the presence of oxygen in the surrounding atmosphere. As a result of the high α/β phase ratio in the nitrided sample, β-grains with bimodal microstructure and abnormal grain size were developed upon heat-treatment. Formation of a low viscosity liquid phase and high linear shrinkage decreased the porosity of sample from 82.2 vol.% to 78.6 vol.% and increased the flexural strength to ≈ 1.87 MPa.

Formation of fine α-whiskers in the presence of 15 mol.% (≈ 4.2 wt.%) MgO suggested the nitridation of SiO (g). The combination of α/β phase ratio of ≈ 1.75, homogenous liquid phase distribution and simultaneous grain growth at multiple positions led to the formation of β-grains at 1700°C with relatively similar aspect ratio. Compared to the CaO-RBSN samples, higher porosity (≈ 82.6 vol.%) and lower density significantly reduced the flexural strength to a value of ≈ 0.4 MPa.

In the presence of 15 mol.% (≈ 11 wt.%) Al_2O_3, a β-rich microstructure with α/β phase ratio of ≈ 0.08 was developed. This could be attributed to the high chemical and thermal stability of Al_2O_3 and the low content of oxygen in the surrounding atmosphere. This led to fast reduction of silica and formation of α-whiskers in pores by nitridation of SiO (g). Interlocked whiskers and fine inter-particle pores enhanced the flexural strength up to ≈ 2.42 MPa. Partial elimination of whiskers, negligible shrinkage, weight loss and pore formation were also observed upon heat-treatment of Al_2O_3-RBSN at 1700°C, which decreased the flexural strength to ≈ 1.4 MPa.

It is concluded therefore that in order to control the morphology of silicon nitride grains developed in the porous structure, the morphology of pores and thus the mechanical strength of the resultant

samples prepared under the ultra-pure nitrogen gas, we need to design the reaction mechanisms. This becomes feasible through manipulating the composition of the starting materials and the composition of the surrounding Si_3N_4-based powder bed during the heating process.

It is suggested that to fabricate porous RBSN samples with fine pores and a reinforced structure, α-Si_3N_4 whisker formation should be encouraged. With continuous reduction of surface silica and active oxidation of silicon vapor, a whisker-dominated microstructure is developed when SiO vapor nitridation is the dominant reaction and when the partial vapor pressure of oxygen remains low in the system. It is postulated that this happens either in the absence of oxide additives or by the addition of oxides having high thermal and chemical stabilities and high eutectic phase formation temperatures, e.g., Al_2O_3.

On the other hand, it is believed that the addition of oxide powders with high vapor pressure which react with SiO (g) via gaseous phase reaction (e.g., MgO) is a successful approach to hinder the presence of SiO vapor in the reaction site, leading to the formation of a granular, matte-dominated microstructure. Also, phase transformation and grain morphology transition from α-whiskers to β-rods are feasible during the high temperature heat-treatment when volatile oxide species (i.e., MgO vapor) are present in the system. This morphology transition enables high densification, linear shrinkage and formation of a structure with less interconnectivity but larger pores.

In addition, the incorporation of oxide additives with low temperature eutectics is another effective route to fabricate a porous structure with no whiskers present in the system. Hence, introducing CaO to the starting silicon powder is effective in stopping the growth of whiskers resulting in the formation of pores with open cavities, grains with granular morphology and a microstructure with high α-Si_3N_4 content. This results in the formation of a porous structure with less mechanical strength and grains interlocking, but with interconnected channels and large pores with tailored pore morphology. Manipulating the content of added oxide additives makes it feasible to fabricate porous structures with various pore morphologies, textures, strength and pore sizes.

7.2. Contributions

Owing to the broad potential applications of silicon nitride, this study has focused on the fabrication and detailed characterization of porous RBSN ceramics. Emphasis is especially placed on the relationship between the reaction mechanisms at temperature of 525℃ to 1700℃ and the microstructural development during various stages of reactions. This has led to a better understanding of the role of oxide additives on the nitriding behaviour, grain growth mechanism of porous silicon nitride-based ceramics and their corresponding properties. Below are some of the major contributions of the current work:

- This study has illustrated that the microstructure of porous silicon nitride ceramics is highly sensitive to the dominant nitriding reactions and therefore, a well understood formation mechanism is required to control the morphology of RBSN grains and consequently their engineering properties. The understanding of the nitriding and formation mechanisms in highly porous RBSN structures in the presence of additives is the major contribution of this study. This research has illustrated that volatility and reactivity of the oxide additives with surface silica as well as melting point of the eutectic phases are among the important parameters which could be effective in determining the dominant nitriding reaction. Accordingly, formation of intermediate products, liquid phases or vapor species affect the reaction mechanisms and preferentially promote the development of specific porous silicon nitride microstructures.
- The effects of MgO, CaO and Al_2O_3 on the morphology of RBSN grains, phases presented, and the homogeneity of the microstructure have been investigated in depth. This study has illustrated a strong correlation between composition of the starting powder (type and amount of additives) and chemical composition, morphology and size of grains developed during the nitriding process at T≤ 1425℃ and the heat-treatment at T≤ 1700℃.
- Previously produced porous RBSN structures severely lack open-pores and high interconnectivity. The ability to achieve a more precise control over the morphology of grains and thus shape, size and interconnectivity of pores has been another important contribution of this study. A successful route for the production of fully interconnected

porous structures with granular grains is provided by incorporating MgO into the starting silicon powder. Additionally, this study illustrates for the first time that CaO is effective in fabrication of porous Si_3N_4 ceramics with granular grains and open spherical cavities. Our observations showed that compared to MgO, a lower wt.% of CaO could fully eliminate whisker formation and modify the morphology of grains appearing in the porous structure.

- This research has shown that the morphology of grains significantly influenced the characteristics and structure of pores. By formation of RBSN grains ranging from matte, whiskers and rods, various pore morphologies, a wide range of pore size distribution, and pores with open- or closed cavities have been fabricated. This study has illustrated that compared with the normal pores with spherical cavities, inter-particle pores formed from whiskers have a finer size and more complex morphology. Hence, a whisker-free and open-pore microstructure has higher permeability.
- The role of powder bed composition on the microstructure of heat-treated RBSN grains has never been investigated in literature. This study has illustrated that by designing the composition of the surrounding powder bed, magnesia as a volatile oxide can be introduced into the RBSN, and via a solution-precipitation process, the pore structure can be modified from fine irregular pores occupied with α-whiskers to large, clean and spherical pores. Subsequently, linear shrinkage, porosity and density, and grain-coarsening have been highly affected. In addition to the presence of MgO in the powder bed, this microstructural change is dependent on the temperature and duration of heating. Consequently, post heat-treatment process can be adopted as a novel approach to significantly modify the properties of reaction bonded Si_3N_4 ceramics containing no oxide additive.
- Strength of porous ceramics has been studied and linked to the pore structure and grain morphologies. This study has illustrated that the level of porosity, grain morphology, pore size, grain aspect ratio, degree of nitridation and composition of the ceramic significantly influenced the strength of porous ceramics both under compressive and bending stresses. The porous ceramics formed with Si_3N_4 whiskers demonstrated improved mechanical strengths. Hence, having the advantage of better compressive and

flexural strengths, whiskers may be considered as reinforcing material for porous composites.

7.3. Suggestions for Future Work

To understand the influence of oxide additives and fabrication process on the RBSN properties and pore structure there is much work yet to be performed. To continue this investigation, the following recommendations are proposed:

- It is important to investigate the influences of pore structure and grain morphology of porous reaction bonded Si_3N_4 on their permeability behaviour. Effect of pore size, porosity and tortuosity on the permeability performance of samples and the behaviour of flows must be studied. It has been observed previously that lower porosity, smaller pore size and higher tortuosity led to the lower permeability and thus a higher pressure drop across the samples. Gas permeation experiments using nitrogen gas flowing through porous medium and disc-shaped samples (e.g., 3 mm thickness and 20 mm diameter) can be used for this investigation [76]. Finding the inlet and outlet pressure and a relation between gas pressure drop and gas velocity are important to study.
- Gaseous nitriding reactions are encouraged by the presence of surface silica on silicon particles and lead to substantial Si_3N_4 whisker formation in pore networks. The thickness of the silica layer is highly dependent on both the porosity levels and the history of the fabrication process. While a high porosity level might increase the content of silica during the initial heating process through oxidation of silicon, a pre-heat-treatment step prior to the nitridation under H_2 atmosphere could help to remove the oxide layer. Accordingly, the chemical composition of the nitrogen gas plays a significant role on the characteristics of the RBSN grain microstructure. The influences of preheat-treatment, porosity content and composition of nitrogen gas on the fabrication of Si_3N_4 whiskers and morphology of pores in porous RBSN structures need further investigation.
- Few studies have been done to date on the modification of the RBSN microstructure to obtain a highly porous silicon nitride body with controlled pore morphology. In the presence of additives, intermediate materials might be developed which affect the

kinetics of the nitriding reactions. Understanding the influence of different amount and types of additives and impurities (e.g., carbon) on the dominant nitriding mechanism, developed microstructures and the variations of strength would help in the design of the microstructure of porous RBSN and to modify its properties.

- In this research, samples were prepared using aqueous gel casting which is a promising technique for fabrication of structural ceramics with excellent properties and complex shapes. Gel casting of Si-PMMA beads has been studied in detailed previously [19] however no investigation has been made on gel casting behaviour of silicon slurry in the presence of oxide additives. To enhance the mechanical strength of porous structures, it is important to obtain the optimal properties of green bodies. This will be achieved by controlling the gel casting process, by adjusting the concentration of ceramic slurry and rheological agents, and by reducing air bubbles and agglomerates [94]. In order to better control the final properties of the fabricated part, zeta potential and sedimentation height of suspensions, viscosity and rheological properties of slurries, and strength and linear shrinkage of green bodies must be investigated.
- The mechanical strength of porous ceramics is attributed to the porosity content and morphology of grains. The high porosity of RBSN ceramics with large pores generally degraded the mechanical properties while sufficient strength is always required. To find the best combination of properties, it is therefore necessary to improve the mechanical strength of the RBSN foams. It is widely acknowledged that grains with high aspect ratio significantly improve the fracture toughness [139], and composite materials such as whisker-reinforced ceramics exhibit excellent mechanical strength [195]. Crack deflection has been suggested as the main toughening mechanism in samples with coarse-grained microstructures while elastic bridging and pull-out have been observed in samples with fine needles [190]. A comparative study on the toughening behaviour of porous composites reinforced with thick β-rods or thin interlocked whiskers should be investigated.

References

[1] G. Lu, G. Lu (Max) and Z. Xiao, Mechanical properties of porous materials, J. Porous Mat. 6 (1999) 359-368.

[2] B. Seeber, U. Gonzenbach and L. Gauckler, Mechanical properties of highly porous alumina foams, J. Mater. Res. 28 (2013) 2281-2287.

[3] P. Wu, Y. Xu, Z. Huang and J. Zhang, A review of preparation techniques of porous ceramic membranes, J. Ceram. Process. Res. 16 (2015) 102-106.

[4] T. Fukasawa, M. Ando, T. Ohji and S. Kanzaki, Synthesis of porous ceramics with complex pore structure by freeze-dry processing, J. Am. Ceram. Soc. 84 (2001) 230-232.

[5] D. Liu, Influence of porosity and pore size on the compressive strength of porous hydroxyapatite ceramic, Ceram. Int. 23 (1997) 135-139.

[6] P. Sepulveda, F. Ortega, M. Innocentini and V. Pandolfelli, Properties of highly porous hydroxyapatite obtained by the gelcasting of foams, J. Am. Ceram. Soc. 83 (2000) 3021-3024.

[7] Y.J. Park, B.W. Park, S.H. Lee, J.W. Lee, H.S. Yun and I.H. Song, The characterization of porous sintered reaction-bonded silicon nitride ceramics fabricated by Si-additive mixture granules, Int. J. Appl. Ceram. Tec. 8 (2011) 1501–1508.

[8] B.D. Zdravkov, J.J. Cermak, M. Sefara and J. Janku, Pore classification in the characterization of porous materials: A perspective, Cent. Eur. J. Chem. 5 (2007) 385-395.

[9] E.R. Hem, Silicon for silicon nitride based products, M.Sc. dissertation, Norwegian University of Science and Technology, Trondheim, 2014.

[10] S. Hampshire, Silicon nitride ceramics–review of structure, processing and properties, J. Achiev. Mater. Manuf. Eng. 24 (2007) 43-50.

[11] D.V. Tuyen, Y.J. Park, H.D. Kim and B.T. Lee, Formation of rod-like Si_3N_4 grains in porous SRBSN bodies using $6Y_2O_3$-2MgO sintering additives, Ceram. Int. 35 (2009) 2305-2310.

[12] J.F. Yang, Z.Y. Deng and T. Ohji, Fabrication and characterisation of porous silicon nitride ceramics using Yb_2O_3 as sintering additive, J. Eur. Ceram. Soc. 23 (2003) 371-378.

[13] H.L. Hu, Y.P. Zeng, K.H. Zuo, Y.F. Xia, D.X. Yao, J. Günster, J.G. Heinrich and S.Li, Synthesis of porous Si_3N_4/SiC ceramics with rapid nitridation of silicon, J. Eur. Ceram. Soc. 35 (2015) 3781-3787.

[14] W. Guo, L. Wu, T. Ma, Y. You and H. Lin, Rapid fabrication of Si_3N_4 ceramics by reaction-bonding and pressureless sintering, J. Eur. Ceram. Soc. 36 (2016) 3919-3924.

[15] J. Xu, D. Zhu, F. Luo, W. Zhou and P. Li, Dielectric properties of porous reaction-boned Si_3N_4 ceramics with controlled porosity and pore size, J. Mater. Sci. Technol. 24 (2009) 207-210.

[16] J. Xu, F. Luo, D. Zhu, X. Su and W. Zhou, Effect of presintering on the dielectric and mechanical properties of porous reaction-bonded silicon nitride, Mater. Sci. Eng. A 488 (2008) 167-171.

[17] L. Yuan, J. Yu and S. Zhang, Effect of pore-forming agent on porous reaction-bonded silicon nitride ceramcis, IOP Conf. Ser.: Mater. Sci. Eng. 18 (2011) 1-4.

[18] Y.J. Park and H.D. Kim, Permeability enhancement in porous-sintered reaction-bonded silicon nitrides, Int. J. Appl. Ceram. Tec. 8 (2011) 809-814.

[19] A. Alem, M.D. Pugh and R.A.L. Drew, Open-cell reaction bonded silicon nitride foams: fabrication and characterization, J. Eur. Ceram. Soc. 34 (2014) 599-609.

[20] H.M. Jennings and M.H. Richman, Structure. formation mechanisms and kinetics of reaction-bonded silicon nitride, J. Mater. Sci. 11 (1976) 2087-2098.

[21] A.J. Moulson, Reaction-bonded silicon nitride: its formation and properties, J. Mater. Sci. 14 (1979) 1017-1051.

[22] H.M. Jennings, Review, On reactions between silicon and nitrogen, Part 1, Mechanisms, J. Mater. Sci. 18 (1983) 951-967.

[23] A. Alem, R.A.L. Drew and M.D. Pugh, The influence of the nitriding parameters on the microstructure and strength of the open-cell reaction bonded silicon nitride foams fabricated via wet processing, J. Mater. Sci. 49 (2014) 4780-4789.

[24] A. Alem, R.A.L. Drew and M.D. Pugh, The influence of α- and β-Si_3N_4 seeds on the on the properties of reaction bonded silicon nitride foams produced via wet processing, Ceram. Int. 40 (2014) 14287-14294.

[25] A. Alem, M.D. Pugh and R.A.L. Drew, Reaction bonded silicon nitride foams: The influence of iron disilicide on microstructure and mechanical strength, Ceram. Int. 41 (2015) 4966-4974.

[26] C. Kawai and A. Yamakawa, Network formation of Si_3N_4 whiskers for the preparation of membrane filters, J. Mater. Sci. Lett. 17 (1998) 873-875.

[27] P. Becher, C. Hsueh, P. Angelini and T. Tiegs, Toughening behavior in whisker-reinforced ceramic matrix composites, J. Am. Ceram. Soc. 71 (1988) 1050-1061.

[28] P. Becher and G. Wei, Toughening behavior in SiC-whisker-reinforced alumina, J. Am. Ceram. Soc. 67 (1984) C267-C269.

[29] O. Lukianova and O. Ivanov, The effect of Al_2O_3-MgO additives on the microstructure of spark plasma sintered silicon nitride, Ceram. Int. 44 (2018) 390-393.

[30] L. Bowen, T. Carruthers and R. Brook, Hot-pressing of Si_3N_4 with Y_2O_3 and Li_2O as additives, J. Am. Ceram. Soc. 61 (1978) 7-8.

[31] J. Almeida, A. Fonseca, R. Correia and J. Baptista, Pressureless sintering of silicon nitride with additives of the Y_2O_3-Al_2O_3-SiO_2 system, Mater. Sci. Eng. A. 109 (1989) 395-400.

[32] L. Cardenas, J. Lemus-Ruiz, D. Jaramillo-Vigueras and S. de la Torre, Spark plasma sintering of α-Si_3N_4 ceramics with Al_2O_3 and Y_2O_3 as additives and its morphology transformation, J. Alloy. Comp. 501 (2010) 345-351.

[33] A. Alem, R.A.L. Drew and M.D. Pugh, Sintered reaction-bonded silicon nitride foams with a high level of interconnected porosity, J. Mater. Sci. 50 (2015) 570-576.

[34] A. Giachello, P.C. Martinengo, G. Tommasini and P. Propper, Sintering of silicon nitride in a powder bed, J. Mater. Sci. 14 (1979) 2825-2830.

[35] S.H. Lee, G. Rixecker and F. Aldinger, Effects of powder bed conditions on the liquid-phase sintering of Si_3N_4, J. Mater. Res. 17 (2002) 465-472, 2002.

[36] F.L. Riley, Silicon nitride and related materials, J. Am. Ceram. Soc. 83 (2000) 245-265.

[37] B. Motavic, Low temperature sintering additives for silicon nitride, Ph.D. dissertation, Universität Stuttgart, Max-Planck-Institut für Metallforschung, Stuttgart, 2003.

[38] H. Lange, G. Wötting and G. Winter, Silicon nitride-From powder synthesis to ceramic materials, angewandte. chemie. 30 (1991) 1579-1597.

[39] S. Yin, L. Pan, X. Fang, Y. Li , Y. Li , Y. Feng , T. Qiu and J. Yang, Porous Si_3N_4 ceramics prepared by aqueous gelcasting using low–toxicity DMAA system: Regulatable microstructure and properties by monomer content, Ceram. Int. 45 (2019) 9994-10003.

[40] M. Mazzocchi and A. Bellosi, On the possibility of silicon nitride as a ceramic for structural orthopaedic implants. Part I: processing, microstructure, mechanical properties, cytotoxicity, J. Mater. Sci. Mater. Med. 19 (2008) 2881–2887.

[41] G. Ziegler, J. Heinrich and G. Wotting, Review, Relationships between processing, microstructure and properties of dense and reaction-bonded silicon nitride, J. Mater. Sci. 22 (1987) 3041-3086.

[42] M. Muller, J. Rogner, B. Okolo, W. Bauer and R. Knitter, Processing of micro-components made of sintered reaction-bonded silicon nitride (SRBSN). Part 2: Sintering behaviour and micro-mechanical properties, Ceram. Int. 36 (2010) 707-717.

[43] A. Barek, Sintering and post sintering of silicon nitride materials, Ph.D. dissertation, Lulea University of Technology, Lulea, 1992.

[44] R.G. Pigeon, A. Varma and A.E. Miller, Some factors influencing the formation of reaction-bonded silicon nitride, J. Mater. Sci. 28 (1993) 1919-1936.

[45] J.F. Yang, G.J. Zhang and T. Ohji, Fabrication of low-shrinkage, porous silicon nitride ceramics by addition of a small amount of carbon, J. Am. Ceram. Soc. 84 (2001) 1639-1641.

[46] L. Li, J.W. Wang, H. Zhong, L.Y. Hao, H. Abadikhah, X. Xu, C.S. Chen and S. Agathopoulos, Novel α-Si_3N_4 planar nanowire superhydrophobic membrane prepared through in-situ nitridation of silicon for membrane distillation, J. Membr. Sci. 543 (2017) 98-105.

[47] D. Yao, Y. Xia, K.H. Zuo, D. Jiang, J. Gunster, Y.P. Zeng and J.G. Heinrich, The effect of fabrication parameters on the mechanical properties of sintered reaction bonded porous Si_3N_4 ceramics, J. Eur. Ceram. Soc. 34 (2014) 3461-3467.

[48] S.C. Danforth, H.M. Jennings and M.H. Richman, The influence of microstructure on the strength of reaction bonded silicon nitride (RBSN), Acta Metall. 27 (1979) 123-130.

[49] N. Miyakawa, H. Sato, H. Maeno and H. Takahashi, Characteristics of reaction-bonded porous silicon nitride honeycomb for DPF substrate, JSAE Review. 24 (2003) 269-276.

[50] B.S. Bal and M.N. Rahaman, Orthopedic applications of silicon nitride ceramics, Acta Biomaterialia. 8 (2012) 2889-2898.

[51] B.T. Lee and H.D. Kim, Effect of sintering additives on the nitridation behavior of reaction-bonded silicon nitride, Mater. Sci. Eng. 364 (2004) 126-131.

[52] S.M. Boyer and A.J. Moulson, A mechanism for the nitridation of Fe-contaminated silicon, J. Mater. Sci. 13 (1978) 1637-1646.

[53] M. Long , Y. Li, X. Jin, G. Yao, J. Sun and R.V.K. Kumar, Silicon nitridation mechanism in reaction-bonded Si_3N_4–SiC and Si_3N_4-bonded ferrosilicon nitride, J. Am. Ceram. Soc. 101 (2018) 4350-4356.

[54] K. Sillapasa, S. Danchaivijit and K. Sujirote, Effects of silicon powder size on the processing of reaction-bonded silicon nitride, J. M. M. M. 15 (2005) 97-102.

[55] G. Yao, Y. Li, P. Jiang, X. Jin, M. Long, H. Qin and R.V. Kumar, Formation mechanisms of Si_3N_4 and Si_2N_2O in silicon powder nitridation, Solid State Sci. 66 (2017) 50-56.

[56] M.D. Pugh and A.J. Moulson, Vapour transport of magnesia into reaction-bonded silicon nitride, J. Mat. Sci. 30 (1995) 1425-1428.

[57] J.R.G. Evans and A.J. Moulson, The effect of impurities on the densification of reaction-bonded silicon nitride (RBSN), J. Mater. Sci. 18 (1983) 3721–3728.

[58] B.T. Lee, J.H. Yoo and H.D. Kim, Size effect of raw Si powder on microstructures and mechanical properties of RBSN and GPSed-RBSN bodies, Mater. Sci. Eng. A. 333 (2002) 306–313.

[59] F. Swinkels and M. Ashby, A second report on sintering diagrams, Acta Metallurgica. 29 (1981) 259-281.

[60] R.M. German, P. Suri and S.J. Park, Review: liquid phase sintering, J. Mater. Sci. 44 (2009) 1–39.

[61] X. Zhu and Y. Sakka, Textured silicon nitride: processing and anisotropic properties, Sci. Technol. Adv. Mater. 9 (2008) 1-47.

[62] K.P. Plucknett, M. Quinlan, L. Garrido and L. Genova, Microstructural development in porous β-Si_3N_4 ceramics prepared with low volume RE_2O_3-MgO-(CaO) additions (RE=La, Nd, Y, Yb), Mater. Sci. Eng. A. 489 (2008) 337-350.

[63] S.I. Go, Y. Li, J.W. Ko, H.N. Kim, S.H. Kwon, H.D. Kim and Y.J. Park, Microstructure and thermal conductivity of sintered reaction-bonded silicon nitride: the particle size effects of MgO additive, Adv. Mater. Sci. Eng. 2018 (2018) 1-5.

[64] G. Ling and H. Yang, Pressureless sintering of silicon nitride with Magnesia and Yttria, Mater. Chem. Phys. 90 (2005) 31-34.

[65] H. Liang, X. Yao, X. Liu and Z. Huang, The effect of powder bed on the liquid phase sintering of α-SiC, Mater. Des. 56 (2014) 1009-1013.

[66] J.R.G. Evans and A.J. Moulson, On the use of powder beds in the nitridation and subsequent densification of RBSN, J. Mater. Sci. Lett. 2 (1983) 236-238.

[67] J. Rouquerol, D. Avnir, D. Fairbridge, D.H. Everett, J.H. Haynes, N. Pernicone, J.D.F. Ramsay, K.S.W. Sing and K.K. Unger, Recommendations for the characterization of porous solids, Pure. & Appl. Chem. 66 (1994) 1739-1758.

[68] W. Huo, X. Zhang, Y. Chen, Z. Hu, D. Wang and J. Yang, Ultralight and high-strength bulk alumina/zirconia composite ceramic foams through direct foaming method, Ceram. Int. 45 (2019) 1464–1467.

[69] N. Michailidis, A. Tsouknidas, L. Lefebvre, T. Hipke and N. Kanetake, Production, charaterization, and applications of porous materials, Adv. Mater. Sci. Eng. 2015 (2014) 1-2.

[70] B. Bruckschen, H. Seitz, T.M. Buzug, C. Tille, B. Leukers and S. Irsen, Comparing different porosity measurement methods for characterization of 3D printed bone replacement scaffolds, Biomedizinische Technik. 50 (2005) 1609-1610.

[71] J. Seuba, S. Deville, C. Guizard and A. Stevenson, Mechanical properties and failure behavior of unidirectional porous ceramics, Sci. Rep. 6 (2016) 1-11.

[72] J. Yang, S. Shan, R. Janssen, G. Schneider, T. Ohji and S. Kanzaki, Synthesis of fibrous β-Si_3N_4 structured porous ceramics using carbothermal nitridation of silica, Acta Materialia, 53 (2005) 2981-2990.

[73] Z. Du, D. Yao, Y. Xia, K. Zuo, J. Yin, H. Liang and Y.P. Zeng, The high porosity silicon nitride foams prepared by the direct foaming method, Ceram. Int. 45 (2019) 2124-2130.

[74] Y. Hu, Z. Xiao, H. Wang, C. Ye, Y. Wu and S. Xu, Fabrication and characterization of porous $CaSiO_3$ ceramics, Ceram. Int. 45 (2019) 3710-3714.

[75] C. Kawai and A. Yamakawa, Effect of porosity and microstructure on the strength of Si_3N_4: Designed microstructure for high strength, high thermal shock resistance, and facile machining, J. Am. Ceram. Soc. 10 (1997) 2705-2708.

[76] X. Li, D. Yao, K. Zuo, Y. Xia, J. Yin, H. Liang and Y.P. Zeng, Fabrication, microstructural characterization and gas permeability behavior of porous silicon nitride ceramics with controllable pore structures, J. Eur. Ceram. Soc. 39 (2019) 2855-2861.

[77] F. Chen, Q. Shen, F. Yan and L. Zhang, Pressureless sintering of α-Si_3N_4 porous ceramics using a H_3PO_4 pore-forming agent, J. Am. Ceram. Soc. 90 (2007) 2379-2383.

[78] Y. Shao, D. Jia and B. Liu, Characterization of porous silicon nitride ceramics by pressureless sintering using fly ash cenosphere as a pore-forming agent, J. Eur. Ceram. Soc. 29 (2009) 1529-1534.

[79] A. Kalemtas, G. Topates, H. Ozcoban, H. Mandal, F. Kara and R. Janssen, Mechanical characterization of highly porous β-Si_3N_4 ceramics fabricated via partial sintering & starch addition, J. Eur. Ceram. Soc. 33 (2013) 1507-1515.

[80] Y. Lu, J. Yang, W. Lu, R. Liu, G. Qiao and C. Bao, Porous silicon nitride ceramics fabricated by carbothermal reduction-reaction bonding, Mater. Manuf. Process. 26 (2011) 855-861.

[81] J.F. Yang, G.J. Zahng, N. Kondo, T. Ohji and S. Kanzaki, Synthesis of porous Si_3N_4 ceramics with rod-shaped pore structure, J. Am. Ceram. Soc. 88 (2005) 1030-1032.

[82] J. Yu, J. Yang and H. Li, Pore structure control of Si_3N_4 ceramics based on particle-stabilized foams, J. Porous Mater. 19 (2012) 883-888.

[83] J. Zhang, D. Jiang, Q. Lin, Z. Chen and Z. Huang, Properties of silicon carbide ceramics from gelcasting and pressureless sintering, Mater. Des. 65 (2015) 12-16.

[84] M. Kokabi, A. Pirooz and M. Nekoomanesh H., Gel-casting of engineering ceramics, Iran. Polym. J. 7 (1998) 169-175.

[85] P. Tabrizian, F. Golestanifard, A. Alem and E. Ghasemmi, The influence of gel-casting parameters on the preparation of Si porous bodies, Mater. Lett. 183 (2016) 19-22.

[86] W. Zeng, X. Gan, Z. Li and K. Zhou, The preparation of silicon nitride ceramics by gelcasting and pressureless sintering, Ceram. Int. 42 (2016) 11593-11597.

[87] J. Tong and D. Chen, Preparation of alumina by aqueous gelcasting, Ceram. Int. 30 (2004) 2061-2966.

[88] J. Ma, Z. Xie, H. Miao, B. Zhang, L. Xuping and Y. Cheng, Gelcasting of alumina ceramic components in nontoxic Na-alginate–$CaIO_3$–PVP systems, Mater. Des. 26 (2005) 291-296.

[89] T. Zhang, Z. Zhang, J. Zhang and Q.J.D. Lin, Preparation of dense SiC ceramics by aqueous gelcasting, J. Inorg. Mater. 41 (2007) 355-363.

[90] X. Wang, Z. Xie, Y. Huang and Y. Cheng, Gelcasting of silicon carbide based on gelation of sodium alginate, Ceram. Int. 28 (2002) 865-871.

[91] H. Shahbazi, H. Shokrollahi and A. Alhaji, Optimizing the gel-casting parameters in synthesis of $MgAl_2O_4$ spinel, J. Alloy. Compd. 712 (2017) 732-741.

[92] L. Yuan, Z. Liu, X. Hou, Z. Liu, Q. Zhu, S. Wang, B. Ma and J. Yu, Fibrous ZrO_2-mullite porous ceramics fabricated by a hydratable alumina based aqueous gel-casting process, Ceram. Int. 45 (2019) 8824-8831.

[93] C. Zou, C. Zhang, B. Li, S. Wang and F. Cao, Microstructure and properties of porous silicon nitride ceramics prepared by gel-casting and gas pressure sintering, Mater. Des. 44 (2013) 114-118.

[94] X. Guo, Gel casting of high strength ceramics, M.Sc. dissertation, Chalmers University of Technology, Goteborg, 2011.

[95] A. Alem, A novel method to fabricate open-cell silicon nitride foams with a high and controlled level of porosity, Ph.D. dissertation, Concordia University, Montreal, 2014.

[96] J. Wu, X. Zhang and J. Yang, Novel porous Si_3N_4 ceramics prepared by aqueous gelcasting using Si_3N_4 poly-hollow microspheres as pore-forming agent, J. Eur. Ceram. Soc. 34 (2014) 1089-1096.

[97] L.J. Gibson and M.F. Ashby, Cellular solids, structure and properties, second ed., University of Cambridge, 1997.

[98] E. Guzi de Moraes, D. Li, P. Colombo and Z. Shen, Silicon nitride foams from emulsions sintered by rapid intense thermal radiation, J. Eur. Ceram. Soc. 35 (2015) 3263–3272.

[99] K. Yamamoto and T. Sakai, Effect of pore structure on soot deposition in diesel particulate filter, Comput. 4 (2016) 1-11.

[100] I. Sabree, J. E. Gough and B. Derby, Mechanical properties of porous ceramic scaffolds: Influence of internal dimensions, Ceram. Int. 41 (2015) 8425-8432.

[101] K. Bodisova, M. Kasiarova, M. Domanicka, M. Hnatko, Z. Lences, Z. Varchulova Novakova, J. Vojtassak, S. Gromosova and P. Sajgalik, Porous silicon nitride ceramics designed for bone substitute applications, Ceram. Int. 39 (2013) 8355-8362.

[102] A. Jena and K. Gupta, Pore structure characterization of ceramic hot gas fiters, Ceram. Eng. Sci. Proc. 22 (2008) 1-8.

[103] J.F. Despois and A. Mortensen, Permeability of open-pore microcellular materials, Acta Mater. 53 (2005) 1381-1388.

[104] T. Wan, D. Yao, J. Yin, Y. Xia, K. Zuo and Y. Zeng, The microstructure and mechanical properties of porous silicon nitride ceramics prepared via novel aqueous gelcasting, Int. J. Appl. Ceram. Tec. 12 (2015) 1-11.

[105] J. Zhou, J.P. Fan, G.L. Sun, J.Y. Zhang, X.M. Liu, D.H. Zhang and H.J. Wang, Preparation and properties of porous silicon nitride ceramics with uniform spherical pores by improved pore-forming agent method, J. Alloy. Comp. 632 (2015) 655-660.

[106] L. Yin, X. Zhou, J. Yu and H. Wang, Highly porous silicon nitride foam prepared using a route similar to the making of aerated food, Int. J. Appl. Ceram. Tec. 13 (2015) 395-404.

[107] L. Yin, X. Zhou, J. Yu and H. Wang, Preparation of silicon nitride foam with three-dimensional interconnected pore structure, Mater. Design. 89 (2016) 620–625.

[108] L. Han, J. Wang, F. Li and H. Wang, Low-temperature preparation of Si_3N_4 whiskers bonded/reinforced SiC porous ceramics via foam-gelcasting combined with catalytic nitridation, J. Eur. Ceram. Soc. 38 (2018) 1210-1218.

[109] I.C. Jung, S.H. Cho, S.W. Na, J. Lee, H.S. Lee and W.S. Cho, Synthesis of Si_3N_4 whiskers in porous SiC bodies, Mater. Lett. 61 (2007) 4843-4846.

[110] T. Imai, M. Mabuchi, Y. Tozawa and M. Yamada, Superplasticity in β-silicon nitride whisker-reinforced 2124 aluminium composite, J. Mater. Sci. Lett. 9 (1990) 255-257.

[111] J. Dusza, P. Sajgalik, Z. Bastl, V. Kavecansky and J. Durisin, Properties of β-silicon nitride whiskers, J. Mater. Sci. Lett. 11 (1992) 208-211.

[112] P. Sajgalik and J. Dusza, High-temperature strength and fracture toughness of Si_3N_4-β-Si_3N_4 composites, J. Mater. Sci. Lett. 10 (1991) 776-778.

[113] W.S. Park, D.J. Choi and H.D. Kim, Modification of inner pores with silicon carbide whiskers onto the Al_2O_3 substrate by CVI process, Key Eng. Mat. 287 (2005) 212-219.

[114] J.F. Yang, G.J. Zhang, N. Kondo and T. Ohji, Synthesis and properties of porous Si_3N_4/SiC nanocomposites by carbothermal reaction between Si_3N_4 and carbon, Acta Mater. 50 (2002) 4831-4840.

[115] Y. Xu, S. Sang, Y. Li, L.L.Y. Zhao and L. Shujing, Pore structure, permeability, and alkali attack resistance of Al_2O_3-C refractories, Metall. Mater. Trans. A. 45 (2014) 2885-2893.

[116] M. Muller, W. Bauer and R. Knitter, Processing of micro-components made of sintered reaction-bonded silicon nitride (SRBSN). Part 1: Factors influencing the reaction-bonding process, Ceram. Int. 35 (2009) 2577-2585.

[117] C. Gazzara and D. Messier, Determination of phase content of Si_3N_4 by X-ray diffraction analysis, Am. Ceram. Soc. Bull. 56 (1977) 777-780.

[118] X. Xi, H. Xiong, W. Guo, Q. Jiang, Y. Cheng and H.T. Lin, Effect of nitrogen pressure on preparation of β-Si_3N_4 whiskers, Ceram. Int. 43 (2017) 10610–10613.

[119] M.J. Wang and H. Wada, Synthesis and characterization of silicon nitride whiskers, J. Mater. Sci. 25 (1990) 1690-1698.

[120] C. Kawai and A. Yamakawa, Crystal growth of silicon nitride whiskers through a VLS mechanism using SiO_2-Al_2O_3-Y_2O_3 oxides as liquid phase, Ceram. Int. 24 (1998) 135-138.

[121] G.R. Terwilliger and F.F. Lange, Hot-pressing behavious of Si_3N_4, J. Am. Ceram. Soc. 57 (1974) 25-29.

[122] G.W. Brindley and R. Hayami, Kinetics and mechanism of formation of forsterite (Mg_2SiO_4) by solid state reaction of MgO and SiO_2, Philos. Mag. 12 (1965) 505-514.

[123] T. Sasamoto, H.L. Lee and T. Sata, Effects of porosity on vacuum-vaporization of magnesia, J. Ceram. Assoc. 82 (1974) 603-610.

[124] R.H. Lamoreaux and D.L. Hildenbrand, High-temperature vaporization behavior of oxides ll. Oxides of Be, Mg, Ca, Sr, Ba, B, Al, Ga, In, Ti, Si, Ge, Sn, Pb, Zn, Cd and Hg, J. Phys. Chem. Ref. Data. 16 (1987) 419-443.

[125] J.L. de la Pena and M.I. Pech-Canul, Microstructure and kinetics of formation of Si_2N_2O and Si_3N_4 into Si porous preforms by chemical vapor infiltration (CVI), Ceram. Int. 33 (2007) 1349–1356.

[126] P. Kroll and M. Milko, Theoretical investigation of the solid state reaction of silicon nitride and silicon dioxide forming silicon oxyniride under pressure, Z. Anorg. Allg. Chem. 629 (2003) 1737-1750.

[127] B. Bill and H. Heping, The influence of different oxides on the formation of Si_2N_2O from SiO_2 and Si_3N_4, J. Eur. Ceram. Soc. 6 (1990) 3-8.

[128] Z.K. Huang, P. Greil and G. Petzov, Formation of silicon oxinitride from Si_3N_4 and SiO_2 in the presence of Al_2O_3, Ceram. Int. 10 (1984) 14-17.

[129] D. Yao, H. Chen, K.H. Zuo, Y. Xia, J. Yin, H. Liang and Y.P. Zeng, High temperature mechanical properties of porous Si_3N_4 prepared via SRBSN, Ceram. Int. 44 (2018) 11966-11971.

[130] Y. Zhou, H. Hyuga, D. Kusano, C. Matsunaga and K. Hirao, Effects of yttria and magnesia on densification and thermal conductivity of sintered reaction-bonded silicon nitrides, J. Am. Ceram. Soc. 102 (2019) 1579-1588.

[131] W. Li, Y. Wu, R. Huang, S. Ye and H.T. Lin, Effect of Si addition on the mechanical and thermal properties of sintered reaction bonded silicon nitride, J. Eur. Ceram. Soc. 37 (2017) 4491-4496.

[132] J. Chen, N. Li, Y. Wei, B. Han, G. Li, W. Yan and Y. Zhang, Synthesis of Si_3N_4-SiC reaction-bonded SiC refractories: The effects of Si/C molar ratio on microstructure and properties, Ceram. Int. 43 (2017) 16518-16524.

[133] R. Nikonam M., M.D. Pugh and R.A.L. Drew, Formation mechanism of porous reaction-bonded silicon nitride with interconnected pores in the presence of MgO, J. Eur. Ceram. Soc. 39 (2019) 915-927.

[134] L.X. Wu, W.M. Guo, L.Y. Zeng and H.T. Lin, Equiaxed β–Si_3N_4 ceramics prepared by rapid reaction-bonding and post-sintering using TiO_2–Y_2O_3–Al_2O_3 additives, J. Am. Ceram. Soc. 100 (2017) 5353-5357.

[135] C. Yu, J. Ding, C. Deng, H. Zhu and N. Peng, The effects of sintering temperature on the morphology and physical properties of in situ Si_3N_4 bonded MgO–C refractory, Ceram. Int. 44 (2018) 1104-1109.

[136] A.K. Garg and L.C. De Jonghe, Microencapsulation of silicon nitride particles with yttria and yttria-alumina precursors, J. Mater. Res. 5 (1990) 136-142.

[137] B. Bergman and H. Heping, The influence of different oxides on the formation of Si_2N_2O from SiO_2 and Si_3N_4, J. Eur. Ceram. Soc. 6 (1990) 3-8.

[138] P.F. Becher, Multiple scale processes in microstructural evolution: case study of self-reinforced β-Si_3N_4, J. Korean Ceram. Soc. 53 (2016) 575-580.

[139] M. Kramer, M.J. Hoffmann and G. Petzow, Grain growth studies of silicon nitride dispersed in an oxynitride glass, J. Am. Ceram. Soc. 76 (1993) 2778-2784.

[140] D.R. Clarke and G. Thomas, Grain boundary phases in a hot-pressed MgO fluxed silicon nitride, J. Am. Ceram. Soc. 60 (1977) 491-495.

[141] K. Mediaswanti, C. Wen, E.P. Ivanova, C.C. Berndt, F. Malherbe, V.T.H. Pham and J. Wang, A review on bioactive porous metallic biomaterials, J. Biomim. Biomater. Tissue Eng. 18 (2013) 1-8.

[142] M. Mitomo, Pressure sintering of Si_3N_4, J. Mater. Sci. 11 (1976) 1103-1107.

[143] F. Lange, Volatilization associcated with the sintering of polyphase Si_3N_4 materials, J. Am. Ceram. Soc. 65 (1982) 120-121.

[144] D. Li, B. Li, X. Yang, S. Gao and Y. Zheng, Fabrication and properties of in situ silicon nitride nanowires reinforced porous silicon nitride (SNNWs/SN) composites, J. Eur. Ceram. Soc. 38 (2018) 2671-2675.

[145] Z. Du, D. Yao, Y. Xia, K. Zuo, J. Yin, H. Liang and Y.P. Zeng, The high porosity silicon nitride foams prepared by the direct foaming method, Ceram. Int. 45 (2019) 2124-2130.

[146] G.P. Jiang and J.F. Yang, Extrusion of highly porous silicon nitride ceramics with bimodal pore structure and improved gas permeability, J. Am. Ceram. Soc. 101 (2018) 520-524.

[147] J. Zhao, C. Yang, S. Shimai, X. Guan, G. Zhou, J. Zhang, J. Liu and S. Wang, The effect of wet foam stability on the microstructure and strength of porous ceramics, Ceram. Int. 44 (2018) 269-274.

[148] X. Zhang, W. Huo, Y. Lu, K. Gan, S. Yan, J. Liu and J. Yang J, Porous Si_3N_4-based ceramics with uniform pore structure originated from single-shell hollow microspheres, J. Mater. Sci. 54 (2019) 4484-4494.

[149] S. Van Bael, Y.C. Chai, S. Truscello, M. Moesen, G. Kerckhofs, H. Van Oosterwyck, J.P. Kruth and J. Schrooten, The effect of pore geometry on the in vitro biological behavior of human periosteum-derived cells seeded on selective laser-melted Ti6Al4V bone scaffolds, Acta Biomater. 8 (2012) 2824-2834.

[150] M.C. Anderson and R. Olsen, Bone ingrowth into porous silicon nitride, J. Biomed. Mater. Res. A. 92 (2010) 1598-1605.

[151] A.C. Jones, C.H. Arns, D.W. Hutmacher, B.K. Milthorpe, A.P. Sheppard and M.A. Knackstedt, The correlation of pore morphology, interconnectivity and physical properties of 3D ceramic scaffolds with bone ingrowth, Biomaterials 30 (2009) 1440-1451.

[152] T. Konegger, L. Williams and R. Bordia, Planar, polysilazane-derived porous ceramic supports for membrane and catalysis applications, J. Am. Ceram. Soc. 98 (2015) 3047-3053.

[153] H.S. Lee, J.G. Kim and D.J. Choi, The effects of SiC whiskers and an SiC film coating deposited by chemical vapor infiltration (CVI) on a porous cordierite substrate, J. Mater. Sci. 43 (2008) 5574-5578.

[154] L. Li, J.W. Wang, H. Zhong, L.Y. Hao, H. Abadikhah, X. Xu, C.S. Chen and S. Agathopoulos, Novel α-Si_3N_4 planar nanowire superhydrophobic membrane prepared through in-situ nitridation of silicon for membrane distillation, J. Membrane Sci. 543 (2017) 98-105.

[155] A. Mattern, B. Huchler, D. Staudenecker, R. Oberacker, A. Nagel and M. Hoffmann, Preparation of interpenetrating ceramic–metal composites, J. Eur. Ceram. Soc. 24 (2002) 3399-3408.

[156] J. Binner, H. Chang and R. Higginson, Processing of ceramic-metal interpenetrating composites, J. Eur. Ceram. Soc. 29 (2009) 837-842.

[157] F. Ye, J. Zhang, L. Liu and H. Zhan, Effect of solid content on pore structure and mechanical properties of porous silicon nitride ceramics produced by freeze casting, Mater. Sci. Eng. A. 528 (2011) 1421–1424.

[158] T. Isobe, Y. Kameshima, A. Nakajima, K. Okada and Y. Hotta, Gas permeability and mechanical properties of porous alumina ceramics with unidirectionally aligned pores, J. Eur. Ceram. Soc. 27 (2007) 53-59, 2007.

[159] B. Li, P. Jiang, M.W. Yan, Y. Li, X.M. Hou and J.H. Chen, Characterization and properties of rapid fabrication of netwrok porous Si_3N_4 ceramics, J. Alloy Compd. 709 (2017) 717-723.

[160] R. Nikonam M., M.D. Pugh and R.A.L. Drew, Microstructural evolution mechanism of porous reaction bonded silicon nitride ceramics heat-treated in two powder beds, Ceram. Int. 45 (2019) 21986-21997.

[161] J. Zhou and C.A. Wang, Porous yttria-stabilized zirconia ceramics fabricated by nanoaqueous-based gelcasting process with PMMA microsphere as pore-forming agent, J. Am. Ceram. Soc. 96 (2013) 266-271.

[162] R. Liu and C.A. Wang, Effects of mono-dispersed PMMA micro-balls as pore-forming agent on the properties of porous YSZ ceramics, J. Eur. Ceram. Soc. 3 (2013) 1859-1865.

[163] S. Wang, Z. Yang, X. Duan, D. Jia, W. Cui, B. Sun and Y. Zhou, Effects of pore size on microstructure, mechanical and dielectric properties of gel casting BN/Si_3N_4 ceramics with spherical-shaped pore structures, J. Alloy Compd. 581 (2013) 46-51.

[164] J. Bin, W. Zejun and Z. Naiqin, Effect of pore size and relative density on the mechanical properties of open cell aluminum foams, Scripta. Mater. 56 (2007) 169-172.

[165] T.Y. Mays, A new classification of pore sizes, Stud. Surf. Sci. Catal. 160 (2007) 57-62.

[166] M. Saladino, T. Motaung, A.S.A. Luyt, G. Nasillo and E. Caponetti, The effect of silica nanoparticles on the morphology, mechanical properties and thermal degradation kinetics of PMMA, Polym. Degrad. Stabil. 97 (2012) 452-459.

[167] A.J. Wang, Y.P. Lu, R.F. Zhu, S.T. Li, G.Y. Xiao, G.F. Zhao and W.H. Xu, Effect of sintering on porosity, phase, and surface morphology of spray dried hydroxyapatite microspheres, J. Biomed. Mater. Res. A. 87 (2008) 557-562.

[168] H. Giesche, Mercury porosimetry: a general (practival) overview, Part. Part. Syst. Char. 23 (2006) 1-11.

[169] A. Jena and K. Gupta, Characterization of pore structure of filteration media, Fluid/Part. Sep. J. 14 (2002) 1-36,

[170] Z. Luo, H. Liang, C. Qin, J. Zhang, T. Liu and A. Lu, Sintering behavior, microstructures and mechanical properties of porous CaO-Al_2O_3-SiO_2-Si_3N_4 glass-ceramics, J. Alloy. Comp. 773 (2019) 71-77.

[171] M. Precnerova, K. Bodisova, F. Frajkorova, D. Galuskova, Z. V. Novakova, J. Vojtassak, Z. Lences and P. Sajgalik, In vitro bioactivity of silicon nitride–hydroxyapatite composites, Ceram. Int. 41 (2015) 8100-8108.

[172] X. Yang, B. Li, C. Zhang, S. Wang, K. Liu and C. Zou, Fabrication and properties of porous silicon nitride wave-transparent ceramics via gel-casting and pressureless sintering, Mater. Sci. Eng. A. 663 (2016) 174-180.

[173] F. Wang, J. Guo, K. Li, J. Sun, Y. Zeng and C. Ning, High strength polymer/silicon nitride composites for dental restorations, Dent. Mater. 35 (2019) 1254-1263.

[174] G. Pia, L. Casnedi and U. Sanna, Porous ceramic materials by pore-forming agent method: An intermingled fractal units analysis and procedure to predict thermal conductivity, Ceram. Int. 41 (2015) 6350-6357.

[175] J.F. Yang, G.J. Zahng, N. Kondo, T. Ohji and S. Kanzaki, Synthesis of porous Si_3N_4 ceramics with rod-shaped pore structure, J. Am. Ceram. Soc. 88 (2005) 1030-1032.

[176] R. Nikonam M., M.D. Pugh and R.A.L. Drew, Pore structure, porosity and compressive strength of highly porous reaction bonded silicon nitride ceramics with various grain morphologies, J. Mater. Sci. 55 (2020) 509-523.

[177] F. Porz and F. Thummler, Oxidation mechanism of porous silicon nitride, J. Mater. Sci. 19 (1984) 1283-1295.

[178] J. Yang, J.F. Yang, S.Y. Shan, J.Q. Gao and T. Ohji, Effect of sintering additives on microstructure and mechanical properties of porous silicon nitride ceramics, J. Am. Ceram. Soc. 89 (2006) 3843-3845.

[179] Y.F. Kargin, A.S. Lysenkov, S.N. Ivicheva, V.V. Zakorzhevskii, I.P. Borovinskaya, S.V. Kutsev and K.A. Solntsev, Hot-pressed Si_3N_4 ceramics containing $CaO–Al_2O_3–AlN$ modifying additives, Inorg. Mater. 48 (2012) 1158-1163.

[180] H. Yue, X. Wang and J. Tian, Formation of Si_3N_4 reticulated porous ceramics reinforced by needle-like β-Si_3N_4, Ceram. Int. 40 (2014) 8525-8532.

[181] V.A. Hackley, U. Paik, B.H. Kim and S.G. Malghan, Aqueous processing of sintered reaction-bonded silicon nitride: I, dispersion properties of silicon powder, J. Am. Ceram. Soc. 80 (1997) 1781-1788.

[182] P. Silva and J.L. Figueiredo, Production of SiC and Si_3N_4 whiskers in $C+SiO_2$ solid mixtures, Mater. Chem. Phys. 72 (2001) 326-331.

[183] H. Wang, Q. Zhang, H. Yang and H. Sun, Synthesis and microwave dielectric properties of $CaSiO_3$ nanopowder by the sol-gel process, Ceram. Int. 34 (2008) 1405-1408.

[184] G.J. Talwar, C. Joshi, S. Moharil, S. Dhopte, P. Muthal and V. Kondawar, A new precipitation based method for preparation of metasilicate phosphors, J. Alloy Compd. 35 (2011) 8742-8747.

[185] X. Liu, M. Morra, A. Carpic and B. Li, Bioactive calcium silicate ceramics and coatings, Biomed. Pharmacother. 62 (2008) 526-529.

[186] N. Karakus and H. Ozkan Toplan, Synthesizing Si_3N_4 from a mixture of SiO_2-CaO, Mater. Tech. 48 (2014) 171-173.

[187] S. Ni, J. Chang, L. Chou and W. Zhai, Comparison of osteoblast-like cell responses to calcium silicate and tricalcium phosphate ceramics in vitro, J. Biomed. Mater. Res. B 80 (2007) 174-183.

[188] C.M. Wang, X. Pan, M. Rühle, F.L. Riley and M. Mitomo, Review: Silicon nitride crystal structure and observations of lattice defects, J. Mater. Sci. 31 (1996) 5281-5298.

[189] R. Satet and M. Hoffmann, Grain growth anisotropy of β-silicon nitride in rare-earth doped oxynitride glasses, J. Eur. Ceram. Soc. 24 (2004) 3437-3445.

[190] P. Sajgalik, J. Dusza and M.J. Hoffmann, Relationship between microstructure, toughening mechanisms, and fracture toughness of reinforced silicon nitride ceramics, J. Am. Ceram. Soc. 78 (1995) 2619-2624.

[191] M. Mitorno, Microstructural development during gas-pressure sintering of α-silicon nitride, J. Am. Ceram. Soc. 75 (1992) 103-108.

[192] H. Dean Batha and E. Dow Whitney, Kinetics and mechanism of the thermal decomposition of Si_3N_4, J. Am. Ceram. Soc. 56 (1973) 365-369.

[193] C. Chen, X. Liang, M. Luo, S. Zhou, J. Ji, Z. Huang and M. Xu, Preparation and characterization of porous Si_3N_4-bonded SiC ceramics and morphology change mechanism of Si_3N_4 whiskers, Ceram. Int. 45 (2019) 5922-5926.

[194] S. Xiao, H. Mei, D. Han, W. Yuan and L. Cheng, Porous (SiCw-Si_3N_4w)/(Si_3N_4-SiC) composite with enhanced mechanical performance fabricated by 3D printing, Ceram. Inte. 44 (2018) 14122-14127.

[195] M.D. Pugh and L. Gavoret, Nitridation of whisker-reinforced reaction bonded silicon nitride ceramics, J. Mater. Sci. 35 (2000) 3257-3262.

- **Si (ABCR GMBH& CO. KG)**

Silicon powder, -8 micron, 99.995%

Lot Number: 1260957

Table A.1. Si powder specifications	
Size	-8 micron
D90	7.7 µm
D50	3.6 µm
D10	0.6 µm
Purity	99.995%
Al	< 0.001%
C	0.1%
Ca	0.0002%
Fe	< 0.001%
O	1.2%

- **MgO (SIGMA-ALDRICH)**

Magnesium oxide powder, ≥ 99% trace metals basis

Formula Weight: 40.3 gr. mol^{-1}

Lot Number: MKBK1085V

Table A.2. MgO powder specifications		
	Specification	Result
Size	-325 Mesh	
Loss on ignition 1000°C	< 10.0 %	4.8 %
Purity	≥ 99% based on trace metals analysis	
Trace Metal Analysis	< 10000.0 ppm	8348.8 ppm

Aluminum (Al)	438.0 ppm
Barium (Ba)	0.1 ppm
Boron (B)	220.8 ppm
Calcium (Ca)	6404.8 ppm
Chromium (Cr)	6.5 ppm
Iron (Fe)	1012.0 ppm
Manganese (Mn)	140.9 ppm
Nickel (Ni)	14.9 ppm
Potassium (K)	8.7 ppm
Sodium (Na)	40.3 ppm
Titanium (Ti)	27.5 ppm
Vanadium (V)	17.1 ppm
Zinc (Zn)	17.1ppm

- **CaO (ALFA AESAR)**

Calcium oxide powder, 99.95% metal basis

Lot Number: Z01C026

Table A.3. CaO powder specifications

Size	-20 mesh powder
Purity	99.95% metal basis
As	31 ppm
Fe	30 ppm
K	< 1 ppm
Na	10 ppm
Te	35 ppm
Cd	3 ppm
Hg	1 ppm
Mg	10 ppm
Pb	< 10 ppm

- **Al_2O_3 (SIGMA-ALDRICH)**

Aluminum oxide powder, 99.7% trance metal basis

Formula Weight: 101.96 gr. mol^{-1}

Lot Number: MKBJ1604V

Table A.4. Al_2O_3 powder specifications

	Specification	Result
Size	< 10.00 micron	3.00 micron
Purity	99.7% based on trace metals analysis	
Trace Metal Analysis	< 4000.0 ppm	3859.1 ppm
Silver (Ag)		< 1.0 ppm
Arsenic (As)		< 1.0 ppm
Gold (Au)		< 1.0 ppm
Boron (B)		18.0 ppm
Barium (Ba)		5.0 ppm
Beryllium (Be)		< 0.1 ppm
Bismuth (Bi)		< 0.1 ppm
Calcium (Ca)		300.0 ppm
Cadmium (Cd)		< 1.0 ppm
Cerium (Ce)		0.1 ppm
Cobalt (Co)		< 0.1 ppm
Chromium (Cr)		10.0 ppm
Cesium (Cs)		< 0.1 ppm
Copper (Cu)		1.3 ppm
Iron (Fe)		255.0 ppm
Gallium (Ga)		110.0 ppm
Germanium (Ge)		< 1.0 ppm
Hafnium (Hf)		< 0.1 ppm
Mercury (Hg)		< 1.0 ppm
Indium (In)		< 0.5 ppm

Potassium (K)	9.0 ppm
Lanthanum (La)	0.2 ppm
Lithium (Li)	< 0.1 ppm
Magnesium (Mg)	50.0 ppm
Manganese (Mn)	1.2 ppm
Molybdenum (Mo)	0.4 ppm
Sodium (Na)	3000.0 ppm
Niobium (Nb)	< 0.5 ppm
Nickel (Ni)	4.2 ppm
Lead (Pb)	0.3 ppm
Rubidium (Rb)	< 0.1 ppm
Rhenium (Re)	< 0.1 ppm
Antimony (Sb)	< 0.5 ppm
Scandium (Sc)	< 0.1 ppm
Selenium (Se)	< 5.0 ppm
Tin (Sn)	0.7 ppm
Strontium (Sr)	2.0 ppm
Tantalum (Ta)	< 5.0 ppm
Terbium (Tb)	< 0.5 ppm
Thorium (Th)	< 0.1 ppm
Titanium (Ti)	40.0 ppm
Thallium (Tl)	< 0.1 ppm
Uranium (U)	< 0.1 ppm
Vanadium (V)	6.0 ppm
Tungsten (W)	5.0 ppm
Yttrium (Y)	0.1 ppm
Zinc (Zn)	15.0 ppm
Zirconium (Zr)	6.5 ppm

- **XRD Analyses of the Starting Materials**

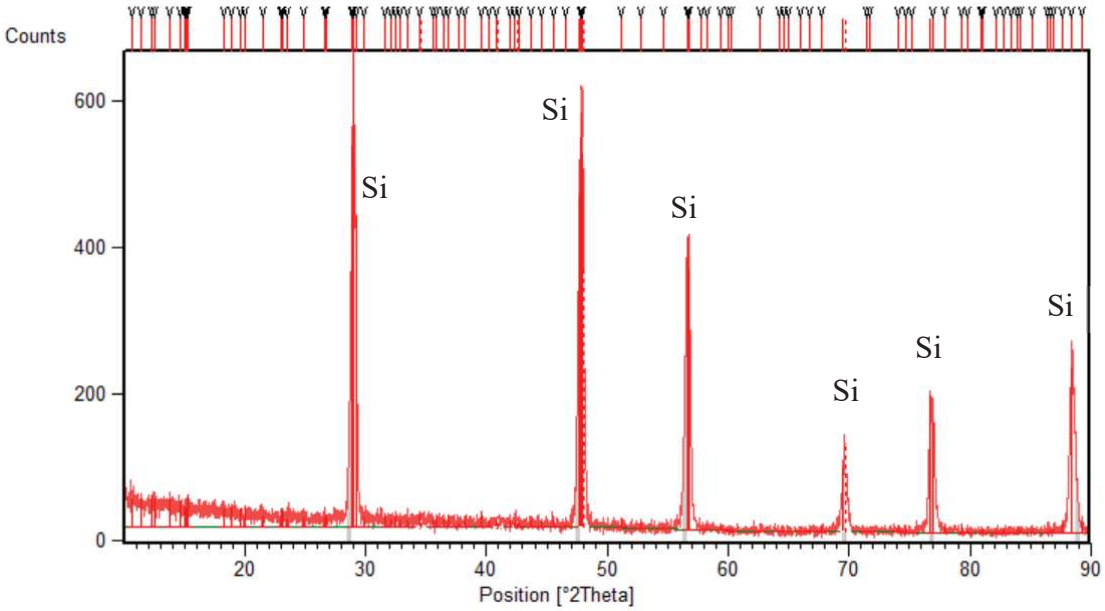

Fig. A.1. XRD analysis of the starting Si powder

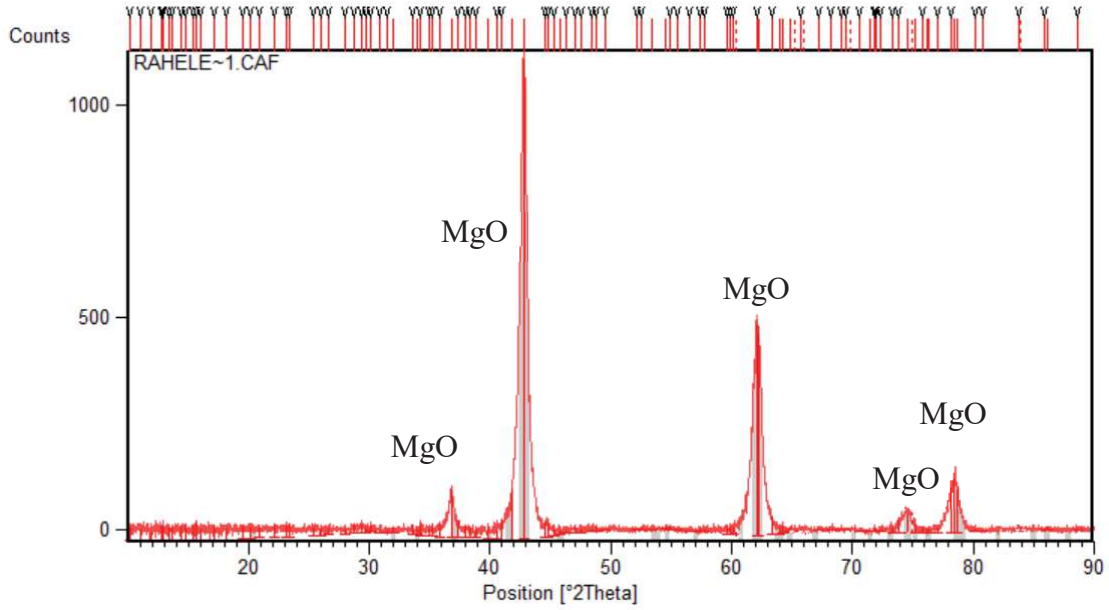

Fig. A.2. XRD analysis of the starting MgO powder

- **TGA Analyses of the Starting Materials**

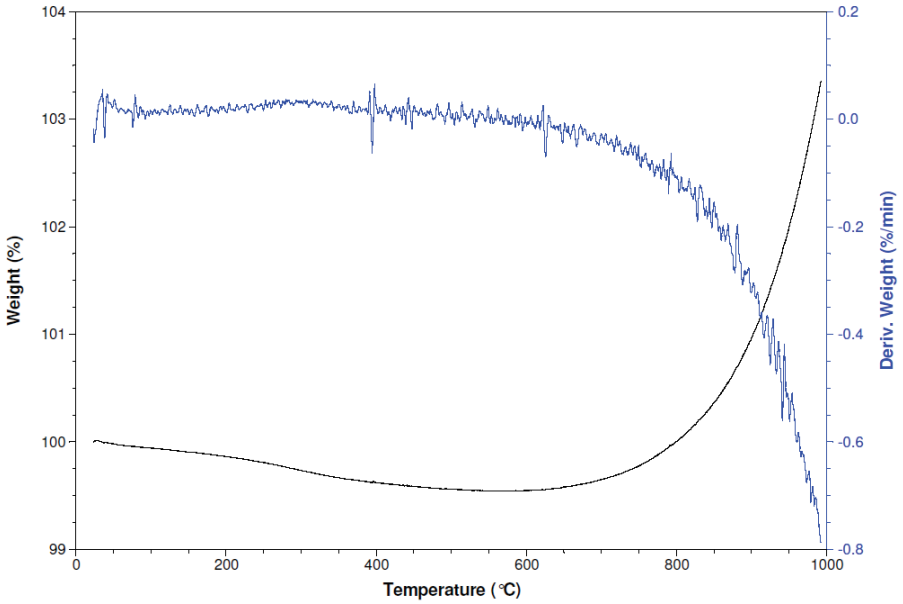

Fig. A.3. TGA analysis of the starting Si powder

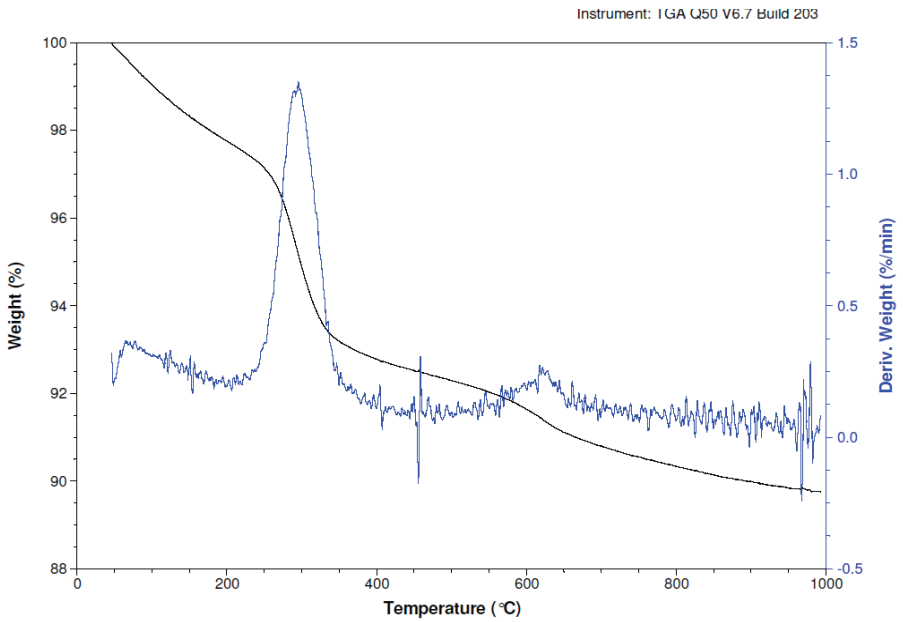

Fig. A.4. TGA analysis of the starting MgO powder

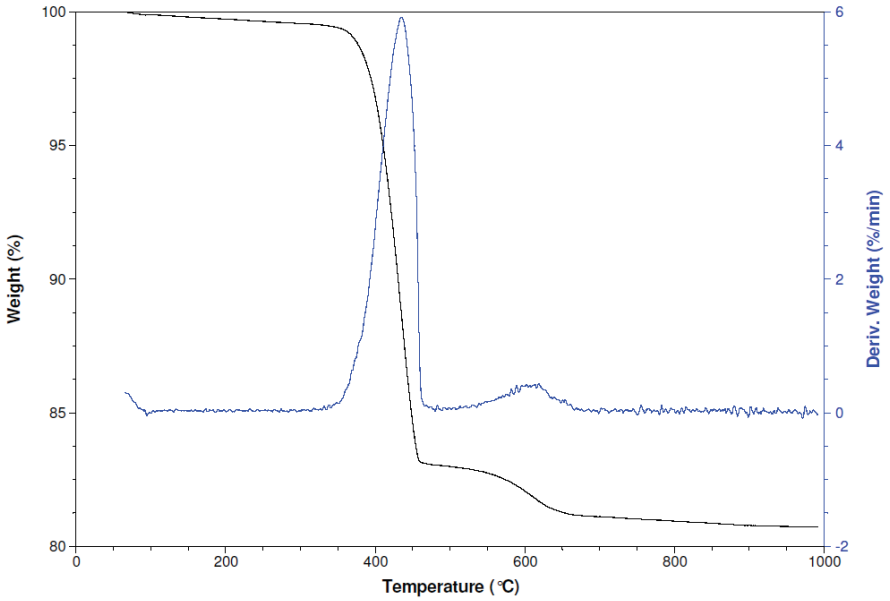

Fig. A.5. TGA analysis of the starting CaO powder

- **SEM Micrographs of the Starting MgO Powder**

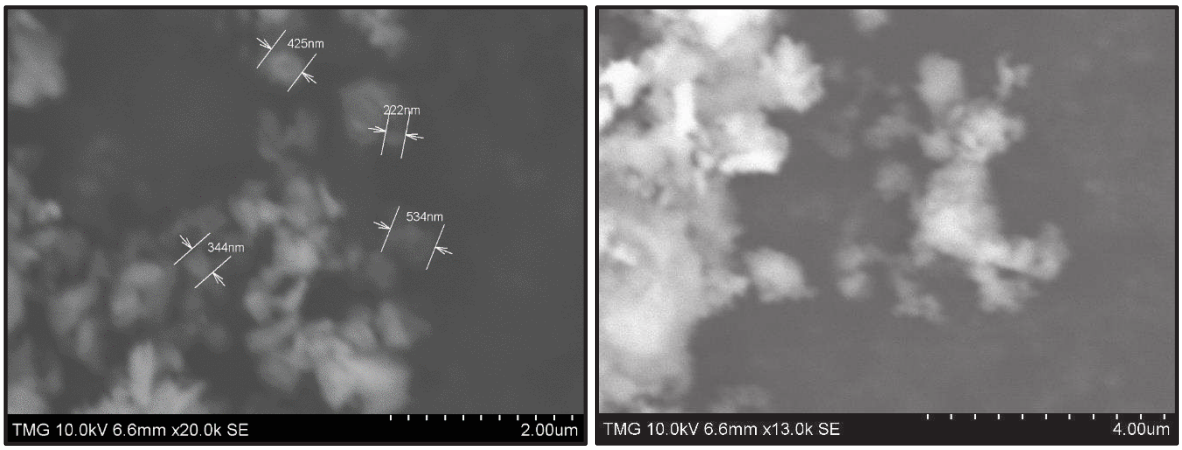

Fig. A.6. SEM micrograph of the starting MgO powder

- **Liquid Eutectic Formation Temperatures**

Table A.5. Eutectic temperatures in the presence of various oxide aids [37]

Additive	Temperature of liquid formation, °C	
M_xO_y	Silicate	Oxynitride
	M_xO_y-SiO_2	M_xO_y-SiO_2-Si_3N_4
Li_2O	1030	1030

CaO	1435	1435
MgO	1543	1390
CeO_2	1560	1460
Al_2O_3	1595	1470
ZrO_2	1640	1590
Y_2O_3	1650	1480

- **Details of the Sample Preparation Procedure**

The premix solution[1] was prepared by dissolving acrylamide (AM, $C_2H_3CONH_2$, SIGMA-ALDRICH CANADA CO.) as the monomer, and N,N'-methylenebisacrylamide (MBAM, $(C_2H_3CONH_2)_2CH_2$, SIGMA-ALDRICH CANADA CO.) as the crosslinker in deionized water. The mixture was stirred using a magnet bar and a stir plate under the fume hood for 30 min. The silicon powder (99.995%, -8 micron, ABCR GMBH & Co. KG) was dispersed in the premix solution after adding the dispersant[2] (DS001, Polymer Innovations Inc.). This is then followed by the addition of the binder[3] (PAM, Poly(acrylamide), Acros Organics, M.W.=5,000,000 6,000,000) and the antifoaming agent[4] (DF002, Polymer Innovations Inc.). PMMA beads (Microbeads) of three particle sizes, 10, 20 and 40 μm, were used in the same weight proportions as space holder and were dispersed for 5 min with the weight ratio of PMMA: Si: H_2O equal to 44: 16: 40.

To study the influences of metallic oxides on microstructural development, MgO (≥99% trace metals basis, -325 mesh powder, SIGMA-ALDRICH CANADA CO.), CaO (99.95% metals basis, -20 mesh powder, Alfa Aesar) and Al_2O_3 (99.7% trace metal basis, <10 μm, SIGMA-ALDRICH CANADA CO.) were mixed to the suspension. Using 1N NH_4OH and HNO_3, pH was adjusted to 8.5, whereupon a strong repulsion between particles exists. After setting the pH, the solution was mixed thoroughly for 30 min through a milling process using polyethylene jars and Si_3N_4 balls to make a homogenous suspension. pH of the slurry was then readjusted using 1N NH_4OH and HNO_3. De-airing of the suspension was done for 10 min under vacuum followed by 5 min slow mixing

[1] AM+MBAM=25 wt.% of DI water with the ratio of AM/MBAM=15
[2] 1.5 wt.% of Si
[3] 2 wt.% of the powder mixture (Si+PMMA)
[4] 0.6 wt.% of the powder mixture (Si+PMMA)

and was repeated to ensure the removal of almost all the trapped air bubbles introduced during milling. N,N,N',N'-tetramethylethylenediamine[5] (TEMED, $C_6H_{16}N_2$, Sigma-Aldrich) was added as the catalyst to start the polymerization reaction and after 5 min mixing ammonium persulfate[6] (APS, 10 wt.% solution, $(NH_4)_2S_2O_8$, Sigma-Aldrich) as the free radical initiator was added. After mixing for 2 min, the slurry was cast in silicon rubber mold and was covered by plastic sheets to stop water evaporation. The molds were kept at 50°C for 3 hr to complete polymerization of the monomers. Then the samples were cooled down to room temperature approximately two hours and then demolded. To dry the demolded sample, it was kept at room temperature for 1 day while covered by a plastic bag followed by 1 day uncovered. Then the drying process continued at 50°C for 1 day, at 70°C for 1 day and at 120°C for 5 hr. Porous silicon structures were formed by polymer burning out at 525°C for 2 hr with a heating rate of 0.5°C min^{-1}. Then the samples were placed on alumina plates and inserted in a furnace chamber which was evacuated by both roughing and diffusion pumps down to 10^{-6} torr.

Nitridation was performed after the furnace chamber was backfilled with N_2 gas (99.999% purity, O_2<2 ppm, H_2O<3 ppm, THC<0.5 ppm, AIR LIQUIDE). To produce porous RBSN, nitridation of the porous silicon body was carried out in the nitrogen atmosphere heated up to 1425°C via the following heating profile: from room temperature to 1350°C with the heating rate of 10°C min^{-1}, to 1425°C with the heating rate of 0.5°C min^{-1} and then dwell for 2 hr and 4 hr at 1425°C.

The post heat-treatment process was performed under the N_2 gas (99.999% purity, O_2<2 ppm, H_2O<3 ppm, THC<0.5 ppm, AIR LIQUIDE) by heating the samples up to 1700°C via the following heating profile: from room temperature to 600°C with the heating rate of 10°C min^{-1}, to 1200°C with the heating rate of 7.5°C min^{-1}, to 1500°C with the heating rate of 6°C min^{-1}, to 1700°C with the heating rate of 5°C min^{-1} and then dwell for 2 hr to 6 hr at 1700°C.

To prevent the decomposition and loss of oxide additive and Si_3N_4, the nitrided samples were embedded in a powder bed of Si_3N_4 and additive powder in the same proportions as the sample. Also, boron nitride (BN, COMBAT, SAINT-GOBAIN ADVANCED CERAMICS) was added to

[5] For 9 ml DI water, 60 µl
[6] For 9 ml DI water, 30 µl

the mixture to prevent the silicon nitride powder sintering with the weight ratio of Si_3N_4: BN equal to 1:1.

To define the role of MgO in the powder bed on the densification, phase transformation and morphology changes of the heat-treated grains, nitrided samples with no additive were prepared in a powder bed containing 12 wt.% MgO, and nitrided samples with 12 wt.% MgO were heat-treated in a powder bed composed of only Si_3N_4 and BN.

- **More Information About the Mechanical Testing Machine**

Instron Machine: designed for tension and compression, Capacity: 100KN**,** Serial No: Q7263**,** Type: Electromechanical

Instron Transducer: designed for tension and compression, Capacity: 5KN**,** Serial No: 57071

The forces verified with machine indicator are within ±0.35 accuracy. Based on Loadcell test certificate sheet, loadcell accuracy has been found to be equal to or better that ±0.25% of the indicated force.